RICE UNIVERSITY

Carbon Based Nanomaterials for Electrochemical Energy Storage Applications

by

Lei Li

A THESIS SUBMITTED
IN PARTIAL FULFILLMENT OF THE
REQUIREMENTS FOR THE DEGREE

Doctor of Philosophy

APPROVED, THESIS COMMITTEE

James M. Tour, Chair
T. T. and W. F. Chao Professor, Chemistry

Pulickel Ajayan
Professor, Department of Mechanical Engineering and Materials Science

Angel A. Martí
Assistant Professor, Chemistry

HOUSTON, TEXAS
April 2015

ABSTRACT

Carbon Based Nanomaterials for Electrochemical Energy Storage Applications

by

Lei Li

Ever-growing energy needs, limited energy resources, and the need to decrease soaring greenhouse gas emissions have brought about an urgent demand on the pursuit of energy alternatives, including both renewable energy sources and sustainable storage technologies. Electrochemical capacitors (ECs) and reversible lithium ion batteries (LIBs) are two promising energy storage technologies that are well positioned to satisfy this need in a green energy future. However, their large-scale deployment has been significantly hindered by several major technological barriers, such as high cost, intrinsically poor safety characteristic, limited life, and low energy density and/or power density. One promising solution is to develop advanced electrodes materials for these devices. In this thesis, various nanomaterials and nanostructures have been developed to improve the electrochemical performance of ECs and LIBs.

My thesis begins with the introduction of energy storage systems of ECs and LIBs in Chapter 1. Chapter 2 to 4 discuss the synthesis of nitrogen-doped carbonized cotton, brush-like structured nanocomposites of polyaniline nanorods-graphene nanoribbons, laser induced graphene-MnO_2, and laser induced graphene-polyaniline and their applications in ECs. All of them demonstrated excellent performance in energy storage, showing high potential applications as electrode materials in ECs. Chapter 5 to 8 discuss a graphene

wrapping strategy designed to synthesize graphene-metal oxide/sulfide-graphene nanoribbons, including graphene-MnO_2-GNRs, graphene-NiO-rGONRs, graphene-Fe_3O_4-GNRs, and graphene-FeS-GNRs. This sandwich structure mitigated the pulverization of these anode materials from their conversion reactions during extended cycling, leading to a large improvement in the cycling stability of anodes in LIBs. To address the volume change of SnO_2-based anode materials, a facile and cost-effective approach was developed to prepare a thin layer SnO_2 on reduced graphene oxide nanoribbons. Chapter 9 discusses how this nanocomposite demonstrated excellent cycling stability with high capacity. For LIBs cathode materials, a hierarchical polyaniline matrix was designed to reduce the dissolution of the intermediate lithium polysulfide into the electrolyte as shown in Chapter 10. This material showed great improvement in cycling stability with high capacity.

Acknowledgments

Here I express my deeply sincere gratitude to my PhD advisor, Professor James M. Tour, for his visionary guidance, insightful advice and genuine support in my PhD program, without which this thesis would not have been accomplished. As one of the world's most famous chemists, Prof. Tour's attitude, behavior, passion and enthusiasm toward science has always been a great encouragement for me to conquer any difficulty in my graduate career. It is truly a fortune that I can have him as my advisor. His mentoring will be a lifelong treasure for me.

I would like to thank Dr. Dustin K. James and Dr. Paul Cherukuri, the lab managers of the Tour lab. They are always the first readers of my manuscript. Their revisions and comments on my writing and research have been so valuable. I truly appreciate their precious time and work. During my graduate years, I would also like to thank Dr. Yu Zhu, Dr. Yang Yang, Dr. Namdong Kim, Dr. Yongsung Li, Dr. Wei Lu, Dr. Chih-Chau Hwang, Dr. Changsheng Xiang, Dr. Zheng Yan, Zhiwei Peng, Gedeng Ruan, Abdul-Rahman O. Raji, E. Loic Samuel, Huilong Fei, Caitian Gao, Qifeng Zhong, Yilun Li, Jibo Zhang, Dr. Bo Chen, Dr. Gang Liang, Carter Kittrell and more, for their generous help in many ways. They assisted and collaborated with me in various aspects. Additionally I appreciate the funding support from Chinese scholarship council.

Last but certainly not least, my family has always been there for me with their unconditional love and support. This dissertation is dedicated to my parents, who I simply could not owe more. They brought me into this world, raised me and made me who I am. I am so proud of them.

Contents

List of Figures

List of Tables

List of Equations

Nomenclature

BET	Brunauer-Emmett-Teller measurement
CVD	Chemical vapor deposition
CV	Cyclic voltammetry
DI water	Deionized water
ECs	Electrochemical capacitors
EDLCs	Electrical double layer capacitors
EIS	Electrochemical impedance spectroscopy
ESR	Equivalent series resistance
FSCs	Flexible supercapacitors
ESEM	FEI Quanta 400 ESEM FEG
GNRs	Graphene nanoribbons
GONRs	Graphene oxide nanoribbons
LIBs	Lithium ion batteries
LIG	Laser induced graphene
LSBs	Lithium sulfur batteries
MSCs	Microsupercapacitors
MWCNTs	Multiwalled carbon nanotubes
NCC	Nitrogen doped carbonized cotton
PANI	Polyaniline
PI	Polyimide
PTFE	Polytetrafluoroethylene

PVA	Poly(vinyl alcohol)
rGONRs	Reduced graphene oxide nanoribbons
SEI	Solid electrolyte interface
SEM	Scanning electron microscopy
TEM	Transmission electron microscopy
TGA	Thermogravimetric analyses
XRD	X-ray diffraction

Chapter 1

Introduction to Energy Storage Devices

Current concerns about limited energy resources and the need to decrease soaring greenhouse gas emissions has brought about an urgent quest to develop renewable resources such as solar, wind, and geothermal that offer sustainable energy without sacrificing environmental quality.[1-3] In particular, solar and wind energy rely heavily on natural conditions and therefore tend to be intermittent and/or diffuse in their output and utility. Thus efficient energy storage is required to balance the off-peak electricity and energy shortfalls during peak periods. Electrochemical capacitors (ECs) and lithium ion batteries (LIBs) are very well positioned to satisfy this need in a green energy future.

ECs and LIBs play an important role in advanced energy storage and management for efficient use of renewable energy. Figure 1.1 shows a Ragone plot comparing the relations among different energy storage systems. ECs have a high power density (2-30 kW/kg) and low energy density (< 10 Wh/kg). Whereas, LIBs have a high energy density (120–200 W h/kg), but a lower power density (0.4-3 kW/kg).[1-2] When LIBs and ECs are

hybridized, they play complementary functions taking the advantages of the former high energy density and the latter high power density.[3]

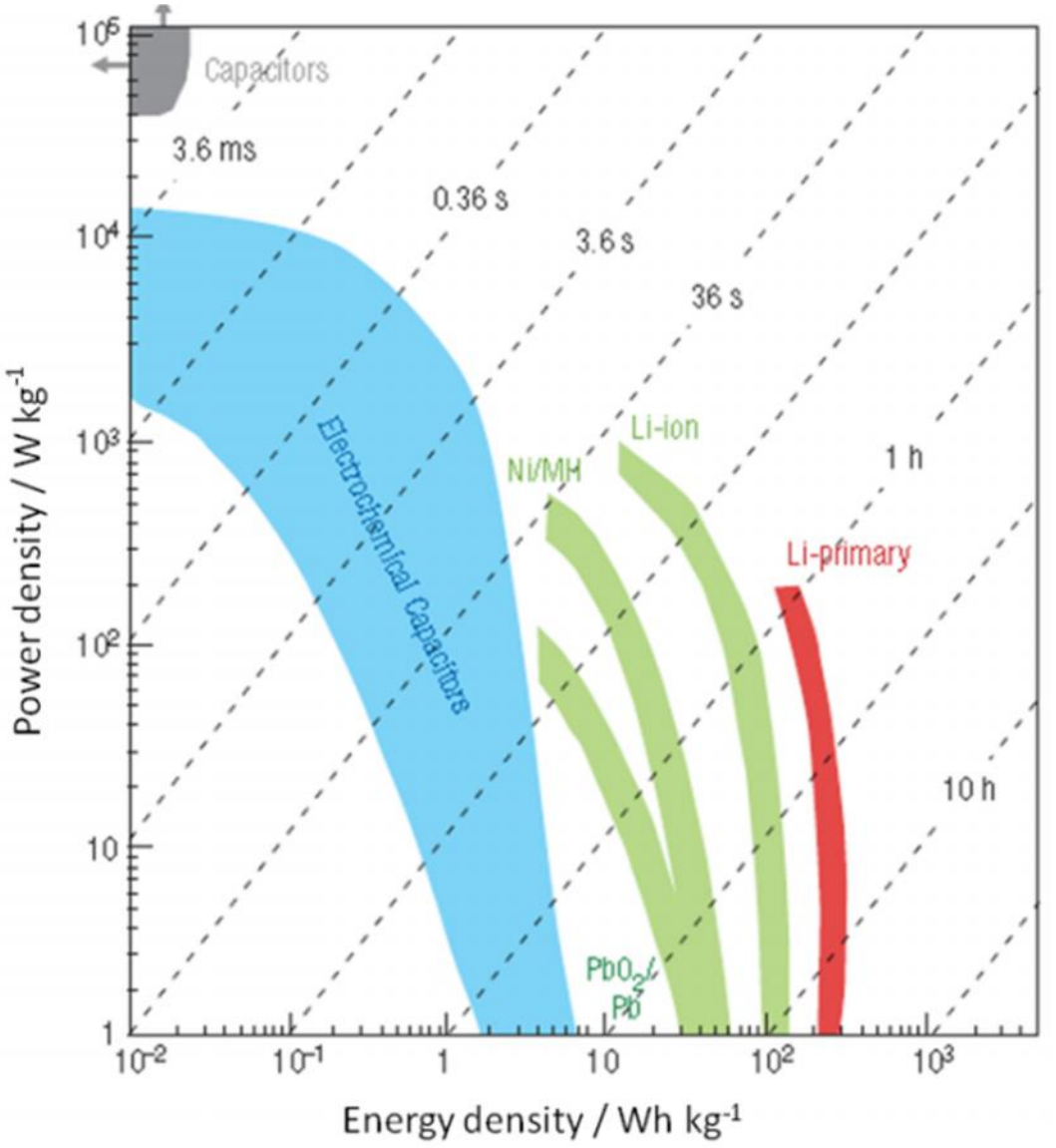

Figure 1.1. Ragone plot showing the power density versus energy density for different electrical energy storage systems. The times shown are the time constants of the systems, which are obtained by dividing energy density by power. (Reproduced with permission from reference 1 2008, Macmillan Publishers Limited)

Currently, both technologies require further optimization due to the increasing demand of new applications. In addition to having a higher energy density and power density, and long cyclic performance, they need to be robust when working in extreme temperature and pressure environments. They also need to ensure environmentally safe and low cost maintenance for future consumer, industrial, military, and space applications.[1-4]

1.1. Current technologies: Electrochemical capacitors and lithium ion batteries

ECs, also named supercapacitors, have attracted great attention thanks to their high long life time (> 100,000), power density (> 10,000 W/Kg), and low cost maintenance.[5-8] ECs have been widely used in many fields, such as consumer electronics, memory back-up systems, and energy management.[7,9] One example is to use ECs for powering the emergency doors of an Airbus A380, which need the large scale implementation.[10]

In 1991, Sony was the first company to commercialize rechargeable LIBs.[11-13] Since then, LIBs have been wildly used in various portable electronic devices, and commercial electric vehicles due to their high energy density, good cycle life, design flexibility, and low self-discharge rate.[12-15]

Recently, ECs drew researcher's attention in the field of hybrid electric vehicles and fuel cell vehicles. When coupled with LIBs or fuel cells, ECs can provide the power for brakes and acceleration.[5,16] ECs demonstrate an equal significance to batteries and fuel cell. As a result, ECs have been designated as important as LIBs for future energy storage systems by the US Department of Energy.[1]

1.2. Introduction to electrochemical capacitors

1.2.1. Construction

The construction of ECs is shown in Figure 1.2. ECs consist of two electrodes, two current collectors, an electrolyte, and one separator. The electrode materials are the most important component in the ECs. Charges are stored and separated at the interface between the electrode and electrolyte. They determine the electrochemical performance of the ECs, such as specific capacitance, life expectancy, resistance, and the cost of the devices. Generally speaking, the electrode materials can be categorized into three classes: carbon materials, conducting polymers, and transitional metal oxide or hydroxide.[5,17]

Carbon materials have many advantages, such as natural abundance, non-toxicity, high chemical and physical stability, easy processing, good electronic conductivity, and lower cost.[5,18] They are one type of the prospective electrode materials in ECs. Carbon materials mainly include activated carbon, carbon nanotubes, graphene, carbon fibers, mesoporous carbon, carbide-derived carbon, and other templated carbons.[5,8,18]

Conducting polymers, such as polyaniline,[19] polypyrrol,[20] polythiophene,[21] poly(3,4-ethylene-dioxythiophene),[22] and poly(3-methyl thiophene) [23] are suitable electrode materials in ECs, which store energy based on their redox reactions. They have many advantages such as low cost, high specific capacitance, good environmental stability, electro-activity, and adjustable redox activity through chemical modification.[24-26]

Transition metal oxides and hydroxides are another type of electrode material that store energy based on reversible Faradic reactions at the interface in ECs. They have higher

specific capacitance and provide higher energy density compared to the carbon materials. The characteristic transition metal oxide and hydroxides are RuO_2, MnO_2, Co_3O_4, NiO, SnO_2, V_2O_5, $Co(OH)_2$, and $Ni(OH)_2$.[5,27]

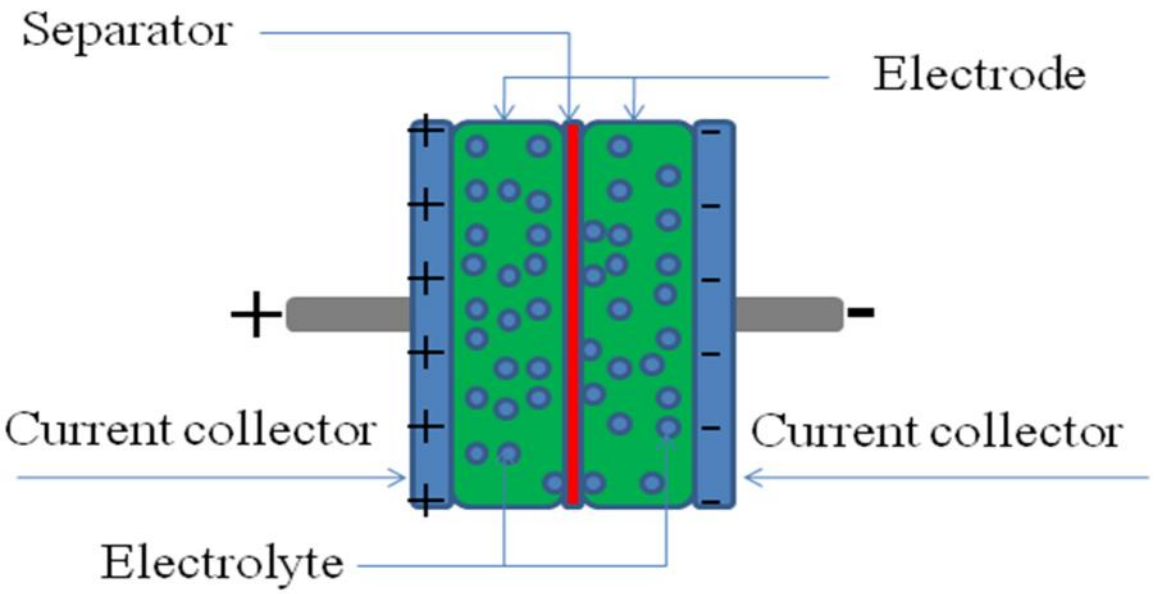

Figure 1.2. Principles of electrochemical capacitors.

Electrolyte is another important component in ECs and can be classified into three types: aqueous, organic, and ionic liquids. [5] Aqueous electrolytes, such as aqueous H_2SO_4, NaOH, KOH, and Na_2SO_4, are the most used in ECs. They all have a high ionic concentration, smaller ionic radius, and low resistance, leading to a higher capacitance and power in ECs. Meanwhile, aqueous electrolytes simplify device fabrication in ambient environments. However, a major disadvantage of aqueous electrolyte is its small potential window range, typically less than 1 V, which limits both the energy density and power density in ECs. Organic electrolyte is another type electrolyte, which can provide a high potential window range of 0 to 3 V. It contains organic salts, such as tetraethylammonium

tetrafluoroborate, in a solvent of acetonitrile or propylene carbonate.[5] However, the large size of the organic electrolytes reduces the capacitance of ECs and presents safety issues due to its flammability, and when used in the assembly of devices, the fabrication processes and conditions should be strictly controlled without moisture and oxygen. Ionic liquids are molten salts existing in liquid form at designated temperatures. It demonstrates desirable properties, such as low vapor pressure and flammability, high thermal and chemical stability, and a large potential window range. The most used ionic liquids are imidazolium and pyrrolidinium with anions such as tetrafluoroborate or trifluoromethanesulfonate.[5] However, the issues of the lower conductivity and poor wettability between ionic liquids and electrode materials should be addressed when ionic liquids are used in ECs.[5]

In ECs, the separator allows the free transfer of charged ions but forbids electronic contact between the electrodes. In an aqueous electrolyte, glass fiber separator, ceramic separator, and paper are used in ECs, whereas in an organic electrolyte, a typical polymer or paper separator are applied.[5]

1.2.2. Mechanism

ECs can be categorized into three types based on the energy storage mechanisms.[5-8,28] The first type of ECs is the Electrical double layer capacitors (EDLCs), which store energy by electrostatic charge accumulation at the interface between the electrode and the electrolyte. Electrons travel from the negative electrode to the positive electrode through the external circuit in the charging process. The positive electrode has extra electric charge and the negative electrode has a deficit of electric charge. In the electrolyte, the movement of anions and cations meet the electron neutrality of the device. The reverse process takes

place during the discharge process. The properties of the electrode and the electrolyte play an important role in the performance of EDLCs. The charge-discharge processes are non-degradative between the electrode and the electrolyte due to the non-Faradic reactions. Therefore, EDLCs can provide ultrahigh power and excellent life cycles.[27,28]

The second type of EC is the pseudocapacitor. In the pseudocapacitor, a reversible Faradic reaction near the electrode surface takes place when a potential is applied. Unlike EDLCs, the charges transfer across the interface between the electrode and the electrolyte in a charge-discharge process similar to the process that occurs in batteries. Pseudocapacitors have higher values in specific capacitance and energy densities compared to EDLCs. However, their power densities is limited due to the relatively low Faradic reaction. Generally speaking, there are three types of Faradic processes occurred on the electrode surface. They are the redox reactions of transition metal oxides, reversible electrochemical doping-dedoping in conductive polymer, and reversible adsorption, respectively.[27,28]

The third type of EC is the hybrid supercapacitor, including the composite symmetric supercapacitor, asymmetric supercapacitor, battery-supercapacitor hybrid.[5] Composite symmetric supercapacitors store energy based on both the electric double layer absorption-desorption and faradic redox reaction in the same two electrodes. Asymmetric supercapacitors consist of two different electrodes. During the charge discharge processes, one electrode stores energy based on the double layer absorption-desorption (Non-Faradic reaction), the other is the redox reaction (Faradic reaction) with or without a double layer absorption-desorption. In this type of hybrid supercapacitor, both Faradic capacitance and EDLCs mechanisms occur simultaneously while one of them plays a greater role.[28]

1.2.3. Fabrication

ECs devices can be fabricated in five steps: the coating electrode, winding, filling with an electrolyte, testing, and welding and sealing.[5] Active materials, binders and conductive additives are mixed in a certain mass ratio to form a homogeneous slurry, which is then spread onto the current collectors forming the electrode. The electrode is dried and roll-pressed to obtain a uniform electrode coating layer. Based on the types of electrolyte, the electrolyte filling process is different. If organic electrolytes or ionic liquids are used in the device, the electrodes should be put into a glove box with ultra-low moisture. The electrolyte is filled into the sandwiched device of electrode-separator-electrode. If aqueous electrolyte is used in the device, the filling process can be done in an ambient environment doing the same operation. The amount of electrolyte used in the device plays a significant role in the electrochemical performance because excessive gassing or leakage in operation may happen if excess electrolyte is used. After the electrolyte filling, the device is tested, normally two to five formation cycles to remove away the abnormal devices. The devices may be cycled further to establish stable capacity, depending on applications.[5]

1.2.4. Measurement

Cyclic voltammetry, galvanostatic charge discharge experiments, and electrochemical impedance spectroscopy are done in order to study the electrochemical performance of the ECs in energy storage. Six criteria are used to evaluate the performance of ECs: specific capacitance, energy density, power density, cycling stability of electrode, safe operation, and cost.

The gravimetric specific capacitance is calculated based on the information from galvanostatic charge-discharge curve using equation 1.1:

$$C = 4I \quad t / (\quad V \times m) \quad (1)$$

where I is the current applied, t is the discharging time, V is the potential range after the IR drop, and m is the mass of two electrode materials.

The maximum energy density is obtained by using equation 1.2:

$$E = C\ V^2 / 8 \quad (2)$$

where C is the specific capacitance, V is the voltage, m is the mass of two electrode materials.

The power densities include the maximum power density and average power density obtained by using equation 1.3 and equation 1.4:

$$P = V^2 / (4 \times R \times m) \quad (3)$$

$$P_{(\text{average})} = E / \text{t} \quad (4)$$

respectively, where E is the energy density, V is the voltage, m is the mass of two electrode materials, t is the total discharge time, and R is the equivalent series resistance obtained from the IR drop by equation 1.5:

$$R = V_{drop}/(2I) \quad (5)$$

Where V_{drop} is the potential difference at the beginning of the discharge and I is the constant current.

Therefore, the high specific capacitance, large operating potential window range, and small equivalent series resistance are required to obtain the high electrochemical performance in ECs.

1.3. Introduction to lithium ion batteries

1.3.1. Construction

The construction of LIBs is depicted in Figure 1.3, which consists of an anode, a cathode, a separator, two current collectors and an electrolyte. Copper foil and aluminum foil are normally used as current collectors in the anode and cathode, respectively.

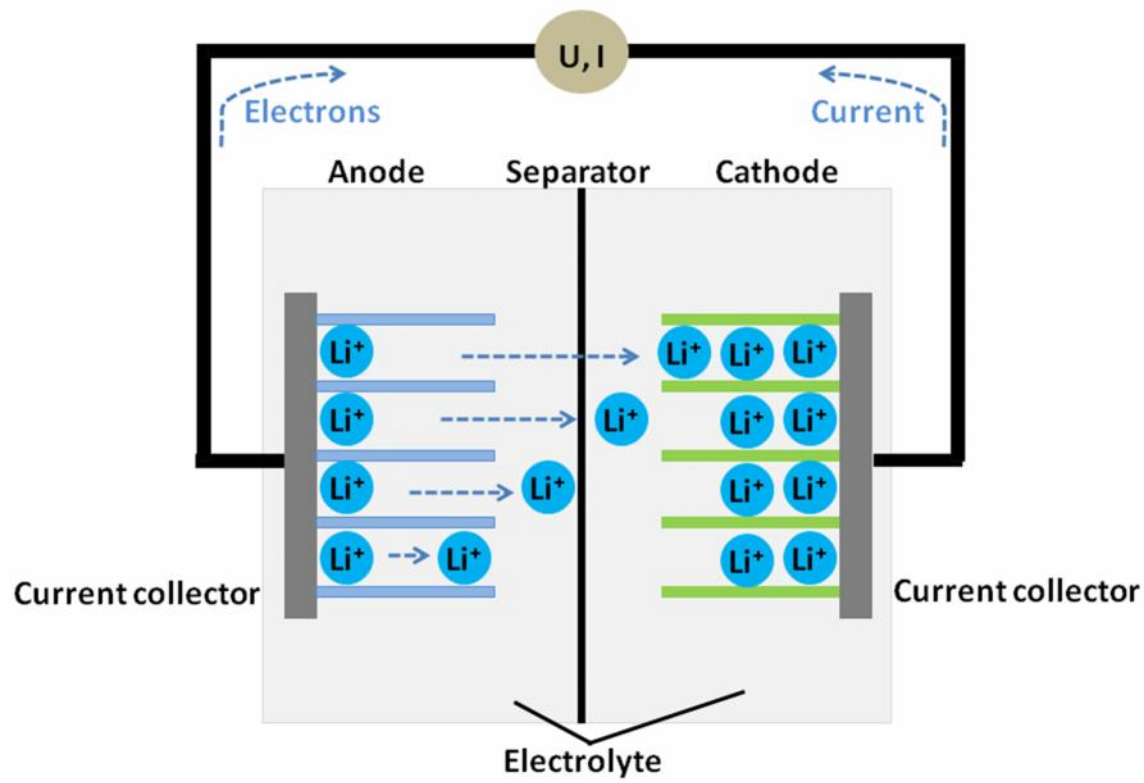

Figure 1.3. Principle of the lithium ion batteries.

Electrode materials are the most important components in LIBs. Anode materials in LIBs can be classified into three types based on energy storage mechanisms.[29] The first type is the intercalation/de-intercalation mechanism. The materials include some transition metal oxides and other compounds with a two-dimensional (2D) layer structure or three-dimensional (3D) network structure, such as graphite and TiO_2. They can reversibly intercalate/de-intercalate Li ions into/from the lattice without destroying the crystal structure. The second type is the alloying/de-alloying mechanism. Many elements, such as Si, Sn, In, Bi, and Zn, and transition metal oxides such as SnO_2 and SnO belong to this type. They react with Li forming alloys at low potentials (≤ 1.0 V vs Li).[29,30] The third type is the conversion reaction or redox reaction mechanism. This type is general and

includes oxides, fluorides, oxyfluorides, sulfides, nitrides, and phosphides, such as MnO_2, MnS, Fe_2O_3, FeS, FeF_3, NiO, NiS, and NiP_3.[31]

Cathodes also play an significant role in the LIBs. The energy density of LIBs is the result of the product's capacity and voltage. When the anodes are fixed, the higher voltage and capacity of the cathode, the higher the energy of the LIBs. Therefore, many research efforts have been devoted to the development of the cathode materials. Generally speaking, there are two major types based on the structure of the cathode materials. The first type of cathode material is a layered structure, which enables the 2D diffusion of lithium ions in the structure. The characteristic samples of this type include $LiCoO_2$, Li_2MoO_3, $Li_{0.7}MnO_2$, $LiNiO_2$, and $LiCrO_2$.[32] The cathode materials in the spinal structure, which enables the 3D diffusion of the lithium ions, can also be treated as a layer type structure. The other group of cathode materials, such as VO_2 and $LiFePO_4$, has a more open structures. This type materials generally have better safety and lower cost compared to the first group.

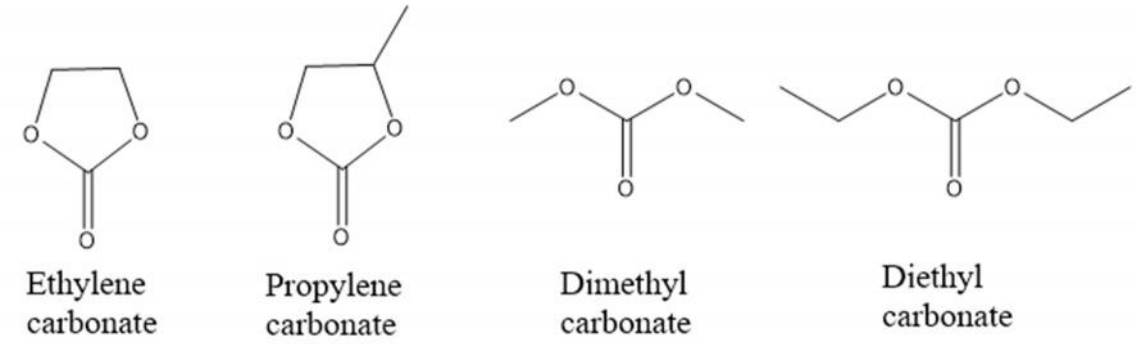

Figure 1.4. Carbonate solvents of electrolytes used in lithium ion batteries.

Electrolyte is another important component in LIBs that acts as an ionic conductor to transport lithium ions back and forth between the cathodes (positive electrodes) and anodes (negative electrodes) during charge-discharge processes in LIBs. The electrolyte must be in good contact with the electrode materials for better performance in LIBs. Normally, the commercialized electrolytes are non-aqueous electrolyte solutions in the market, where lithium salts are dissolved in aprotic organic solvents. Lithium hexafluorophosphate ($LiPF_6$) is the most popular lithium salt in electrolytes. Other lithium salts, such as lithium hexafluoroarsenate ($LiAsF_6$) and lithium bis(trifluoromethanesulfonyl)imide (LiTFSI), have also been developed.[15,33] The aprotic organic solvents are normally a mixture of carbonate solvents. Figure 1.4 shows the common carbonate solvents used in electrolytes for LIBs. A characteristic sample of the electrolytes is 1 M $LiPF_6$ in ethylene carbonate and diethyl carbonate (EC: DEC, 1:1 in volume). Polymer electrolytes and aqueous electrolytes are also developed according to the application requirements.[15,34]

Table 1.1. Major manufacturers of separators along with their typical products for lithium ion batteries.

Manufacturer	Structure	Composition	Process	Trade name
Asahi Kasai	single layer	PE	wet	HiPore
Entek Membranes	single layer	PE	Wet	Teklon
Mitsui Chemical	single layer	PE	Wet	
Nitto Denko	single layer	PE	Wet	
DSM	single layer	PE	Wet	Solupur
Tonen	single layer	PE	wet	Setela
Ube Industries	multi layer	PP/PE/PP	dry	U-Pore
Celgard LLC	single layer	PP, PE	Dry	Celgard
	Multilayer	PP/PE/PP	Dry	Celgard
	PVdF coated	PVdF, PP, PE, PP/PE/PP	Dry	Celgard

Separators are an important component in LIBs. A separator is placed between positive electrode and negative electrode in LIBs. It can allow the ionic flow but prevent the directly electric contact of the electrodes. Many different separators have been developed in LIBs. On the market, separators are manufactured in different format based on the chemical and physical characteristics of materials, such as cellulosic papers, nonwoven fabrics, foams, ion exchange membranes, and microporous flat sheet membranes of polymeric materials. Table 1.1 shows the major manufacturers of separators along with their typical products for LIBs.[15,35]

1.3.2. Mechanism

Figure 1-3 shows the operating principle of a Li-ion battery. In the discharge process, the Li^+ are moved from the anode to the cathode while the electrons move through an external circuit from the anode to the cathode. In this process, Li^+ are oxidized. In the charge process, the reverse process happens and ions are reduced (Figure 1.3). The electrons in the external circuit are produced by the oxidation reaction.

1.3.3. Fabrication

LIBs can be fabricated in five steps: coating active materials on current collectors, winding them with a separator, assemble the wound electrodes into a battery case, filling with electrolyte, and finally sealing the battery case, respectively.[15]

1.3.4. Measurement

CR2032 coin-type cells are used to study the electrochemical performance of the electrode materials in LIBs. CV and EIS experiments are carried out on a CHI660D

electrochemical station. The galvanostatic discharge charge experiments are done on the LAND CT2001A battery system. All the experiments are carried out at room temperature. Normally, there are three factors to determine the electrochemical performance of the LIBs, which are the capacity, rate, and cycling performance.

1.4. Advantages and disadvantages of electrochemical capacitors and lithium ion batteries

Table 1.2 shows the advantages and disadvantages of ECs and LIBs. ECs demonstrate many advantages, such as high power density, the long life expectancy, environmental friendliness, good safety, and high efficiency. However, low energy density, the high cost and high self discharging rate of ECs limits their applications. On the contrary to ECs, LIBs show high energy density, low self-discharging rate, and low maintenance. LIBs also suffer from many problems, such as the low power density, lacked safety, and aging, which hinder their wild applications, especially in commercial electric vehicle markets.[5,15,27]

Table 1.2. Advantages and disadvantages of electrochemical capacitors and lithium ion batteries.

Devices	Advantages	Disadvantages
Electrochemical capacitor	High power density, long life expectancy, long shelf life, high efficiency, wide range of operating temperatures, environmental friendliness, good safety	Low energy density, high cost, high self-discharging rate
Lithium ion battery	High energy density, low self-discharge rate, Low Maintenance	Low power density, bad safety, aging

1.5. Current marketing

The global market for ECs is $470 million in the world in 2010 and will reach $1.2 billion at the annual growing rate of 21.4% by 2015.[36,37] It is projected to be $3.5 billion in 2020, taking 5% of the battery market.[36] The global market for LIBs is $11.8 billion in the world in 2010.[29,38] About 60% of LIBs are used in mobile phones and the rest are for medical, power tools, notebook computers, and other uses.[29] It will be expected to dramatically increase to $31.4 billion in 2015 and even up to $53.7 billion in 2020.[29,38]

1.6. References

1. Simon, P.; Gogotsi, Y. Materials for electrochemical capacitors. *Nat. Mater.* **2008**, 7, 845-854.

2. An, K. H.; Kim, W. S.; Park, Y. S.; Moon, J. M.; Bae, D. J.; Lim, S. C.; Lee, Y. S.; Lee, Y. H., Electrochemical Properties of High-Power Supercapacitors Using Single-Walled Carbon Nanotube Electrodes. *Adv. Funct. Mater.* **2001,** *11*, 387-392.

3. Béguin, F.; Presser, V.; Balducci, A.; Frackowiak, E., Carbons and Electrolytes for Advanced Supercapacitors. *Adv. Mater.* **2014,** *26*, 2219-2251.

4. Cao, Z.; Wei, B., A perspective: carbon nanotube macro-films for energy storage. *Energy Environ. Sci.* **2013,** *6*, 3183-3201.

5. Wang, G.; Zhang, L.; Zhang, J., A review of electrode materials for electrochemical supercapacitors. *Chem. Soc. Rev.* **2012,** *41*, 797-828.

6. Simon, P.; Gogotsi, Y., Capacitive Energy Storage in Nanostructured Carbon–Electrolyte Systems. *Acc. . Chem. Res.* **2012,** *46*, 1094-1103.

7. Zhang, L. L.; Zhao, X. S., Carbon-based materials as supercapacitor electrodes. *Chem. Soc. Rev.* **2009,** *38*, 2520-2531.

8. He, Y.; Chen, W.; Gao, C.; Zhou, J.; Li, X.; Xie, E., An overview of carbon materials for flexible electrochemical capacitors. *Nanoscale* **2013,** *5*, 8799-8820.

9. E5. J. R. Miller and A. F. Burke, Electrochem. Soc. Interface Spring,2008, 17, 53.

10. Jiang, H.; Lee, P. S.; Li, C., 3D carbon based nanostructures for advanced supercapacitors. *Energy Environ. Sci.* **2013,** *6*, 41-53.

11. Nishi, Y., Lithium ion secondary batteries; past 10 years and the future. *J. Power Sources* **2001,** *100*, 101-106.

12. Kucinskis, G.; Bajars, G.; Kleperis, J., Graphene in lithium ion battery cathode materials: A review. *J. Power Sources* **2013,** *240*, 66-79.

13. Kraytsberg, A.; Ein-Eli, Y., Higher, Stronger, Better A Review of 5 Volt Cathode Materials for Advanced Lithium-Ion Batteries. *Adv. Energy Mater.* **2012,** *2*, 922-939.

14. Scrosati, B.; Garche, J., Lithium batteries: Status, prospects and future. *J. Power Sources* **2010,** *195*, 2419-2430.

15. Lithium Batteries: Science and Technology (Eds: G.-Abbas Nazri , G. Pistoia), Kluver Academic Publishers, Boston/Dordrecht/New York/London 2004.

16. Zhang, J.; Song, T.; Shen, X.; Yu, X.; Lee, S.-T.; Sun, B., A 12%-Efficient Upgraded Metallurgical Grade Silicon–Organic Heterojunction Solar Cell Achieved by a Self-Purifying Process. *ACS Nano* **2014**.

17. Daiwon C.; Prashant N. K. Nanocrystalline TiN Derived by a Two-Step Halide Approach for Electrochemical Capacitors *J. Electrochem. Soc*, **2006**, 153, A2298.

18. Ghosh, A.; Lee, Y. H., Carbon-Based Electrochemical Capacitors. *ChemSusChem* **2012,** *5*, 480-499.

19. Li, L.; Raji, A.-R. O.; Fei, H.; Yang, Y.; Samuel, E. L. G.; Tour, J. M., Nanocomposite of Polyaniline Nanorods Grown on Graphene Nanoribbons for Highly Capacitive Pseudocapacitors. *ACS Appl. Mater. Interfaces* **2013,** *5* (14), 6622-6627.

20. Clemente, A.; Panero, S.; Spila, E.; Scrosati, B., Solid-state, polymer-based, redox capacitors. *Solid State Ionics* **1996,** *85* (1–4), 273-277.

21. Laforgue, A.; Simon, P.; Sarrazin, C.; Fauvarque, J.-F., Polythiophene-based supercapacitors. *J. Power Sources* **1999,** *80*, 142-148.

22. Lota, K.; Khomenko, V.; Frackowiak, E., Capacitance properties of poly(3,4-ethylenedioxythiophene)/carbon nanotubes composites. *J. Phys. Chem. Solids* **2004,** *65*, 295-301.

23. Sivaraman, P.; Thakur, A.; Kushwaha, R. K.; Ratna, D.; Samui, A. B. Poly(3-methyl thiophene)-Activated Carbon Hybrid Supercapacitor Based on Gel Polymer Electrolyte. *Electrochem. Solid-State Lett.*, **2006**, 9, A435.

24. Prasad, K. R.; Koga, K.; Miura, N., Electrochemical Deposition of Nanostructured Indium Oxide: High-Performance Electrode Material for Redox Supercapacitors. *Chem. Mater.* **2004,** *16*, 1845-1847.

25. Fan, L.-Z.; Maier, J., High-performance polypyrrole electrode materials for redox supercapacitors. *Electrochem. Commun.* **2006,** *8*, 937-940.

26. B. E. Conway, Electrochemical Supercapacitors, Kluwer Academic/Plenum Press, New York, 1999.

27. Docherty, C. J.; Parkinson, P.; Joyce, H. J.; Chiu, M.-H.; Chen, C.-H.; Lee, M.-Y.; Li, L.-J.; Herz, L. M.; Johnston, M. B., Ultrafast Transient Terahertz Conductivity of Monolayer MoS2 and WSe2 Grown by Chemical Vapor Deposition. *ACS Nano* **2014**.

28. Wang, F.; Xiao, S.; Hou, Y.; Hu, C.; Liu, L.; Wu, Y., Electrode materials for aqueous asymmetric supercapacitors. *RSC Adv.* **2013,** *3*, 13059-13084.

29. Reddy, M. V.; Subba Rao, G. V.; Chowdari, B. V. R., Metal Oxides and Oxysalts as Anode Materials for Li Ion Batteries. *Chem. Rev.* **2013,** *113*, 5364-5457.

30. Armstrong, M.; O'Dwyer, C.; Macklin, W.; Holmes, J. D., Evaluating the performance of nanostructured materials as lithium-ion battery electrodes. *Nano Res.* **2014,** *7*, 1-62.

31. Cabana, J.; Monconduit, L.; Larcher, D.; Palacín, M. R., Beyond Intercalation-Based Li-Ion Batteries: The State of the Art and Challenges of Electrode Materials Reacting Through Conversion Reactions. *Adv. Mater.* **2010,** *22*, E170-E192.

32. Wang, Y.; Cao, G., Developments in Nanostructured Cathode Materials for High-Performance Lithium-Ion Batteries. *Adv. Mater.* **2008,** *20*, 2251-2269.

33. Aravindan, V.; Gnanaraj, J.; Madhavi, S.; Liu, H.-K., Lithium-Ion Conducting Electrolyte Salts for Lithium Batteries. *Chem. Eur. J.* **2011,** *17*, 14326-14346.

34. Xu, K., Nonaqueous Liquid Electrolytes for Lithium-Based Rechargeable Batteries. *Chem. Rev.* **2004,** *104*, 4303-4418.

35. Arora, P.; Zhang, Z., Battery Separators. *Chem. Rev.* **2004,** *104*, 4419-4462.

36. Zhi, M.; Xiang, C.; Li, J.; Li, M.; Wu, N., Nanostructured carbon-metal oxide composite electrodes for supercapacitors: a review. *Nanoscale* **2013,** *5* (1), 72-88.

37. http://www.reportlinker.com/p0363454/Supercapacitors-Technology-Developments-and-Global-Markets.html, accessed 24 July 2012.

38. http://www.isuppli.com/semiconductor-value-chain/pages/strong-growth-to-drive-lithium-ion-battery-market-to-61-billion-by-2020.aspx (Accessed on Feb. 29, 2012).

Chapter 2

Nitrogen-doped Carbonized Cotton for Highly Flexible Supercapacitors

This chapter was entirely copied from reference 1.

2.1. Introduction

Supercapacitors have attracted great attention owning to their high power density, fast charge-discharge rate, cycle efficiency, and low maintenance cost.[2-5] They can be widely used in many critical areas, such as electronics, mobile electrical systems, energy management, memory back-up systems, and industrial power.[5-7] The urgent needs for sustainable and renewable power sources in modern electronic industry have promoted the increasing demand for the development of high performance energy storage systems that are lightweight, flexible, and environmentally friendly.[8-11] Flexible supercapacitors (FSCs) become one of the most promising candidates that satisfy these demands in these systems.[12] The electrode materials are the key part in FSCs. Therefore, developing the

high performance electrode materials of FSCs becomes very necessary. Much effort has been devoted on the development of the electrode materials and has made great achievements. Based on the energy storage mechanisms, the electrode materials can be classified into two types. The first type of electrode materials stores energy based on the electrostatic charge accumulation on the surface between electrode and electrolyte.[13] Carbon materials with a large specific surface area and good mechanical properties belong to this type and have been widely used as electrode materials, such as graphene,[14,15] carbon nanotubes,[16] carbon fibers,[17] activated carbon,[18] and mesoporous carbon.[19] However, these electrode materials suffer from the low energy density, normally less than 5 KW/kg.[3] The other type stores energy depends on the fast and reversible faradic reaction near the surface. The widely developed electrode materials of this type were transitional metal oxide and hydroxide,[20-24] and conducting polymers.[25,26] This type of electrode materials greatly improved the energy density of the devices. However, they were limited in applications due to their poor electrical conductivity, natural rigidity, and bad cycling stability caused by the fragile structure in the redox processes.[4]

Cotton is an inexpensive nature product, which mainly composited of cellulose fibers.[27] The thermal treated cotton has high electrical conductivity, good mechanical properties and structural compatibility. It represents one type of lightweight electrode materials for FSCs. Xue *et al*. prepared the carbonized cotton that demonstrated high flexibility in FSCs.[27] The discharge capacity had no decay after 1,000 folding times. However, its specific capacitance was only ~ 14 F/g at the current density of 0.216 A/g, which is too low to practical applications. Therefore, improving the energy storage capacity of carbonized cotton becomes the critical for its practical applications in FSCs.

In this study, we describe the design and preparation of the free-standing microporous nitrogen doped carbonized cotton (NCC) by a facile template-free method. NCC is prepared through the thermal treatment of cotton in the flow of Ar and NH_3. NH_3 reacts with carbon in cotton forming the microporous structure in NCC. NCC possesses the unique features of the high electrical conductivity, interconnected porous structure, and good mechanical flexibility. They provide multiple pathways for electron transport and facilitate the access of electrolyte ions into and from its internal surface, resulting in the high charge-discharge rate performance. The N doping increases the electronic conductivity and induces the pseudocapacitive effects of NCC. It can also improve the wettability of NCC, which is beneficial for the contact between electrode material and electrolyte.[28,29] What is more, the free-standing NCC can simplify the device fabrication processes with no need for the binder, conductive additives, and current collectors. Compared to conventional supercapacitors, NCC reduces the overall weight and save the space of the FCSs, widening its practical applications. NCC demonstrated excellent performance in energy storage, showing high potential applications as electrode materials in the FSCs.

2.2. Experiments

2.2.1. Material Synthesis

Nitrogen doped carbonized cotton (NCC) was prepared in the CVD system. The cotton was loaded into the CVD system in the mixture flow of Ar (100 sccm) and NH_3 (65 sccm). The reaction chamber was evaporated to ~ 16 mT by completely open the vacuum valve and kept this condition for 10 min in order to completely remove the oxygen in the

chamber. Then, the chamber pressure was adjusted to ambient pressure by turning off the vacuum valve. The temperature was increased to 800 °C from room temperature at the heating rate of 5 °C/min. The reaction time was varied for different samples at 800 °C. After the reaction, the heating power was shut off and the sample was naturally cooled down to room temperature in the flow of Ar. When the reaction time was 0.5 h, 1 h, and 2 h, the nitrogen doped carbonized cotton were labeled as NCC-0.5h, NCC-1h, and NCC-2h, respectively. CC-1h was obtained by the carbonizing cotton at the same condition of NCC-1h excluding NH_3.

2.2.2. Materials Characterization

Production were characterized by XRD (Rigaku D/Max Ultima II), XPS (PHI Quantera), Raman (Renishaw Raman RE01 scope), BET (Quantachrome Autosorb-3b BET Surface Analyzer), SEM (JEOL 6500), and TEM (JEM2100F TEM).

2.2.3. Device fabrication

2.2.3.1. Fabrication of the conventional supercapacitor

The conventional supercapacitors were assembled using two-electrode system cells with filter paper (Qualitative, Whatman, 1001-042) as separator between two symmetrical working electrodes. The electrode material was the freestanding slice of the carbonized cotton with/without NH_3 treatment (~ 1.3 mg, 0.5 cm by 0.5 cm per electrode). 1 M H_2SO_4 was used as the electrolyte.

2.2.3.2. Fabrication of the flexible supercapacitor

Two pieces of the freestanding slices of NCC-1h (~ 7.5 mg, 1 cm by 2 cm) were assembled with one piece of cotton as separator, sandwiched in between. In order to test the device, two pieces of Au-PET were placed to improve the contact of NCC-1h with the electrochemical workstation. The device was packed by plastic film (Stretch-tite, POLYVINYL FILM INC.), forming the simple proof-of-concept prototype of flexible supercapacitor. 1 M H_2SO_4 was used as the electrolyte.

2.2.4. Electrochemical measurement

Electrochemical measurement The supercapacitors were characterized by cyclic voltammetry, galvanostatic charge-discharge experiments, and electrochemical impedance spectroscopy. An electrochemical station (CHI 660D) was used to perform the above characterization. The gravimetric specific capacitance was obtained from galvanostatic charge-discharge curve using equation 1.1. The energy density and power density were obtained by using equation 1.2 and 1.4.

2.3. Results and Discussion

2.3.1. Synthesis and structure analysis

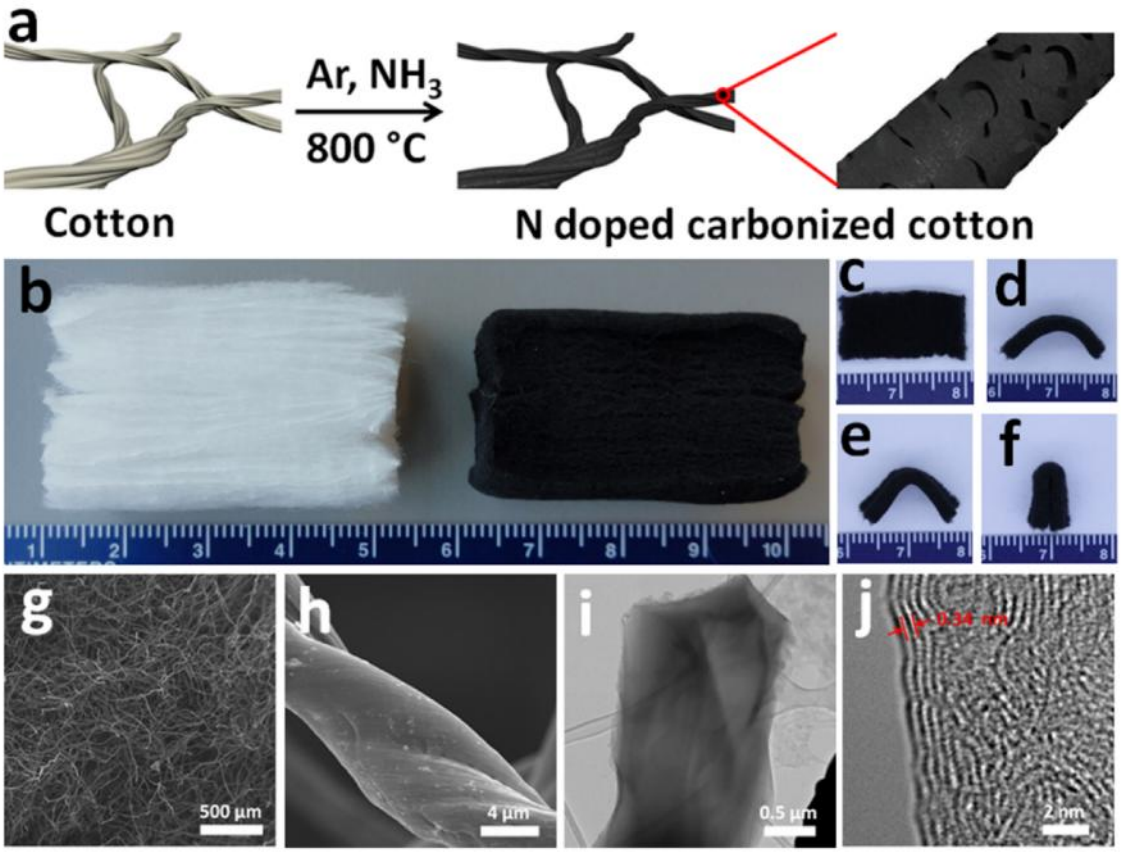

Figure 2.1. (a) Schematic illustration of the synthesis of nitrogen doped carbonized cotton. (b) Digital images of natural cotton (left) and NCC-1h (right) (c) NCC-1h in flat state. (d-f) NCC-1h in bent state. (g,h) SEM images of NCC-1h at different magnifications.

The synthesis of NCC is depicted in Figure 2.1a. The natural cotton was used as precursor. NCC was obtained after the thermal annealing of cotton at 800 °C at different reaction time in the flow of Ar and NH_3 at ambient environment. NCC-0.5h, NCC-1h, and NCC-2h were obtained by changing the reaction time from 0.5 h to 1 h and 2 h,

respectively. Carbonized cotton (CC-1h) was also prepared at the same reaction condition of NCC-1h excluding NH_3. The white cotton (Figure 2.1b) became black NCC-1h after the thermal annealing. According to application demands, NCC-1h can be sliced into pieces with different size, which were flexible enough to be bended and folded as shown in Figure 2.1c-f.

The morphology of NCC-1h was characterized by scanning electron microscopy (SEM) and transmission electron microscopy (TEM). Figure 2.1g,h showed the SEM images of NCC-1h at different magnifications. The fibers with the width of ~ 7 μm were partially helical. They were entangled together forming the entirety. Figure 2-1i showed the morphology of one piece fiber detached from NCC-1h because the fiber was too thick to take the TEM image of whole fiber. From the high resolution TEM image of NCC-1h (Figure 2.1j), it can be observed that the sample was defective even though the existence of graphitic plane.

X-ray diffraction (XRD), Raman spectrum, and X-ray photoelectron spectroscopy (XPS) were also used to characterize the materials. Figure 2.2a showed the XRD patterns of carbonized cotton with or without NH_3 treatment. All the samples of CC-1h, NCC-0.5h, NCC-1h, and NCC-2h demonstrated the diffraction peaks (002) and (100) of graphite at 25.37° and 43.89°, respectively.[28,30-32] Figure 2.2b showed their Raman spectra. There were two peaks centered at 1350 cm^{-1} and 1596 cm^{-1}, respectively. The peak at 1350 cm^{-1} was D-band, which resulted from the vibrations of carbon atoms with dangling bonds in plane terminations of the disordered graphite from the defects and disorders of structures in carbon materials. The peak at 1596 cm^{-1} was G-band due to the vibration of sp^2 hybridized carbon atoms in a 2D hexagonal lattice.[33-35] As shown in Table 2.1, the

intensity ratios of D-band to G-band ($R_{D/G}$) of CC-1h, NCC-0.5h, NCC-1h, and NCC-2h were 0.81, 0.89, 0.84, 0.86, respectively, demonstrating all of them in the high graphitization.[33]

Table 2.1. Structural, compositional analyses, and specific capacitance of CC-1h, NCC-0.5h, NCC-1h, and NCC-2h.

Samples	Atomic Concentration (%)			Deconvolution results (%)				$R_{D/G}$	BET surface area ($m^2 g^{-1}$)	Specific capacitance (F/g) (1 A/g)
	C	N	O	Pyridinic	Pyrrolic	Quaternary	N-oxide			
CC-1h	93.6	0	6.4	0	0	0	0	0.81	356.0	1.5
NCC-0.5h	82.7	11.5	5.8	45.4	36.3	11.7	6.6	0.89	713.0	179.5
NCC-1h	85.3	9.6	5.1	52.5	37.7	6.6	3.2	0.84	1085.0	206.7
NCC-2h	87.5	7.7	4.8	49.4	33.9	10.9	5.8	0.86	898.0	197.0

Figure 2.2c was the survey XPS spectra of these samples. It was seen that all of NCC-0.5h, NCC-1h, and NCC-2h contained N, excluding CC-1h without NH_3 treatment. This demonstrated that N doping was successfully obtained after NH_3 treatment. NH_3 treatment increased the defects in the carbonized cotton. As shown in Table 2.1, C atomic concentration of CC-1h was 93.6 %. It decreased to 82.7 %, 85.3 %, 87.5 % for NCC-0.5h (N concentration, 11.5 %), NCC-1h (N concentration, 9.6 %), and NCC-2h (N concentration, 7.7 %), respectively. Therefore, the NH_3 treated carbonized cotton had high $R_{D/G}$. Meanwhile, long time thermal treatment will improve the crystallization of graphite. O concentration decreased from 5.8 % of NCC-0.5h to 5.1 % of NCC-1h and 4.8 % of NCC-2h. $R_{D/G}$ of NCC-1h was the lowest in all of NCC due to both effects of NH_3 treatment and thermal treatment. As shown in Figure 2.2d, N1s in NCC-0.5h, NCC-1h, and NCC-2h was detected in fine spectrum. It was deconvoluted into four peaks located at 398.1, 400.4, 402.6, and 405.2 eV, which were assigned to pyridinic N, pyrrolic N, quaternary N, and N-oxide, respectively.[28,36] The relative proportion of the N state in NCC was shown in Table

2.1. The proportion of N state varied with the reaction time. NCC-1h had the highest content of pyridinic N and pyrrolic N and the lowest content of quaternary N and N-oxide among these samples. All the data discussed above demonstrated that NCC was indeed obtained after the thermal annealing of cotton in the environment of Ar and NH_3.

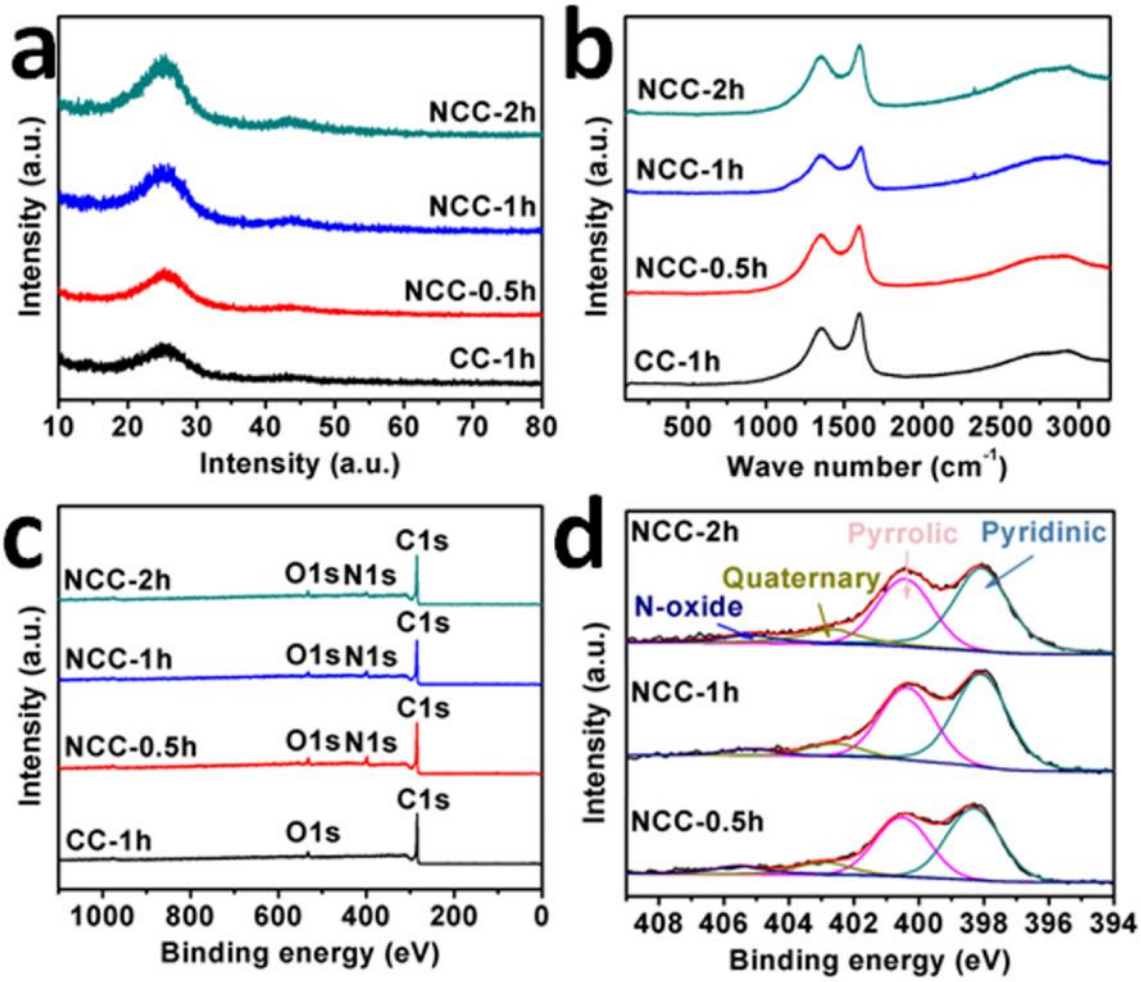

Figure 2.2. XRD patterns (a), Raman spectra (b), XPS (c) of CC-1h, NCC-0.5h, NCC-1h, and NCC-2h. (d) N1s core level XPS of NCC-0.5h, NCC-1h, and NCC-2h.

In order to study the development of porosity in carbonized cotton with or without NH_3 treatment, the nitrogen adsorption-desorption isotherms of CC-1h, NCC-0.5h, NCC-

1h, and NCC-2h were carried out as shown in Figure 2.3a. All the samples were in type I isotherms, indicating that they were mainly microporous materials. NH_3 treatment increased the microporous characteristic. Nitrogen sorption capacity of NCC was higher than that of CC-1h. NCC-1h had the highest value in the sorption capacity. Corresponding to BET surface area of these samples, NCC-1h had the highest value of 1085 m^2g^{-1}, and CC-1h was the lowest one of 356 m^2g^{-1} (Table 2.1). Figure 2.3b showed the pore size distribution curves regarding these samples. The pore size distribution was in ~ 2nm. The longer time treatment of NH_3 reduced the contribution of microporous characteristic, leading to the decrease of BET surface area (NCC-2h, 898 m^2g^{-1}). The coexistence of micro/meso scale pores in NCC provided multiple pathways for electron transport and facilitated the access of electrolyte ions into and from the micropores, resulting in the improved electrochemical performance in supercapacitors.

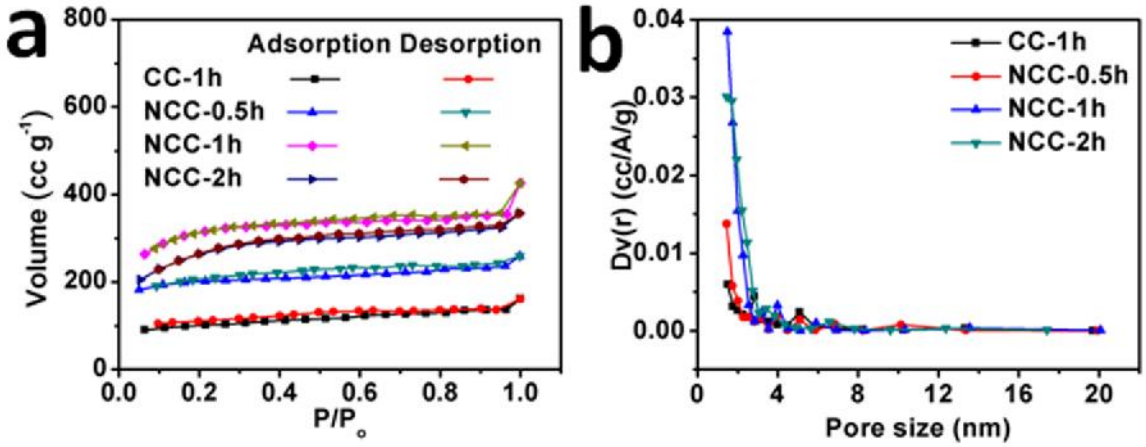

Figure 2.3. Nitrogen adsorption-desorption isotherms (a) and pore size distribution curves (b) of CC-1h, NCC-0.5h, NCC-1h, and NCC-2h.

2.3.2. Electrochemical evaluation

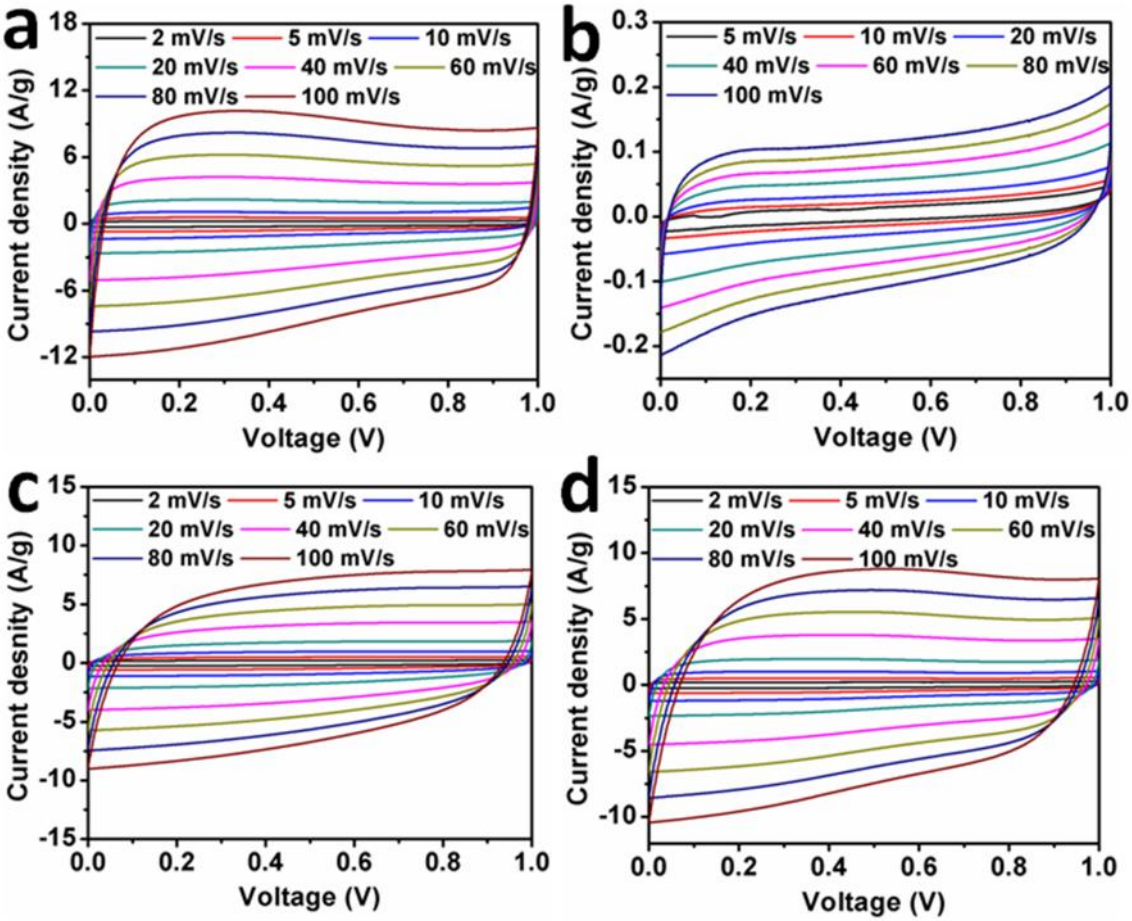

Figure 2.4. Cyclic voltammetry curves of NCC-1h (a), CC-1h (b), NCC-0.5h (c), and NCC-2h (d) at the scan rate ranges of 2 to 100 mV/s in 1 M H_2SO_4.

The electrochemical performance of NCC-1h was first evaluated in conventional supercapacitor configuration (two-electrode system) by measurements of cyclic voltammetry (CV), galvanostatic charge-discharge experiments, and electrochemical impedance spectroscopy (EIS). Figure 2.4a showed the CV curves of NCC-1h at different scan rates from 2 to 100 mV s^{-1} in the potential window range of 0 to 1.0 V. The current response demonstrated a corresponding increase with the increase of scan rate.

Furthermore, the composite electrode maintained the CV shape even at high scan rate up to 100 mV s^{-1}. These characteristics demonstrated a good capacitive behavior of NCC-1h. CC-1h, NCC-0.5h, and NCC-2h had similar phenomena shown in Figure 2.4b-d. At the same scan rate of 40 mV s^{-1}, the CV curve of CC-1h was minuscule compared to the others. This demonstrated that CC-1h had the lowest energy storage performance due to the small area of the enclosed CV, which stood for the capacitance of the electrodes.[36] For other three materials, NCC-1h had the highest value of CV area, demonstrating that it had the highest energy storage ability among all of them.

Figure 2.5a showed the galvanostatic charge-discharge curves of NCC-1h at different current densities. The almost symmetrical charging and discharging curves demonstrated that the materials had good capacitive behaviors. The discharging time gradually decreased with the increase of the current density. NCC-0.5h, NCC-2h, and CC-1h showed the similar trend as shown in Figure 2.5b-d. Figure 2-5e showed the galvanostatic charge-discharge curves of CC-1h, NCC-0.5h, NCC-1h, and NCC-2h at the same current density of 1 A/g. The galvanostatic charge-discharge curve of CC-1h was almost a line, which was consistent with the variation of its CV. The specific capacitance was obtained based on the galvanostatic charge-discharge curves as shown in Figure 2-5f. NCC-1h produced the best performance. Its specific capacitance was as high as 206.7 F/g at a current density of 1 A/g (Table 2-1). It decreased to 177.0 F/g at the high current density of 14 A/g. It exhibited excellent rate performance with the capacitance retention of 85.5% as current density was varied from 1 A/g to 14 A/g. The specific capacitance of NCC-0.5h and NCC-2h had similar trends with the variation of current density. At the same current density, the value of specific capacitance of NCC-0.5h and NCC-2h was lower than

that of NCC-1h (Table 2-1), especially in the high current density. The specific capacitance of CC-1h was only 1.5 F/g at 1 A/g. It was minuscule compared to other three materials. Therefore, the high specific surface area and the N functionalities in NCC-1h resulted in the great enhanced capacitance in supercapacitors.

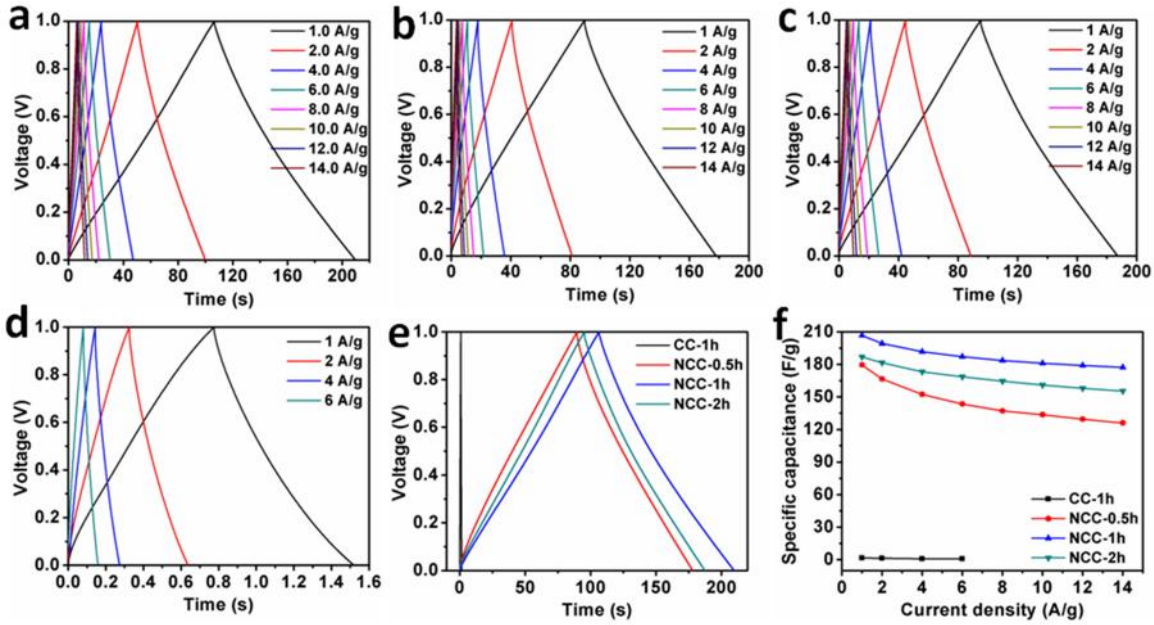

Figure 2.5. Galvanostatic charge discharge curves of NCC-1h (a), NCC-0.5h (b), NCC-2h (c), and CC-1h (d) at a current density ranges of 1 to 14 A/g. (e) Galvanostatic charge discharge curves of CC-1h, NCC-0.5h, NCC-1h, and NCC-2h at the same current density of 1 A/g. (f) The specific capacitance *versus* current density for CC-1h, NCC-0.5h, NCC-1h, and NCC-2h.

The cyclic stability of NCC-1h was also evaluated through the extended galvanostatic charge-discharge experiment. As shown in Figure 2.6a, NCC-1h not only showed no capacitance decay, but also increased with the augment of the cycle numbers. It increased 34% when the cycle number reached 10,000. The phenomenon showed that NCC-1h had an activation process. The contact between NCC-1h and electrolyte was not

good due to its high hydrophobic nature. With more charge-discharge cycles, the internal parts of NCC-1h became electrochemically active as they became contact with the electrolyte. Figure 2-6b was the Ragone plot of energy density versus power density for NCC-0.5h, NCC-1h, and NCC-2h. NCC-1h had the highest energy density of 7.18 Wh/kg at the current density of 1 A/g. Its energy density decreased to 6.15 Wh/kg with the power density of 3823.15 W/kg at the current density of 14 A/g. This value was far better than that obtained in other carbon materials based on electrostatic charge adsorption as electrodes in supercapacitors.[3]

EIS is a powerful tool to study the electrochemical behavior of the electrodes.[30] Nyquist plots regarding of NCC-0.5h, NCC-1h, and NCC-2h were obtained in the frequency ranges of 100 kHz to 0.01 Hz at the open circuit potential as shown in Figure 2.6c. The intersection by the x intercept of the Nyquist plot was the equivalent series resistances (R_s), which was the combination of electrolyte resistance and electrode resistance.[26,38,39] They were 0.94, 0.80, and 1.90 Ω for NCC-0.5h, NCC-1h, and NCC-2h, respectively. It demonstrated that NCC-1h had the best electrical conductivity among them. In the high frequency range of plots, the semicircles showed good electrode contact between the electrode and electrolyte. The vertical lines in the low frequency range of the plot implied that the supercapacitors showed the good ion diffusion in the electrode structure. It showed the almost ideal capacitive behavior of NCC.

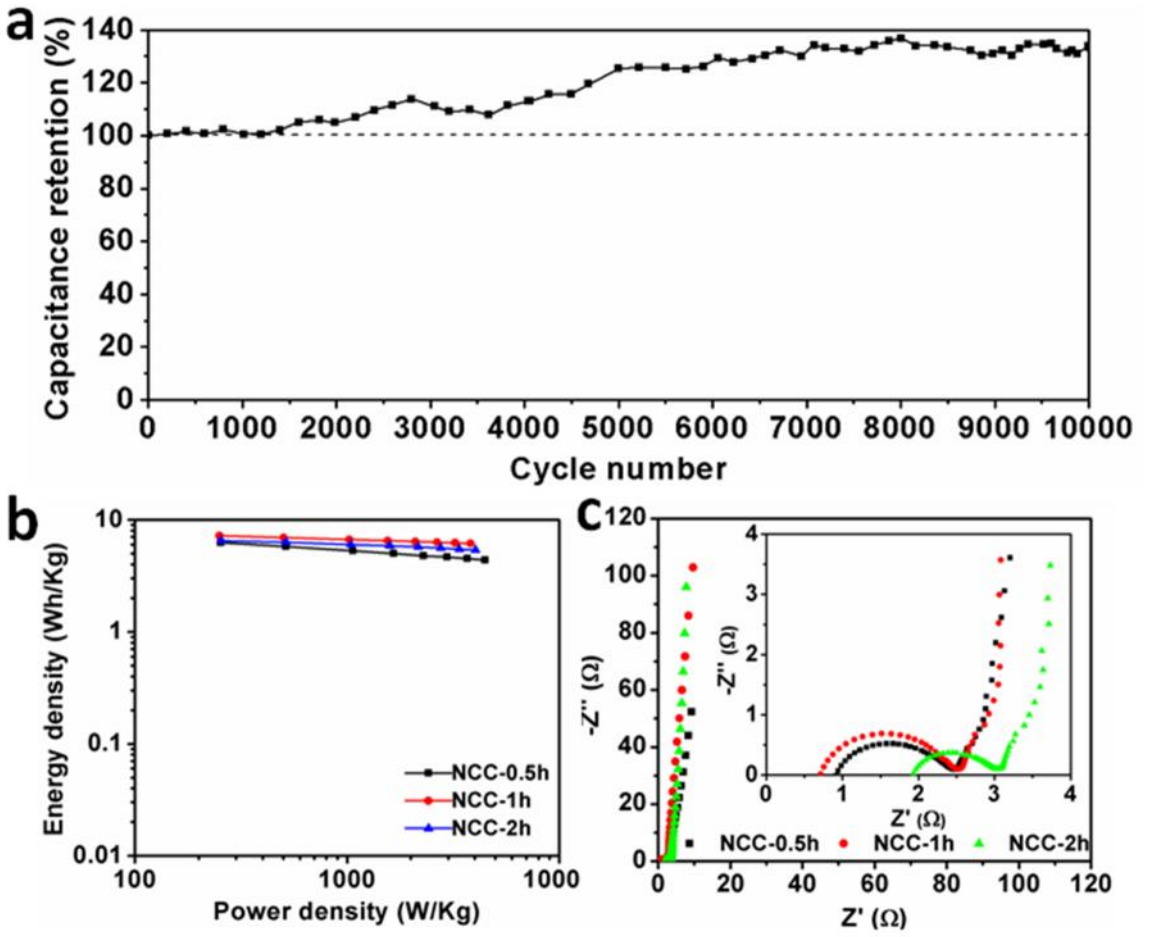

Figure 2.6. (a) Cycling stability of NCC-1h at a current density of 6 A/g. (b) Ragone plot of NCC-0.5h, NCC-1h, and NCC-2h. (c) Nyquist plots of NCC-0.5h, NCC-1h, and NCC-2h (the inset is an enlarged view of the Nyquist curves).

In order to test the flexibility of NCC-1h and study the influence of the flexibility in electrochemical performance, NCC-1h was assembled into FSCs. Since NCC-1h is freestanding and electrical conductivity, no additional insulating binder and conductivity additives were used when assemble the devices. This will reduce the whole mass of device and increase its possibility in practical applications. In order to test the device, two pieces of Au-PET were placed to improve the contact of NCC-1h with the electrochemical

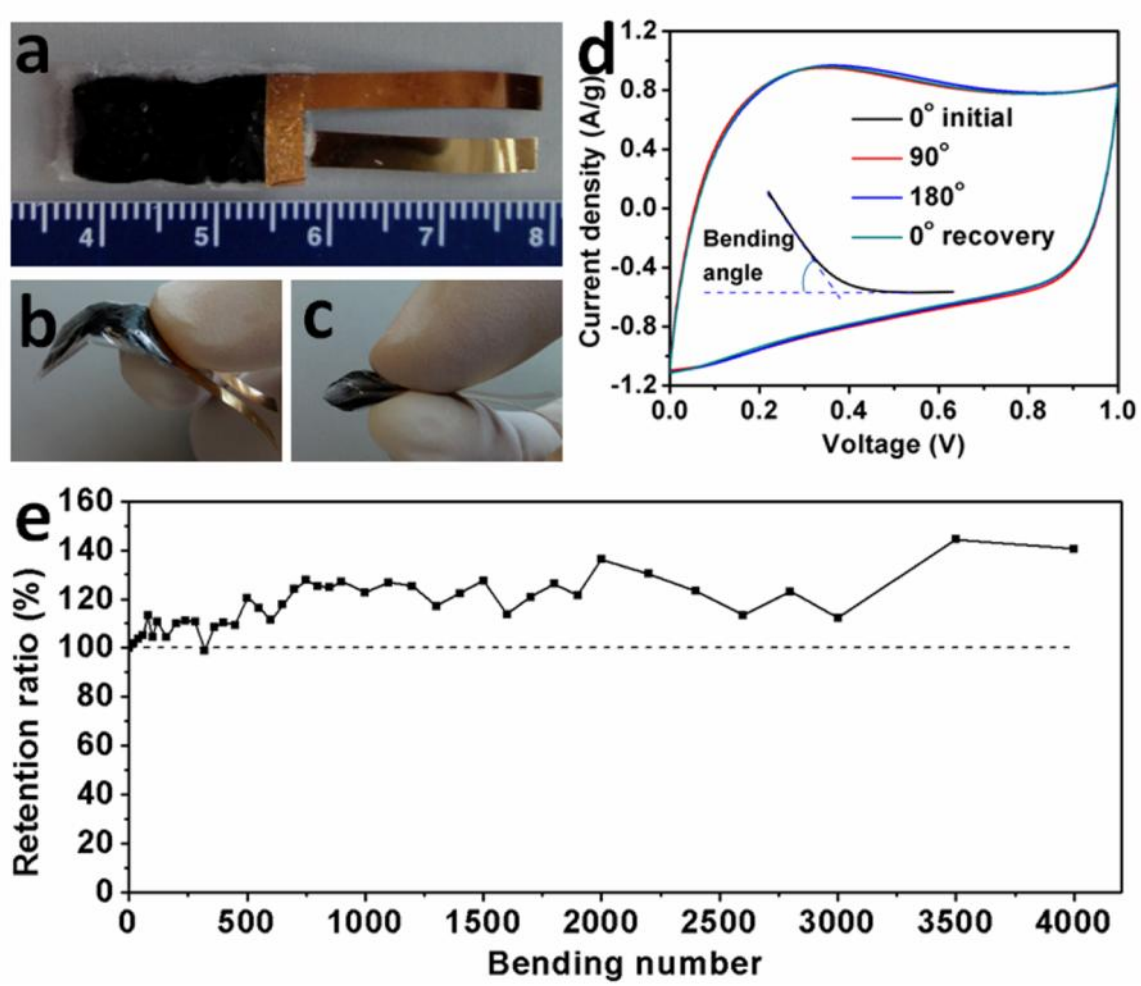

Figure 2.7. (a-c) Digital images of flexible supercapacitor and its different bending states. (d) CV curves of the flexible supercapacitor at the scan rate of 10 mV/s when bent by 0°, 90°, and 180°. (e) Dependence of capacitance retention ratio on bending cycles with ~ 90° bending angle.

workstation. Figure 2.7a showed digital image of a simple proof-of-concept prototype of the FSCs. It can be bended to different angles as shown in Figure 2.7b,c. The electrochemical performance of this device was first studied by CV experiments at 10 mV/s at different bending angles. As shown in Figure 2.7d, NCC-1h showed the almost rectangular CV curve. When the flexible device was bent by 90°, 180°, and then recovery

to 0°, no obvious CV changes were observed. This demonstrated that the electrochemical performance of the flexible device was stable at different bending states. In addition, the flexibility tests were also carried out by bending the device to ~ 90° for 4,000 times (Figure 2-7e). The capacitance increased with the augment of the bending number. It increased 40% after 4,000 bending cycles. The trend of the increased capacitance in FSCs was same as that in conventional supercapacitor shown in Figure 2.6a. Bending process might facilitate the contact between the electrode and electrolyte, leading to the increase of the capacitance. The above results demonstrated that NCC-1h was a superb candidate for use as electrode materials in FSCs.

2.4. Conclusion

In summary, a novel strategy for preparing free-standing microporous nitrogen doped carbonized cotton (NCC) is proposed and realized. This material (NCC-1h) demonstrated the enhanced specific capacitance (206.70 F/g at 1 A/g), energy density (7.18 Wh/kg at 1 A/g), power density (3823.15 W/kg at 14 A/g), and excellent cycling stability (capacitance increase by 34% after 10,000 cycles), which resulted from its synergetic of microporous structure and N functionalities. The material was assembled into a flexible supercapacitor, which also demonstrated excellent electrochemical performance, especially the flexibility (capacitance increase by 40% after 4,000 bending cycles). All these results demonstrated that the material had great potential application in energy storage for flexible and lightweight electronics. The design concert developed here opens up a new avenue for constructing the electrode materials with the improved electrochemical stability for flexible supercapacitors.

2.5. References

1. Li, L.; Zhong, Q. F.; Kim, N. D.; Ruan, G. D.; Gao, C. T.; Yang, Y.; Fei, H. L.; Li, Y. L.; Ji, Y. S.; Tour, J. M. Microporous Nitrogen Doped Carbonized Cotton for Highly Flexible Supercapacitor **Submitted** (L.L. conceived and designed the experiments. L.L. and Z.Q.F. prepared the materials. L.L., K.N.D., R.G.D., G.C.T., L.Y.L., and J.Y.S. performed material characterization. L.L., Z.Q.F., Y.Y. and F.H.L. tested the devices. L.L. wrote the paper. Finally, T.J.M. oversaw all research phases, provided regular guidance to the research and revised the manuscript. All authors discussed and commented on the manuscript.)

2. Simon, P.; Gogotsi, Y. Materials for electrochemical capacitors. *Nat. Mater.* **2008**, 7, 845-854.

3. Miller, J. R.; Simon, P. Materials science-electrochemical capacitors for energy management. *Science* **2008**, 321, 651-652.

4. He, Y.; Chen, W.; Gao, C.; Zhou, J.; Li, X.; Xie, E., An overview of carbon materials for flexible electrochemical capacitors. *Nanoscale* **2013,** *5*, 8799-8820.

5. Jiang, H.; Lee, P. S.; Li, C., 3D carbon based nanostructures for advanced supercapacitors. *Energy Environ. Sci.* **2013,** *6*, 41-53.

6. Zhang, L. L.; Zhao, X. S., Carbon-based materials as supercapacitor electrodes. *Chem. Soc. Rev.* **2009,** *38*, 2520-2531.

7. Jiang, H.; Yang, L.; Li, C.; Yan, C.; Lee, P. S.; Ma, J., High-rate electrochemical capacitors from highly graphitic carbon-tipped manganese oxide/mesoporous carbon/manganese oxide hybrid nanowires. *Energy Environ. Sci.* **2011,** *4*, 1813-1819.

8. Bao, L.; Zang, J.; Li, X., Flexible Zn2SnO4/MnO2 Core/Shell Nanocable−Carbon Microfiber Hybrid Composites for High-Performance Supercapacitor Electrodes. *Nano Lett.* **2011,** *11*, 1215-1220.

9. Wang, Y.; Xia, Y., Recent Progress in Supercapacitors: From Materials Design to System Construction. *Adv. Mater.* **2013,** *25*, 5336-5342.

10. X. W. Yang, C. Cheng , Y. F. Wang , L. Qiu , D. Li , Liquid-Mediated Dense Integration of Graphene Materials for Compact Capacitive Energy Storage. *Science* **2013**, 341, 534.

11. Xie, K.; Wei, B., Materials and Structures for Stretchable Energy Storage and Conversion Devices. *Adv. Mater.* **2014,** *26*, 3592-3617.

12. H. Nishide , K. Oyaizu , Toward Flexible Batteries *Science* 2008, 319, 737-738.

13. Béguin, F.; Presser, V.; Balducci, A.; Frackowiak, E., Carbons and Electrolytes for Advanced Supercapacitors. *Adv. Mater.* **2014,** *26*, 2219-2251.

14. Yuxi Xu, Zhaoyang Lin, Xing Zhong, Xiaoqing Huang, Nathan O. Weiss, Yu Huang, Xiangfeng DuanHoley graphene frameworks for highly efficient capacitive energy storage. *Nature Commun.* **2014**, 5, 4554

15. M. F. El-Kady, V. Strong, S. Dubin and R. B. Kaner, Laser Scribing of High-Performance and Flexible Graphene-Based Electrochemical Capacitors *Science*, **2012**, 335, 1326-1330.

16. Kaempgen, M.; Chan, C. K.; Ma, J.; Cui, Y.; Gruner, G., Printable Thin Film Supercapacitors Using Single-Walled Carbon Nanotubes. *Nano Lett.* **2009,** *9*, 1872-1876.

17. Tao, X. Y.; Zhang, X. B.; Zhang, L.; Cheng, J. P.; Liu, F.; Luo, J. H.; Luo, Z. Q.; Geise, H. J., Synthesis of multi-branched porous carbon nanofibers and their application in electrochemical double-layer capacitors. *Carbon* **2006,** *44*, 1425-1428.

18. Frackowiak, E.; Béguin, F., Carbon materials for the electrochemical storage of energy in capacitors. *Carbon* **2001,** *39*, 937-950.

19. Zhi, M.; Xiang, C.; Li, J.; Li, M.; Wu, N., Nanostructured carbon-metal oxide composite electrodes for supercapacitors: a review. *Nanoscale* **2013,** *5*, 72-88.

20. Yuan, L.; Lu, X.-H.; Xiao, X.; Zhai, T.; Dai, J.; Zhang, F.; Hu, B.; Wang, X.; Gong, L.; Chen, J.; Hu, C.; Tong, Y.; Zhou, J.; Wang, Z. L., Flexible Solid-State Supercapacitors Based on Carbon Nanoparticles/MnO2 Nanorods Hybrid Structure. *ACS Nano* **2011,** *6*, 656-661.

21. Yang, P.; Xiao, X.; Li, Y.; Ding, Y.; Qiang, P.; Tan, X.; Mai, W.; Lin, Z.; Wu, W.; Li, T.; Jin, H.; Liu, P.; Zhou, J.; Wong, C. P.; Wang, Z. L., Hydrogenated ZnO Core–Shell Nanocables for Flexible Supercapacitors and Self-Powered Systems. *ACS Nano* **2013,** *7*, 2617-2626.

22. He, Y.; Chen, W.; Li, X.; Zhang, Z.; Fu, J.; Zhao, C.; Xie, E., Freestanding Three-Dimensional Graphene/MnO2 Composite Networks As Ultralight and Flexible Supercapacitor Electrodes. *ACS Nano* **2012,** *7*, 174-182.

23. Yang, Y.; Ruan, G.; Xiang, C.; Wang, G.; Tour, J. M., Flexible Three-Dimensional Nanoporous Metal-Based Energy Devices. *J. Am. Chem. Soc.* **2014,** *136*, 6187-6190.

24. Dong, X.; Guo, Z.; Song, Y.; Hou, M.; Wang, J.; Wang, Y.; Xia, Y., Flexible and Wire-Shaped Micro-Supercapacitor Based on Ni(OH)2-Nanowire and Ordered Mesoporous Carbon Electrodes. *Adv. Funct. Mater.* **2014,** *24*, 3405-3412.

25. Liu, L.; Niu, Z.; Zhang, L.; Zhou, W.; Chen, X.; Xie, S., Nanostructured Graphene Composite Papers for Highly Flexible and Foldable Supercapacitors. *Adv. Mater.* **2014,** *26*, 4855-4862.

26. Meng, Y.; Wang, K.; Zhang, Y.; Wei, Z., Hierarchical Porous Graphene/Polyaniline Composite Film with Superior Rate Performance for Flexible Supercapacitors. *Adv. Mater*. **2013,** *25*, 6985-6990.

27. Xue, J.; Zhao, Y.; Cheng, H.; Hu, C.; Hu, Y.; Meng, Y.; Shao, H.; Zhang, Z.; Qu, L., An all-cotton-derived, arbitrarily foldable, high-rate, electrochemical supercapacitor. *Phys. Chem. Chem. Phys.* **2013,** *15*, 8042-8045.

28. Kim, N. D.; Kim, S. J.; Kim, G.-P.; Nam, I.; Yun, H. J.; Kim, P.; Yi, J., NH3-activated polyaniline for use as a high performance electrode material in supercapacitors. *Electrochim. Acta* **2012,** *78*, 340-346.

29. Zhou, M.; Pu, F.; Wang, Z.; Guan, S., Nitrogen-doped porous carbons through KOH activation with superior performance in supercapacitors. *Carbon* **2014,** *68*, 185-194.

30. Li, L.; Raji, A.-R. O.; Tour, J. M., Graphene-Wrapped MnO2–Graphene Nanoribbons as Anode Materials for High-Performance Lithium Ion Batteries. *Adv. Mater.* **2013,** *25*, 6298-6302.

31. Li, L.; Raji, A.-R. O.; Fei, H.; Yang, Y.; Samuel, E. L. G.; Tour, J. M., Nanocomposite of Polyaniline Nanorods Grown on Graphene Nanoribbons for Highly Capacitive Pseudocapacitors. *ACS Appl. Mater. Interfaces* **2013,** *5*, 6622-6627.

32. Vázquez-Santos, M. B.; Geissler, E.; László, K.; Rouzaud, J.-N.; Martínez-Alonso, A.; Tascón, J. M. D., Comparative XRD, Raman, and TEM Study on Graphitization of PBO-Derived Carbon Fibers. *J. Phys. Chem. C* **2011,** *116*, 257-268.

33. Tan, Y.; Xu, C.; Chen, G.; Liu, Z.; Ma, M.; Xie, Q.; Zheng, N.; Yao, S., Synthesis of Ultrathin Nitrogen-Doped Graphitic Carbon Nanocages as Advanced Electrode Materials for Supercapacitor. *ACS Appl. Mater. Interfaces* **2013,** *5*, 2241-2248.

34. Wang, Y.; Su, F.; Wood, C. D.; Lee, J. Y.; Zhao, X. S., Preparation and Characterization of Carbon Nanospheres as Anode Materials in Lithium-Ion Secondary Batteries. *Ind. Eng. Chem. Res.* **2008,** *47*, 2294-2300.

35. Hou, S.; Cai, X.; Wu, H.; Yu, X.; Peng, M.; Yan, K.; Zou, D., Nitrogen-doped graphene for dye-sensitized solar cells and the role of nitrogen states in triiodide reduction. *Energy Environ. Sci.* **2013,** *6*, 3356-3362.

36. Bi, E.; Chen, H.; Yang, X.; Peng, W.; Gratzel, M.; Han, L., A quasi core-shell nitrogen-doped graphene/cobalt sulfide conductive catalyst for highly efficient dye-sensitized solar cells. *Energy Environ. Sci.* **2014,** *7*, 2637-2641.

37. Wang, H.; Hao, Q.; Yang, X.; Lu, L.; Wang, X., A nanostructured graphene/polyaniline hybrid material for supercapacitors. *Nanoscale* **2010,** *2*, 2164-2170.

38. Chen, J.; Sheng, K.; Luo, P.; Li, C.; Shi, G., Graphene Hydrogels Deposited in Nickel Foams for High-Rate Electrochemical Capacitors. *Adv. Mater.* **2012,** *24*, 4569-4573.

39. Hu, L.; Chen, W.; Xie, X.; Liu, N.; Yang, Y.; Wu, H.; Yao, Y.; Pasta, M.; Alshareef, H. N.; Cui, Y., Symmetrical MnO2–Carbon Nanotube–Textile Nanostructures for Wearable Pseudocapacitors with High Mass Loading. *ACS Nano* **2011,** *5*, 8904-8913.

Chapter 3

Nanocomposite of Polyaniline Nanorods Grown on Graphene Nanoribbons for Highly Capacitive Pseudocapacitors

This chapter was entirely copied from reference 1.

3.1. Introduction

Electrochemical capacitors are attracting interest due to their high power density, long life cycle and well-known operational principles.[2-4] Based on their energy storage mechanism,[5] electrochemical capacitors can be categorized as electrical double layer capacitors (EDLCs) or pseudocapacitors. In an EDLC device, the electrostatic charge accumulation occurs at the interface between the electrode and the electrolyte. The performance of EDLCs is strongly dependent on the properties of the electrode and the electrolyte. EDLCs can provide ultrahigh power and excellent life cycles because of the nondegradative processes between the electrode and the electrolyte. The performance of

EDLCs is determined by the available surface area of the electrodes and the finite charge separation between the electrode materials and the electrolyte. [2,6] However, in a pseudocapacitor (or redox supercapacitor), the fast and reversible faradic reaction near the surface determines its energy storage capability.[2,7] Typically, the specific capacitance of a pseudocapacitor electrode far exceeds that of an electrode operating as an EDLC.[8] Therefore pseudocapcitors are preferred in applications where high capacitance is required.

Conducting polymers have been studied for their potential application as electrodes in energy storage devices.[9-12] Among conducting polymer, polyaniline (PANI) has attracted interest due to its high specific capacitance, good environmental stability, electro-activity, and doping-dedoping chemistry.[13-16] The major drawback that hinders the application of PANI in energy storage is its poor cyclic stability due to the mechanical degradation by the big volumetric change in the doping/dedoping process; it is not stable to cycling through charge-discharge processes over long periods of time.[1] Interfacing other carbon materials with PANI is one effective way to improve the electrochemical stability of the composite. Results have been recently reported based on this strategy. Wu *et al*. reported the synthesis of chemically modified graphene and PANI nanofiber composites by *in situ* polymerization of aniline in the presence of graphene oxide; the composites had a high specific capacitance of 480 F/g at a current density 0.1 A/g; 70% of the original capacitance was retained after 400 cycles in a three electrode system.[17] Shi *et al*. prepared composite films of chemically converted graphene and PANI nanofibers by vacuum filtration. The composite films had a specific capacitance of 210 F/g at a current density 0.3 A/g. The capacitance only decreased 21% after 800 charging discharging cycles at a current density 3 A/g.[14] Zhang *et al*. grew oriented arrays of PANI nanorods on expanded

graphite by *in situ* polymerization, and the composite showed a high specific capacitance of 1665 F/g at a current density 1 A/g and 87% original capacitance retention after 2000 cycles at a scan rate of 100 mV/s in a three electrode system.[18] Wang *et al*. synthesized graphene-wrapped PANI nanofibers with a specific capacitance of 250 F/g at a current density of 0.5 A/g and 74% capacitance retention after 1000 cycles at a current density of 1 A/g in a three electrode system [19] Ruoff *et al*. reported that composites of PANI and graphene oxide afforded a high specific capacitance that could reach 500 F/g at scan rate of 50 mV s^{-1}, with almost no loss of capacitance over 680 cycles in a three electrode system.[20] However, all of these materials are either relatively complicated to produce, are limited in scalability or still suffer from the electrochemical stability problem.

In this work, graphene nanoribbons (GNRs), due to their high surface area, high electrical conductivity, and scalability, were selected as a template on which PANI nanorods were grown.[21] A nanocomposite of PANI-GNRs was prepared by the *in situ* polymerization of aniline in the presence of GNRs. In this composite, GNRs not only work as substrate to grow the PANI nanorods and improve the electrical conductivity of the composite, but also increase the effectively utilization of PANI and enhance the mechanical property of the composite. The high specific capacitance of the PANI will increase the capacitance of the composite. PANI-GNRs displayed good electrochemical properties in energy storage. A specific capacitance 340 F/g was achieved at a current density of 0.25 A/g in a two electrode system. The capacity retention was about 90% after 4200 cycles of charging and discharging, making PANI-GNRs a superb electrode material for long-lived energy storage devices.

3.2. Experiments

3.2.1. Materials synthesis

GNRs were prepared by treatment of multiwalled carbon nanotubes with NaK in 1,2-dimethoxyethane and quenching of the reaction with MeOH as described previously.[21] Typically, 35 mL 1,2-dimethoxylethane and 0.29 mL NaK was added to 100 mg MWCNTs (MWCNT, Mitsui & Co, lot no. 05072001K28) in a nitrogen dry box and secured tightly with septum/copper wire. The mixture was carefully transferred outside dry box and stirred for 4 d at room temperature. The intercalated K was quenched with CH_3OH, thus inducing splitting of the MWCNT to GNR through H_2 formation. The GNRs were then oxidized in 3 M HNO_3 at reflux for 12 h in order to increase their wettability. PANI-GNRs were prepared by direct polymerization of aniline on the HNO_3-treated GNRs. In the typical procedure for PANI-GNRs-40, 22.5 mg of HNO_3-treated GNRs were added to 40 mL of 1 M H_2SO_4 solution and the mixture was ultrasonicated (2510 Branson) to fully disperse the GNRs. Aniline (900 mg, 9.65 mmol) was added to the dispersion and it was stirred to form a uniform mixture while cooling in a NaCl-ice bath (-3 °C to -5 °C). The APS oxidant (554 mg, 2.4 mmol), was dissolved in 40 mL of 1 M H_2SO_4 and kept in the NaCl-ice bath for 10 min. The solutions were mixed with continued stirring in the NaCl-ice bath for 10 h. The black solid sample was collected by vacuum filtration and sequentially washing with water (400 mL) and acetone (100 mL). The final PANI-GNRs (130 mg) were obtained after drying in a vacuum oven overnight. In the control experiment, PANI was prepared using the same method above without the HNO_3-treated GNRs. The

composite samples were designated as PANI-GNRs-20, -40, or -64 based on the starting weight ratio of aniline to GNRs.

3.2.2. Materials characterization

Products were characterized by XRD (Rigaku D/Max Ultima II); XPS (PHI Quantera); SEM (JEOL 6500); and TEM (JEM2100F TEM).

3.2.3. Device fabrication

The electrochemical performance analyses were done using two electrode system cells with filter paper (Qualitative, Whatman, 1001-042) as separator between two symmetrical working electrodes. The electrode material was a mixture of 90% active materials and 10% binder polytetrafluoroethylene (PTFE, 60% dispersion in H_2O, Sigma Aldrich). The well-mixed mixture was uniformly pasted on the platinum foil as the current collector. Normally, the average mass per electrode was ~ 3.5 mg of active materials and binder.

3.2.4. Electrochemical measurement

The prepared two-electrode cell was characterized by CV, galvanostatic charge discharge test and EIS measurements. 1 M H_2SO_4 was used as the electrolyte in the performance testing. An electrochemical station (CHI 660D) was used to perform the above characterization. The gravimetric specific capacitance was obtained from galvanostatic charge-discharge curve using equation 1.1. The energy density and power density were obtained by using equation 1.2 and equation 1.3, respectively. *R* is the equivalent series resistance from the *IR* drop obtained by equation 1.5.

3.3. Results and Discussion

3.3.1. Synthesis and structure analysis

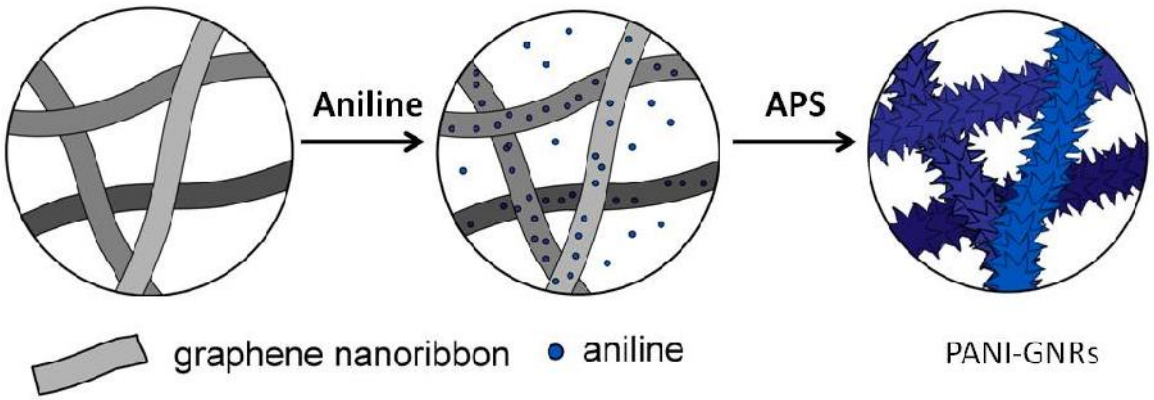

Figure 3.1. Schematic illustration of the synthesis of the PANI-GNRs composite with PANI polymerized directly on the GNRs using APS.

The GNRs were prepared through solution-based chemical splitting of carbon nanotubes; the GNRs were edge functionalized with protons by quenching the reaction with MeOH.[20] The GNRs were oxidized in 3 M HNO_3 for 12 h at reflux in order to increase their wettability.[22] The nanocomposites of PANI-GNRs were prepared by the direct polymerization of PANI on GNRs. As depicted in Figure 3.1, aniline was adsorbed on GNRs forming active nucleation sites. After the addition of ammonium persulfate (APS), PANI grew outward from the initial nuclei. Ordered, vertically aligned PANI was thus produced on the GNRs. The composite samples were designated as PANI-GNRs-20, -40 or -64 based on the weight ratio of aniline to GNRs: 20:1 (PANI-GNRs-20), 40:1 (PANI-GNRs-40 or 64:1 (PANI-GNRs-64).

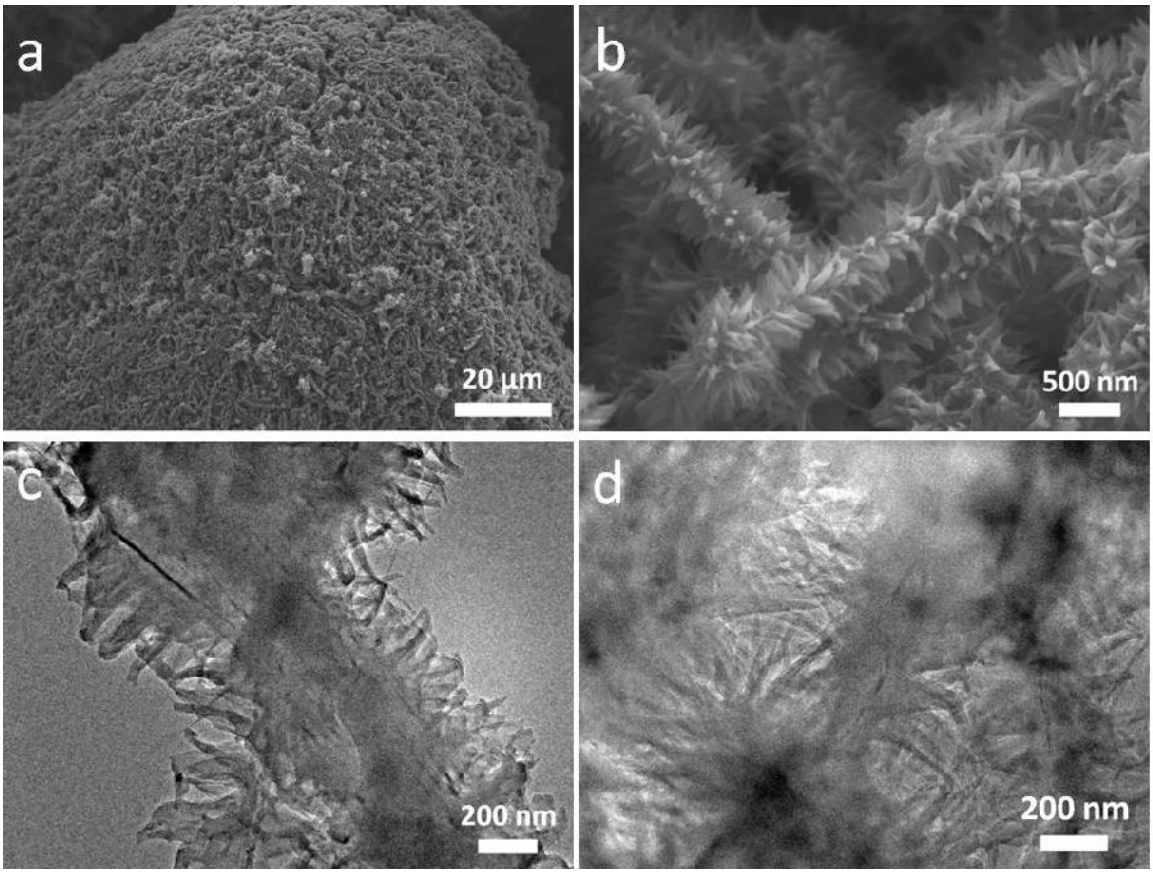

Figure 3.2. SEM images of composite PANI-GNRs-40 at (a) low resolution and (b); high resolution; (c) and (d) TEM images of composite PANI-GNRs-40.

As shown in Figure 3.2a,b, scanning electron microscopy (SEM) images showed the interesting morphology of the nanocomposite. Figure 3.2a is a low resolution SEM image and Figure 3.2b is a high resolution SEM image that shows ordered, vertically aligned PANI directly growing on and around the GNRs, forming one dimensional wires with porcupine-like quills. The structural detail was also found in the transmission electron microscopy (TEM) images, as shown in Figure 3.2c,d. TEM images of PANI-GNRs revealed that PANI nanorods covered the external surface of the GNRs. They were ~ 20 nm wide and almost 300 nm in length.

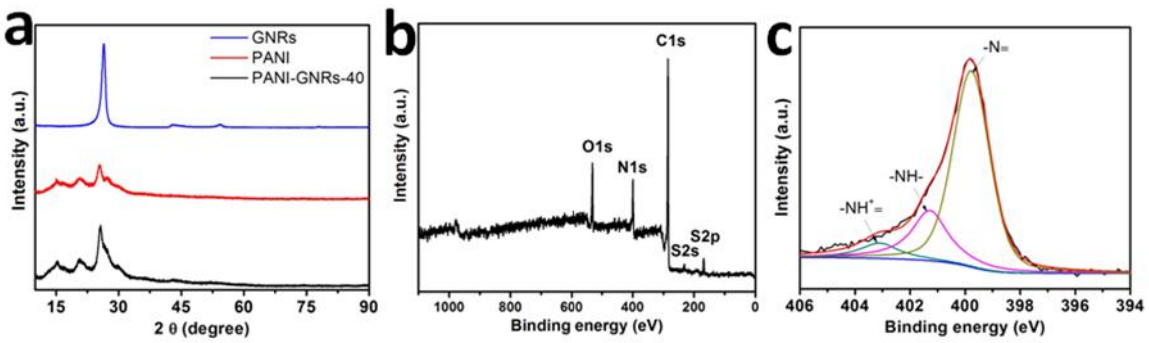

Figure 3.3. (a) XRD patterns of GNRs, PANI, PANI-GNRs-40. (b) XPS scan spectrum of PANI-GNRs-40. (c) N 1s core level XPS of PANI-GNRs-40.

X-ray diffraction (XRD) and X-ray photoelectron spectroscopy (XPS) were also used to characterize the nanocomposite PANI-GNRs. Figure 3.3a shows the XRD pattern of GNRs, pure PANI, and the PANI-GNRs composite. The GNRs showed a strong diffraction peak (002) of graphite at 26.5°.[21,24] The XRD pattern of PANI showed three characteristic peaks. The peaks at 2θ of 15.3° and 25.6° resulted from the periodicity both perpendicular and parallel to the polymer chain, respectively.[18,25] The peak at 2θ of 21.0° is caused by the layers of polymer chains at alternating distances.[18,26] The XRD pattern of composite PANI-GNRs had similar peaks as PANI, excluding the obvious increase in peak intensity at 26.5° due to the incorporated effect of GNRs in the composite.[18] XPS was used to analyze the composite PANI-GNRs. Figure 3.3b indicates that the composite PANI-GNRs only contained four elements, C, N, O, and trace S from the APS and/or sulfuric acid. As shown in Figure 3.3c, the deconvolution of the N 1s core-level XPS of PANI-GNRs-40 led to three peaks resulting from three different electronic states: the quinoid amine (-N=) with binding energy centered at 399.74 eV; the benzenoid amine (-

NH-) with binding energy centered at 401.28 eV; and the positively charged nitrogen (-NH^+=) binding energy centered at 403.10 eV.[27-29]

3.3.2. Electrochemical evaluation

In order to evaluate the electrochemical performance of PANI-GNRs as active electrode materials, cyclic voltammetry (CV), galvanostatic charge discharge experiments, and electrochemical impedance spectroscopy (EIS) experiment were carried out using a two-electrode configuration in 1 M H_2SO_4 aqueous solution. Figure 3.4 shows the CV curves of the PANI-GNRs-20, PANI-GNRs-40, PANI-GNRs-64, GNRs, and pure PANI in the potential window range of 0 to 0.8 V. As shown in Figure 3.4a, the CV curve of GNRs was minuscule compared to the others, demonstrating that GNRs had almost no contribution to capacitance. Therefore, GNRs improved the electrical conductivity of the composite. The capacitance mainly resulted from the PANI. For PANI-GNRs-64, PANI-GNRs-40, PANI-GNRs-20, and pure PANI, there were two pairs of redox peaks in the CV curves at the 5 mV s^{-1} scan rate. The peaks from 0.15 V to 0.08 V result from the redox transitions of PANI from leucoemeraldine to emeraldine. The transition in form between emeraldine and pernigraniline leads to the peaks from 0.4 V to 0.3 V.[30] Figure 3.4b shows the CV curves of PANI-GNRs-40 at different scan rates from 5 to 100 mV s^{-1}. It is clear that the current response demonstrates a corresponding increase with the scan rate increase. Furthermore, the composite electrode maintained a broad CV shape even at high scan rate up to 100 mV s^{-1}. These characteristics demonstrate a good capacitive behavior of the electrode using the composite materials.

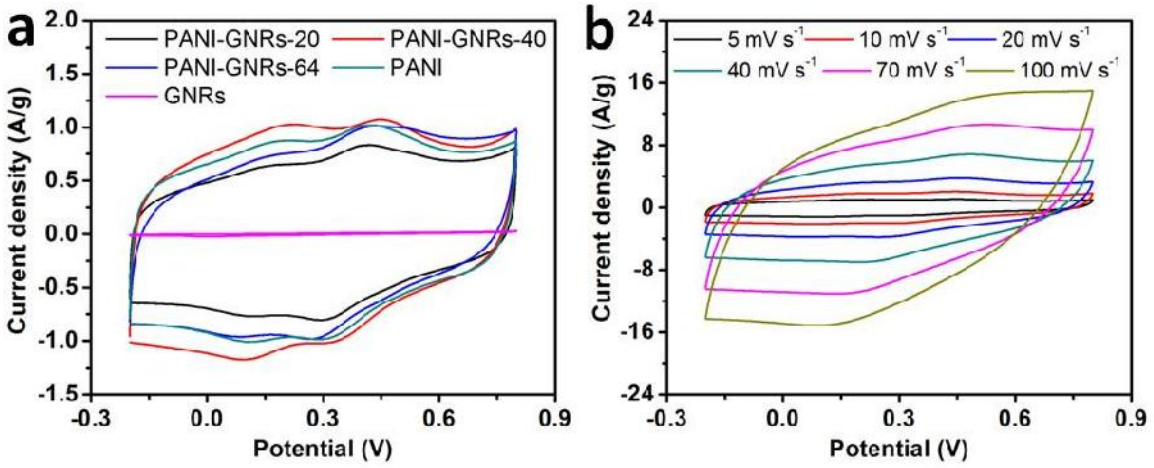

Figure 3.4. (a) Cyclic voltammetry curves of pure PANI, PANI-GNRs-20, PANI-GNRs-40, and PANI-GNRs-64 at the scan rate of 5 mV s-1 in 1 M H2SO4; (b) Cyclic voltammetry curves for PANI-GNRs-40 at the scan rate range of 5 to 100 mV s-1 in 1 M H2SO4.

The galvanostatic charge-discharge experiment was also carried out in order to evaluate the electrochemical properties of the composite. Figure 3.5a shows the galvanostatic charge-discharge curves of the PANI-GNRs-40 composite in the potential range from 0 to 0.8 V at varying current densities. The almost symmetrical charging and discharging curves demonstrate that the electrode materials had good capacitive behavior. With the increase of the current density, the discharging time gradually reduced. Figure 3.5b shows the galvanostatic charge-discharge curves of PANI, PANI-GNRs-20, PANI-GNRs-40, and PANI-GNRs-64 at the same current density. Based on the galvanostatic charge-discharge curves, the specific capacitance was obtained as shown in Figure 3.5c. PANI-GNRs-40 produced the best performance. Its specific capacitance was as high as 340 F/g at a current density of 0.25 A/g. With the increase of the current density, the value of specific capacitance decreased to 257 F/g at a current density of 4 A/g. Moreover, the

specific capacitance of PANI and PANI-GNRs-20 had similar trends with the variation in current density. At the same current density, the value of specific capacitance of PANI and PANI-GNRs-20 was lower than that of PANI-GNRs-40. The former might result from the low electrical conductivity compared to PANI-GNRs-40 embedded with GNRs, which are presumed to increase the electrical conductivity of the composite. The latter resulted from the high GNR content in the composite, which decreased the value of the specific capacitance. The difference in discharge time of PANI, PANI-GNRs-20, and PANI-GNRs-40 was also consistent with the variation of their CV curves at the same scan rates of 5 mV s^{-1} as shown in Figure 3.4a. The endurance galvanostatic charge-discharge experiment was also carried out to study the cyclic stability of the composite materials. As shown in Figure 3.5d, the capacity of PANI decreased quickly; 41% capacity was retained after 880 cycles. Conversely, the capacity retention of PANI-GNRs-40 still remained at ~ 90% after 4200 cycles. The great improvement in the cycling performance resulted from the enhanced mechanical strength of the composite due to the embedded GNRs. Moreover, the special structure of PANI-GNRs-40 is also helpful for the relaxation of the volume expansion during doping/dedoping process.[2] This demonstrates that the incorporation of GNRs into the composite greatly improves the cyclic stability and makes the PANI-GNRs-40 composite a suitable material for energy storage electrodes.

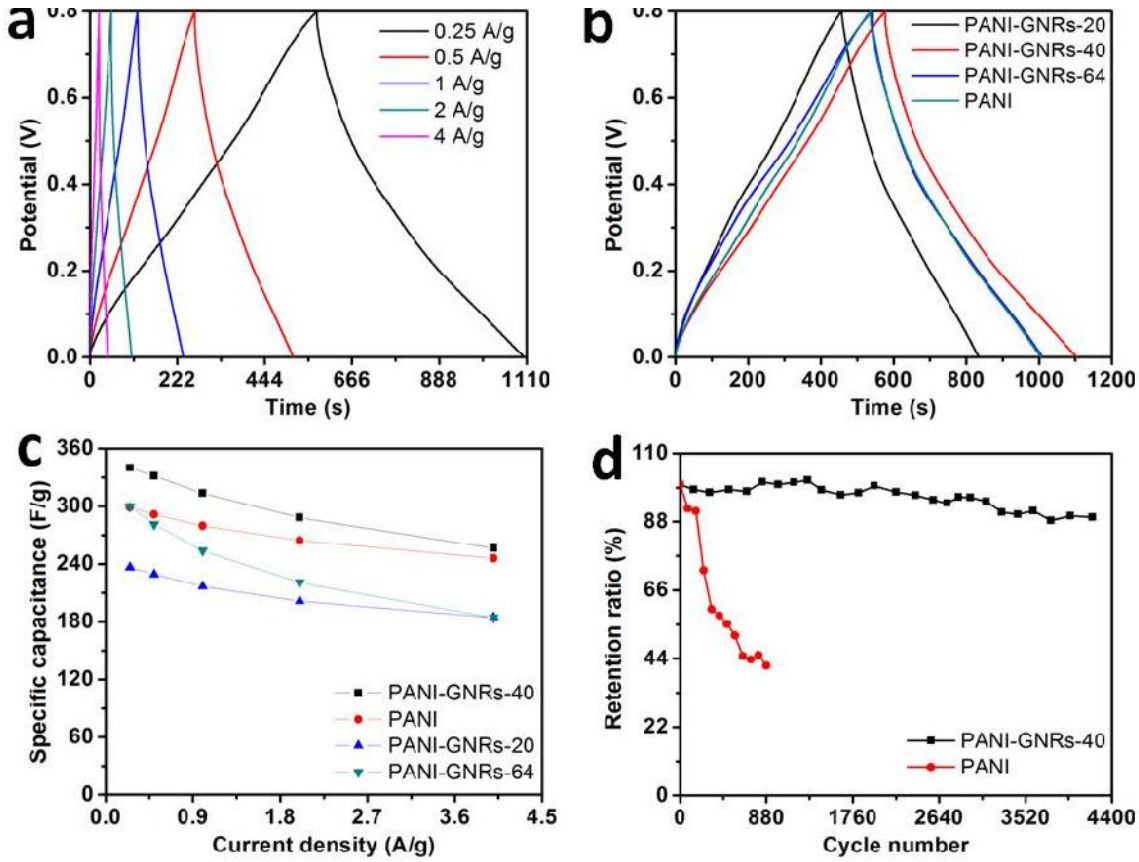

Figure 3.5. (a) Galvanostatic charge discharge curves of PANI-GNRs-40 at a current density range of 0.25 to 4 A/g. (b) Galvanostatic charge discharge curves of PANI, PANI-GNRs-20, PANI-GNRs-40, and PANI-GNRs-64 at a current density of 0.25 A/g. (c)The capacitance *versus* current density for the pure PANI and composites. (d) Cycling stability of PANI and PANI-GNRs-40 at a current density of 1 A/g.

Electrochemical impedance spectroscopy is a powerful tool to study the electrochemical behavior of PANI, PANI-GNRs-20, PANI-GNRs-40, and PANI-GNRs-64 in bulk and at the interface between the electrode and electrolyte.[31-33] The impedance was tested in the frequency range from 20 kHz to 0.01 Hz at the open circuit potential as shown in Figure 3.6a. At the higher frequency of 20 kHz, the value of impedance, which

is obtained by the intersection between the line and real axes, is the combination of electrolyte resistance and electrode resistance.[34-36] The 45° region in the plots demonstrated the porous structure properties of the PANI-GNRs. At the low frequencies, the straight line is nearly perpendicular to the real y axes, demonstrating that PANI-GNRs had pure capacitive behaviors.[35,36] The resistance of PANI-GNRs-20 was 0.73 Ω. The value of resistance increased as the GNR content decreased: 0.76 Ω for PANI-GNRs-40, 0.79 Ω for PANI-GNRs-64, and 0.96 Ω for PANI without GNRs. Therefore, more PANI loading in the composite would reduce the conductivity of the electrode. This result was in agreement with the potential variation of the *IR* drop (V_{IR} is 5 mV for PANI-GNRs-20, 12.7 mV for PANI-GNRs-40, 14.4 mV for PANI-GNRs-64, and 15.8 mV for PANI). Figure 3.6b is the Ragone plot of energy density versus power density for PANI, PANI-GNRs-20, PANI-GNRs-40, and PANI-GNRs-64. PANI-GNRs-40 had the highest energy density of 7.56 Wh/kg with the power density of 3149 W/kg at the current density of 0.25 A/g. PANI-GNRs-20 had the highest power density of 9467 W/kg with an energy density of 4.10 Wh/kg at a current density of 4 A/g. This value was far better than obtained in conventional supercapacitor.[5,3]

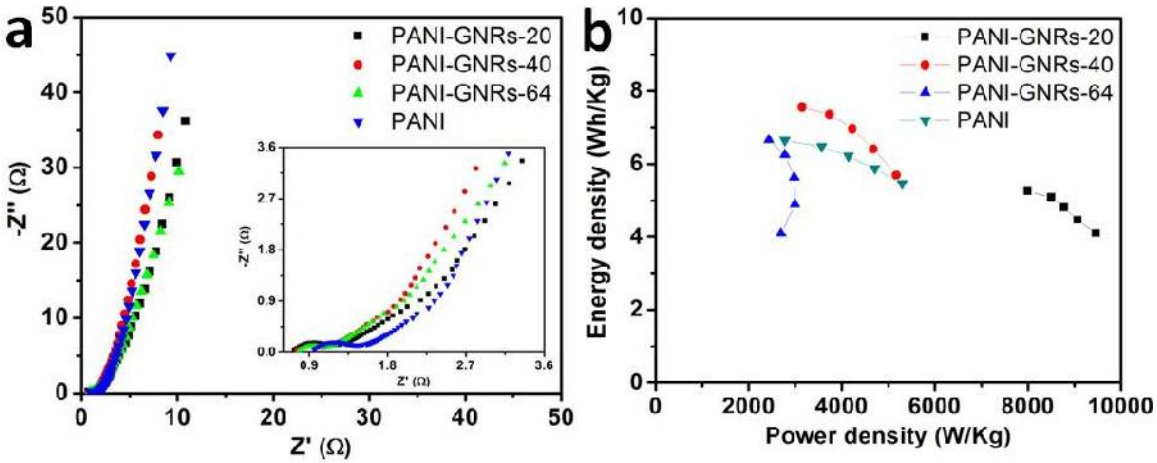

Figure 3.6. (a) Nyquist plots of PANI, PANI-GNRs-20, PANI-GNRs-40, and PANI-GNRs-64 (the inset is an enlarged view of the Nyquist curves). (b) Ragone plot of PANI, PANI-GNRs-20, PANI-GNRs-40, and PANI-GNRs-64.

3.4. Conclusion

In summary, ordered, vertically aligned PANI nanorods were grown on GNRs by the direct polymerization of aniline in the presence of GNRs. The nanostructures of the composite PANI-GNRs were characterized by SEM, TEM, XPS, and XRD and the results indicated that the PANI polymerized on the GNRs. Electrochemical studies demonstrated that synergy between PANI and GNRs affords the composites showing good electrochemical performance in energy storage, a high specific capacitance and greatly improved electrochemical stability in the extended time charge discharge process.

3.5. References

1. Li, L.; Raji, A.-R. O.; Fei, H.; Yang, Y.; Samuel, E. L. G.; Tour. J. M. Nanocomposite of Polyaniline Nanorods Grown on Graphene Nanoribbons for Highly Capacitive Pseudocapacitors. *ACS Appl. Mater. Interfaces* **2013**, *5*, 6622-6627. (L.L. conceived and designed the experiments. L.L. prepared the materials. L.L., R.A.R.O., F.H., and S.E.L.G. performed material characterization. L.L. and Y.Y. tested the devices. L.L. wrote the paper. Finally, J.M.T. oversaw all research phases, provided regular guidance to the research and revised the manuscript. All authors discussed and commented on the manuscript.)

2. Zhang, L. L.; Zhao, X. S. Carbon-based materials as supercapacitor electrodes. *Chem. Soc. Rev.* **2009,** *38* , 2520-2531.

3. Winter, M.; Brodd, R. J. What Are Batteries, Fuel Cells, and Supercapacitors? *Chem. Rev.* **2004,** *104* , 4245-4269.

4. Miller, J. R.; Simon, P. Electrochemical Capacitors for Energy Management. *Science* **2008,** *321* , 651-652.

5. Simon, P.; Gogotsi, Y. Materials for electrochemical capacitors. *Nat Mater.* **2008,** *7*, 845-854.

6. Chen, W.; Rakhi, R. B.; Hu, L.; Xie, X.; Cui, Y.; Alshareef, H. N. High-Performance Nanostructured Supercapacitors on a Sponge. *Nano Lett.* **2011,** *11*, 5165-5172.

7. Arico, A. S.; Bruce, P.; Scrosati, B.; Tarascon, J.-M.; van Schalkwijk, W. Nanostructured materials for advanced energy conversion and storage devices. *Nat Mater*. **2005,** *4*, 366-377.

8. Yu, G.; Hu, L.; Vosgueritchian, M.; Wang, H.; Xie, X.; McDonough, J. R.; Cui, X.; Cui, Y.; Bao, Z. Solution-Processed Graphene/MnO2 Nanostructured Textiles for High-Performance Electrochemical Capacitors. *Nano Lett.* **2011,** *11*, 2905-2911.

9. Xu, J.; Wang, K.; Zu, S.-Z.; Han, B.-H.; Wei, Z. Hierarchical Nanocomposites of Polyaniline Nanowire Arrays on Graphene Oxide Sheets with Synergistic Effect for Energy Storage. *ACS Nano* **2010,** *4*, 5019-5026.

10. Feng, X.-M.; Li, R.-M.; Ma, Y.-W.; Chen, R.-F.; Shi, N.-E.; Fan, Q.-L.; Huang, W. One-Step Electrochemical Synthesis of Graphene/Polyaniline Composite Film and Its Applications. *Adv.Funct.Mater.* **2011,** *21*, 2989-2996.

11. Bhadra, S.; Khastgir, D.; Singha, N. K.; Lee, J. H. Progress in preparation, processing and applications of polyaniline. *Prog. Polym. Sci.* **2009,** *34*, 783-810.

12. Wang, Y. G.; Li, H. Q.; Xia, Y. Y. Ordered Whiskerlike Polyaniline Grown on the Surface of Mesoporous Carbon and Its Electrochemical Capacitance Performance. *Adv. Mater.* **2006,** *18*, 2619-2623.

13. Kang, E. T.; Neoh, K. G.; Tan, K. L. Polyaniline: A polymer with many interesting intrinsic redox states. *Prog. Polym. Sci.* **1998,** *23*, 277-324.

14. Wu, Q.; Xu, Y.; Yao, Z.; Liu, A.; Shi, G. Supercapacitors Based on Flexible Graphene/Polyaniline Nanofiber Composite Films. *ACS Nano* **2010,** *4*, 1963-1970.

15. Li, D.; Huang, J.; Kaner, R. B. Polyaniline Nanofibers: A Unique Polymer Nanostructure for Versatile Applications. *Acc. Chem. Res.* **2008,** *42*, 135-145.

16. Ryu, K. S.; Kim, K. M.; Park, N.-G.; Park, Y. J.; Chang, S. H. Symmetric redox supercapacitor with conducting polyaniline electrodes. *J. Power Sources* **2002,** *103*, 305-309.

17. Zhang, K.; Zhang, L. L.; Zhao, X. S.; Wu, J. Graphene/Polyaniline Nanofiber Composites as Supercapacitor Electrodes. *Chem. Mater.* **2010,** *22*, 1392-1401.

18. Li, Y.; Zhao, X.; Yu, P.; Zhang, Q. Oriented Arrays of Polyaniline Nanorods Grown on Graphite Nanosheets for an Electrochemical Supercapacitor. *Langmuir* **2012,** *29*, 493-500.

19. Zhou, S.; Zhang, H.; Zhao, Q.; Wang, X.; Li, J.; Wang, F. Graphene-wrapped polyaniline nanofibers as electrode materials for organic supercapacitors. *Carbon* **2013,** *52*, 440-450.

20. Lai, L.; Yang, H.; Wang, L.; Teh, B. K.; Zhong, J.; Chou, H.; Chen, L.; Chen, W.; Shen, Z.; Ruoff, R. S.; Preparation of Supercapacitor Electrodes through Selection of Graphene Surface Functionalities. *ACS Nano* **2012**, *6*, 5941-5951.

21. Genorio, B.; Lu, W.; Dimiev, A.; Zhu, Y.; Raji, A.-R. O.; Novosel, B.; Alemany, L. B.; Tour, J. M. In Situ Intercalation Replacement and Selective Functionalization of Graphene Nanoribbon Stacks. *ACS Nano* 2012, 6, 4231-4240.

22. Zhao, X.; Zhang, L.; Murali, S.; Stoller, M. D.; Zhang, Q.; Zhu, Y.; Ruoff, R. S. Incorporation of Manganese Dioxide within Ultraporous Activated Graphene for High-Performance Electrochemical Capacitors. *ACS Nano* 2012, *6*, 5404-5412.

23. Bi, R.-R.; Wu, X.-L.; Cao, F.-F.; Jiang, L.-Y.; Guo, Y.-G.; Wan, L.-J. Highly Dispersed RuO2 Nanoparticles on Carbon Nanotubes: Facile Synthesis and Enhanced Supercapacitance Performance. *J. Phys. Chem. C* **2010**, *114*, 2448-2451.

24. Campos-Delgado, J.; Romo-Herrera, J. M.; Jia, X.; Cullen, D. A.; Muramatsu, H.; Kim, Y. A.; Hayashi, T.; Ren, Z.; Smith, D. J.; Okuno, Y.; Bulk Production of a New Form of sp2 Carbon: Crystalline Graphene Nanoribbons. *Nano Lett.* **2008**, *8*, 2773-2778.

25. Pouget, J. P.; Jozefowicz, M. E.; Epstein, A. J.; Tang, X.; MacDiarmid, A. G. X-ray structure of polyaniline. *Macromolecules* **1991**, *24*, 779-789.

26. Li, Y.; Zhao, X.; Xu, Q.; Zhang, Q.; Chen, D. Facile Preparation and Enhanced Capacitance of the Polyaniline/Sodium Alginate Nanofiber Network for Supercapacitors. *Langmuir* **2011**, *27*, 6458-6463.

27. Yue, J.; Epstein, A. J. XPS study of self-doped conducting polyaniline and parent systems. *Macromolecules* **1991**, *24*, 4441-4445.

28. An, J.; Liu, J.; Zhou, Y.; Zhao, H.; Ma, Y.; Li, M.; Yu, M.; Li, S. Polyaniline-Grafted Graphene Hybrid with Amide Groups and Its Use in Supercapacitors. *J. Phys. Chem. C* **2012**, *116*, 19699-19708.

29. Kim, B.-J.; Oh, S.-G.; Han, M.-G.; Im, S.-S. Synthesis and characterization of polyaniline nanoparticles in SDS micellar solutions. *Synth. Met.* **2001**, *122*, 297-304.

30. Li, H.; Wang, J.; Chu, Q.; Wang, Z.; Zhang, F.; Wang, S. Theoretical and experimental specific capacitance of polyaniline in sulfuric acid. *J. Power Sources* **2009**, *190*, 578-586.

31. Taberna, P. L.; Simon, P.; Fauvarque, J. F. Electrochemical Characteristics and Impedance Spectroscopy Studies of Carbon-Carbon Supercapacitors. *J. Electrochem. Soc.* **2003**, *150*, A292-A300.

32. Masarapu, C.; Zeng, H. F.; Hung, K. H.; Wei, B. Effect of Temperature on the Capacitance of Carbon Nanotube Supercapacitors. *ACS Nano* **2009**, *3*, 2199-2206.

33. Choi, B. G.; Hong, J.; Hong, W. H.; Hammond, P. T.; Park, H. Facilitated Ion Transport in All-Solid-State Flexible Supercapacitors. *ACS Nano* **2011**, *5*, 7205-7213.

34. Hu, L.; Chen, W.; Xie, X.; Liu, N.; Yang, Y.; Wu, H.; Yao, Y.; Pasta, M.; Alshareef, H. N.; Cui, Y. Symmetrical MnO2–Carbon Nanotube–Textile Nanostructures for Wearable Pseudocapacitors with High Mass Loading. *ACS Nano* **2011**, *5*, 8904-8913.

35. Sheng, K.; Sun, Y.; Li, C.; Yuan, W.; Shi, G. Ultrahigh-rate supercapacitors based on eletrochemically reduced graphene oxide for ac line-filtering. *Sci. Rep* **2012**, 2, 247.

36. Chen, J.; Sheng, K.; Luo, P.; Li, C.; Shi, G. Graphene Hydrogels Deposited in Nickel Foams for High-Rate Electrochemical Capacitors. *Adv. Mater.* **2012**, *24*, 4569-4573.

37. Meng, C.; Liu, C.; Chen, L.; Hu, C.; Fan, S. Highly Flexible and All-Solid-State Paperlike Polymer Supercapacitors. *Nano Lett.* **2010**, *10*, 4025-4031.

Chapter 4

High-performance Microsupercapacitors from Laser Induced Graphene

This chapter was entirely copied from reference 1.

4.1. Introduction

The development and miniaturization of energy storage devices facilitate the growth of modern micro-electronic systems.[2-4] Microbatteries are presently the major power source for miniaturized electronic devices even though they suffer from sluggish charge/discharge processes and then show a limited cycle life.[3-8] Microsupercapacitors (MSCs), on the other hand, have high power density, fast charge/discharge rates, and long service life, and with in-plane interdigitated electrodes show a promising future to replace microbatteries.[3-8] However, developing MSCs with a high energy density close to or exceeding microbatteries without sacrificing other electrochemical characteristics is a crucial challenge.[5,9] The most common strategy is the use of photolithography to prepare interdigitated patterns of highly conductive carbon materials to provide the electrochemical double layer capacitance (EDLC).[9-15] In order to improve their energy storing ability, pseudocapacitive materials, such as transition metal oxides [11,13,16-18] and electrically

conductive polymers,[19,20] are loaded onto the electrodes to provide capacitance from surface redox reactions. However, this fabrication strategy is limited by either high-cost patterning processes or harsh synthetic conditions. Recently, laser writing technology has also been used to reduce and pattern graphene oxide (GO) as interdigitated electrodes in MSCs.[21-23] However, the synthesis and post-reaction treatment of GO and the problematic stability of the remaining GO in such devices presents commercialization challenges.[24,25]

Recently, our group developed a simple and scalable method to prepare patterned porous graphene on a polyimide (PI) substrate by laser writing patterns in air, and the resulting laser induced graphene (LIG) showed its promising applications in miniaturized energy storage devices.[26-28] Here, we combine the laser induction process with subsequent electrodeposition of pseudocapacitive materials for the fabrication of flexible MSC devices that show greatly improved electrochemical performance. A CO_2 laser is first used to convert the PI into porous LIG with an interdigitated architecture, which works not only as EDLC electrodes, but also as a flexible and conductive matrix for the electrodeposition of pseudocapacitive materials. Two types of pseudocapacitive materials, manganese oxide (MnO_2) and polyaniline (PANI), representing characteristic transition metal oxides and conductive polymers, are electrodeposited onto the LIG forming LIG-MnO_2 and LIG-PANI composites. They are then assembled into all-solid-state flexible MSCs that are free of current collectors, binder, and separator due to the well-defined pattern which avoids short circuiting the electrodes. Both LIG-MnO_2-MSCs and LIG-PANI-MSCs demonstrate comparable energy densities to microbatteries without sacrificing their good rate performance, cycling stability, and mechanical flexibility.

4.2. Experiments

4.2.1. Materials synthesis

4.2.1.1. Synthesis of LIG

The synthesis and patterning of LIG from a polyimide sheet was done as we described previously.[27,28] Kapton polyimide films (McMaster-Carr, Cat. No. 2271K3, thickness: 0.005") were used as received. LIG was generated using a CO_2 laser cutter system (Universal X-660 laser cutter platform) on Kapton polyimide film at a power of 4.8 W. All samples were prepared under room temperature and ambient air. LIG was patterned into 12 interdigitated electrodes with a length of 4.1 mm, a width of 1 mm, and a spacing of ~300 µm between two neighboring microelectrodes (Figure S12). After that, Pellco® colloidal silver paint (No. 16034, Ted Pella) was first applied on the common areas of both electrodes for better electrical contact. The electrodes were then extended with conductive copper tape which were connected to an electrochemical workstation for testing. A Kapton polyimide tape was employed followed by an epoxy (Machineable-fast set, Reorder # 04002, Hardman®) sealing to protect the common areas of the electrodes from electrolyte.

4.2.1.2. Synthesis of LIG-MnO_2

Electrodeposition of MnO_2 on LIG was achieved with a three-electrode setup. LIG on a PI sheet served as the working electrode, which was immersed into an aqueous solution containing 0.01 M $Mn(CH_3COO)_2$ at ~ 60 °C. Platinum foil (Sigma-Aldrich) was the counter electrode and Ag/AgCl (Fisher Scientific) was the reference electrode. A constant current density of 1 mA/cm^2 was applied for a certain time to ensure good

deposition of MnO_2 on the sample. The amount of MnO_2 onto LIG was controlled by adjusting the deposition time. After electrodeposition, the sample was taken out and washed with deionized water to remove excess electrolyte, and then placed in a vacuum desiccator overnight (~120 mm Hg).

4.2.1.3. Synthesis of LIG-PANI

Electrodeposition of PANI on LIG was achieved with a three-electrode setup. LIG on a PI sheet served as the working electrode, which was immersed into an aqueous solution containing 0.1 M aniline and 1.0 M H_2SO_4. With a platinum counter electrode and $Hg/HgCl_2$ (Fisher Scientific) reference electrode, PANI was electrochemically deposited onto LIG by cycling within the potential window from -0.20 V to 0.95 V *vs.* $Hg/HgCl_2$. The amount of PANI onto LIG was controlled by the cycle number of deposition. After electrodeposition, LIG-PANI was treated with 1.0 M H_2SO_4 for 1 h. A uniform dark green film was obtained after washing with deionized water to remove excess electrolyte and drying in a vacuum desiccator overnight (~120 mm Hg).

4.2.2. Materials characterization

Products were characterized by X-ray diffraction (XRD, Rigaku D/Max Ultima II); X-ray photoelectron spectroscopy (XPS, PHI Quantera); scanning electron microscopy (SEM, JEOL 6500; FEI Quanta 400 ESEM FEG); thermogravimetric analysis (TGA, TA Instruments, Q50); and transmission electron microscopy (TEM, JEM2100F TEM).

4.2.3. Device fabrication

Polymeric gel electrolytes of PVA/LiCl and PVA/H_2SO_4 were prepared according to the previously reported method[22,42] and used in LIG-MnO_2 and LIG-PANI, respectively. For PVA/LiCl, it was made by stirring 10 mL of DI water, 2.0 g of LiCl (Sigma-Aldrich), and 1.0 g of PVA (M_w = 50000, Aldrich No. 34158-4) at 80℃ overnight. For PVA/H_2SO_4, it was made by stirring 10 mL of DI water, 1.0 mL of sulfuric acid (98%, Sigma-Aldrich), and 1.0 g of PVA at 80℃ overnight. ~ 0.25 mL of the electrolyte was applied to the active area of the devices, and was dried under ambient conditions for 4 h. The all-solid-state MSCs were obtained after drying in a vacuum desiccator (~120 mm Hg) overnight for further solidification of the electrolyte.

4.2.4. Electrochemical measurement

The electrochemical performances of the flexible all-solid-state MSCs were characterized by CV, galvanostatic charge-discharge experiments, and EIS using an electrochemical station (CHI 660D). The areal specific capacitance (C_A) and volumetric specific capacitance (C_V) of electrode materials were calculated from galvanostatic charge-discharge curves according to eq 4.1 and eq 4.2, respectively:

$$C_A = 4I / (A_{Device} \times (dV/dt)) \qquad (1)$$

$$C_V = 4I / (V_{Device} \times (dV/dt)) \qquad (2)$$

where I is the current applied, A_{Device} is the total area of the device (Figure 4.12), V_{Device} is the total volume of the device (Figure 4.12), and dV/dt is the slope of the discharge curve.

The areal capacitance ($C_{Device,A}$) and volumetric capacitance ($C_{Device,V}$) of the MSCs were calculated by using eq 4.3 and 4.4, respectively:

$$C_{Device,A} = C_A / 4 \qquad (3)$$

$$C_{Device,V} = C_V / 4 \qquad (4)$$

The areal energy density ($E_{Device,A}$) and volumetric energy density ($E_{Device,V}$) of the MSCs were calculated by using eq 4.5 and 4.6, respectively:

$$E_{Device,A} = C_{Device,A}V^2/ (2 \times 3600) \qquad (5)$$

$$E_{Device,V} = C_{Device,V}V^2/ (2 \times 3600) \qquad (6)$$

where V is the applied voltage.

The areal power density ($P_{Device,A}$) and volumetric power density ($P_{Device,V}$) of the MSCs were calculated by using eq 4.7 and 4.8, respectively:

$$P_{Device,A} = E_{Device,A} \times 3600/t \qquad (7)$$

$$P_{Device,V} = E_{Device,V} \times 3600/t \qquad (8)$$

where t is the discharge time.

4.3. Results and Discussion

4.3.1. Synthesis and structure analysis

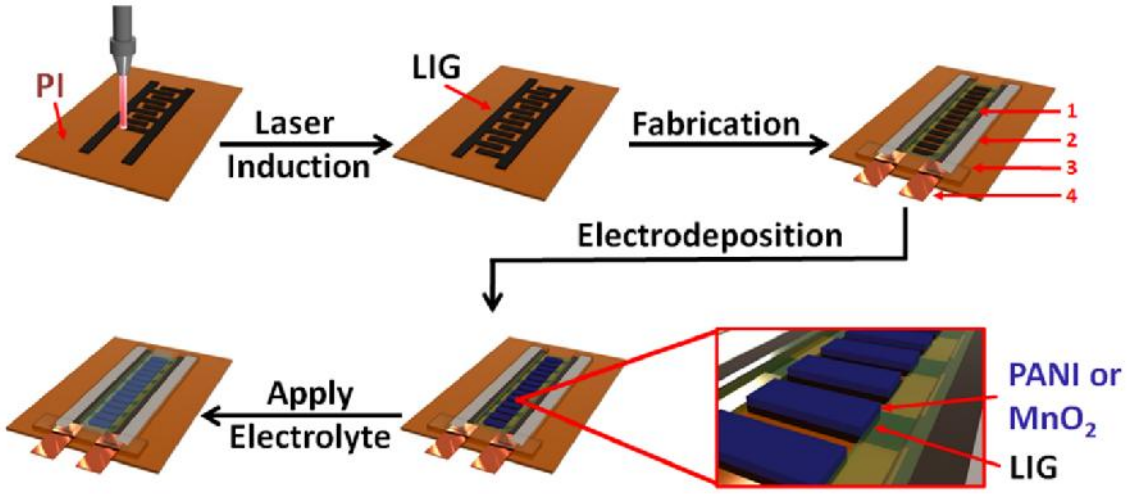

Figure 4.1. Scheme of the fabrication of MSCs with LIG-MnO_2 or LIG-PANI as electrodes. 1, 2, 3, and 4 are epoxy adhesive, silver paste, Kapton tape and copper tape, respectively.

The two-step syntheses of the hybrid materials, LIG-MnO_2 and LIG-PANI, and their fabrication into MSCs are shown in Figure 4.1. CO_2 laser induction of the PI substrate was first conducted to form a patterned LIG with 12 in-plane interdigitated electrodes (6 per polarity), onto which the pseudocapacitive material, MnO_2 or electrically conductive PANI, was then electrodeposited to form the composites of PANI-MnO_2 or LIG-PANI. The amount of MnO_2 or PANI in the composites was easily controlled by adjusting the deposition time or cycles, and here labeled as LIG-MnO_2-X (where X represents the deposition time) and LIG-PANI-Y (where Y represents the number of deposition cycles). Details for LIG synthesis and electrodeposition of MnO_2 or PANI can be found in the

experimental section. Solid-state polymer electrolyte containing poly(vinyl alcohol) (PVA) was used to complete the fabrication of the MSC devices. MSCs of various sizes can be prepared on demand by computer-controlled patterning during the laser induction process (Figure 4.2).

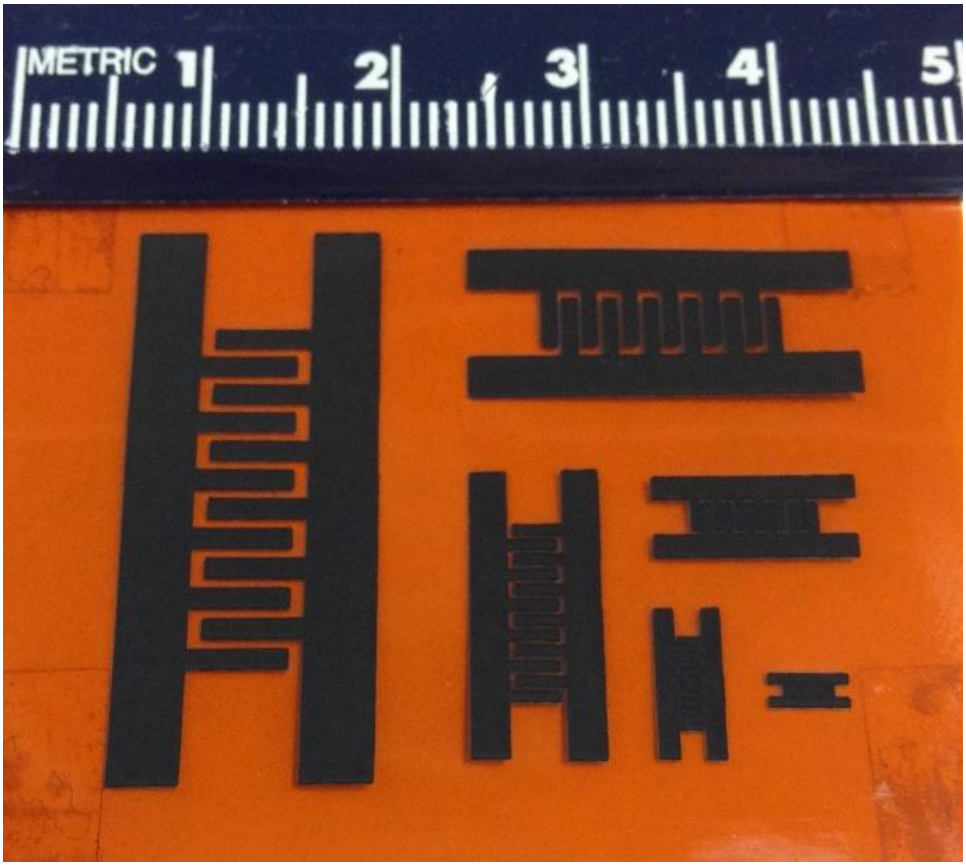

Figure 4.2. Digital image of LIG on PI sheet with different sizes. The unit of the ruler in the image is centimeters.

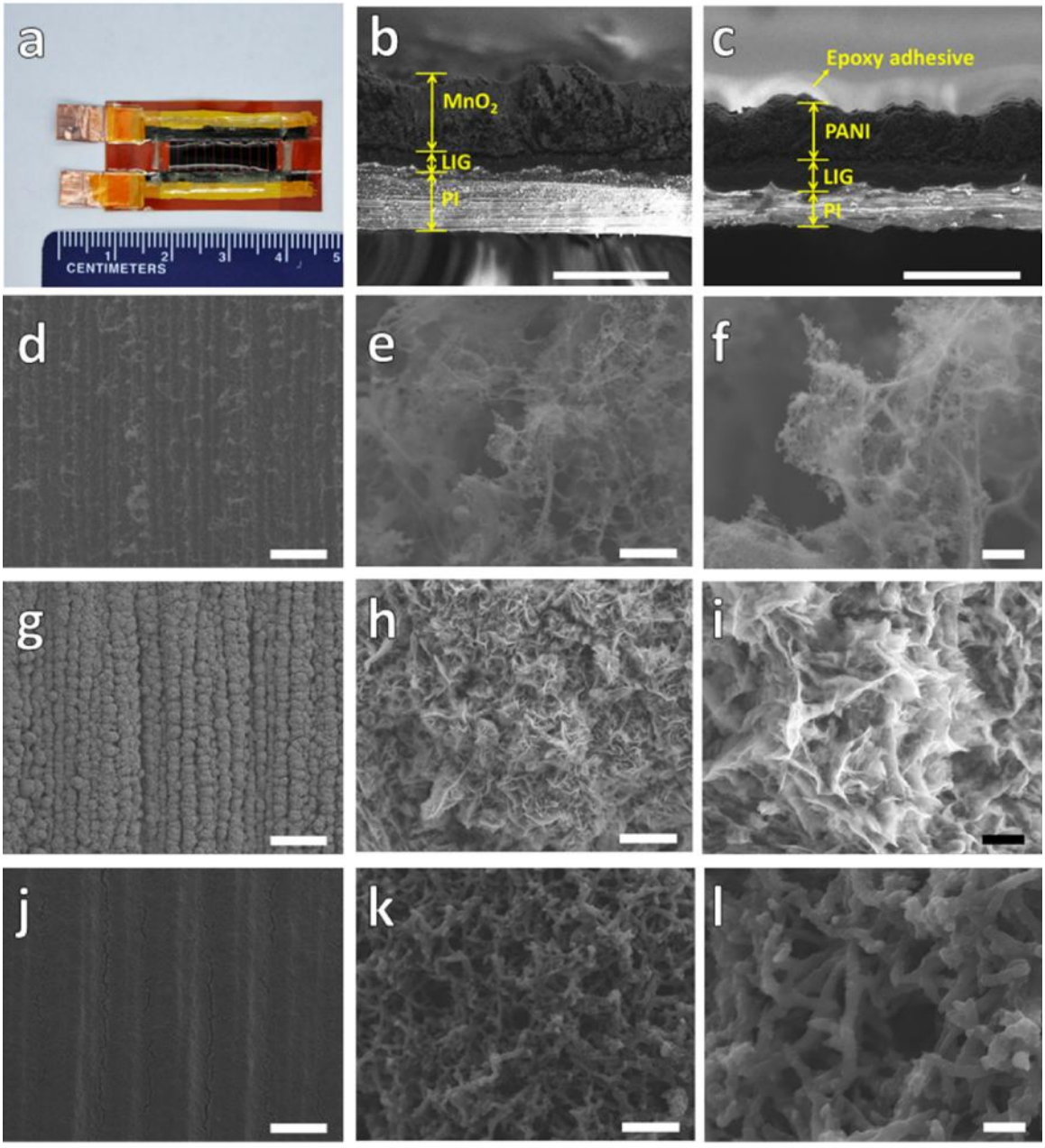

Figure 4.3. (a) Digital photograph of a LIG-PANI-MSC device. (b, c) Cross-sectional SEM images of PANI-MnO_2 and LIG-PANI. Scale bars are 100 µm. SEM images of top view of (d-f) LIG, (g-i) MnO_2 in LIG-MnO2, and (j-l) PANI in LIG-PANI. The scale bars are 100 µm for Figure b, d, g, and j, 2 µm for Figure e, h, and k, and 0.5 µm for Figure f, i, and l.

Figure 4.3a shows a digital photograph of one fully fabricated MSC device using this method. Figure 4.3b,c show the cross-sectional scanning electron microscopy (SEM) images of LIG-MnO_2-2.5h and LIG-PANI-15, in which MnO_2 or PANI was observed to deposit onto the LIG layer. The average thickness of the composite depends on the electrodeposition time or cycles and increases from 34 µm of LIG alone to 101 µm of LIG-MnO_2-4.0h and 76 µm of LIG-PANI-15 (Figure 4.4,5,6). Figure 4.3d-l show the top view SEM images of LIG (Figure 4.3d-f), LIG-MnO_2 (Figure 4.3g-i), and LIG-PANI (Figure 4.3j-l) at different resolution, respectively. While LIG forms a porous thin film structure that could work as a conductive matrix for the following electrodeposition, the deposited MnO_2 forms a flower shape and PANI forms a nanofiber structure.

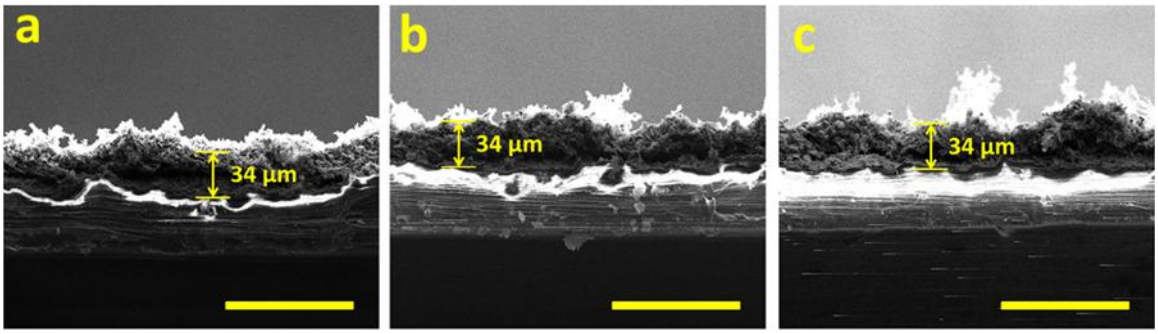

Figure 4.4. Cross-sectional SEM images of (a-c) LIG, indicating the height of the samples is ~ 34 µm. The scale bars are 100 µm.

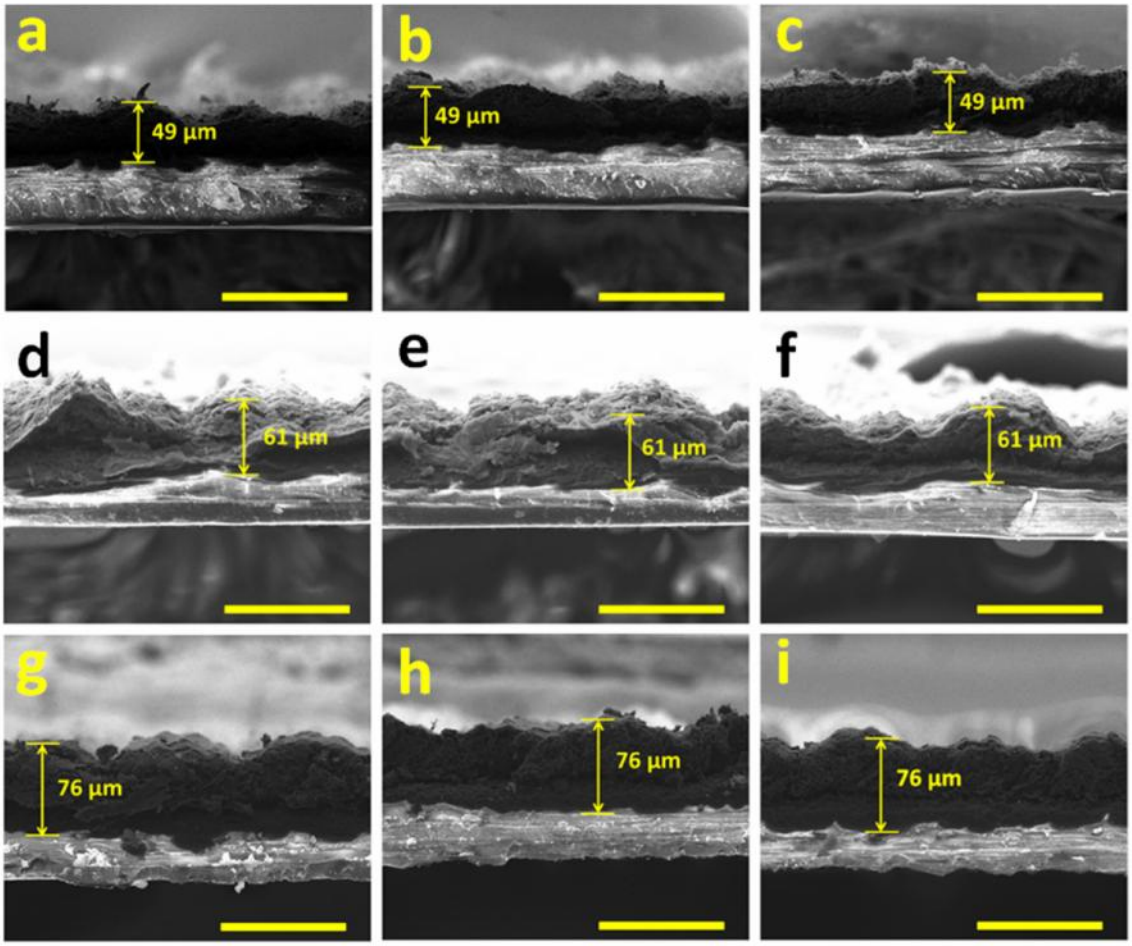

Figure 4.5. Cross-sectional SEM images of (a-c) LIG-PANI-5, (d-f) LIG-PANI-10, and (g-i) LIG-PANI-15, indicating the height of the samples are ~ 49 µm, ~ 61 µm, and ~ 76 µm, respectively. The scale bars are 100 µm.

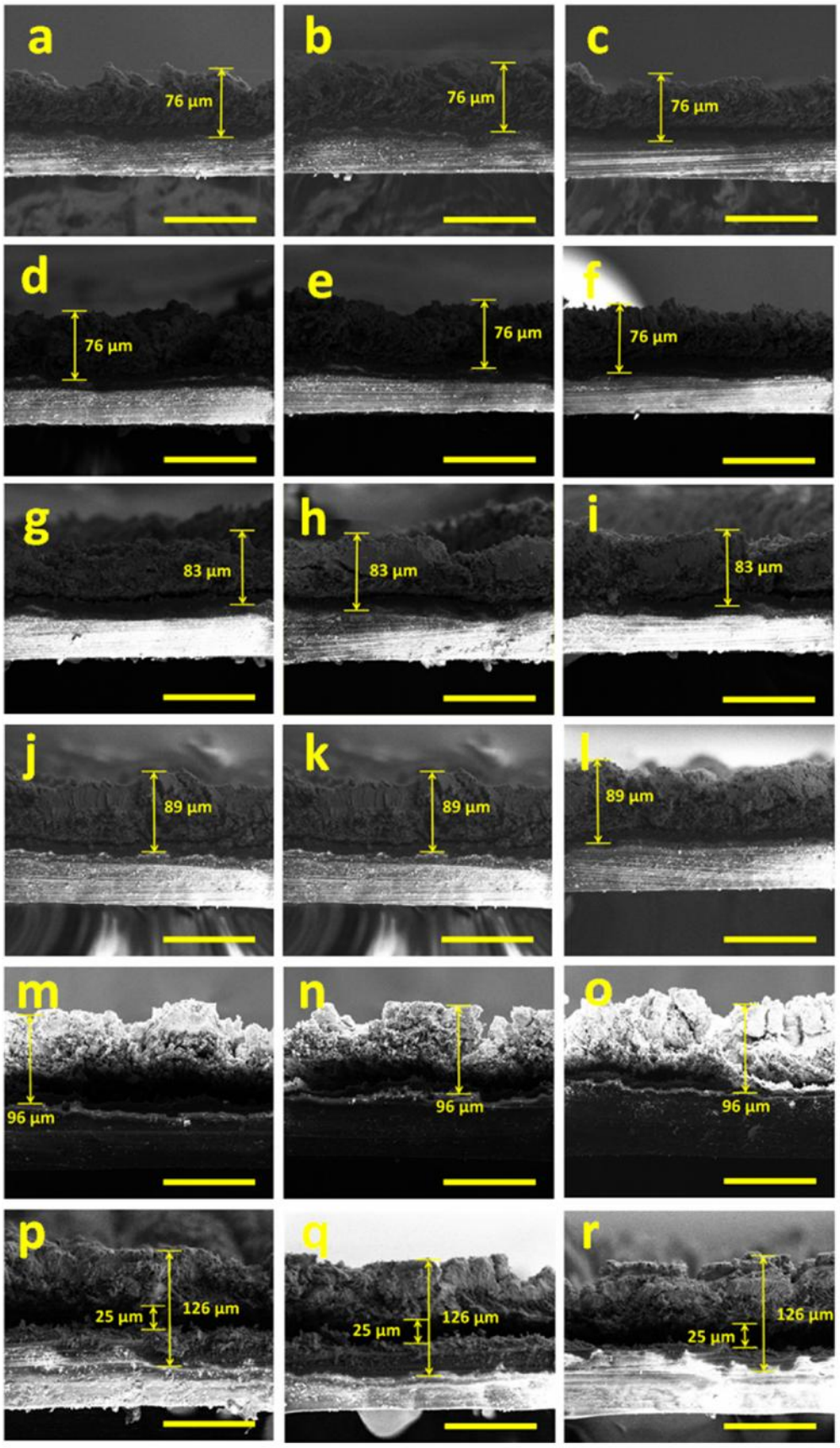
a
76 µm
b
76 µm
c
76 µm
d
76 µm
e
76 µm
f
76 µm
g
83 µm
h
83 µm
i
83 µm
j
89 µm
k
89 µm
l
89 µm
m
96 µm
n
96 µm
o
96 µm
p
25 µm
126 µm
q
25 µm
126 µm
r
25 µm
126 µm

Figure 4.6. Cross-sectional SEM images of (a-c) LIG-MnO_2-1.0h, (d-f) LIG-MnO_2-1.5h, (g-i) LIG-MnO_2-2.0h, (j-l) LIG-MnO_2-2.5h, (m-o) LIG-MnO_2-3.0h, and (p-r) LIG-MnO_2-4.0h, indicating the height of these samples are ~ 76 µm, ~ 76 µm, ~ 83 µm, ~ 89 µm, ~ 96 µm, and ~ 101 µm, respectively. The scale bars are 100 µm.

The morphologies of PANI-MnO_2 and LIG-PANI are further characterized by transmission electron microscopy (TEM) as shown in Figure 4.7. Crystallized MnO_2 and nanofiber-shaped PANI were found to directly attach onto LIG.

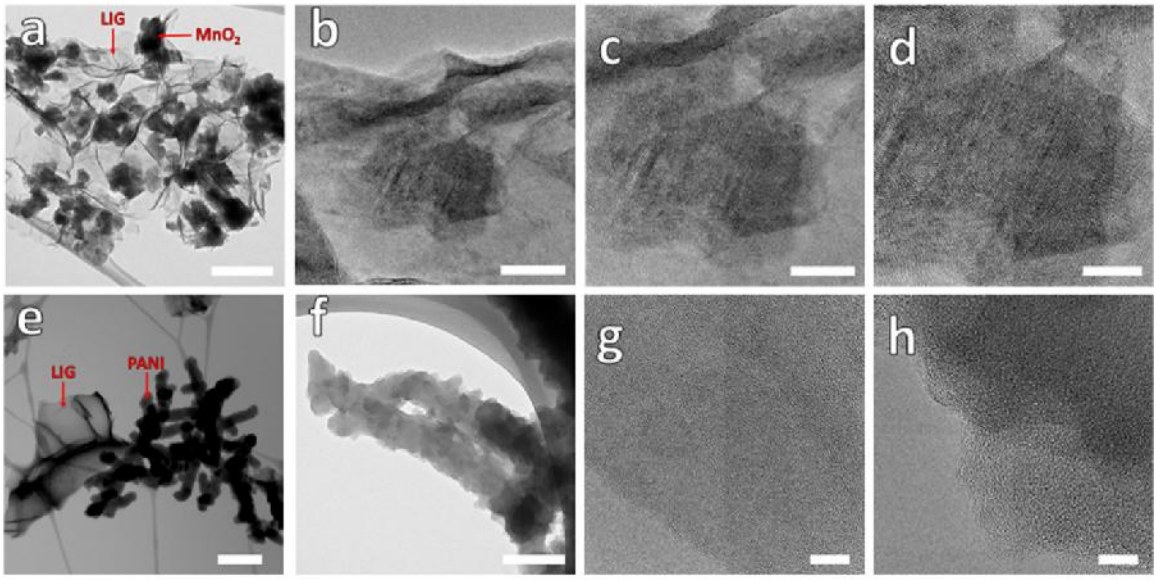

Figure 4.7. TEM images of the LIG-MnO_2 and LIG-PANI hybrid materials. (a) The TEM image of the LIG-MnO_2 hybrid material. (b-d) The TEM images of MnO2 in LIG-MnO_2 at different resolutions. The scale bar is 400 nm for Figure a, 20 nm for Figure b,c, and 10 nm for Figure d. (e) The TEM image of the LIG-PANI hybrid material. The scale bar is 4 µm. (f) The TEM image of PANI. The scale bar is 200 nm. (g) HRTEM image of LIG with graphitic edges. The scale bar is 10 nm. (h) HRTEM image of PANI with amorphous character. The scale bar is 10 nm.

Raman spectra, X-ray diffraction (XRD), X-ray photoelectron spectroscopy (XPS) were also used to study the composites and proved their compositions (Figure 4.8).[28-31] Figure 4.8a shows the Raman spectra of LIG and LIG-PANI-15. The characteristic peaks at ~ 1350 cm^{-1}, ~ 1597 cm^{-1} and ~ 2707 cm^{-1} from LIG sample represent the D band, G band and 2D bands, respectively, indicating the graphitic structure of LIG.[27,28] The polyaniline peaks from 1000 cm^{-1} to 1600 cm^{-1} in LIG-PANI-15 sample confirm the formation of PANI.[30] Figure 4.8b shows the XRD patterns of LIG, LIG-PANI-15, and LIG-MnO_2-2.5h. LIG showed a strong diffraction peak (002) of graphite at 26°.[27,28] LIG-PANI-15 show two peaks centered at 15.3° and 26°, resulting from the periodicity both perpendicular and parallel to the polymer chain, respectively.[30] The XRD pattern of LIG-MnO_2-2.5h can be indexed to α-MnO_2.[31] Due to the relatively small size of the crystals, the XRD pattern peaks of MnO_2 in LIG-MnO_2-2.5h become broad and weak.[31] The XRD peak of LIG in LIG-MnO_2-2.5h is covered by MnO_2. Figure 4.8c shows XPS spectra of LIG, LIG-PANI-15, and LIG-MnO_2-2.5h. LIG-PANI-15 contained four elements, C, N, O, and trace S from the sulfuric acid. LIG-MnO_2-2.5h contained three main elements, C, O, and Mn. The oxidation state of Mn in LIG-MnO_2-2.5h is further confirmed by high-resolution XPS as shown in Figure 4.8d. The spin energy separation of Mn $2p_{3/2}$ and Mn $2p_{1/2}$ centered at 642.5 eV and 654.2 eV is 11.7 eV, which is in good agreement with reported data of Mn $2p_{3/2}$ and Mn $2p_{1/2}$ in MnO_2.[31]

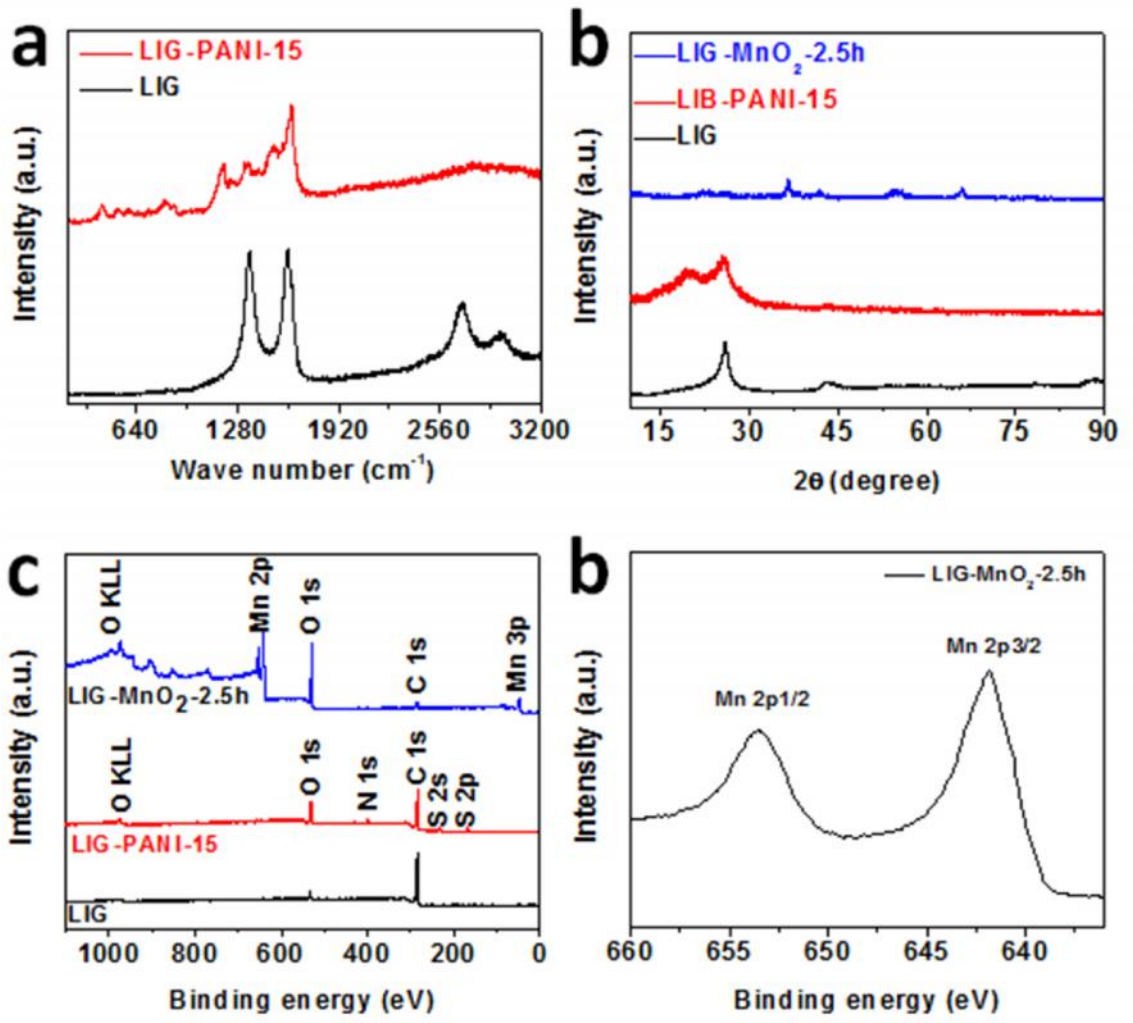

Figure 4.8. (a) Raman spectra of LIG and LIG-PANI-15, (b) XRD patterns of LIG, LIG-PANI-15, and LIG-MnO_2-2.5h, (c) XPS spectra of LIG, LIG-PANI-15, and LIG-MnO_2-2.5h, (d) Elemental XPS spectrum of Mn 2p for LIG-MnO_2-2.5h. C1s peak (284.5 eV) was used as standard to corret the data.

4.3.2. Electrochemical evaluation

We firstly studied the electrochemical performance of LIG-MnO_2-MSCs using LiCl/PVA as the electrolyte from cyclic voltammetry (CV) and galvanostatic charge-discharge experiments in a potential window from 0 to 1.0 V. Figure 4.9a shows the CV

curves of LIG-MnO_2-X and LIG at a scan rate of 5 mV/s. Although LIG is known to contribute capacitance by the EDLC mechanism,[26-28] the CV curve of LIG is minuscule compared to those of LIG-MnO_2-X, demonstrating that most of the capacitance comes from the pseudocapacitance of MnO_2. Also, aside from the much larger CV curve area, the nearly rectangular CV shape of LIG-MnO_2-X indicates good capacitive behavior.

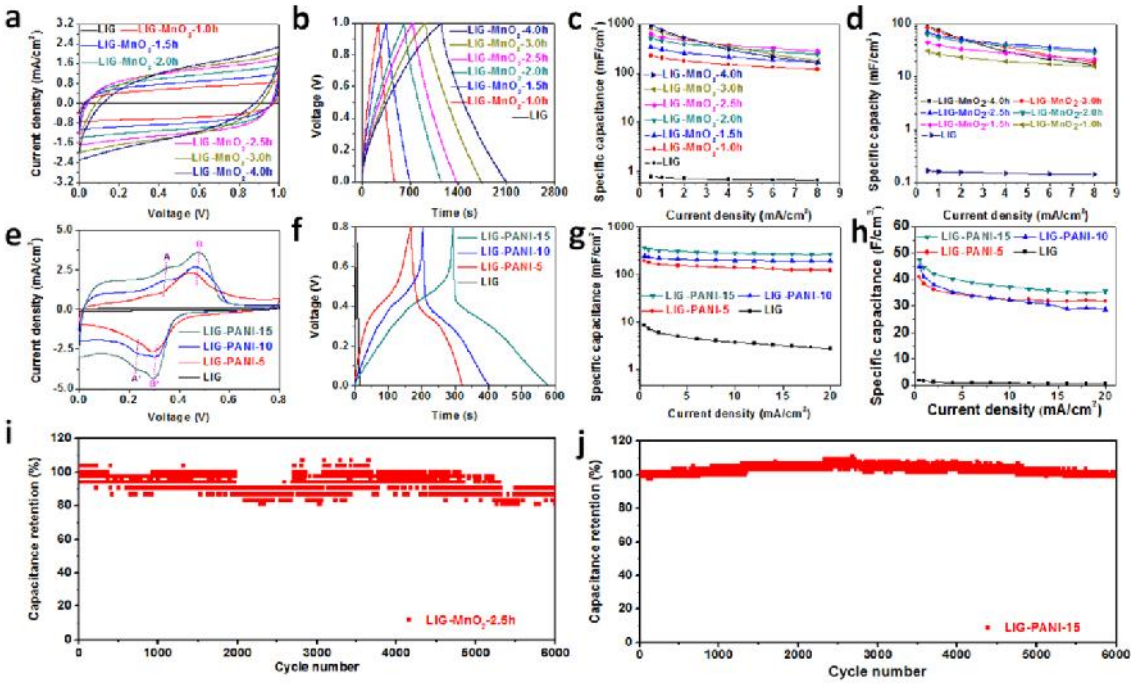

Figure 4.9. Electrochemical performance of LIG-MnO_2 and LIG-PANI MSCs. (a) CV curves of LIG-MnO_2-X and LIG at a scan rate of 5 mV/s. (b) Galvanostatic charge discharge curves of LIG-MnO_2-X and LIG at a current density of 0.5 mA/cm². (c) Areal specific capacitance and (d) volumetric specific capacitance of LIG-MnO_2-X and LIG over a current density range of 0.5 and 8.0 mA/cm². (e) CV curves of LIG-PANI-Y and LIG at a scan rate of 10 mV/s. (f) Galvanostatic charge discharge curves of LIG-PANI-Y and LIG at a current density of 0.5 mA/cm². (g) Areal specific capacitance and (h) volumetric specific capacitance of LIG-PANI-Y and LIG over a current density range of 0.5 and 20.0 mA/cm². (i) Cycling stability of LIG-MnO_2-2.5h at the current density of 1.0 mA/cm². (j) Cycling stability of LIG-PANI-15 at the current density of 0.8 mA/cm².

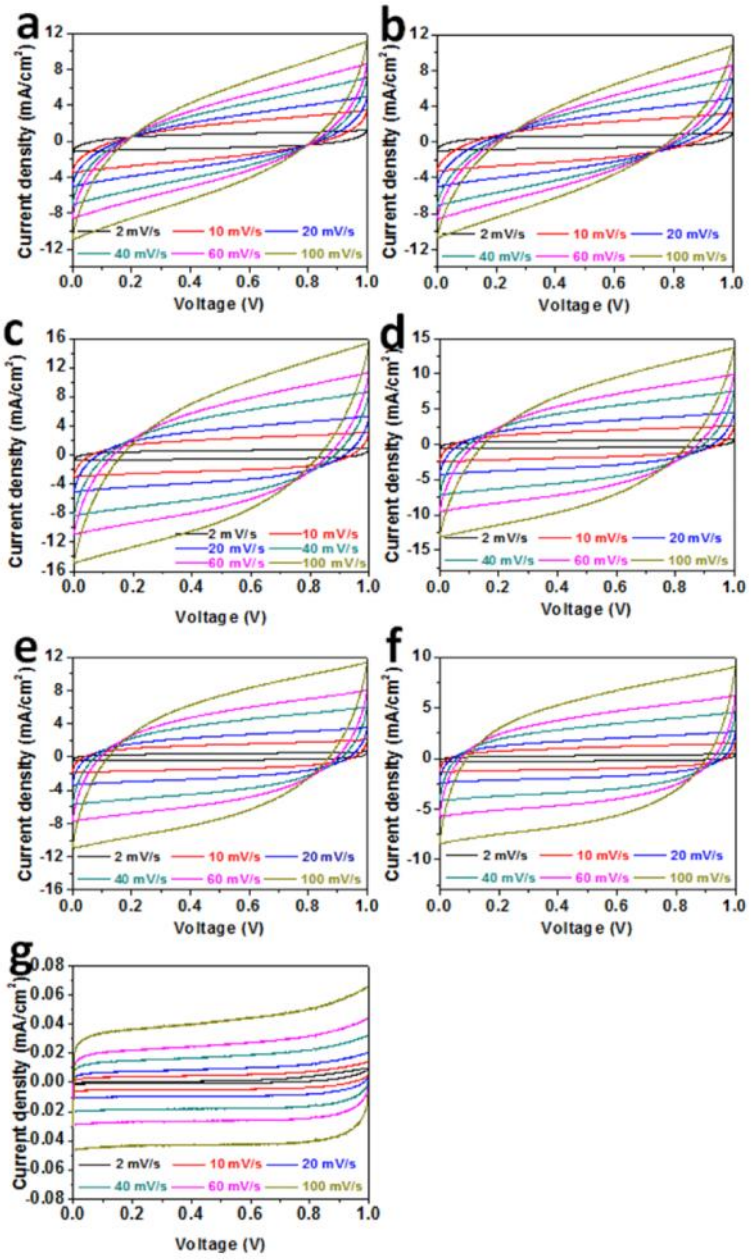

Figure 4.10. Cyclic voltammetry curves of (a) LIG-MnO_2-4.0h, (b) LIG-MnO_2-3.0h, (c) LIG-MnO_2-2.5h, (d) LIG-MnO_2-2.0h, (e) LIG-MnO_2-1.5h, (f) LIG-MnO_2-1.0h, and (g) LIG over a scan rate range of 2 and 100 mV/s in the potential window from 0 to 1.0 V.

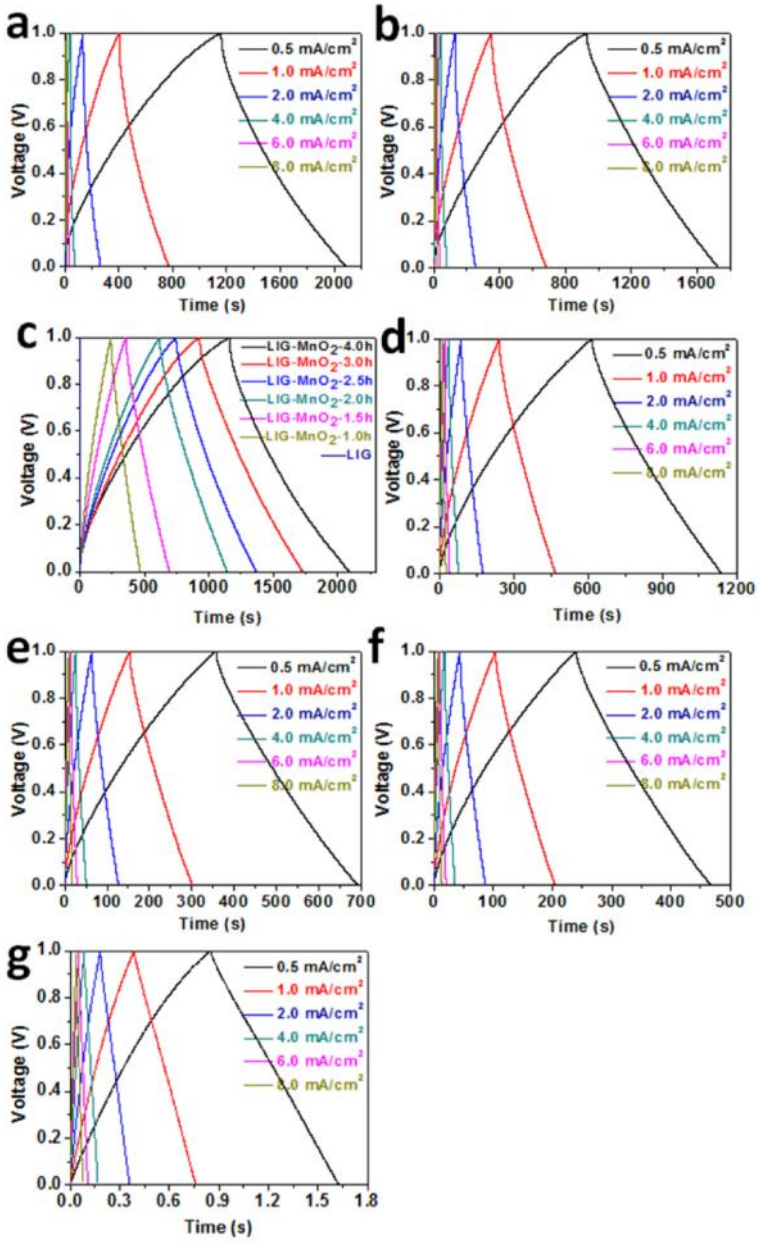

Figure 4.11. Galvanostatic charge discharge curves of (a) LIG-MnO_2-4.0h, (b) LIG-MnO_2-3.0h, (c) LIG-MnO_2-2.5h, (D) LIG-MnO_2-2.0h, (E) LIG-MnO_2-1.5h, (F) LIG-MnO_2-1.0h, and (G) LIG over a current density range of 0.5 to 8.0 mA/cm2 in the potential window from 0 to 1.0 V.

Figure 4.10 shows CV curves of LIG-MnO_2-X at a scan rate ranging from 2 to 100 mV/s, demonstrating a proportional current increase with an increasing scan rate. The

distorted CV shapes of the samples with more MnO_2 content at high scan rates may result from the decreased electrical conductivity.[32]

Figure 4.9b shows the galvanostatic charge-discharge curves of LIG-MnO_2-X at a current density of 0.5 mA/cm^2. The curve from LIG alone is nearly negligible, again demonstrating little contribution in capacitance from LIG in the composite of LIG-MnO_2, which is consistent with the CV analysis.[8] Figure 4.11 further shows the galvanostatic charge-discharge curves of these samples at varying current densities. The nearly symmetrical charging and discharging curves and small voltage drops at initial discharge state indicate good capacitive behavior and high conductivity within the electrodes.[18] Based on the galvanostatic charge-discharge curves, the areal and volumetric specific electrode capacitance of LIG-MnO_2-X are calculated as shown in Figure 4.9c,d. Here, the total area of each MSC device (A_{Device}) includes the interdigitated electrodes and the space between them, and the volume is equal to A_{Device} multiplied by the height of the composite (Figure 4.12). It is equal to electrode width (W) multiplied by the length (L): $A_{Device} = W \times L$ = 0.41 cm × 1.85 cm = 0.75 cm^2. The device volume (V_{Device}) is estimated as: $V_{Device} = W \times L \times H$, where H stands for the height of the hybrid material and can be measured from previous cross-sectional SEM images. More MnO_2 content in the LIG-MnO_2 composite tends to result in a higher capacitance at low current density, as evidenced by the highest areal and volumetric capacitances of 934 mF/cm^2 and 93.4 F/cm^3, respectively, from LIG-MnO_2-4.0h at a current density of 0.5 mA/cm^2. At the same current density, the areal and volumetric capacitance of LIG alone is less than 0.8 mF/cm^2 and 0.2 F/cm^3, indicating that most of the capacitance is coming from the pseudocapacitance of MnO_2 in the LIG-MnO_2 composite. With increasing current density, the capacitance from the sample with less

MnO_2 tends to decrease more slowly. At a high current density of 8.0 mA/cm^2, the capacitance of LIG-MnO_2-2.5h is maximized, with an areal value of 281 mF/cm^2 and a volumetric value of 31.5 F/cm^3, most likely due to the relatively higher conductivity of the LIG-MnO_2 composite when less MnO_2 was deposited.

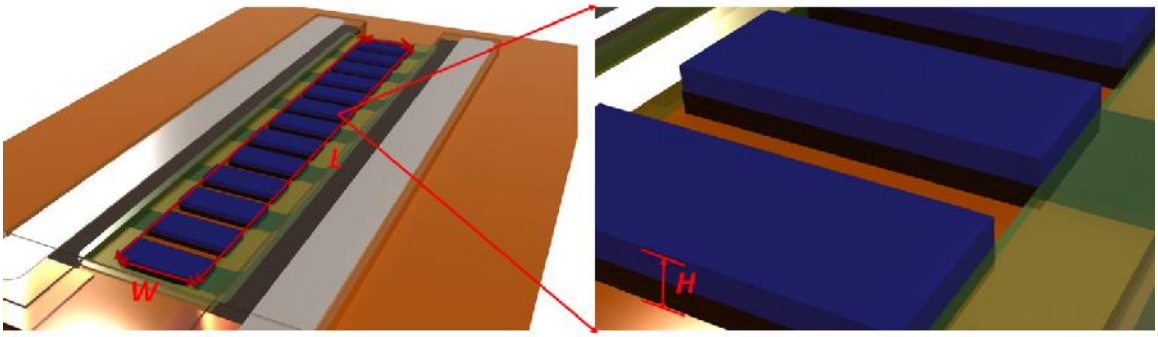

Figure 4.12. The dimension of the MSCs with the interdigitated electrodes in plane.

LIG-PANI-MSCs using H_2SO_4/PVA as the electrolyte were also studied in a potential window from 0 to 0.8 V. Figure 4.9e shows the CV curves of LIG-PANI-Y samples and LIG at a scan rate of 10 mV/s. Similar to LIG-MnO_2, the CV curve of LIG is minuscule compared to the others, indicating little contribution from the EDLC of LIG in the composite to the total capacitance. For LIG-PANI-15, LIG-PANI-10, and LIG-PANI-5, there were two pairs of redox peaks in the CV curves. The peak *A* at ~ 0.35 V and peak *A'* at ~ 0.23 V result from the redox transition of PANI between leucoemeraldine and emeraldine, and the peak *B* at ~ 0.47 V and peak *B'* at ~ 0.30 V are caused by the transition between emeraldine and pernigraniline.[30,33] LIG-PANI-15 has the highest value in the CV curve area, demonstrating that it has the highest areal energy storage ability among all tested samples. Figure 13 shows CV curves of these samples at a scan rate ranging from 2

to 100 mV/s with an increased current, similar to that of LIG-MnO_2. When compared to LIG-PANI-Y, the galvanostatic charge-discharge curve of LIG alone is negligible, further demonstrating little contribution in capacitance from LIG in the composite of LIG-PANI (Figure 4.9f). Based on the galvanostatic charge-discharge curves of these samples (Figure 4.14), the calculated areal and volumetric specific electrode capacitance of LIG-PANI-Y are shown in Figure 4.9g,h. LIG-PANI-15 has the best performance among all the samples with an areal and volumetric capacitance of 361 mF/cm^2 and 47.5 F/cm^3, respectively, at a current density of 0.5 mA/cm^2. In comparison, LIG itself is only 8.4 mF/cm^2 and 1.8 F/cm^3 at the same current density. When the current density increases to 20 mA/cm^2, the capacitance of LIG-PANI-15 still remains at 271 mF/cm^2 and 35.6 F/cm^3 with a high capacitance retention of 75 %, indicating the good rate performance of LIG-PANI-15. Compare to LIG-MnO_2 samples, although the capacitance of LIG-PANI samples is smaller, they are advantageous to maintain high capacitance at higher current density because of the better conductivity of PANI over MnO_2.

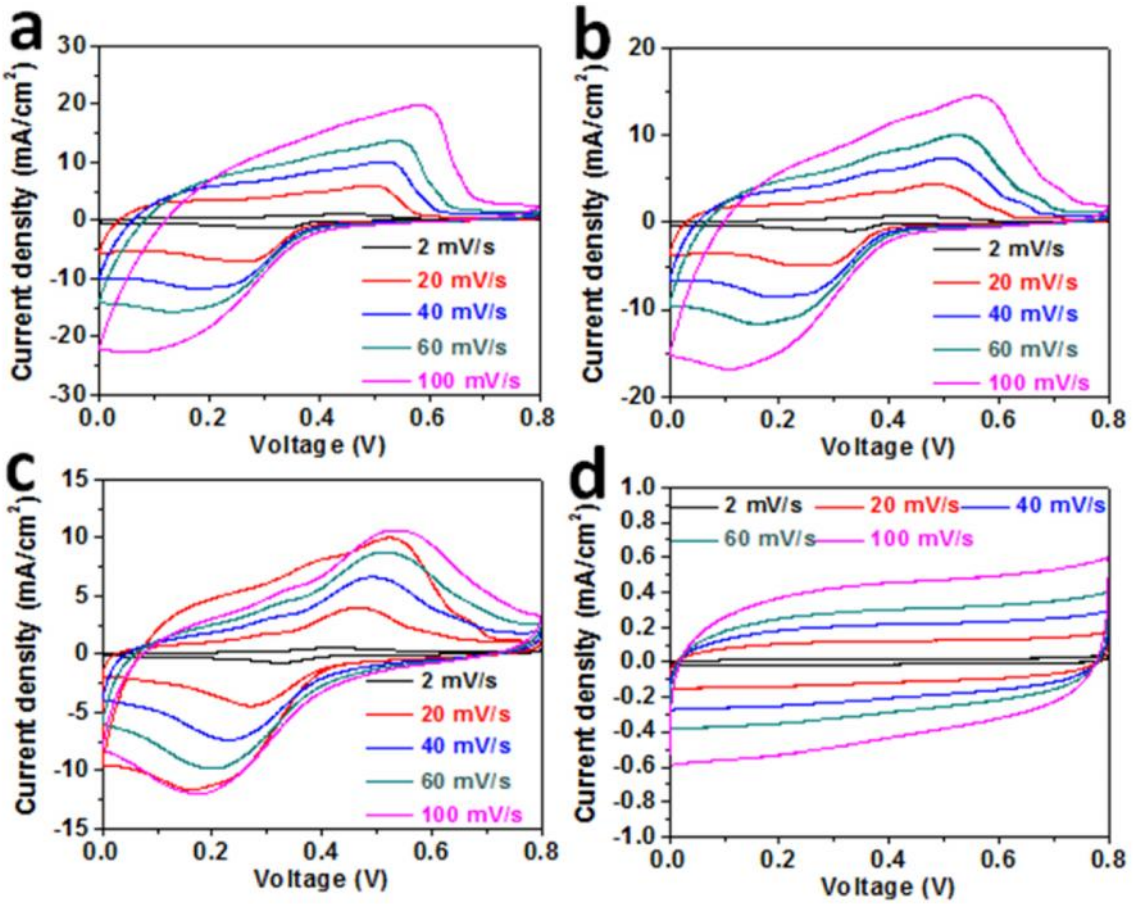

Figure 4.13. Cyclic voltammetry curves of (a) LIG-PANI-15, (b) LIG-PANI-10, (c) LIG-PANI-5, and (d) LIG over a scan rate range of 2 and 100 mV/s in the potential window from 0 to 0.8 V.

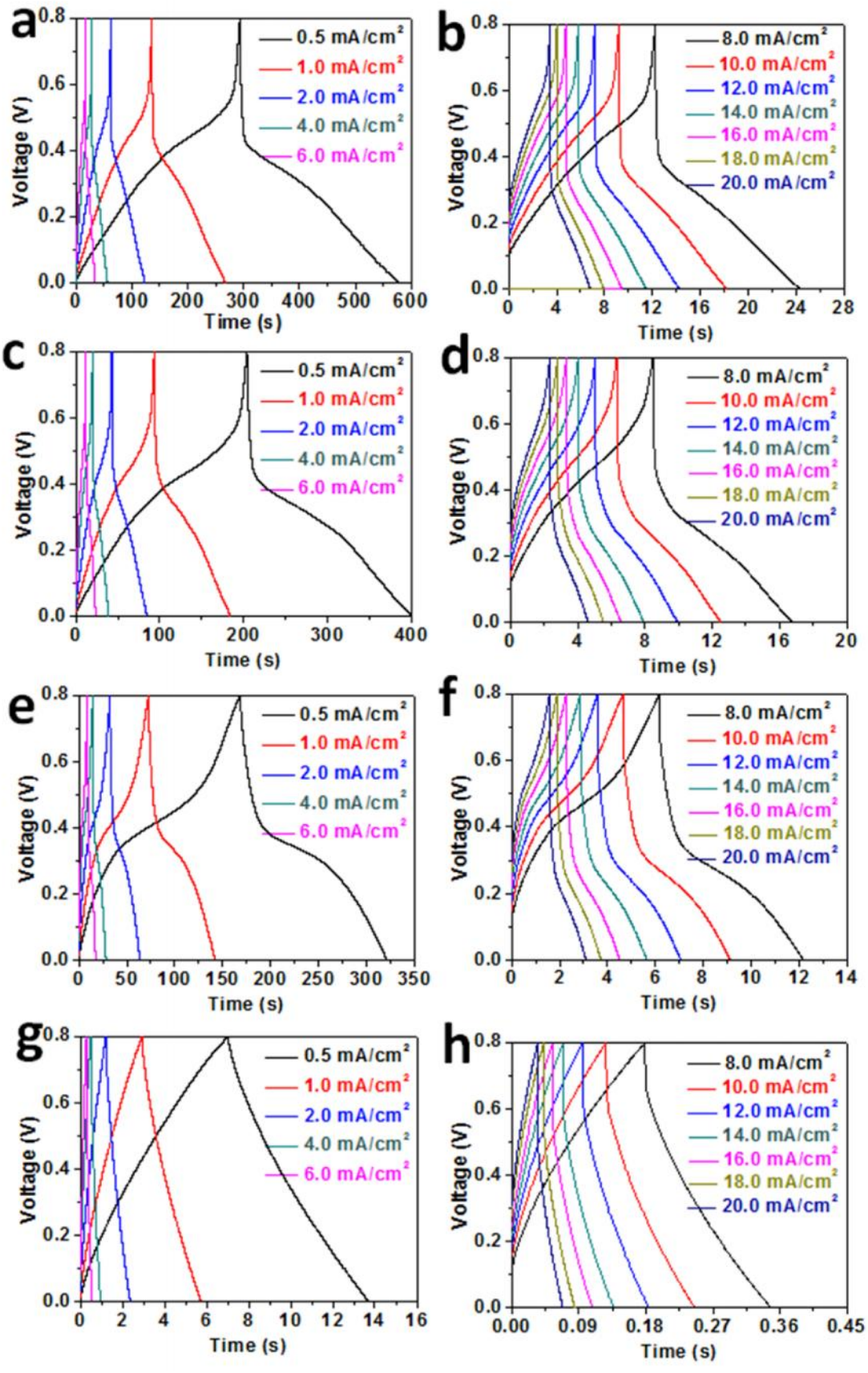
a
Voltage (V)
Time (s)
0.5 mA/cm²
1.0 mA/cm²
2.0 mA/cm²
4.0 mA/cm²
6.0 mA/cm²
b
Voltage (V)
Time (s)
8.0 mA/cm²
10.0 mA/cm²
12.0 mA/cm²
14.0 mA/cm²
16.0 mA/cm²
18.0 mA/cm²
20.0 mA/cm²
c
Voltage (V)
Time (s)
0.5 mA/cm²
1.0 mA/cm²
2.0 mA/cm²
4.0 mA/cm²
6.0 mA/cm²
d
Voltage (V)
Time (s)
8.0 mA/cm²
10.0 mA/cm²
12.0 mA/cm²
14.0 mA/cm²
16.0 mA/cm²
18.0 mA/cm²
20.0 mA/cm²
e
Voltage (V)
Time (s)
0.5 mA/cm²
1.0 mA/cm²
2.0 mA/cm²
4.0 mA/cm²
6.0 mA/cm²
f
Voltage (V)
Time (s)
8.0 mA/cm²
10.0 mA/cm²
12.0 mA/cm²
14.0 mA/cm²
16.0 mA/cm²
18.0 mA/cm²
20.0 mA/cm²
g
Voltage (V)
Time (s)
0.5 mA/cm²
1.0 mA/cm²
2.0 mA/cm²
4.0 mA/cm²
6.0 mA/cm²
h
Voltage (V)
Time (s)
8.0 mA/cm²
10.0 mA/cm²
12.0 mA/cm²
14.0 mA/cm²
16.0 mA/cm²
18.0 mA/cm²
20.0 mA/cm²

Figure 4.14. Galvanostatic charge discharge curves of (a,b) LIG-PANI-15, (c,d) LIG-PANI-10, (e,f) LIG-PANI-5, (g,h) LIG over a current density range of 0.5 to 20.0 mA/cm2 in the potential window from 0 to 0.8 V.

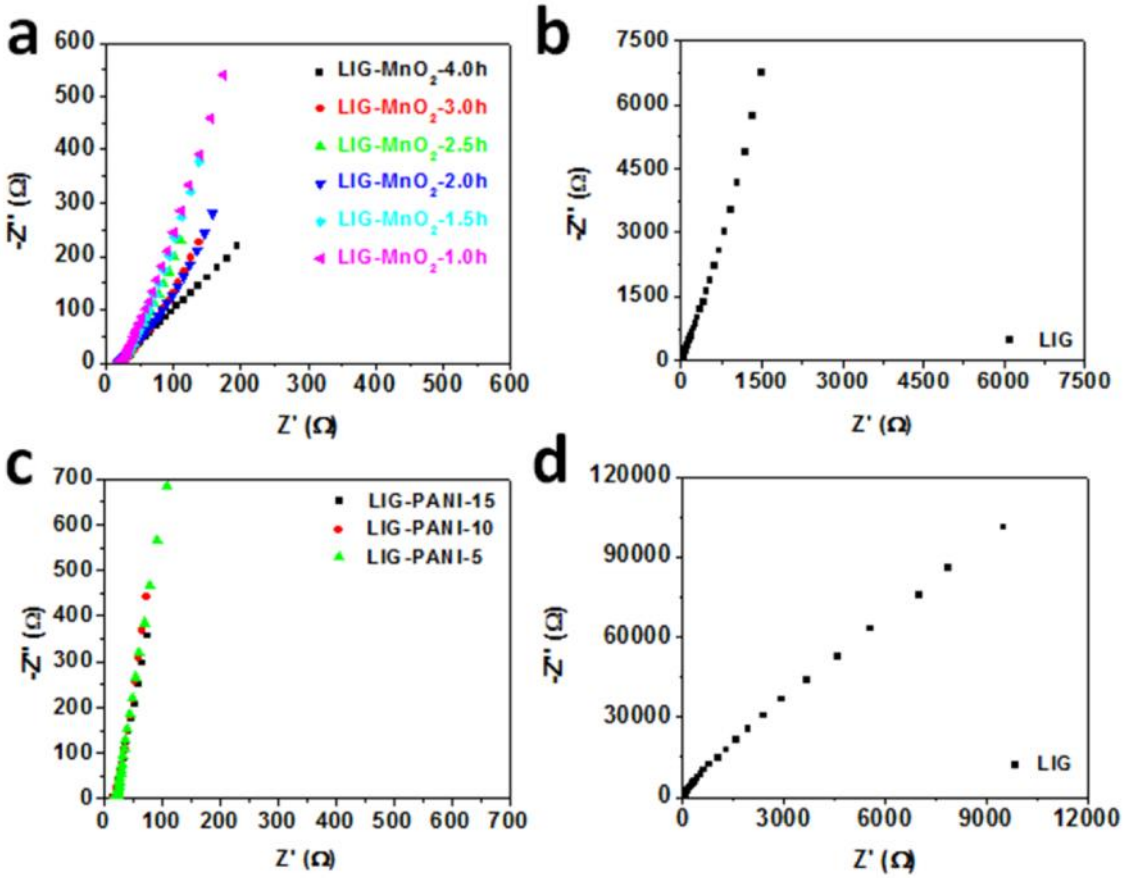

Figure 4.15. Nyquist plots for EIS study. (a) LIG-MnO_2-4.0h, LIG-MnO_2-3.0h, LIG-MnO_2-2.5h, LIG-MnO_2-2.0h, LIG-MnO_2-1.5h, LIG-MnO_2-1.0h, and (b) LIG in PVA/LiCl. (c) LIG-PANI-15, LIG-PANI-10, LIG-PANI-5 and (d) LIG in PVA/H_2SO_4 in a frequency range of 100 kHz and 0.01 Hz.

This is also supported by the electrochemical impedance spectroscopy (EIS) study in the frequency range from 100 kHz to 0.01 Hz (Figure 4.15), as the calculated equivalent series resistances (ESRs) from LIG-PANI-Y is lower than LIG-MnO_2-X (Table 4.1). At

low frequencies, the straight lines are nearly perpendicular to the y axis, demonstrating that LIG-MnO_2-X and LIG-PANI-Y have good capacitive behaviors.[5] The equivalent series resistances (ESRs) obtained from the intercept of the x axis and plots are similar among LIG-MnO_2-X, LIG-PANI-Y and LIG, indicating good ionic conductivity of the electrolyte and the low internal resistance of the electrode materials (Table 4.1).[5] The increasing content of MnO_2 or PANI in the composites increases ESRs, which reduce the rate performance of these hybrids in MSCs. This is consistent with the variation of their rate performance.

Table 4.1. ESRs of LIG-MnO_2 and LIG-PANI with different MnO2 and PANI deposition amount. ESRs were obtained from the x intercept of the Nyquist plots.

Electrode	Electrolyte	Equivalent Series Resistance (Ω)
LIG-MnO_2-4.0h	PVA/LiCl	21.6
LIG-MnO_2-3.0h	PVA/LiCl	20.4
LIG-MnO_2-2.5h	PVA/LiCl	16.3
LIG-MnO_2-2.0h	PVA/LiCl	17.2
LIG-MnO_2-1.5h	PVA/LiCl	17.5
LIG-MnO_2-1.0h	PVA/LiCl	17.2
LIG	PVA/LiCl	15.8
LIG-PANI-15	PVA/H_2SO_4	16.5
LIG-PANI-10	PVA/H_2SO_4	16.8
LIG-PANI-5	PVA/H_2SO_4	16.5
LIG	PVA/H_2SO_4	15.3

The cyclability of the fabricated devices from LIG-MnO_2 and LIG-PANI were also tested. After 6000 cycles of charge-discharging test, the capacitance of LIG-MnO_2-2.5h

and LIG-PANI-15 remained over 82 % and 97 %, respectively, showing excellent stability of the devices based on these hybrid composites (Figures 4.9i,j).

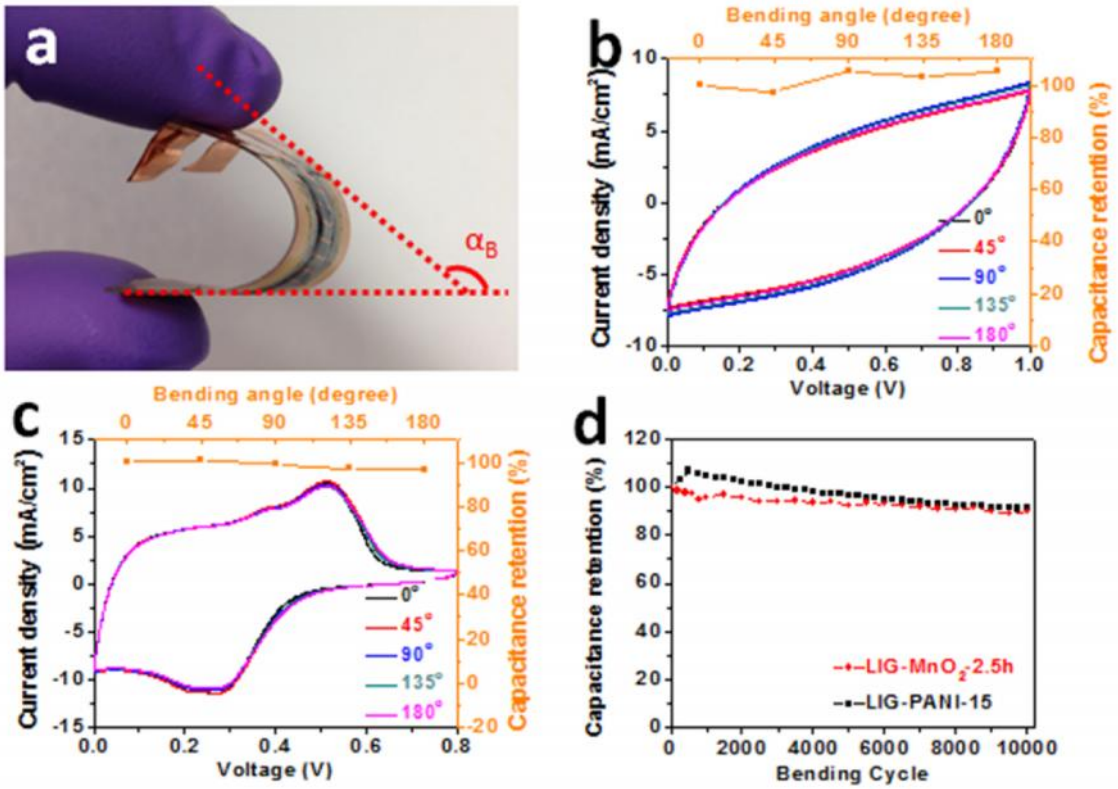

Figure 4.16. Flexibility testing of LIG-MnO_2-2.5h and LIG-PANI-15. (a) Digital photograph of a device under bending. The angle labeled as αB in the image is defined as the bending angle. (b) CV curves and capacitance retention of LIG-MnO_2-2.5h under bending angles of 0°, 45°, 90°, 135°, and 180° at a scan rate of 40 mV/s. (c) CV curves and capacitance retention of LIG-PANI-15 under various bending angles of 0°, 45°, 90°, 135°, and 180° at a scan rate of 40 mV/s. (d) Capacitance retention of LIG-MnO_2-2.5h and LIG-PANI-15 devices at different bending cycles with a α_B of ~ 90°.

The flexibility of MSCs from LIG-MnO_2 and LIG-PANI was also studied as shown in Figure 4.16. Figure 4.16a shows a digital image of one MSC device that is manually bent with a bending angle (α_B) of ~ 135°. The CV curves at different α_B are nearly

overlapped with each other, and the calculated capacitance remained almost the same, indicating the stable performance of LIG-MnO_2-2.5h and LIG-PANI-15 at these states (Figure 4.16b, c). The flexibility tests carried out by bending the device with a α_B of ~ 90° (Figure 4.16d) show a good mechanical flexibility of these materials with only 10% capacitance decay after 10000 bending cycles. These results demonstrate that both LIG-PANI-15 and LIG-MnO_2-2.5h are superb candidate electrode materials in flexible MSCs.

Unlike traditional supercapacitors where the performance is evaluated per weight of the active material, the footprint area of MSCs becomes the key consideration, making the spacial energy and power density the most important performance metrics.[34] Figure 4.17 shows the Ragone plots demonstrating the areal and volumetric energy and power density of LIG-related MSCs and their comparison with commercially available energy storage devices. In the LIG-MnO_2-MSCs, the highest energy densities are 32.4 $\mu Wh/cm^2$ and 3.2 mWh/cm^3, which increase more than 1200 and 291 times, respectively, compared with LIG at a current density of 0.5 mA/cm^2. For LIG-PANI-MSCs, the highest energy densities are 8.0 $\mu Wh/cm^2$ and 1.1 mWh/cm^3, which are 41 and 15 times higher, respectively, than that of LIG at a current density of 0.5 mA/cm^2 (Table 4.2). Such energy densities from LIG-MnO_2 and LIG-PANI are much higher than the commercial supercapacitors (SCs) (2.75 V/44 mF and 5.5 V/100 mF), and even comparable to Li thin-film batteries (4 V/500 μAh).[22,35] The maximum areal and volumetric power density are 2334.0 $\mu W/cm^2$ and 298.1 mW/cm^3 for LIG-MnO_2 and 649.4 $\mu W/cm^2$ and 1511.4 mW/cm^3 for LIG-PANI, which are comparable to commercial SCs, and > 100 times higher than Li thin-film batteries. The results of LIG-MnO_2 and LIG-PANI show much better performance than our previously studied LIG-MSCs and boron doped LIG-MSCs in

aqueous or polymeric acidic electrolyte (Figure 4.18),[26,28] and also better performance than most of other reported carbon and pseudocapacitive materials as shown in Table 4.3.[9,10,18,23,36-42] Note that in most of the results in Table 4.3, high-cost lithography for electrode patterning and often a high temperature and multi-step synthetic processes are required. In this work, the synthesis and patterning of LIG are simultaneously achieved in the first step, and both the laser induction step and subsequent electrodeposition are done under mild temperature and ambient atmosphere.

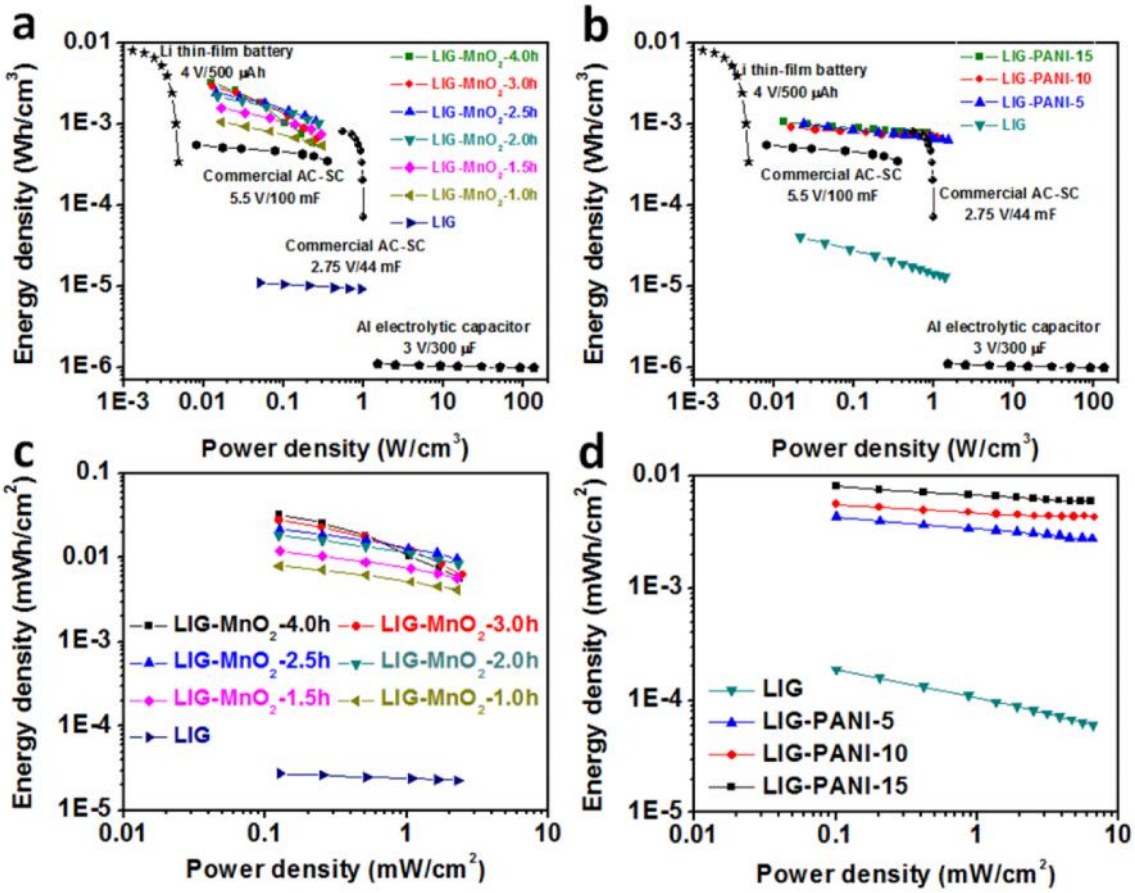

Figure 4.17. Ragone plot of LIG-MnO_2 and LIG-PANI. Volumetric energy and power density of (a) LIG-MnO_2-X and (b) LIG-PANI-Y and their comparison with commercially available energy storage devices. Areal energy and power density of (c) LIG-MnO_2-X and (d) LIG-PANI-Y with different MnO_2 and PANI

deposition amounts. The data for the Li thin-film battery, Al electrolytic capacitor, commercial AC-SC and SC were reproduced from literature 9, 21, 22, and 37.

Table 4.2. Electrochemical performances of MSCs of LIG-MnO_2 and LIG-PANI with interdigitated architectures in plane.

		Specific capacitance[a]		Energy density[a]		Power density[b]	
Electrode	Electrolyte	Areal (mF/cm²)	Volumetric (F/cm³)	Areal (μWh/cm²)	Volumetric (mW/cm³)	Areal (μWh/cm²)	Volumetric (mW/cm³)
LIG-PANI-15	PVA/H_2SO_4	360.8	47.5	8.0	1.1	629.5	828.3
LIG-PANI-10	PVA/H_2SO_4	250.1	45.0	5.6	0.9	676.2	1108.6
LIG-PANI-5	PVA/H_2SO_4	193.3	41.0	4.3	1.0	649.9	1511.4
LIG	PVA/H_2SO_4	8.4	3.8	1.9×10^{-1}	7.5×10^{-2}	653.9	2615.6
LIG-MnO_2-4.0h	PVA/LiCl	933.6	92.4	32.4	3.2	2334.0	231.1
LIG-MnO_2-3.0h	PVA/LiCl	799.6	83.3	27.8	2.89	2462.5	256.5
LIG-MnO_2-2.5h	PVA/LiCl	623.8	70.1	21.7	2.5	2248.0	252.6
LIG-MnO_2-2.0h	PVA/LiCl	524.2	63.2	18.2	2.2	2293.4	276.3
LIG-MnO_2-1.5h	PVA/LiCl	339.4	44.7	11.8	1.6	2265.7	298.1
LIG-MnO_2-1.0h	PVA/LiCl	229.0	30.2	8.0	1.0	2256.7	297.0
LIG	PVA/LiCl	0.8	0.31	2.7×10^{-2}	1.1×10^{-2}	2287.2	914.9

Notes: [a] The specific capacitance and the energy density was calculated at the current density of 0.5 mA/cm^2. [b] The power density of these samples was obtained at 20.0 mA/cm^2 for LIG-PANI, and 8.0 mA/cm^2 for LIG-MnO_2.

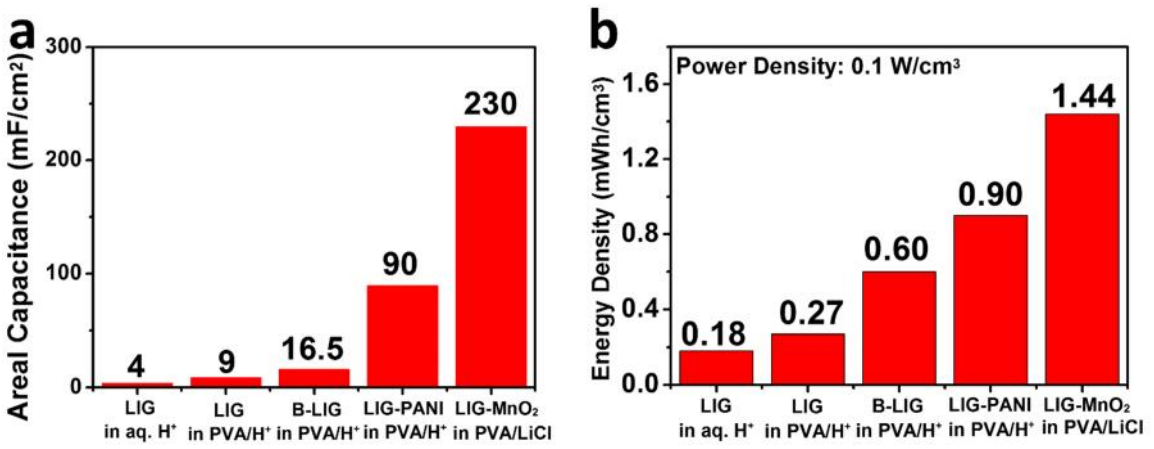

Figure 4.18. Comparison of the areal device capacitance and volumetric energy density of LIG-derived MSCs. Data of LIG-MSCs in aqueous acid electrolyte, LIG-MSCs in PVA/H^+ electrolyte, and boron doped LIG-MSCs in PVA/H^+ electrolyte are from literature 27 and 28.

Table 4.3. Electrochemical performances of MSCs based on carbon materials and pseudocapacitive active materials with in-plane interdigital architectures.

		Specific capacitance		Energy density		Power density		
Electrode[a]	Electrolyte	Areal (mF/cm²)	Volumetric (F/cm³)	Areal (μWh/cm²)	Volumetric (mW/cm³)	Areal (μWh/cm²)	Volumetric (W/cm³)	References
AC	1 M Et_4NBF_4 in PC	11.6 at 0.5 V/s	9.0 at 0.01 V/s	—	18	—	41	8
OLC	1 M Et_4NBF_4 in PC	1.7 at 1 V/s	1.3 at 1 V/s	—	~1.7	—	200–250	8
AC	1 M Et_4NBF_4 in PC	2.1 at 1 mV/s	2.7 at 1 mV/s	—	—	44900	—	35
CNTs	BMIM/BF_4	0.428	—	—	—	280	—	44
rGO	Hydrated GO	0.51	3.1	—	0.43	—	9.4	22
G/CNTs	1 M Na_2SO_4	2.16 at 0.1 mV/s	1.08 at 0.1 mV/s	—	0.16	—	115	45
Graphene	PVA–H_2SO_4	0.3228 at 0.01 V/s	71.6 at 0.01 V/s	—	2.5	—	495	41
GQDs//MnO_2	0.5 Na_2SO_4	1.107 at 15 μA/cm²	—	0.154	—	7.51	—	36
MnO_2	—	56.3 at 27.2 μA/cm²	—	5.01	—	12020	—	17
NiO	1 M KOH	1.24at 2.7 mA/cm²	—	1.0	—	40000	—	40
VS_2	PVA–$BMIMBF_4$	4.76	—	—	—	—	—	37
PPy/C-MEMS	1 M KCl	78.35 at 20 mV/s	—	—	—	630 ± 40	—	39
PANI	PVA–H_2SO_4	23.52 at 0.1 mA/cm²	588 at 0.1 mA/cm²	—	82	—	25	19

Notes: [a] AC: activated carbon, OLC: onion like carbon, CNTs: carbon nanotubes, rGO: reduced graphene oxide, G/CNTs: graphene/carbon nanotubes, GQDs//MnO_2: graphene quantum dots//MnO_2, PPy/C-MEMS: Polypyrrole/Carbon-microelectrochemical system, PANI: polyaniline.

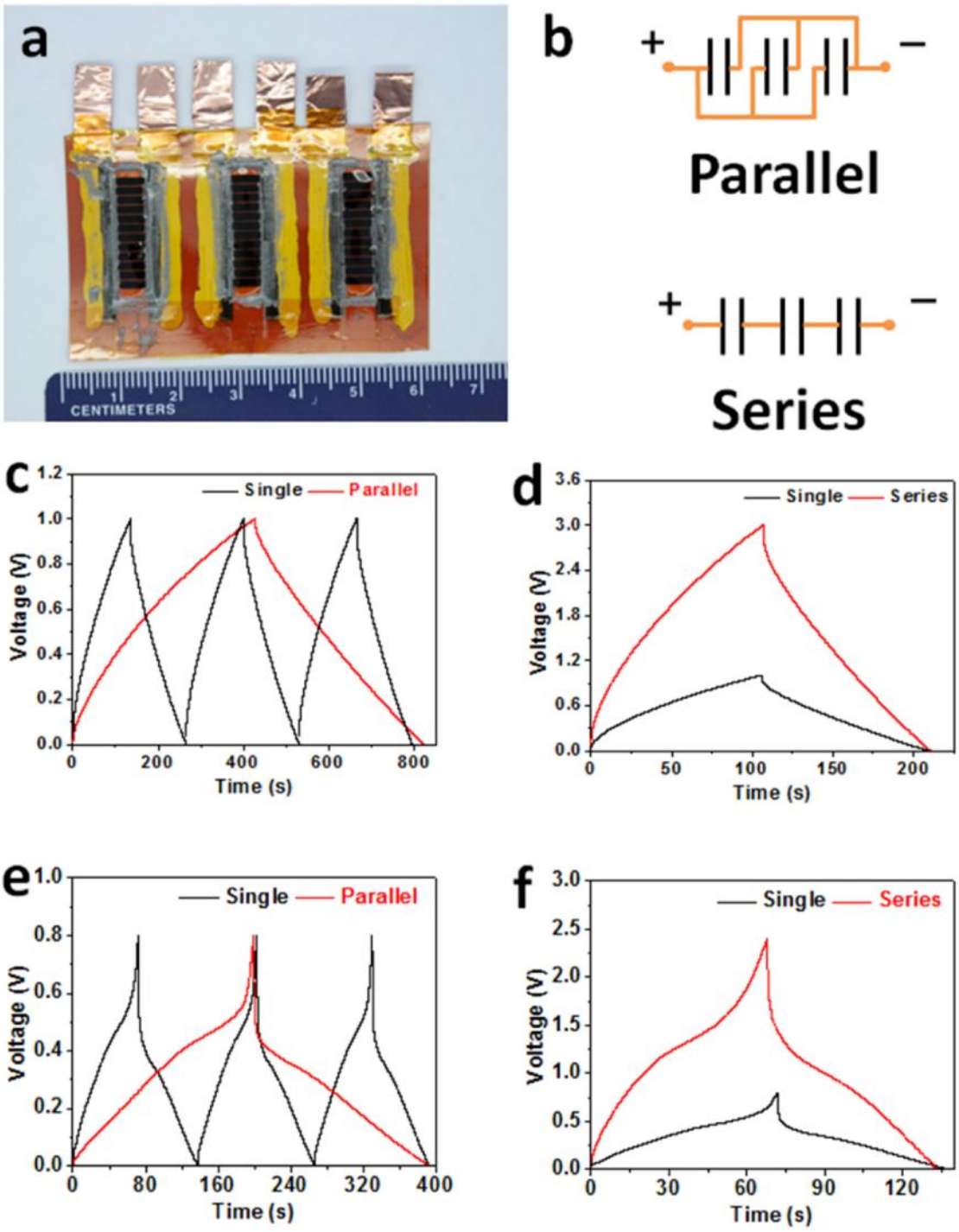

Figure 4.19 Assembling of multiple devices in parallel and series configurations. (a) A digital image of three fabricated devices on a single PI sheet. (b) Three single devices are in parallel and series. (c) Galvanostatic charge discharge curves of LIG-MnO_2-2.5h in single and parallel at a current

density of 2.0 mA/cm² and comparison with a single device. (d) Galvanostatic charge discharge curves of LIG-MnO_2-2.5h in single and series at a current density of 2.0 mA/cm². (e) Galvanostatic charge discharge curves of LIG-PANI-15 in single and parallel device at a current density of 2.0 mA/cm². (f) Galvanostatic charge discharge curves of LIG-PANI-15 in single and series at a current density of 2.0 mA/cm².

To meet the specific energy and power needs for practical applications, multiple MSCs from LIG-MnO_2 or LIG-PANI can also be scaled up and assembled in either series or parallel configurations (Figure 4.19). Compared with a single MSC, the discharge time of three MSCs connected in parallel increased to 3x that of a single MSC when operated at the same current density. When the three MSCs were connected in series, it exhibited a 3x higher voltage window with a similar discharge time at the same current density. These results demonstrate the high potential of LIG-MnO_2 and LIG-PANI hybrid materials in practical applications.

4.4. Conclusion

We have successfully demonstrated a simple route to make flexible MSCs with interdigitated electrodes using a hybrid composite of LIG from laser induction and MnO_2 or PANI from electrodeposition. Two types of pseudocapacitive electrode materials, LIG-MnO_2 and LIG-PANI, are prepared and both of them demonstrate high specific capacitance, promising energy and power densities, excellent cycling stabilities and mechanical flexibilities. This finding not only simplifies device fabrication processes with easy control of the size of devices and scalability, but also demonstrates the applicability to a wide range of other pseudocapacitive materials, beyond that of justMnO_2 and PANI. Therefore, the

design strategy developed here opens up a new avenue for constructing high performance, flexible MSCs with in-plane interdigitated electrodes

4.5. References

1. Li, L.; [#] Peng, Z. W.; [#] Zhang, J. B.; [#] Li, Y. L.; Ji, Y. S.; Ye, R. Q.; Kim, N. D.; Gao, C. T.; Zhong, Q. F.; Yang, Y.; Fei, H. L.; Ruan, G. D.; Tour, J. M. High-Performance Pseudocapacitive Microsupercapacitors from Laser Induced Graphene In submitted (L.L. conceived and designed the experiments. L.L. and P.Z.W. prepared LIG-PANI, fabricated LIG-PANI-MSCs, and performed the electrochemical measurements. L.L., Z.J.B., and P.Z.W. prepared LIG-MnO_2, fabricated LIG-MnO2-MSCs, and performed the electrochemical measurements. L.L., P.Z.W., L.Y.L., Q.R.Y., G.C.T., Z.Q.F. and R.G.D. performed material characterization. J.Y.S. and K.N.K. drew the scheme. L.L., P.Z.W., Y.Y., and F.H.L. analyzed the data. L.L. and P.Z.W. co-wrote the paper. Finally, J.M.T. oversaw all research phases, provided regular guidance to the research and revised the manuscript. All authors discussed and commented on the manuscript.)
2. Beidaghi, M.; Gogotsi, Y.: Capacitive energy storage in micro-scale devices: recent advances in design and fabrication of micro-supercapacitors. *Energy Environ. Sci.* 2014, *7*, 867-884.
3. Wang, Z. L.: Toward self-powered sensor networks. *Nano Today* 2010, *5*, 512-514.
4. Bae, J.; Song, M. K.; Park, Y. J.; Kim, J. M.; Liu, M.; Wang, Z. L.: Fiber supercapacitors made of nanowire-fiber hybrid structures for wearable/flexible energy storage. *Angew. Chem. Int. Ed.* 2011, *50*, 1683-1687.

5. Yu, D.; Goh, K.; Wang, H.; Wei, L.; Jiang, W.; Zhang, Q.; Dai, L.; Chen, Y.: Scalable synthesis of hierarchically structured carbon nanotube-graphene fibres for capacitive energy storage. *Nat. Nanotechnol.* 2014, *9*, 555-562.
6. Chmiola, J.; Largeot, C.; Taberna, P.-L.; Simon, P.; Gogotsi, Y.: Monolithic carbide-derived carbon films for micro-supercapacitors. *Science* 2010, *328*, 480-483.
7. Wu, Z.-S.; Feng, X.; Cheng, H.-M.: Recent advances in graphene-based planar micro-supercapacitors for on-chip energy storage. *Natl. Sci. Rev.* 2013, nwt003.
8. Simon, P.; Gogotsi, Y.: Materials for electrochemical capacitors. *Nat. Mater.* 2008, *7*, 845-854.
9. Pech, D.; Brunet, M.; Durou, H.; Huang, P.; Mochalin, V.; Gogotsi, Y.; Taberna, P.-L.; Simon, P.: Ultrahigh-power micrometre-sized supercapacitors based on onion-like carbon. *Nat. Nanotechnol.* 2010, *5*, 651-654.
10. Lin, J.; Zhang, C.; Yan, Z.; Zhu, Y.; Peng, Z.; Hauge, R. H.; Natelson, D.; Tour, J. M.: 3-dimensional graphene carbon nanotube carpet-based microsupercapacitors with high electrochemical performance. *Nano Lett.* 2012, *13*, 72-78.
11. Liu, C.-C.; Tsai, D.-S.; Chung, W.-H.; Li, K.-W.; Lee, K.-Y.; Huang, Y.-S.: Electrochemical micro-capacitors of patterned electrodes loaded with manganese oxide and carbon nanotubes. *J. Power Sources* 2011, *196*, 5761-5768.
12. Heon, M.; Lofland, S.; Applegate, J.; Nolte, R.; Cortes, E.; Hettinger, J. D.; Taberna, P.-L.; Simon, P.; Huang, P.; Brunet, M.: Continuous carbide-derived carbon films with high volumetric capacitance. *Energy Environ. Sci.* 2010, *4*, 135-138.

13. Hong, S. Y.; Yoon, J.; Jin, S. W.; Lim, Y.; Lee, S.-J.; Zi, G.; Ha, J. S.: High-density, stretchable, all-solid-state microsupercapacitor arrays. *ACS Nano* 2014, *8*, 8844-8855.

14. Beidaghi, M.; Wang, C.: Micro-supercapacitors based on interdigital electrodes of reduced graphene oxide and carbon nanotube composites with ultrahigh power handling performance. *Adv. Funct. Mater.* 2012, *22*, 4501-4510.

15. Kim, M. S.; Hsia, B.; Carraro, C.; Maboudian, R.: Flexible micro-supercapacitors with high energy density from simple transfer of photoresist-derived porous carbon electrodes. *Carbon* 2014, *74*, 163-169.

16. Xue, M.; Xie, Z.; Zhang, L.; Ma, X.; Wu, X.; Guo, Y.; Song, W.; Li, Z.; Cao, T.: Microfluidic etching for fabrication of flexible and all-solid-state micro supercapacitor based on MnO 2 nanoparticles. *Nanoscale* 2011, *3*, 2703-2708.

17. Chen, C.-H.; Tsai, D.-S.; Chung, W.-H.; Lee, K.-Y.; Chen, Y.-M.; Huang, Y.-S.: Electrochemical capacitors of miniature size with patterned carbon nanotubes and cobalt hydroxide. *J. Power Sources* 2012, *205*, 510-515.

18. Wang, X.; Myers, B. D.; Yan, J.; Shekhawat, G.; Dravid, V.; Lee, P. S.: Manganese oxide micro-supercapacitors with ultra-high areal capacitance. *Nanoscale* 2013, *5*, 4119-4122.

19. Xue, M.; Li, F.; Zhu, J.; Song, H.; Zhang, M.; Cao, T.: Structure-based enhanced capacitance: in situ growth of highly ordered polyaniline nanorods on reduced graphene oxide patterns. *Adv. Funct. Mater.* 2012, *22*, 1284-1290.

20. Wang, K.; Zou, W.; Quan, B.; Yu, A.; Wu, H.; Jiang, P.; Wei, Z.: An all-solid-state flexible micro-supercapacitor on a chip. *Adv. Energy Mater.* 2011, *1*, 1068-1072.

21. El-Kady, M. F.; Strong, V.; Dubin, S.; Kaner, R. B.: Laser scribing of high-performance and flexible graphene-based electrochemical capacitors. *Science* 2012, *335*, 1326-1330.
22. El-Kady, M. F.; Kaner, R. B.: Scalable fabrication of high-power graphene micro-supercapacitors for flexible and on-chip energy storage. *Nat. Commun.* 2013, *4*, 1475.
23. Gao, W.; Singh, N.; Song, L.; Liu, Z.; Reddy, A. L. M.; Ci, L.; Vajtai, R.; Zhang, Q.; Wei, B.; Ajayan, P. M.: Direct laser writing of micro-supercapacitors on hydrated graphite oxide films. *Nat. Nanotechnol.* 2011, *6*, 496-500.
24. Marcano, D. C.; Kosynkin, D. V.; Berlin, J. M.; Sinitskii, A.; Sun, Z.; Slesarev, A.; Alemany, L. B.; Lu, W.; Tour, J. M.: Improved synthesis of graphene oxide. *ACS Nano* 2010, *4*, 4806-4814.
25. Dimiev, A. M.; Alemany, L. B.; Tour, J. M.: Graphene oxide. Origin of acidity, its instability in water, and a new dynamic structural model. *ACS Nano* 2012, *7*, 576-588.
26. Peng, Z.; Ye, R.; Mann, J. A.; Zakhidov, D.; Li, Y.; Smalley, P. R.; Lin, J.; Tour, J. M.: Flexible boron-doped laser induced graphene microsupercapacitor. *ACS Nano* 2015.
27. Peng, Z.; Lin, J.; Ye, R.; Samuel, E. L.; Tour, J. M.: Flexible and stackable laser induced graphene supercapacitors. *ACS Appl. Mater. Interfaces* 2015, *7*, 3414-3419.

28. Lin, J.; Peng, Z.; Liu, Y.; Ruiz-Zepeda, F.; Ye, R.; Samuel, E. L.; Yacaman, M. J.; Yakobson, B. I.; Tour, J. M.: Laser-induced porous graphene films from commercial polymers. *Nat. Commun.* 2014, *5*, 5714.

29. Do Nascimento, G. M.; Temperini, M.: Studies on the resonance Raman spectra of polyaniline obtained with near-IR excitation. *J. Raman Spectrosc.* 2008, *39*, 772-778.

30. Li, L.; Raji, A.-R. O.; Fei, H.; Yang, Y.; Samuel, E. L.; Tour, J. M.: Nanocomposite of polyaniline nanorods grown on graphene nanoribbons for highly capacitive pseudocapacitors. *ACS Appl. Mater. Interfaces* 2013, *5*, 6622-6627.

31. Li, L.; Raji, A. R. O.; Tour, J. M.: Graphene-wrapped MnO2-graphene nanoribbons as anode materials for high-performance lithium ion batteries. *Adv. Mater.* 2013, *25*, 6298-6302.

32. Conway, B.: Electrochemical supercapacitor. In *Scientific Fundamentals and Technological Applications*; Kluwer Academic/Plenum Publishers New York, 1999.

33. Li, H.; Wang, J.; Chu, Q.; Wang, Z.; Zhang, F.; Wang, S.: Theoretical and experimental specific capacitance of polyaniline in sulfuric acid. *J. Power Sources* 2009, *190*, 578-586.

34. Gogotsi, Y.; Simon, P.: True performance metrics in electrochemical energy storage. *Science* 2011, *334*, 917-918.

35. Zuo, W.; Wang, C.; Li, Y.; Liu, J.: Directly grown nanostructured electrodes for high volumetric energy density binder-free hybrid supercapacitors: a case study of CNTs//Li4Ti$_5$O$_{12}$. *Sci. Rep.* 2015, *5*.

36. Pech, D.; Brunet, M.; Taberna, P.-L.; Simon, P.; Fabre, N.; Mesnilgrente, F.; Conédéra, V.; Durou, H.: Elaboration of a microstructured inkjet-printed carbon electrochemical capacitor. *J. Power Sources* 2010, *195*, 1266-1269.
37. Liu, W. W.; Feng, Y. Q.; Yan, X. B.; Chen, J. T.; Xue, Q. J.: Superior micro-supercapacitors based on graphene quantum dots. *Adv. Funct. Mater.* 2013, *23*, 4111-4122.
38. Feng, J.; Sun, X.; Wu, C.; Peng, L.; Lin, C.; Hu, S.; Yang, J.; Xie, Y.: Metallic few-layered VS2 ultrathin nanosheets: high two-dimensional conductivity for in-plane supercapacitors. *J. Am. Chem. Soc.* 2011, *133*, 17832-17838.
39. Beidaghi, M.; Chen, W.; Wang, C.: Electrochemically activated carbon micro-electrode arrays for electrochemical micro-capacitors. *J. Power Sources* 2011, *196*, 2403-2409.
40. Beidaghi, M.; Wang, C.: Micro-supercapacitors based on three dimensional interdigital polypyrrole/C-MEMS electrodes. *Electrochim. Acta* 2011, *56*, 9508-9514.
41. Eustache, E.; Frappier, R.; Porto, R. L.; Bouhtiyya, S.; Pierson, J.-F.; Brousse, T.: Asymmetric electrochemical capacitor microdevice designed with vanadium nitride and nickel oxide thin film electrodes. *Electrochem. Commun.* 2013, *28*, 104-106.
42. Wu, Z. S.; Parvez, K.; Feng, X.; Müllen, K.: Graphene-based in-plane micro-supercapacitors with high power and energy densities. *Nat. Commun.* 2013, *4*, 2487.

43. Wang, G.; Lu, X.; Ling, Y.; Zhai, T.; Wang, H.; Tong, Y.; Li, Y.: LiCl/PVA gel electrolyte stabilizes vanadium oxide nanowire electrodes for pseudocapacitors. *ACS Nano* 2012, *6*, 10296-10302.

44. Jiang, Y.; Zhou, Q.; Lin, L. in *Micro Electro Mechanical Systems, 2009. MEMS 2009. IEEE 22nd International Conference on.* 587-590 (IEEE).

45. Lin, J.; Zhang, C.G.; Yan, Z.; Zhu, Y.; Peng, Z.W.; Hauge, R. H.; Natelson, D.; Tour, J. M. 3-dimensional graphene carbon nanotube carpet-based microsupercapacitors with high electrochemical performance. *Nano Lett.*2012, *13*, 72-78.

Chapter 5

Graphene-Wrapped MnO_2-Graphene Nanoribbons as Anode Materials for High Performance Lithium Ion Batteries

This chapter was entirely copied from reference 1.

5.1. Introduction

Lithium ion batteries (LIBs) are considered among the most practical and effective technologies for electrochemical energy storage.[2,3] LIBs can be wildly used in electric vehicles, multifunctional electric devices, communication equipment, and the renewable energy integration.[4,5] Therefore, developing LIBs with high energy density, power density, and excellent cycling performance becomes critical. Numerous efforts have been devoted to develop the new electrode materials to meet these demands of LIBs.[2,4,6] Electrochemically active transition metal oxides (MO_x), such as Fe_2O_3,[7,8] Fe_3O_4,[9] SnO_2,[10] Co_3O_4,[11-13] and TiO_2[14,15] are used as promising candidates for anode materials

due to their high theoretical capacity and natural abundance. Among these metal oxides, manganese dioxide (MnO_2) has attracted great attention due to its high theoretical capacity (1230 mAh/g), low cost, natural abundance, and environmental friendliness.[16,17] However, intrinsic low electrical conductivity and rapid capacity fading of MnO_2 due to volume expansion and aggregation in the discharge-charge process hinder its application in energy storage.[17] An effective way to overcome these obstacles is to fabricate nanostructures and new composites made of electrically conductive carbon materials and MnO_2, in order to improve the electrical conductivity and structural stability of the anode material.[18]

In spite of the favorable properties, little research using MnO_2 as anode materials has been reported.[19-22] Reddy *et al*. reported that the coaxial MnO_2/carbon nanotube (CNT) array electrodes can deliver a reversible specific capacity of 500 mAh/g after 15 cycles at the rate of 50 mA/g between 0.02 and 3.2 V vs. Li/Li^+, but they show serious capacity decay.[23] As reported by Xia *et al*., nanoflake MnO_2/CNT composite electrodes delivered a higher reversible capacity of 801 mAh/g for the first 20 cycles without capacity decay and 77% capacity retention after 50 cycles at a current density of 200 mA/g in the potential range of 0.01 V and 3.0 V vs. Li/Li^+.[22] Lai *et al*. prepared MnO_2/carbon nanohorns (CNHs) composites, which showed the the reversible capacity of MnO_2/CNHs remained at 565 mAh/g after 60 cycles with 98% capacity retention at a current density of 100 mA/g in the potential range of 0.05 V and 3.0 V vs. Li/Li^+.[17] Yu *et al*. synthesized graphene-MnO_2 nanotubes with the reversible specific capacity of 495 mAh/g at a current density of 100 mA/g after 40 cycles with varying current rate from 100 mA/g to 1600

mA/g.[24] However, these materials have limited scalability, or low specific capacity, or still suffer from electrochemical stability problems.

In this study, we designed a unique hierarchical structure, where the graphene wraps the porous MnO_2 directly growing from graphene nanoribbons (GNRs). GNRs[25] are scalable and have high surface area and high electrical conductivity, making them a suitable template on which the MnO_2 in directly grown by a hydrothermal reaction to form MnO_2-GNRs (MG).[22,26] Graphene was produced by the reduction of graphene oxide with hydrazine and then coated on the surface of MG by electrostatic interaction, forming the hierarchical sandwiched structured graphene-MnO_2-GNRs (GMG).[27-29] In this structure, graphene and GNRs are in good contact with MnO_2, improving the electrical conductivity of the composite GMG. More importantly, graphene and GNRs can buffer the volume changes and prevent the loss of MnO_2 during Li ion conversion reaction with Li, thus improving the composite's electrochemical stability performance. The GMG as anode material demonstrates excellent rate capabilities and the cycling performance. The reversible specific discharge capacity can reach 890 mAh/g at 0.1 A/g after 180 cycles with varying current rates from 0.1 to 1.0 A/g and also almost increase about 24% compared to the initial capacity after 245 cycles at a current density of 0.4 A/g. Thus GMG is a superb candidate for use as an anode electrode material for energy storage of LIBs.

5.2. Experiments

5.2.1. Materials synthesis

GNRs were prepared by intercalalation of NaK into multiwalled carbon nanotubes in 1,2-dimethoxyethane as described previously.[25] The GNRs were then oxidized in 3 M HNO_3 at reflux for 12 h in order to increase their wettability. MnO_2-GNRs were prepared by direct redox reaction of $KMnO_4$ on the HNO_3-treated GNRs. In a typical procedure, 20 mg GNRs was added to 40 mL in-house deionized water (D.I. water) and the mixture was ultrasonicated (2510 Branson ultrasonicator) to disperse the GNRs. 63 mg $KMnO_4$ was added to the dispersion and the dispersion was magnetically stirred for 3 h at room temperature. The dispersion was transferred to a Teflon-lined autoclave. After sealing, the autoclave was kept in the oven at 180 °C for 5 h to carry out the hydrothermal reaction, and then it was removed from the oven and cooled to room temperature. MnO_2-GNRs (51 mg) were obtained after vacuum filtration and washing sequentially with water (400 mL) and acetone (100 mL); the filter cake was dried in a vacuum oven at 85 °C for 10 h. Graphene-wrapped MnO_2-GNRs (GMG) was synthesized in two steps. The first step was to positively charge the MnO_2-GNRs by coating it with aqueous polydiallyldimethylammonium chloride (PDDA, Sigma-Aldrich). 40 mg of MnO_2-GNRs was dispersed in 40 mL D.I. water containing 0.4 mL of PDDA. After 5 h stirring at room temperature, positively charged PDDA-MnO_2-GNRs (40 mg) was obtained *via* vacuum filtration and washing the solid with D.I. water (400 mL) and ethanol (100 mL), and drying it in a vacuum oven at 85 °C for 10 h. Then, 30 mg PDDA-MnO_2-GNRs was dispersed in 40 mL D.I. water by ultrasonic treatment and the solution was adjusted to pH ~8 using 1

M ammonia in ethanol. The PDDA-MnO_2-GNRs suspension was added to a negatively charged graphene solution that was prepared by the reported method,[27,28] and the mixture was stirred for 2 h. GMG (32 mg) was obtained after vacuum filtration followed by washing sequentially with D.I. water (400 mL) and ethanol (100 mL), followed by drying in a vacuum oven at 85 °C for 10 h.

5.2.2. Materials characterization

Products were characterized by XRD (Rigaku D/Max Ultima II); XPS (PHI Quantera); SEM (JEOL 6500); and TEM (JEM2100F TEM).

5.2.3. Device fabrication

The anode was prepared by mixing 80 wt% of the active composite, 10 wt% of carbon black (Super P), and 10 wt% of polyvinylidene difluoride (PVDF, Alfa Aesar) dissolved in *N*-methyl-2-pyrrolidone (NMP, Sigma-Aldrich) to form a slurry that then was coated on a copper foil substrate. Electrochemical tests were performed using CR2032 coin-type cells with lithium metal foil as the counter electrode. The electrolyte was 1 M $LiPF_6$ in ethylene carbonate and diethyl carbonate (EC: DEC, 1:1 in volume) and the separator was Celgard 2300 membrane.

5.2.4. Electrochemical measurement

CV tests were done on a CHI660D electrochemical station at a current density of 0.60 mV/s; EIS measurements were carried out on the CHI660D at the open circuit potential in the frequency range of 100 kHz to 10 mHz, and the galvanostatic discharge charge test was carried out on the LAND CT2001A battery system at room temperature.

5.3. Results and Discussion

5.3.1. Synthesis and structure analysis

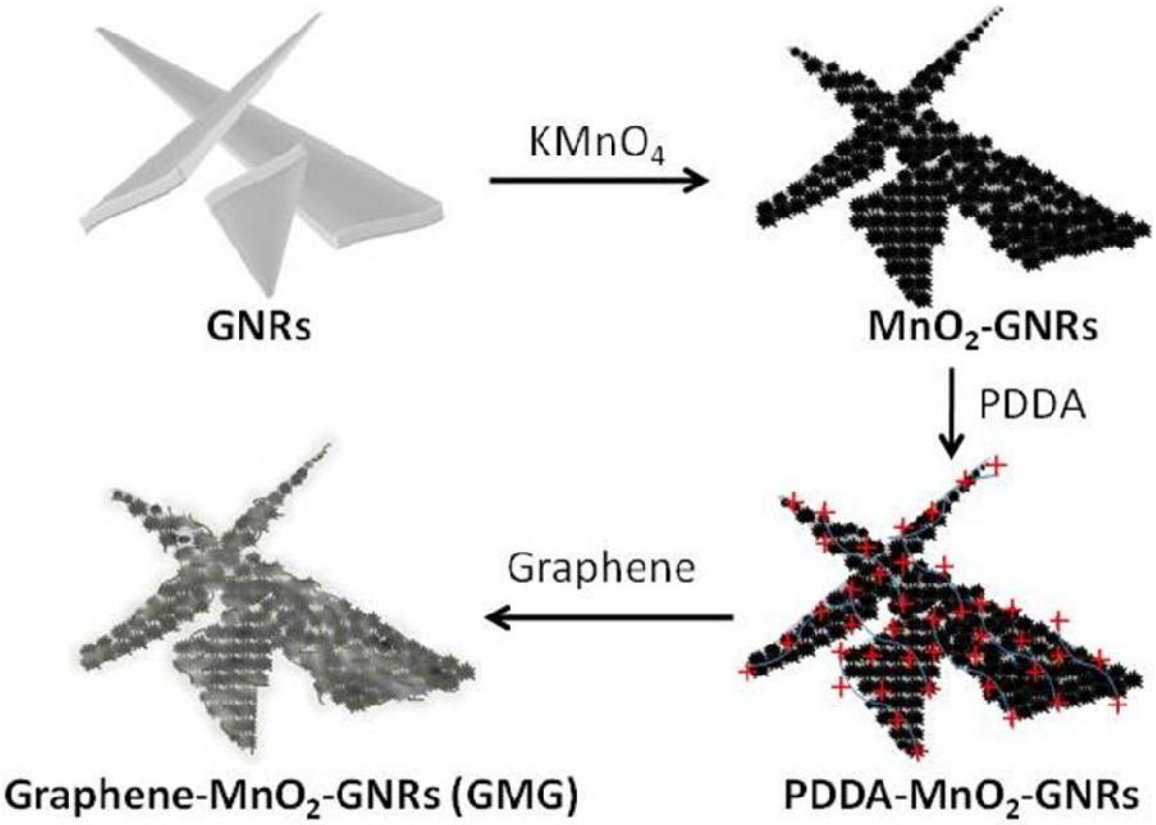

Figure 5.1. Schematic illustration of the synthesis of the GMG composite.

The synthesis of composite GMG is schematically depicted in Figure 5.1. The GNRs were prepared through solution-based chemical unzipping of multiwalled carbon nanotubes.[24] The GNRs were heated to reflux in 3 M HNO_3 for 12 h in order to increase their wettability. MG was prepared by direct redox reaction between $KMnO_4$ and GNRs.[26] Then, MG was positively charged by dispersing it in aqueous polydiallyldimethylammonium chloride (PDDA). Finally, the GMG was obtained by an

electrostatic interaction between the PDDA positively charged MG and the negatively charged graphene, which was prepared by reduction of graphene oxide with hydrazine (Figure 5.1).[28]

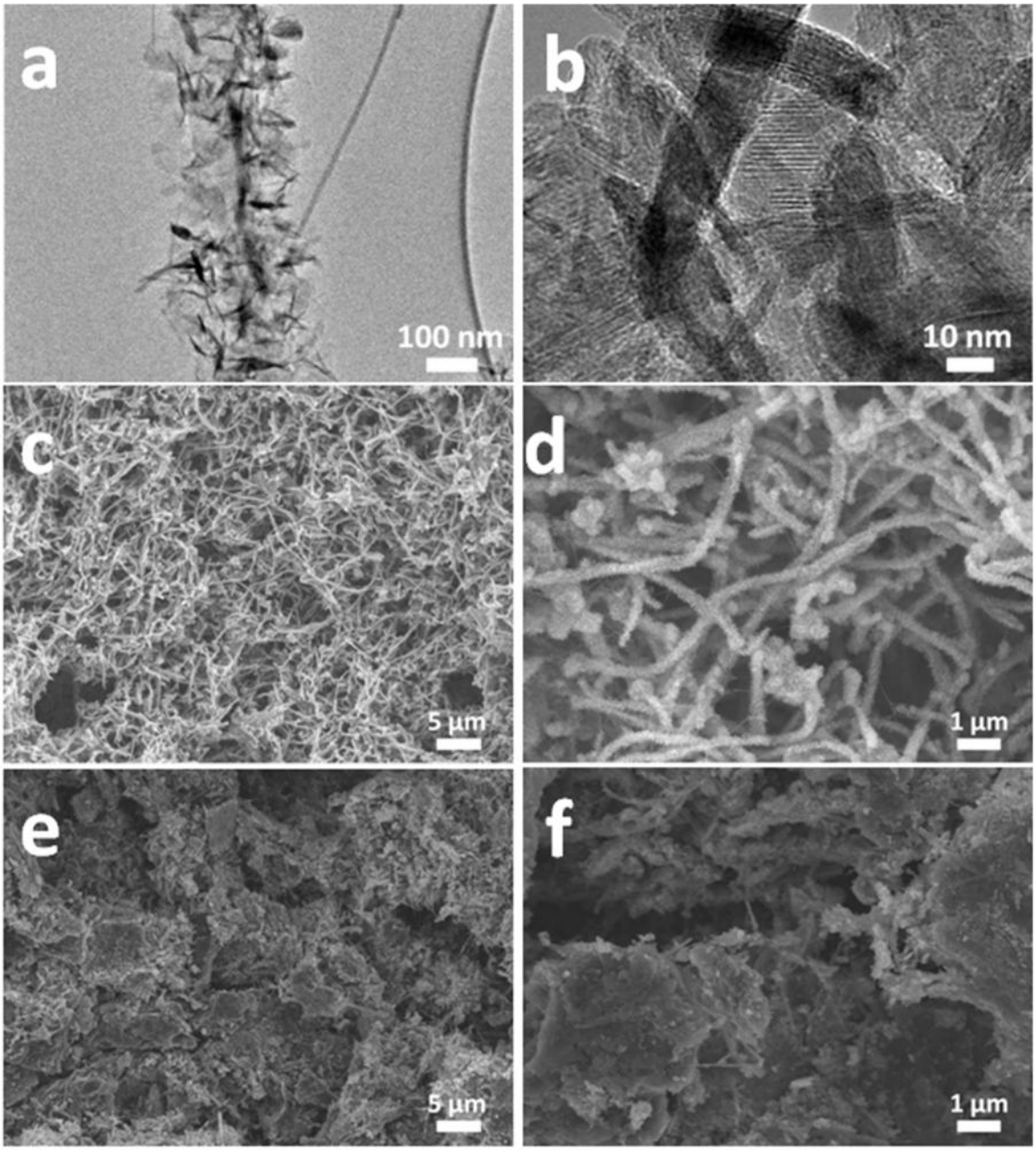

Figure 5.2. (a, b) TEM images of MG; (c, d) SEM images of MG and (e, f) GMG.

The morphology of the intermediate MG and GMG was characterized by transmission electron microscopy (TEM) and scanning electron microscopy (SEM) as shown in Figure 5.2. Figure 5.2a shows the morphology of MG. Nanosized MnO_2 has grown around the GNRs after the hydrothermal treatment. From the high resolution TEM image of MG in Figure 5.2b, the synthesized MnO_2 was nanorod-shaped. The GNRs were uniformly coated by MnO_2 and formed a porous structured MG as shown in Figure 5.2c,d. Figure 5.2e and f show the morphology of GMG at different resolutions. The images indicate that the MG was covered by graphene, playing a role as binder of the MG. MG stripes still can be observed at the edge or surface of the GMG as shown in Figure 5.2f.

X-ray diffraction (XRD) and X-ray photoelectron spectroscopy (XPS) are also used to characterize the composites. Figure 5.3a shows the XRD pattern of GNRs, MnO_2, MG, and GMG. The GNRs have the strong diffraction peak (002) of graphite at 26.5°.[30] The XRD pattern of pure MnO_2 can be indexed to α-MnO_2, which is suitable for energy storage.[31] The characteristic peaks of GNRs and MnO_2 can be observed from the XRD pattern of MG and GMG. Due to the relatively small size of the nanocrystals, all of the XRD pattern peaks of MnO_2 in MG and GMG became broad and weak and some peaks were too small to discern when compared to pure MnO_2.[22] XPS was used to determine the oxidation state of Mn in the composite. Figure 5.3b shows the XPS spectra obtained from the composite GMG. The spin energy separation of Mn $2p_{3/2}$ and Mn $2p_{1/2}$ centered at 642.5 eV and 654.2 eV, respectively, is 11.7 eV, which is in good agreement with reported data of Mn $2p_{3/2}$ and Mn $2p_{1/2}$ in MnO_2.[23,32] The data demonstrates that MnO_2 was indeed grown on the GNRs after the hydrothermal treatment.

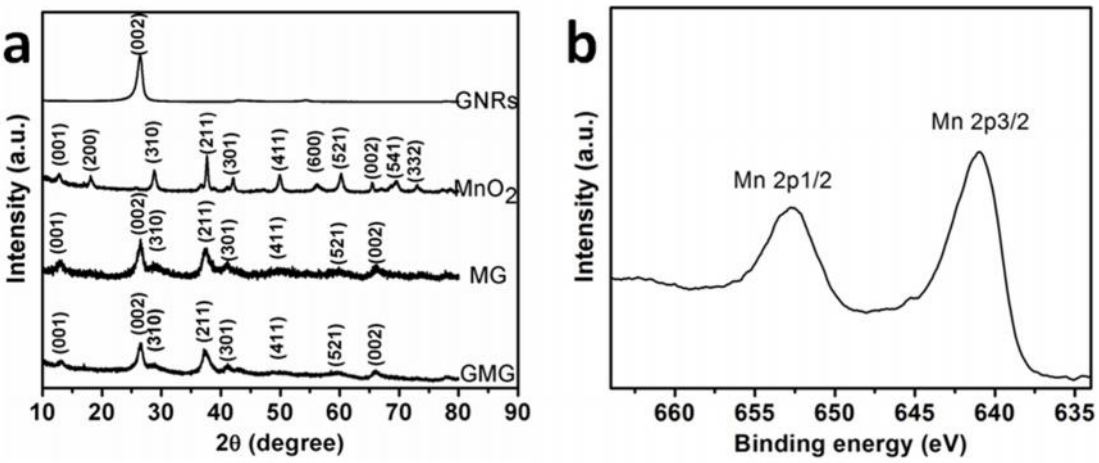

Figure 5.3. (a) XRD patterns of GNRs, MnO2, MG, and GMG. (b) XPS spectrum of Mn2p for GMG.

5.3.2. Electrochemical evaluation

The electrochemical performance of GMG and MG as anodes in LIBs was studied. A wider potential window of 0.01 to 3.0 V was applied in this study because the electrochemical performance of LIBs is strongly dependent on the potential windows.[33] Figure 5.4 shows the cyclic voltammetry (CV) and the first two discharge-charge profiles of GMG, MG, MnO_2, and GNRs. As shown in Figure 5.4a, the cathodic peak at 0.55 V in the first cycle of the CV was a characteristic of the solid electrolyte interface (SEI) formation in the electrode surface. It disappeared in the second cycle, confirming that the formation of SEI occurs in the first cycle. The two anode peaks at 1.3 V and 2.3 V indicate that the electrochemical oxidation reaction may process in two steps. This was further shown by the discharge-charge profiles of GMG. As shown in Figure 5.4b, there were two plateaus, around 1.3 V and 2.3 V in the charge process, according to the anode peaks in the CV. There was one plateau in the discharge process, demonstrating the reduced reaction of

MnO_2 with Li ions in one step. MG and MnO_2 displayed similar phenomena as shown in Figure 5.4c,d and Figure 5.4e,f. The specific capacity of MnO_2 in the second cycle of discharge-charge process shown in Figure 5.4f decreased steeply compared to the first cycle: only 22% capacity retention was attained due to its poor electrical conductivity. When the GNRs and reduced graphene oxide were introduced to form the composite system, the specific capacity improved, with over 58% capacity retention for MG (Figure 5.4d) and 77% for GMG (Figure 5.4b). The unique hierarchical structure of GMG greatly improved the utility of the MnO_2 in the composite when considering that the MnO_2 content was 74% for MG and 32% for GMG as determined by thermogravimetric analyses (TGA) (Figure 5.5). In addition, the first discharge specific capacities of these four materials, GNRs, MnO_2, MG, and GMG, have higher values than the theoretical capacities, which might result from the irreversible reactions of the electrodes, the SEI formation on the surface of the electrodes, and the decomposition of electrolyte.[17]

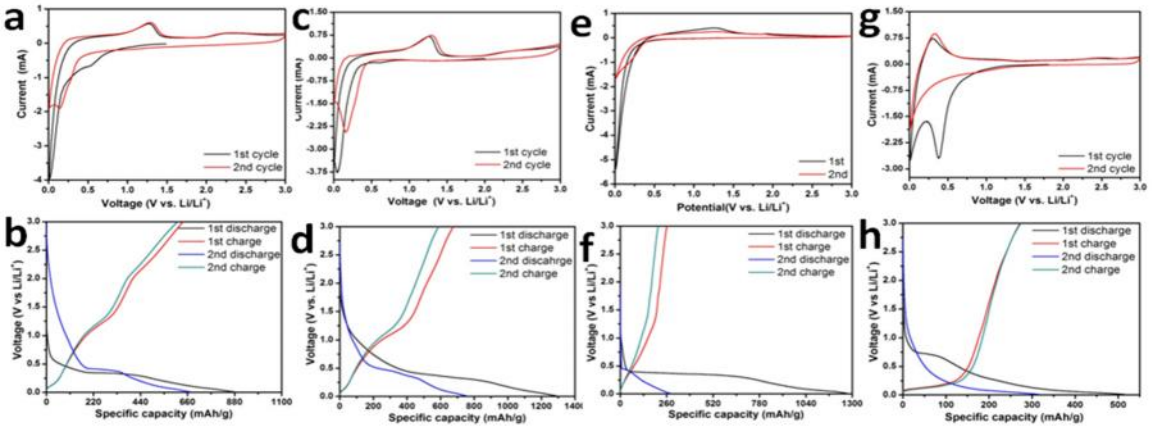

Figure 5.4. Cyclic voltammetry curves in the potential range of 0.01 and 3 V (vs. Li/Li+) for (a) GMG, (c) MG, (e) MnO2, and (g) GNRs at the scan rate of 0.6 mV/s. The first two discharge charge curves in the potential range of 0.01 and 3 V (vs. Li/Li+) for (b) GMG, (d) MG, (f) MnO_2, and (h) GNRs at the current density of 0.1 A/g.

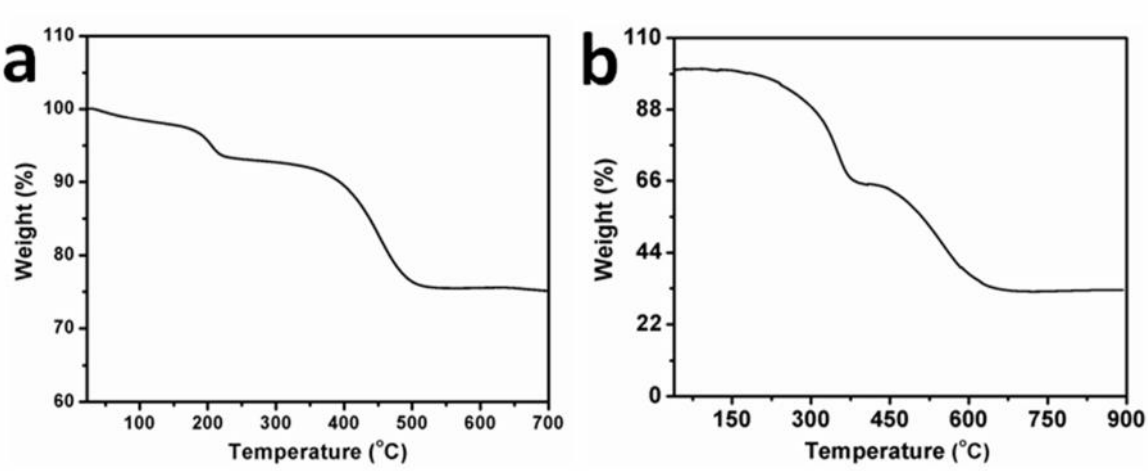

Figure 5.5. TGA curves of (a) MG showing 74% MnO2 content and (b) GMG with a 32% MnO2 content, recorded in argon at a heating rate of 10 °C min^{-1}.

The rate performance of the GMG was studied in the potential window of 0.01 to 3.0 V as shown in Figure 5.6a. The stable capacity at different current densities is observed. When the current density reduced back from 1.0 A/g to 0.1 A/g, the value of specific capacity of GMG not only returned, but more importantly, it increased with the increase in cycle numbers at the same current density. For example, the value of specific capacity increased to 890 mAh/g at the 180^{th} cycle from 672 mAh/g at the 2^{nd} cycle in the current density of 0.1 A/g. The rate performance demonstrates GMG electrode remained stable after extended rate cycles.

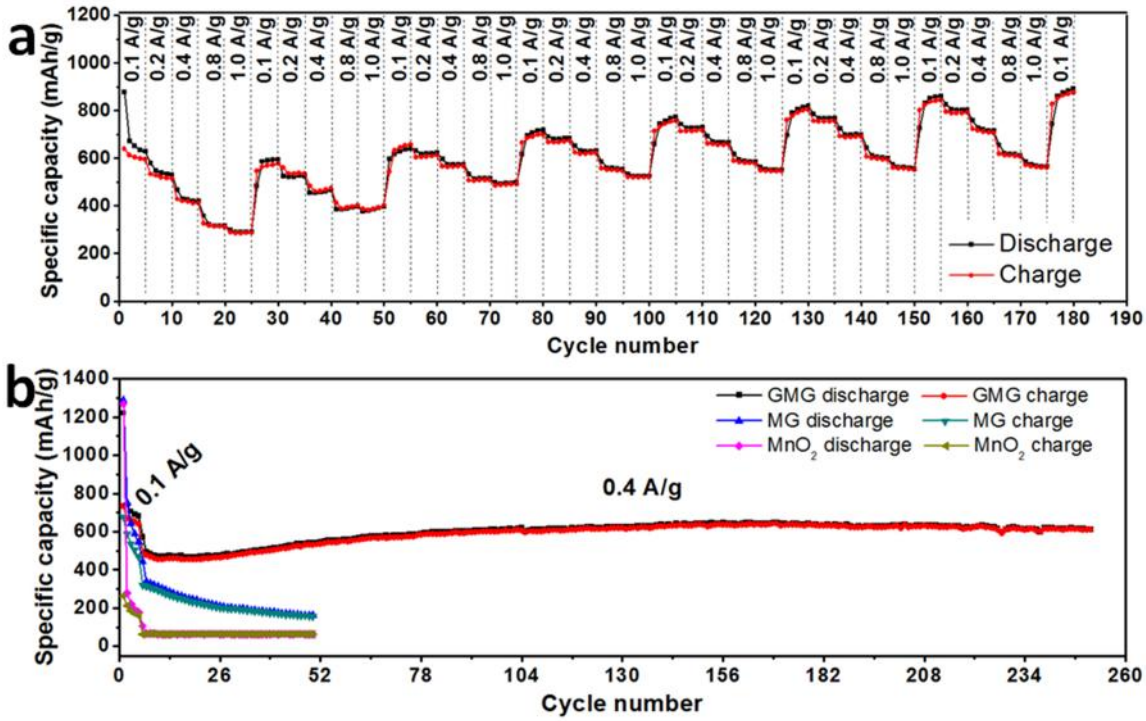

Figure 5.6. (a) Rate performance of GMG at various current rates from 0.1 A/g to 1.0 A/g with respect to the cycle numbers. (b) Cycling performance of MnO2, MG, and GMG at the 0.1 A/g for the first 5 cycles and the 0.4 A/g for the following cycles.

The cycling performance for GMG was evaluated by the discharge-charge experiments in the potential window of 0.01 to 3.0 V. Figure 5.6b shows the cycling performance of GMG, MG, and MnO_2 used as electrodes in LIBs. The first five cycles were carried out at a current density of 0.1 A/g and the current density was increased to 0.4 A/g in the following cycles. For MnO_2, the specific capacity decreased steeply to 105 mAh/g in the 6^{th} cycle, although the following cycles were stable. For MG, the specific capacity was 753 mAh/g at the second cycle and decreased to 470 mAh/g as the cycle numbers increased from the second cycle to the 5^{th}. From the 6^{th} cycle, the current density was increased to 0.4 A/g and the specific capacity dropped to 160 mAh/g at the 50^{th} cycle

from 339 mAh/g, so that 47.6 % capacity remained after 45 cycles. The cycling performance of the MG electrode is better than that shown in the pure MnO_2 electrode due to the introduction of GNRs into the composite that improved the electrochemical performance of MnO_2. The MnO_2 in the fresh MG electrode (Figure 5.7a) merged into the bulk solid after 50 cycle discharge-charge processes as shown in Figure 5.7b. The changed morphology of MnO_2 in the MG electrode after 50 cycle discharge-charge processes was further supported by TEM as shown in Figure 5.7c,d. However, without the graphene encapsulation, the MnO_2 might peel away from the GNRs during the repeated discharge-charge process due to the large volume change in MnO_2, thereby resulting in the decay of the specific capacity of MG.[22] For GMG, in the first 5 cycles, the specific capacity decreased as had been seen with MG. After 5 cycles, the value of GMG discharge capacity decreased from 571 mAh/g at the 6^{th} cycle to 464.7 mAh/g at the 20^{th} cycle, but then increased to 648 mAh/g at the 170^{th} cycle. Even after 250 cycles, the GMG still maintained a specific capacity of 612 mAh/g. Moreover, the Coulombic efficiency of GMG was maintained at over 99%, excluding the first several cycles. The graphene encapsulation apparently hindered direct contact between MnO_2 and the electrolyte. With more discharge-charge cycles, the internal materials become electrochemically active as they come in contact with the electrolyte.[34] Therefore, the unique hierarchical structure greatly improves the cycling performance of GMG in LIBs.

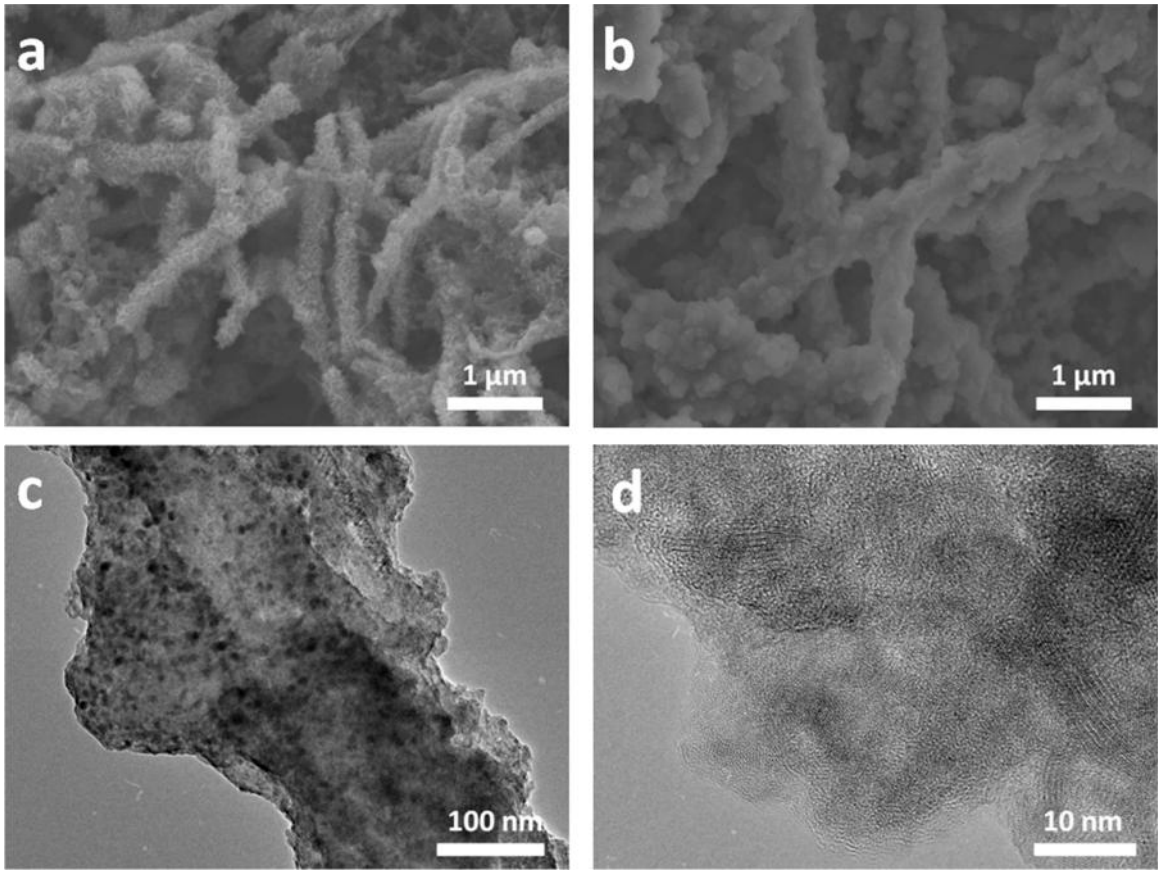

Figure 5.7. (a) SEM image of the fresh MG electrode. (b) SEM image of a MG electrode after 50 cycles discharge-charge processes in the potential range of 0.01 to 3.0 V. (c) and (d) TEM images of a MG electrode after 50 cycles discharge-charge processes in the potentioal range of 0.01 to 3.0 V.

GMG has made significant improvements in specific capacity, rate performance, and cycling stability in energy storage. In order to understand the GMG electrode's enhanced electrochemical performance relative to GNRs, electrochemical impedance spectroscopy (EIS) measurements were carried out after 3 cycles, as shown in Figure 5.8. Figure 5.8e shows the equivalent circuit model of this system. In this model, R_s is the internal resistance of the tested battery, R_{SEI} and R_{ct} represents the SEI surface and charge-transfer resistance, *CPE* and C_{dl} are associated with constant phase element and double

layer capacitance across the surface, Z_w is the Warburg resistance related to the lithium diffusion process, and the C_{int} is the interaction capacitance.[35,36] In the Figure 5.8a, the plots consist of two semicircles in the high and intermediate frequency range (100 kHz to 10 Hz) and a sloping line with an angle ~ 45° to the real axis in the low frequency region. The two semicircles result from the Li^+ ion transport through the SEI film and the interfacial charge transfer reaction (R_{SEI} and R_{ct}) combined with the electrochemical double-layer capacitive behavior *CPE* and C_{dl}, respectively. The sloping line is attributed to the solid-state Li diffusion into the active materials (Z_w).[35] The experimental Nyquist plots are modeled based on the equivalent circuit.[33-37] The fitted impedance parameters are listed in Table 5.1. Both R_{SEI} (15.45 Ω) and R_{ct} (45.35 Ω) of GMG are lower than that of MG (R_{SEI} = 16.64 Ω and R_{ct} = 69.38 Ω). This demonstrates that the incorporation of graphene can greatly increase the electrical conductivity, resulting in significant improvement in the electrochemical performance.

Table 5.1. The EIS simuation parameters of GMG and MG.

Active material	R_s (Ω)	*CPE* (μF)	R_{SEI} (Ω)	R_{ct} (Ω)	C_{dl} (μF)	Z_w (Ω)	C_{int} (mF)
GMG	3.36	81.11	15.45	45.35	26.82	129.45	27.02
MG	2.95	34.74	16.64	69.38	11.24	24.49	925.00

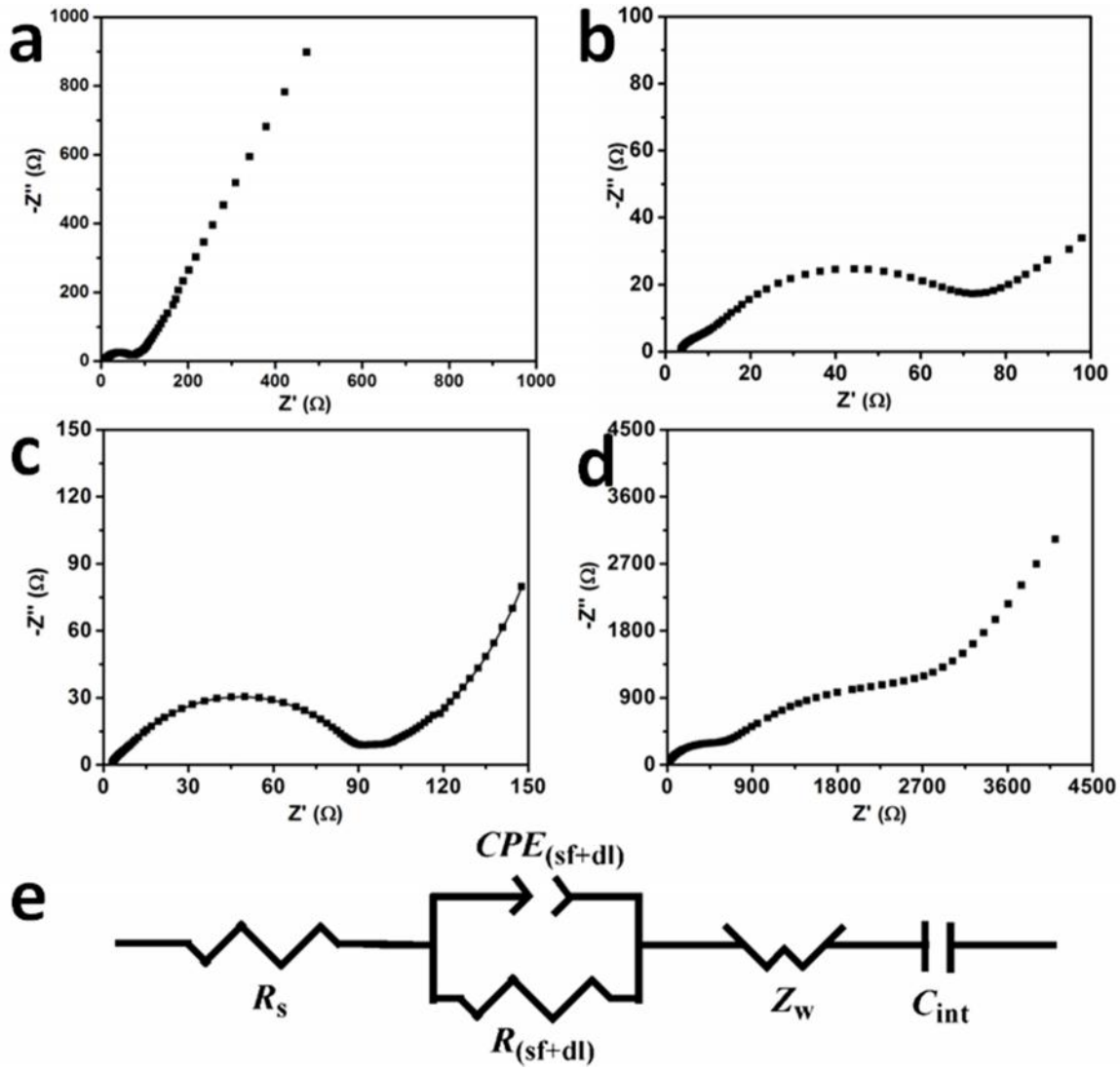

Figure 5.8. Nyquist plots of GMG (a), Enlarged high frequency region of GMG (b), MG (c), MnO2 (d). (e) Equivalent circuit that is used to fit the experimental data.

5.4. Conclusions

In summary, we successfully designed and synthesized a unique hierarchical structure composite of graphene-wrapped MnO_2-GNRs (GMG). In this composite, graphene flakes tightly sandwiched nanosized MnO_2 that grew directly on the GNRs.

Electrochemical experiments demonstrate that the GMG exhibit enhanced specific capacity and improved cycling stability as anode materials compared to MG and pure MnO_2 because of the synergic effect between the graphene, GNRs, and MnO_2. The synthesis of the GMG composite has been shown to produce an effective component to improve the electrochemical stability of the electrode materials for the lithium ion batteries.

5.5. References

1. Li, L.; Raji, A.-R. O.; Tour, J. M. Graphene-Wrapped MnO_2-Graphene Nanoribbons as Anode Materials for High-Performance Lithium Ion Batteries. *Adv. Mater.* **2013**, *25*, 6298-6302. (L.L. conceived and designed the experiments. L.L. prepared, characterized, and tested the materials. R.A.R.O. prepared GNRs and took the TEM characterization. L.L. wrote the paper. Finally, T.J.M. oversaw all research phases, provided regular guidance to the research and revised the manuscript. All authors discussed and commented on the manuscript.)

2. Su, Y.; Li, S.; Wu, D.; Zhang, F.; Liang, H.; Gao, P.; Cheng, C.; Feng, X. Two-Dimensional Carbon-Coated Graphene/Metal Oxide Hybrids for Enhanced Lithium Storage. *ACS Nano* **2012**, *6* , 8349-8356.

3. Etacheri, V.; Marom, R.; Elazari, R.; Salitra, G.; Aurbach, D. Challenges in the development of advanced Li-ion batteries: a review. *Energy Environ. Sci.* **2011**, *4* , 3243-3262.

4. Tarascon, J.-M.; Armand, M. Issues and challenges facing rechargeable lithium batteries. *Nature* **2001**, *414*, 359-367.

5. Wang, B.; Li, X.; Zhang, X.; Luo, B.; Jin, M.; Liang, M.; Dayeh, S. A.; Picraux, S. T.; Zhi, L. Adaptable Silicon–Carbon Nanocables Sandwiched between Reduced Graphene Oxide Sheets as Lithium Ion Battery Anodes. *ACS Nano* **2013**, *7*, 1437.

6. Arico, A. S.; Bruce, P.; Scosati, B.; Tarascon, J. M. Nanostructured Materials for Advanced Energy Conversion and Storage Devices. *Nat. Mater.* **2005**, *4*, 366-377.

7. Zhou, G.-W.; Wang, J.; Gao, P.; Yang, X.; He, Y.-S.; Liao, X.-Z.; Yang, J.; Ma, Z.-F. Facile Spray Drying Route for the Three-Dimensional Graphene-Encapsulated Fe_2O_3 Nanoparticles for Lithium Ion Battery Anodes. *Ind. Eng. Chem. Res.***2012**, *52*, 1197.

8. Wu, C.; Yin, P.; Zhu, X.; OuYang, C.; Xie, Y. Synthesis of Hematite (α- Fe_2O_3) Nanorods: Diameter-Size and Shape Effects on Their Applications in Magnetism, Lithium Ion Battery, and Gas Sensors. *J. Phys. Chem. B* **2006**, *110*, 17806-17812.

9. Jia, X.; Chen, Z.; Cui, X.; Peng, Y.; Wang, X.; Wang, G.; Wei, F.; Lu, Y. Building Robust Architectures of Carbon and Metal Oxide Nanocrystals toward High-Performance Anodes for Lithium-Ion Batteries. *ACS Nano* **2012**, *6*, 9911-9919.

10. Lin, Y.-S.; Duh, J.-G.; Hung, M.-H. Shell-by-Shell Synthesis and Applications of Carbon-Coated SnO_2 Hollow Nanospheres in Lithium-Ion Battery. *J. Phys. Chem. C* **2010**, *114*, 13136-13141.

11. Wu, Z.-S.; Ren, W.; Wen, L.; Gao, L.; Zhao, J.; Chen, Z.; Zhou, G.; Li, F.; Cheng, H.-M. Graphene Anchored with Co_3O_4 Nanoparticles as Anode of Lithium Ion Batteries with Enhanced Reversible Capacity and Cyclic Performance. *ACS Nano* **2010**, *4*, 3187-3194.

12. Huang, H.; Zhu, W.; Tao, X.; Xia, Y.; Yu, Z.; Fang, J.; Gan, Y.; Zhang, W. Nanocrystal-Constructed Mesoporous Single-Crystalline Co_3O_4 Nanobelts with Superior Rate Capability for Advanced Lithium-Ion Batteries. *ACS Appl. Mater. Interfaces* **2012**, *4*, 5974-5980.

13. Yan, N.; Hu, L.; Li, Y.; Wang, Y.; Zhong, H.; Hu, X.; Kong, X.; Chen Q. Co_3O_4 Nanocages for High-Performance Anode Material in Lithium-Ion Batteries. *J. Phys. Chem. C* **2012**, *116*, 7227-7235.

14. Shen, L.; Zhang, X.; Li, H.; Yuan, C.; Cao, G. Design and Tailoring of a Three-Dimensional TiO_2–Graphene–Carbon Nanotube Nanocomposite for Fast Lithium Storage. *J. Phys. Chem. Lett.* **2011**, *2*, 3096-3101.

15. Xin, X.; Zhou, X.; Wu, J.; Yao, X.; Liu, Z. Scalable Synthesis of TiO_2/Graphene Nanostructured Composite with High-Rate Performance for Lithium Ion Batteries. *ACS Nano* **2012**, *6*, 11035-11043.

16. Fang, X.; Lu, X.; Guo, X.; Mao, Y.; Hu, Y.-S.; Wang, J.; Wang, Z.; Wu, F.; Liu, H.; Chen, L. Electrode reactions of manganese oxides for secondary lithium batteries. *Electrochem. Commun.* **2010**, *12*, 1520-1523.

17. Lai, H.; Li, J.; Chen, Z.; Huang, Z. Carbon Nanohorns As a High-Performance Carrier for MnO_2 Anode in Lithium-Ion Batteries. *ACS Appl. Mater. Interfaces* **2012**, *4*, 2325-2328.

18. Wang, Y.; Zeng, H. C.; Lee, J. Y. Highly Reversible Lithium Storage in Porous SnO_2 Nanotubes with Coaxially Grown Carbon Nanotube Overlayers. *Adv. Mater.* **2006**, *18*, 645-649.

19. Zhao, J.; Tao, Z.; Liang, J.; Chen, J. Facile Synthesis of Nanoporous γ-MnO_2 Structures and Their Application in Rechargeable Li-Ion Batteries. *Cryst. Growth Des.* **2008**, *8*, 2799-2805.

20. Li, B.; Rong, G.; Xie, Y.; Huang, L.; Feng, C. Low-Temperature Synthesis of α-MnO_2 Hollow Urchins and Their Application in Rechargeable Li+ Batteries. *Inorg. Chem.* **2006**, *45*, 6404-6410.

21. Wu, M.-S.; Chiang, P.-C. J.; Lee, J.-T.; Lin, J.-C. ynthesis of Manganese Oxide Electrodes with Interconnected Nanowire Structure as an Anode Material for Rechargeable Lithium Ion Batteries. *J. Phys. Chem. B* **2005**, *109*, 23279-23284.

22. Xia, H.; Lai, M.; Lu, L. Nanoflaky MnO_2/carbon nanotube nanocomposites as anode materials for lithium-ion batteries. *J. Mater. Chem.* **2010** *20*, 6896-6902.

23. Reddy, A. L. M.; Shaijumon, M. M.; Gowda, S. R.; Ajayan, P. M. Coaxial MnO_2/Carbon Nanotube Array Electrodes for High-Performance Lithium Batteries. *Nano Lett.* **2009**, *9*, 1002-1006.

24. Yu, A.; Park, H. W.; Davies, A.; Higgins, D. C.; Chen, Z.; Xiao, X. Free-Standing Layer-By-Layer Hybrid Thin Film of Graphene-MnO_2 Nanotube as Anode for Lithium Ion Batteries. *J. Phys. Chem. Lett.* **2011**, *2*, 1855-1860.

25. Genorio, B.; Lu, W.; Dimiev, A. M.; Zhu, Y.; Raji, A.-R. O.; Novosel, B.; Alemany, L. B.; Tour, J. M. In Situ Intercalation Replacement and Selective Functionalization of Graphene Nanoribbon Stacks. *ACS Nano* **2012**, *6*, 4231-4240.

26. Li, Z.; Wang, J.; Wang, Z.; Ran, H.; Li, Y.; Han, X.; Yang, S. Synthesis of a porous birnessite manganese dioxide hierarchical structure using thermally reduced graphene oxide paper as a sacrificing template for supercapacitor application. *New J. Chem.* **2012**, *36*, 1490-1495.

27. Li, D.; Muller, M.B.; Gilje, S.; Kaner, R. B.; Wallace, G. G. Processable Aqueous Dispersions of Graphene Nanosheets. *Nat. Nano.* **2008**, *3*, 101-105.

28. Marcano, D. C.; Kosynkin, D. V.; Berlin, J. M.; Sinitskii, A.; Sun, Z.; Slesarev, A.; Alemany, L. B.; Lu, W.; Tour, J. M. Improved Synthesis of Graphene Oxide. *ACS Nano* **2010**, *4*, 4806-4814.

29. Lei, Z.; Shi, F.; Lu, L. Incorporation of MnO_2-Coated Carbon Nanotubes between Graphene Sheets as Supercapacitor Electrode. *ACS Appl. Mater. Interfaces* **2012**, *4*, 1058-1064.

30. Campos-Delgado, J.; Romo-Herrera, J. M.; Jia, X.; Cullen, D. A.; Muramatsu, H.; Kim, Y. A.; Hayashi, T.; Ren, Z.; Smith, D. J.; Okuno, Y.; Bulk Production of a New Form of sp2 Carbon: Crystalline Graphene Nanoribbons. *Nano Lett.* **2008**, *8*, 2773-2778.

31. Cheng, F.; Zhao, J.; Song, W.; Li, C.; Ma, H.; Chen, J.; Shen, P. Facile Controlled Synthesis of MnO_2 Nanostructures of Novel Shapes and Their Application in Batteries. *Inorg. Chem.* **2006**, *45*, 2038-2044.

32. Liu, D.; Zhang, Q.; Xiao, P.; Garcia, B. B.; Guo, Q.; Champion, R.; Cao, G. Hydrous Manganese Dioxide Nanowall Arrays Growth and Their Li^+ Ions Intercalation Electrochemical Properties. *Chem. Mater.* **2008**, *20*, 1376-1380.

33. Li, L.; Peng, S.; Wang, J.; Cheah, Y. L.; Teh, P.; Ko, Y.; Wong, C.; Srinivasan, M. Facile Approach to Prepare Porous $CaSnO_3$ Nanotubes via a Single Spinneret Electrospinning Technique as Anodes for Lithium Ion Batteries. *ACS Appl. Mater. Interfaces* **2012**, *4*, 6005-6012.

34. Xiao, L.; Cao, Y.; Xiao, J.; Schwenzer, B.; Engelhard, M. H.; Saraf, L. V.; Nie, Z.; Exarhos, G. J.; Liu, J. A Soft Approach to Encapsulate Sulfur: Polyaniline Nanotubes for Lithium-Sulfur Batteries with Long Cycle Life. *Adv. Mater.* **2012**, *24*, 1176-1181.

35. Qian, D.; Xu, B.; Cho, H.-M.; Hatsukade, T.; Carroll, K. J.; Meng, Y. S. Lithium Lanthanum Titanium Oxides: A Fast Ionic Conductive Coating for Lithium-Ion Battery Cathodes. *Chem. Mater.* **2012**, *24*, 2744-2751.

36. Chang, K.; Chen, W. l-Cysteine-Assisted Synthesis of Layered MoS_2/Graphene Composites with Excellent Electrochemical Performances for Lithium Ion Batteries. *ACS Nano* **2011**, *5*, 4720-4728.

37. Ang, W. A.; Gupta, N.; Prasanth, R.; Madhavi, S. High-Performing Mesoporous Iron Oxalate Anodes for Lithium-Ion Batteries. *ACS Appl. Mater. Interfaces* **2012**, *4*, 7011-7019.

Chapter 6

Graphene-NiO-reduced Graphene Oxide Nanoribbons Sandwich Structured Composite as Lithium Ion Battery Anode

This chapter was entirely copied from reference 1.

6.1. Introduction

Lithium ion batteries (LIBs) are practical and effective technologies for electrochemical energy storage due to their high voltage, high capacity, low cost, and environmental friendliness.[2-3] LIBs can be widely used in electric vehicles, multifunctional electric devices, communications equipment, and the integration of renewable energy with energy storage.[5,6] Therefore, developing LIBs with high energy density, power density, and excellent cycling performance would be valuable to meet society's goal for energy sustainability and diversity. Electrochemically active transition metal oxides have evolved as an important family of anode materials as graphite

alternatives, due to their high theoretical capacity and natural abundance.[7-9] Among these transition metal oxides, nickel oxide (NiO) has attracted attention because of its high theoretical capacity (718 mAh/g), low cost, and natural abundance.[9,10] However, the conversion reaction between NiO and Li ions in the discharge-charge process causes volume expansion and aggregation within the battery. The volume variation leads to the pulverization of the NiO and might lead to NiO loss, producing capacity decay. Unfortunately, NiO has a low intrinsic electrical conductivity. These drawbacks hinder the use of NiO in energy storage.[7,11] Extensive efforts have been made to overcome the drawbacks of NiO and improve it electrochemical performance in LIBs.[12-26] One strategy is to prepare a NiO nanocomposite using conductive carbon materials, which would act as a matrix for NiO and improve the electrical conductivity of the composite.[12-17] Another strategy is to combine NiO with other metal oxides to form mixed composites that take advantage of their strengths and minimize their weaknesses.[17-19] Introduction of metals into a NiO composite has proven to be another effective method to improve its electrochemical performance in LIBs.[20-23] However, a drastic capacity decay was noted after 20 cycles in almost all of these cases.[7] Therefore, developing new structurally stable materials based on NiO is an important goal.

In this study, we designed a sandwich-structured composite of graphene-NiO-reduced graphene oxide nanoribbons (G-NiO-rGONRs) in order to improve the electrode stability. The synthesis of graphene oxide nanoribbons (GONRs) is scalable. GONRs have high surface area, making them a suitable template on which to form NiO; this mixture was converted into NiO-rGONRs.[27,28] Graphene was synthesized by the reduction of graphene oxide with hydrazine. Electrostatic interaction of the graphene with the surface of the NiO-

rGONRs was used to, form the G-NiO-rGONRs.[28,29] The close contact of graphene and rGONRs with NiO should improve the electrical conductivity of the composite. In addition, the graphene and rGONRs should buffer the volume changes suffered during the Li ion conversion reaction with Li, thus improving the composite's electrochemical stability performance and prevent NiO loss. The reversible discharge capacity of the G-NiO-rGONRs composite was as high as 977 mAh/g at 0.1 A/g after 55 cycles, at current rates varying from 0.1 to 1.0 A/g. More importantly, there was no capacity decay, with little increase after 100 cycles. Thus G-NiO-rGONRs is an excellent candidate for use as an anode electrode material for energy storage in LIBs.

6.2. Experiments

6.2.1. Materials synthesis

6.2.1.1. Synthesis of $Ni(OH)_2$-rGONRs

Graphene oxide nanoribbons (GONRs) were synthesized according to the protocol previously reported.[28] $Ni(OH)_2$-rGONRs were prepared in two steps. The $Ni(OH)_2$-GONRs hybrid was prepared by dispersing 250 mg of GONRs in 100 mL of DI water by bath sonication (60 min, using Cole Parmer ultrasonic cleaner). Then, 900 mg of $NiSO_4 \cdot 6H_2O$ was added, and this solution was stirred for 15 min. After that, 500 mg of NaOH as added, and the reaction mixture was left for 17 h at room temperature with magnetic stirring. The product obtained was purified by centrifugation (2 cycles/60 min) with DI water. Then, this material (dispersed in 100 mL H_2O by bath sonication within 5 min) underwent reduction with hydrazine at 90 °C within two h by the addition of 0.3 mL

hydrazine hydrate solution and 0.75 mL ammonia hydroxide solution. The final product was purified by filtration with DI water, methanol and diethyl ether and dried under vacuum at 60 °C. The resulting $Ni(OH)_2$-rGONR weighed 470 mg.

6.2.1.2. Synthesis of NiO-rGONRs

NiO-rGONRs (136 mg) was obtained by the heat treatment of $Ni(OH)_2$-rGONRs (180 mg) at 350 °C in Ar (500 sccm) for 3 h.

6.2.1.3. Synthesis of G-NiO-rGONRs

G-NiO-rGONRs was prepared in two steps. The first step was to positively charge the NiO-rGONRs by coating the composite with aqueous polydiallyldimethylammonium chloride (PDDA, Sigma-Aldrich). 80 mg of NiO-rGONRs was dispersed in 80 mL DI water containing 0.8 mL of PDDA. After 5 h stirring at room temperature, the PDDA-NiO-rGONRs (75 mg) was obtained *via* vacuum filtration and washing with DI water and ethanol, followed by drying in a vacuum oven at 85 °C for 10 h. Then, 60 mg PDDA-NiO-rGONRs was dispersed in 60 mL D.I. water by ultrasonic treatment and the solution was adjusted to pH ~ 8 using 1 M ammonia in ethanol. The PDDA-NiO-rGONRs suspension was added to a negatively charged graphene solution that was prepared by the reported method,[27,28] and the mixture was stirred for 5 h. G-NiO-rGONRs (65 mg) was obtained after vacuum filtration followed by washing sequentially with DI water (400 mL) and ethanol (400 mL), followed by drying in a vacuum oven at 85 °C for 10 h.

6.2.2. Materials characterization

Products were characterized by XRD (Rigaku D/Max Ultima II); XPS (PHI Quantera); SEM (JEOL 6500); TEM (JEM2100F TEM); and thermogravimetric analysis (TGA, TA Instruments, Q50)

6.2.3. Device fabrication

The anode was prepared by mixing 80 wt% of the active composite, 10 wt% of carbon black (Super P), and 10 wt% of polyvinylidene difluoride (PVDF, Alfa Aesar) dissolved in *N*-methyl-2-pyrrolidone (NMP, Sigma-Aldrich) to form a slurry that then was coated on a copper foil substrate. Electrochemical tests were performed using CR2032 coin-type cells with lithium metal foil as the counter electrode. The electrolyte was 1 M $LiPF_6$ in ethylene carbonate and diethyl carbonate (EC:DEC, 1:1 by volume) and the separator was a Celgard 2300 membrane. The capacity was obtained based on the total mass of the active materials.

6.2.4. Electrochemical measurement

CV tests were done on a CHI660D electrochemical station at a current density of 0.40 mV/s; EIS measurements were carried out on the CHI660D at the open circuit potential in the frequency range of 100 kHz to 10 mHz, and the galvanostatic discharge charge test was carried out on the LAND CT2001A battery system at room temperature. The capacity value was based on the total mass of the active materials.

6.3. Results and Discussion

6.3.1. Synthesis and structure analysis

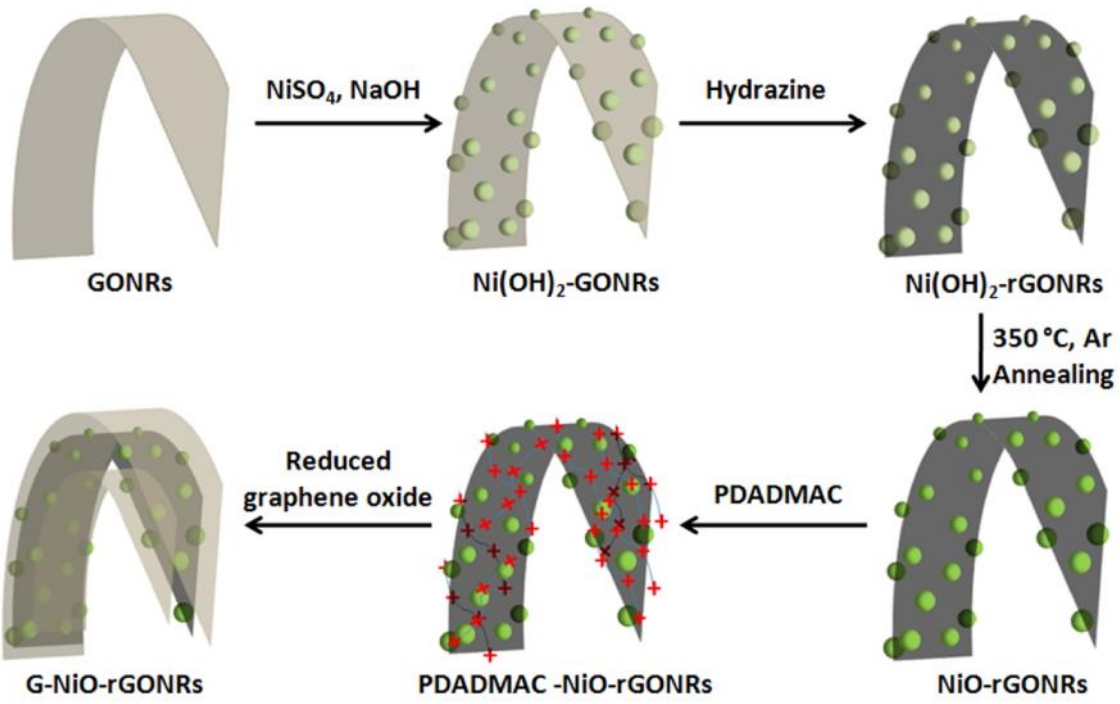

Figure 6.1. Schematic illustration of the synthesis of the G-NiO-rGONRs composite.

The synthesis of the composite G-NiO-rGONRs is depicted in Figure 6.1. $Ni(OH)_2$-rGONRs were synthesized by with the reaction of nickel sulfate hexahydrate with sodium hydroxide in the presence of an aqueous solution of GONRS. GONRs were subsequently chemical reduction hydrazine hydrate. After an annealing treatment at 350 °C in an Ar environment, the $Ni(OH)_2$-rGONRs were converted to NiO-rGONRs. Figure 6.2a,b shows the morphology of the NiO-rGONRs at different magnifications. Nanosized NiO uniformly coated on the surface of rGONRs. Graphene appears to work as a binder to connect the

NiO-rGONRs, forming the G-NiO-rGONR composite, as shown in Figure 6.2c. Individual NiO-rGONRs are observed at the edge and surface of the composite, as shown in Figure 6.2d.The structure of the composite was supported by the TEM images shown in Figure 6.2e,f that reveal that the rGONRs are homogenously coated with NiO. The structure of NiO-rGONRs was further studied by the elemental mapping of carbon, nitrogen, oxygen, and nickel. As shown in Figure 6.2g-j, these elements were uniformly distributed in the NiO-rGONRs.

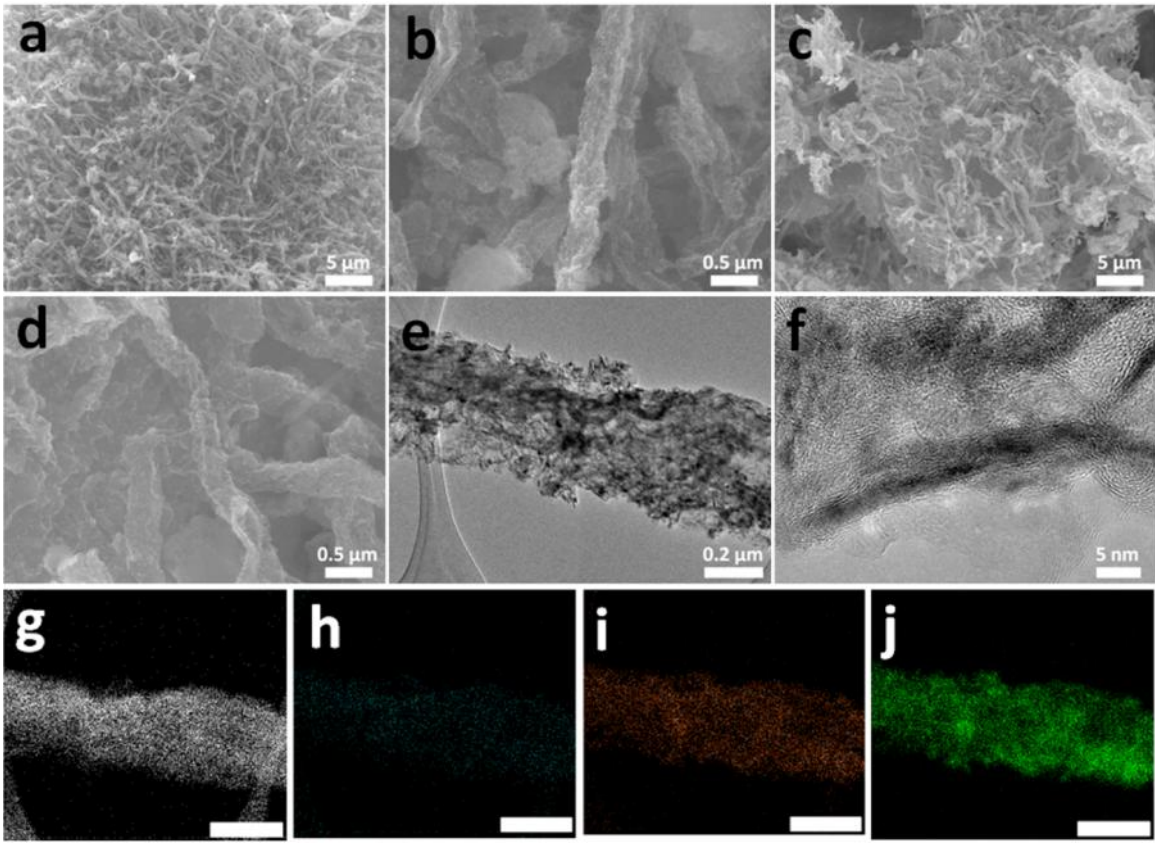

Figure 6.2. SEM images of NiO-rGONRs (a, b) and G-NiO-rGONRs(c, d). TEM images of NiO-rGONRs (e, f) and corresponding elemental mapping of carbon (g), nitrogen (h), oxygen (i), and nickel (j). The scale bars in e-h are 0.3 µm.

X-ray diffraction (XRD) and X-ray photoelectron spectroscopy (XPS) were used to characterize the composites. Figure 6.3a shows the XRD patterns of rGONRs, $Ni(OH)_2$-rGONRs, NiO-rGONRs, and G-NiO-rGONRs. The rGONRs have the strong diffraction peak (002) of graphite at 26.5°.[30] $Ni(OH)_2$ was changed to NiO after the heat treatment in the Argon environment.[31-33] The G-NiO-rGONRs XRD pattern was not obviously changed after the NiO-rGONRs were wrapped by graphene. This demonstrated that NiO-rGONRs were stable during the graphene wrapping process. The diffraction peak (002) of rGONRs became broad and weak due to the NiO covering of its surface. G-NiO-rGONRs only contained four elements: carbon, nitrogen, oxygen, and nickel as shown in Figure 6.3b. Figure 6.3c showed the fine XPS spectra of C1s of G-NiO-rGONRs, which was divided into five peaks. They were located at 284.5, 285.7, 286.8, 288.2, and 289.7 eV. They were assigned to C=C (sp^2 C), C-C(sp^3 C), C-O, C=O, O-C=O, respectively.[34] The weakly oxidized groups of G-NiO-rGONRs suggested that graphene oxide were well reduced by hydrazine. The two characteristic peaks of Ni 2p, as shown in Figure 6.3d, further supported the conclusion that NiO was in the G-NiO-rGONRs.[35]

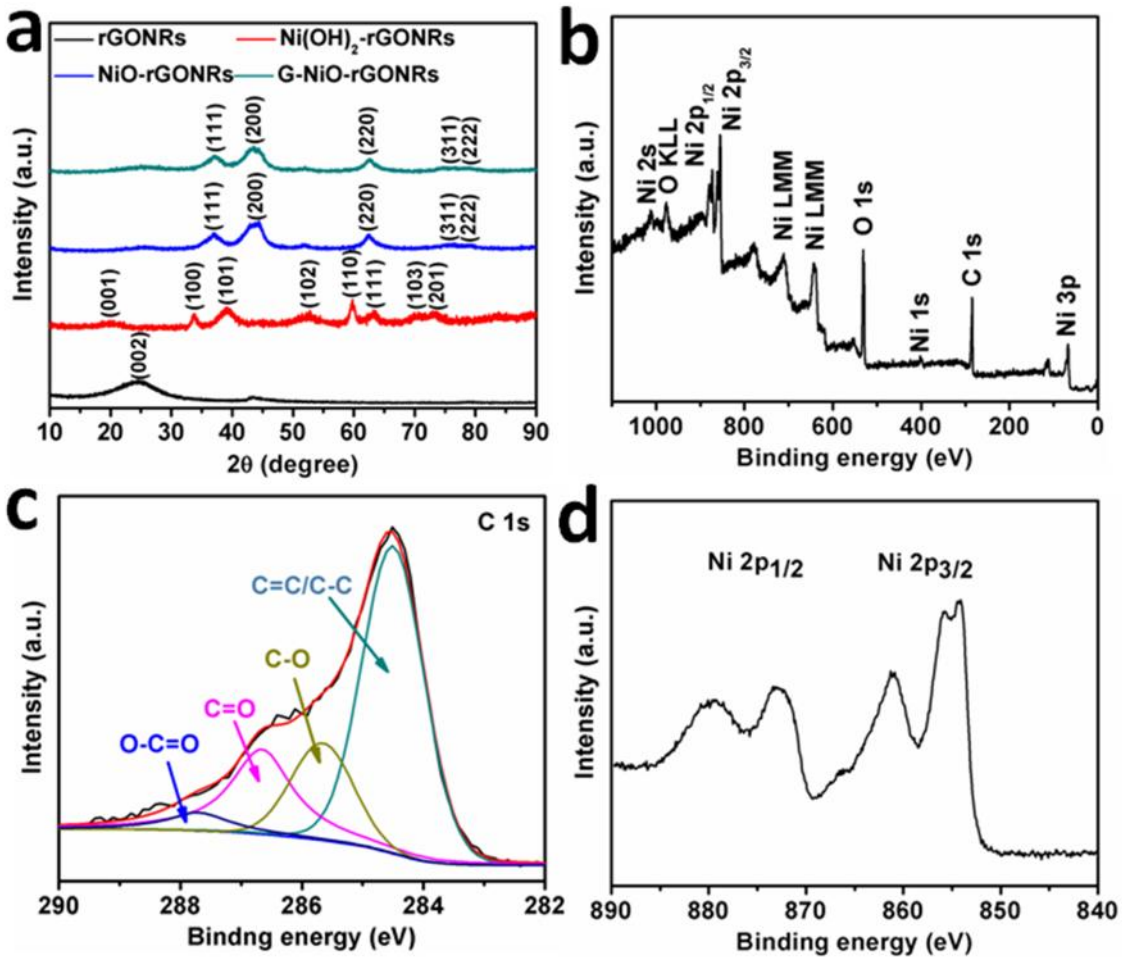

Figure 6.3. (a) XRD patterns of rGONRs, Ni(OH)2-rGONRs, NiO-rGONRs, and G-NiO-rGONRs. (b) XPS spectrum of G-NiO-rGONRs.

Figure 6.4 is the thermogravimetric analysis (TGA) of G-NiO-rGONRs and NiO-rGONRs. Before graphene wrapping, the NiO content of the NiO-rGONRs was 73%. After graphene wrapping, the NiO content in the composite decreased to 56%.

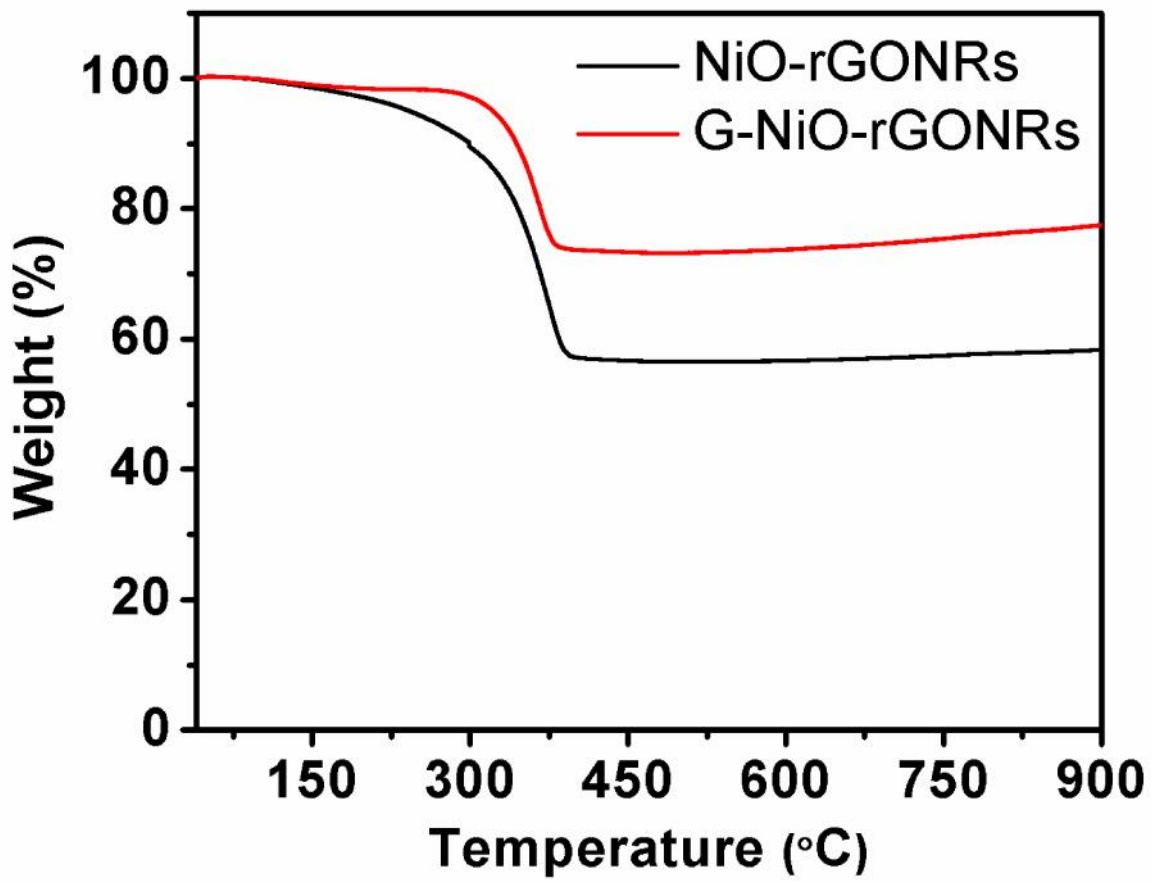

Figure 6.4. TGA curves of G-NiO-rGONRs with 56% NiO content and NiO-rGONRs with 73% NiO content recorded in Air at a heating rate of 5 °C min-1.

6.3.2. Electrochemical evaluation

The electrochemical performance of G-NiO-rGONRs as anodes in LIBs was studied in the potential window of 0.01 to 3.0 V. Figure 6.5a shows the cyclic voltammetry (CV) and the first five discharge-charge profiles of G-NiO-rGONRs. The first cathodic scan started at the open circuit potential. The cathodic peak at 0.36 V in the first cycle corresponds to the reaction of NiO with lithium to form Ni and Li_2O with the characteristic solid electrolyte interface (SEI) formation on the surface of the electrode.

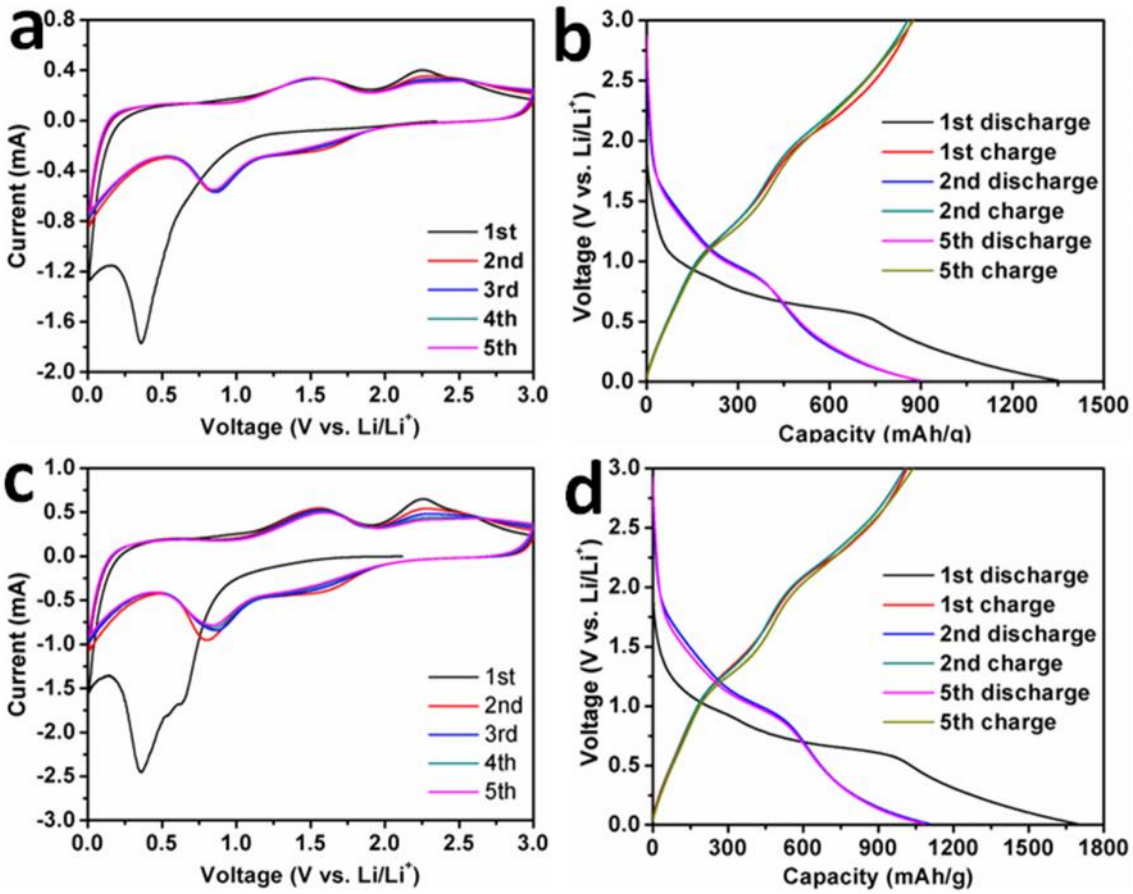

Figure 6.5. Cyclic voltammetry curves of G-NiO-rGONRs (a) and NiO-rGONRs (b) in the potential range of 0.01 and 3.0 V (vs. Li/Li+) at the scan rate of 0.4 mV/s. The first five discharge charge curves of G-NiO-rGONRs (b) and NiO-rGONRs (d) in the potential range of 0.01 and 3.0 V (vs. Li/Li$^+$) at the current density of 0.1 A/g.

There were two broad anode peaks at 1.53 V and 2.52 V, indicating the decomposition of SEI and the electrochemical oxidation reaction, respectively.[34,36,37] During the first cycle, the formed Ni nanoparticles and reformed NiO enhance the reactivity and reduce the overpotential.[38-39] Therefore, the cathodic peaks shifted to 0.85 V in the following cycles. This was further shown by the discharge-charge profiles of G-NiO-rGONRs in Figure 6.5b. There were two plateaus, ~ 1.50 V and 2.50 V in the charge process, corresponding to the

anode peaks in the CV. There was one obvious plateau around 0.85 V in the discharge process. NiO-rGONRs displayed similar phenomena as shown in Figure 6.5c,d. The first discharge capacities of NiO-rGONRs and G-NiO-rGONRs had higher values than their theoretical capacities, which might result from the irreversible reaction of the electrodes, the SEI formation on the surface of the electrodes, and the decomposition of electrolyte.[34]

The rate and cycling performance of the G-NiO-rGONRs were studied at the same potential window. Stable capacity at different current densities as observed as shown in Figure 6.6a. When the current density was reduced from 1.0 A/g to 0.1 A/g, the capacity value of G-NiO-rGONRs not only returned, but more importantly, it increased with the increase in number of cycles at the same current density. For example, the discharge capacity value increased to 977 mAh/g at the 55^{th} cycle from 900 mAh/g at the 2^{nd} cycle in a current density of 0.1 A/g. This data demonstrates the good rate performance of G-NiO-rGONRs. Figure 6.6b shows the cycling performance of G-NiO-rGONRs and NiO-rGONRs used as anodes in LIBs at a current density of 0.4 A/g. For NiO-rGONRs, the discharge capacity gradually decreased to 830 mAh/g at the 20^{th} cycle from 938 mAh/g at the second cycle. Then, the capacity decreased quickly to 185 mAh/g at 100^{th} cycle, with only 20% capacity remaining. After graphene wrapping of NiO-rGONRs, the discharge capacity of G-NiO-rGONRs decreased to 740 mAh/g at 5^{th} cycle from 791 mAh/g at the second cycle. Then, the capacity increased with the increase in cycle numbers and reached 801 mAh/g at the 100^{th} cycle. Based on this result, the hierarchical structure of the composite greatly improves the cycling performance of G-NiO-rGONRs in LIBs.

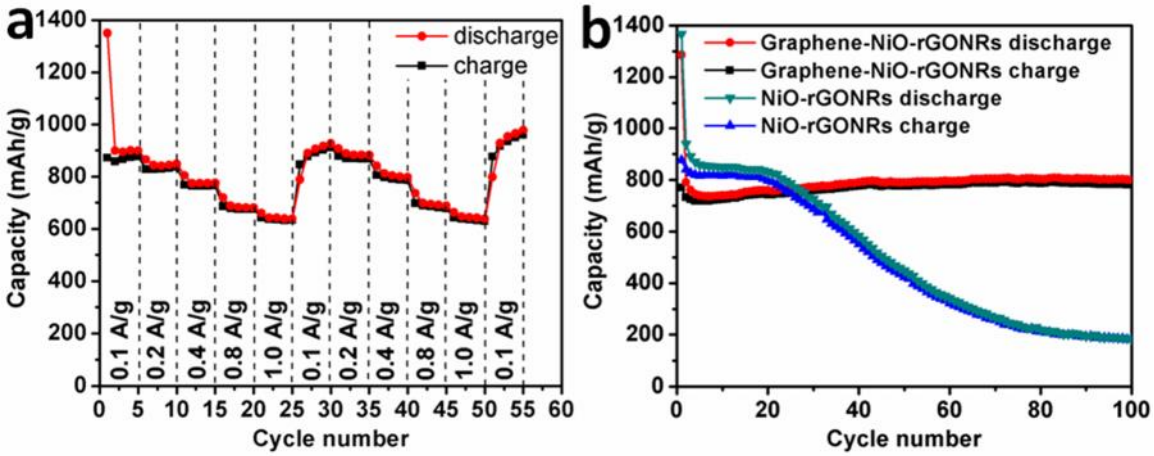

Figure 6.6. (a) Rate performance of G-NiO-rGONRs at various current densities from 0.1 A/g to 1.0 A/g with respect to the cycle numbers. (b) Cycling performance of G-NiO-rGONRs at the current density of 0.4 A/g.

As shown in Figure 6.7a, electrochemical impedance spectroscopy (EIS) experiments were carried out in order to understand the enhanced electrochemical performance of the G-NiO-rGONRs electrode. Figure 6.7b, shows the equivalent circuit model of this system.[34,40-41] In Figure 6.7a, the compressed semicircle in the high-medium frequency region is a result of the Li^+ ion transport through the SEI film and the interfacial charge transfer reaction ($R_{(SEI+ct)}$), combined with the electrochemical double-layer capacitive behavior *CPE* and C_{dl}, respectively. The sloping line was attributed to the solid-state Li diffusion into the active materials (Z_w).[42] The experimental Nyquist plots were modeled based on the equivalent circuit and the impedance parameters that were fit to the data are listed in Table 6.1. The $R_{(SEI+ct)}$ (139.40 Ω) of G-NiO-rGONRs was much lower than that of NiO-rGONRs ($R_{(SEI+ct)}$ = 219.70 Ω). This demonstrated that the incorporation of graphene can greatly increase the electrical conductivity, resulting in significant improvement in the electrochemical performance.

Table 6.1. The EIS simuation parameters of NiO-rGONRs and G-NiO-rGONRs.

Active material	R_s (Ω)	*CPE* (μF)	$R_{(SEI+dl)}$ (Ω)	Z_w (Ω)	C_{int}(mF)
G-NiO-rGONRs	8.21	80.79	139.40	216.97	0.20
NiO-rGONRs	2.40	20.53	219.70	21.21	41.13

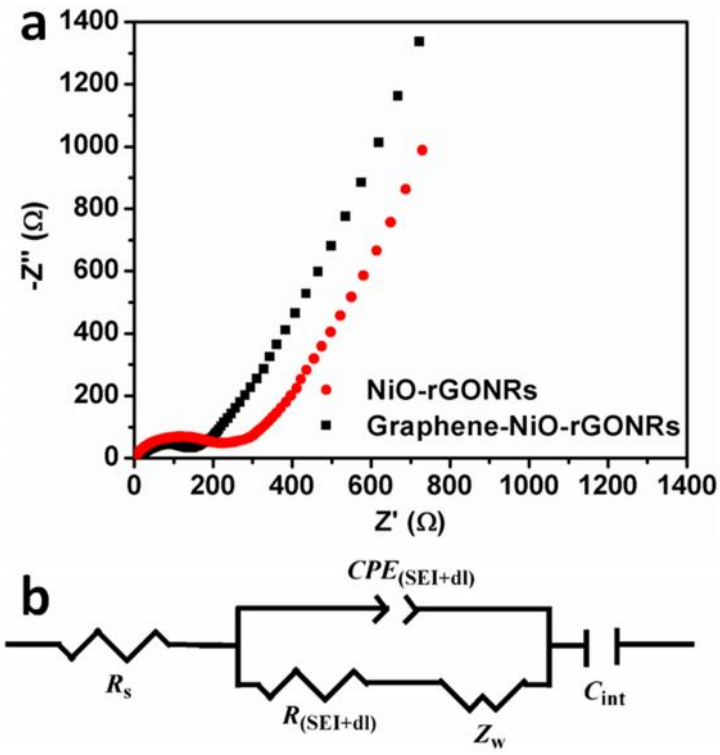

Figure 6.7. (a) Nyquist plots of NiO-rGONRs and G-NiO-rGONRs. (b) Equivalent circuit that is used to fit the experimental data of NiO-rGONRs and G-NiO-rGONRs.

6.4. Conclusion

In summary, we successfully designed and synthesized a unique hierarchical structured composite of G-NiO-rGONRs. In this composite, graphene flakes tightly sandwiched nanosized NiO that was grown directly on the rGONRs. Electrochemical

experiments show that the composite has a high specific capacity, good rate performance, and grealyt improved cycling stability when used as an anode material due to the synergic effect between the graphene, rGONRs, and NiO. The electrochemical performance of the composite shows this it is an potential component that would improve the electrochemical stability of the electrode materials for LIBs. The strategy used here might be appropriate for other anode materials synthesis to produce improved electrochemical performance in LIBs.

6.5. References

1. Li, L.; Kovalchuk, A.; Peng, Z. W.; Gao, C. T.; Zhong, Q. F.; Yang, Y.; Fei H. L.; Tour, J. M. Graphene-NiO-reduced Graphene Oxide Nanoribbons Sandwich Structured Composite As Lithium Ion Battery Anode. **In preparation.** (L.L. conceived and designed the experiments. L.L. and K.A. prepared the materials. L.L., P.Z.W., G.C.T., and Z.Q.F. performed material characterization. L.L., Y.Y., and F.H.L. tested the devices. L.L. wrote the paper. Finally, T.J.M. oversaw all research phases, provided regular guidance to the research and revised the manuscript. All authors discussed and commented on the manuscript.)

2. Dunn, B.; Kamath, H.; Tarascon, J. M. Electrical Energy Storage for the Grid: A Battery of Choices. *Science*, **2011**, *334*, 928–935.

3. Su, Y.; Li, S.; Wu, D.; Zhang, F.; Liang, H.; Gao, P.; Cheng, C.; Feng, X. Two-Dimensional Carbon-Coated Graphene/Metal Oxide Hybrids for Enhanced Lithium Storage. *ACS Nano* **2012**, *6*, 8349-8356.

4. Etacheri, V.; Marom, R.; Elazari, R.; Salitra, G.; Aurbach, D. Challenges in the development of advanced Li-ion batteries: a review. *Energy Environ.Sci.* **2011**, *4*, 3243-3262.

5. Tarascon, J.-M.; Armand, M. Issues and Challenges Facing Rechargeable Lithium Batteries. *Nature* **2001,** *414*, 359-367.

6. Wang, B.; Li, X.; Zhang, X.; Luo, B.; Jin, M.; Liang, M.; Dayeh, S. A.; Picraux, S. T.; Zhi, L. Adaptable Silicon-Carbon Nanocables Sandwiched between Reduced Graphene Oxide Sheets as Lithium Ion Battery Anodes. *ACS Nano* **2013**, *7*, 1437-1445.

7. Reddy, M. V.; Subba Rao, G. V.; Chowdari, B. V. R. Metal Oxides and Oxysalts as Anode Materials for Li Ion Batteries. *Chem. Rev.* **2013**, *113*, 5364-5457.

8. Poizot, P.; Laruelle, S.; Grugeon, S.; Dupont, L.; Tarascon, J. M. Nano-Sized Transition-Metal Oxides as Negative-Electrode Materials for Lithium-Ion Batteries. *Nature* **2000**, 407, 496–499.

9. Cabana, J.; Monconduit, L.; Larcher, D.; Palacín, M. R. Beyond Intercalation-Based Li-Ion Batteries: The State of the Art and Challenges of Electrode Materials Reacting Through Conversion Reactions. *Adv. Mater.* **2010**, *22*, E170-E192.

10. Wen, W.; Wu, J.-M. Eruption Combustion Synthesis of NiO/Ni Nanocomposites with Enhanced Properties for Dye-Absorption and Lithium Storage. *ACS Appl. Mater. Interfaces* **2011,** *3*, 4112-4119.

11. Huang, Y.; Huang, X.-l.; Lian, J.-s.; Xu, D.; Wang, L.-m.; Zhang, X.-b., Self-assembly of ultrathin porous NiO nanosheets/graphene hierarchical structure for high-capacity and high-rate lithium storage. *Journal of Materials Chemistry* **2012,** *22*, 2844-2847.

12. Needham, S. A.; Wang, G. X.; Liu, H. K., Synthesis of NiO nanotubes for use as negative electrodes in lithium ion batteries. *Journal of Power Sources* **2006,** *159*, 254-257.

13. Zou, Y.; Wang, Y., NiO nanosheets grown on graphene nanosheets as superior anode materials for Li-ion batteries. *Nanoscale* **2011,** *3*, 2615-2620.

14. Zhuo, L.; Wu, Y.; Zhou, W.; Wang, L.; Yu, Y.; Zhang, X.; Zhao, F., Trace Amounts of Water-Induced Distinct Growth Behaviors of NiO Nanostructures on Graphene in CO2-Expanded Ethanol and Their Applications in Lithium-Ion Batteries. *Acs Appl Mater Inter* **2013,** *5*, 7065-7071.

15. Hwang, S.-G.; Kim, G.-O. K.; Yun, S.-R.; Ryu, K.-S. NiO nanoparticles with plate structure grown on graphene as fast charge–discharge anode material for lithium ion batteries. *Electrochim. Acta* **2012**, *78*, 406-411.

16. Cheng, M.-Y.; Hwang, B.-J. Mesoporous carbon-encapsulated NiO nanocomposite negative electrode materials for high-rate Li-ion battery. *J. Power Sources* **2010**, *195*, 4977-4983.

17. Hassan, M. F.; Rahman, M. M.; Guo, Z.; Chen, Z.; Liu, H., SnO_2-NiO-C nanocomposite as a high capacity anode material for lithium-ion batteries. *J. Mater. Chem.* **2010**, *20*, 9707-9712.

18. Xiong, Q.-q.; Tu, J.-p.; Xia, X.-h.; Zhao, X.-y.; Gu, C.-d.; Wang, X.-l. A three-dimensional hierarchical Fe_2O_3@NiO core/shell nanorod array on carbon cloth: a new class of anode for high-performance lithium-ion batteries. *Nanoscale* **2013**, *5*, 7906-7912.

19. Choi, S. H.; Lee, J.-H.; Chan Kang, Y. One-pot rapid synthesis of core-shell structured NiO@TiO_2 nanopowders and their excellent electrochemical properties as anode materials for lithium ion batteries. *Nanoscale* **2013**, *5*, 12645-12650.

20. Wen, W.; Wu, J.-M.; Cao, M.-H. NiO/Ni powders with effective architectures as anode materials in Li-ion batteries. *J. Mater. Chem. A* **2013**, *1*, 3881-3885.

21. Wu, H.; Xu, M.; Wu, H.; Xu, J.; Wang, Y.; Peng, Z.; Zheng, G. Aligned NiO nanoflake arrays grown on copper as high capacity lithium-ion battery anodes. *J. Mater. Chem.* **2012,** *22*, 19821-19825.

22. Qiu, M. C.; Yang, L. W.; Qi, X.; Li, J.; Zhong, J. X. Fabrication of Ordered NiO Coated Si Nanowire Array Films as Electrodes for a High Performance Lithium Ion Battery. *ACS Appl. Mater. Interfaces* **2010**, *2*, 3614-3618.

23. Mai, Y. J.; Xia, X. H.; Chen, R.; Gu, C. D.; Wang, X. L.; Tu, J. P. Self-supported nickel-coated NiO arrays for lithium-ion batteries with enhanced capacity and rate capability. *Electrochim. Acta* **2012**, *67*, 73-78.

24. Wang, X.; Yang, Z.; Sun, X.; Li, X.; Wang, D.; Wang, P.; He, D. NiO nanocone array electrode with high capacity and rate capability for Li-ion batteries. *J. Mater. Chem.* **2011**, *21*, 9988-9990.

25. Wang, X.; Li, X.; Sun, X.; Li, F.; Liu, Q.; Wang, Q.; He, D. Nanostructured NiO electrode for high rate Li-ion batteries. *J. Mater. Chem.* **2011,** *21*, 3571-3573.

26. Liu, L.; Li, Y.; Yuan, S.; Ge, M.; Ren, M.; Sun, C.; Zhou, Z. Nanosheet-Based NiO Microspheres: Controlled Solvothermal Synthesis and Lithium Storage Performances. *J. Phys.Chem. C* **2009**, *114*, 251-255.

27. Higginbotham, A. L.; Kosynkin, D. V.; Sinitskii, A.; Sun, Z.; Tour, J. M. Lower-Defect Graphene Oxide Nanoribbons from Multiwalled Carbon Nanotubes. *ACS Nano* **2010**, *4*, 2059-2069.

28. Li, D.; Muller, M.B.; Gilje, S.; Kaner, R. B.; Wallace, G. G., Processable Aqueous Dispersion of Graphene Nanosheets. *Nat. Nano.* **2008**, *3*, 101-105.

29. Lei, Z.; Shi, F.; Lu, L. Incorporation of MnO_2-Coated Carbon Nanotubes between Graphene Sheets as Supercapacitor Electrode. *ACS Appl. Mater. Interfaces* **2012**, *4*, 1058-1064.

30. Li, L.; Raji, A.-R. O.; Tour, J. M. Graphene-Wrapped MnO_2-Graphene Nanoribbons as Anode Materials for High-Performance Lithium Ion Batteries. *Adv. Mater.* **2013,** *25*, 6298-6302.

31. Li, J.; Yang, M.; Wei, J.; Zhou, Z. Preparation and electrochemical performances of doughnut-like $Ni(OH)_2$-$Co(OH)_2$ composites as pseudocapacitor materials. *Nanoscale* **2012,** *4*, 4498-4503.

32. Vijayakumar, S.; Nagamuthu, S.; Muralidharan, G. Supercapacitor Studies on NiO Nanoflakes Synthesized Through a Microwave Route. *ACS Appl. Mater. Interfaces* **2013**, *5*, 2188-2196.

33. Varghese, B.; Reddy, M. V.; Yanwu, Z.; Lit, C. S.; Hoong, T. C.; Subba Rao, G. V.; Chowdari, B. V. R.; Wee, A. T. S.; Lim, C. T.; Sow, C. H. Fabrication of NiO Nanowall Electrodes for High Performance Lithium Ion Battery. *Chem. Mater.* **2008,** *20,* 3360-3367.

34. Zhou, G.; Wang, D.-W.; Yin, L.-C.; Li, N.; Li, F.; Cheng, H.-M. Oxygen Bridges between NiO Nanosheets and Graphene for Improvement of Lithium Storage. *ACS Nano* **2012,** *6,* 3214-3223.

35. Peck, M. A.; Langell, M. A., Comparison of Nanoscaled and Bulk NiO Structural and Environmental Characteristics by XRD, XAFS, and XPS. *Chem. Mater.* **2012**, *24*, 4483-4490.

36. Huang, X. H.; Tu, J. P.; Zhang, B.; Zhang, C. Q.; Li, Y.; Yuan, Y. F.; Wu, H. M. Electrochemical properties of NiO-Ni nanocomposite as anode material for lithium ion batteries. *J. Power Sources* **2006**, *161*, 541-544.

37. Zhang, G.; Chen, Y.; Qu, B.; Hu, L.; Mei, L.; Lei, D.; Li, Q.; Chen, L.; Li, Q.; Wang, T. Synthesis of mesoporous NiO nanospheres as anode materials for lithium ion batteries. *Electrochim. Acta* **2012**, *80*, 140-147.

38. Zai, J.; Yu, C.; Tao, L.; Xu, M.; Xiao, Y.; Li, B.; Han, Q.; Wang, K.; Qian, X. Synthesis of Ni-doped NiO/RGONS nanocomposites with enhanced rate capabilities as anode materials for Li ion batteries. *CrystEngComm* **2013**, *15*, 6663-6671.

39. Poizot, P.; Laruelle, S.; Grugeon, S. Dupont, L.; Tarascon, J M. Nano-sized transition-metal oxides as negative-electrode materials for lithium-ion batteries *Nature* **2000**, *407*, 496.

40. Ang, W. A.; Gupta, N.; Prasanth, R.; Madhavi, S. High-Performing Mesoporous Iron Oxalate Anodes for Lithium-Ion Batteries. *ACS Appl. Mater. Interfaces* **2012**, *4*, 7011-7019.

41. Lin, Y.-M.; Abel, P. R.; Heller, A.; Mullins, C. B. α-Fe_2O_3 Nanorods as Anode Material for Lithium Ion Batteries. *J. Phys. Chem. Lett.* **2011**, *2*, 2885-2891.

42. Qian, D.; Xu, B.; Cho, H. M.; Hatsukade, T.; Carroll, K. J.; Meng, Y. S. Lithium Lanthanum Titanium Oxides: A Fast Ionic Conductive Coating for Lithium-Ion Battery Cathodes. *Chem. Mater.* **2012**, *24*, 2744-2751.

Chapter 7

Enhanced Cycling Stability of Lithium Ion Batteries Using Graphene-Fe_3O_4-Graphene Nanoribbons as Anode Materials

This chapter was entirely copied from reference 1.

7.1. Introduction

Rechargeable lithium ion batteries (LIBs) are considered among the most practical and effective technologies for electrochemical energy storage.[2,3] LIBs have attracted significant attention due to their wide range of applications including uses in electric vehicles and mobile communications.[4,5] With rapidly increasing demand for improved LIBs, the development of energy storage devices with high energy density, power density, and excellent cycling performance has become critical. Numerous efforts have been devoted to develop new electrode materials to meet these demands including using iron oxide (Fe_3O_4) which has attracted great attention due to its high theoretical reversible

capacity (928 mAh/g), low cost, natural abundance, and eco-friendly properties.[2,6-10] However, the volume expansion and contraction during reversible discharge/charge processes leads to pulverization of Fe_3O_4 electrodes, resulting in fast capacity decay and poor cycle life. Therefore, development of Fe_3O_4-based anodes with high capacity and enhanced cycling stability is necessary.

To address these problems, various strategies have been developed to improve the electrical conductivity while enhancing the structural stability of Fe_3O_4-based anode materials. One strategy is to prepare nanostructured materials that can relax the strain caused by the volume variation during discharge/charge processes and thereby improving the rate performance due to the short diffusion length of nanosized materials.[3,11] Nanomaterials prepared on different carbon substrates, such as carbon nanotubes,[12-15] graphene,[8,10,16-20] and amorphous carbon,[3,21,22] not only improve electrical conductivity, but also mitigate volume variation, resulting in improved cycle stability of the composites. Another strategy is carbon coatings or encapsulation of active materials which improves electrical conductivity and prevents their exfoliation of the inner active materials and aggregation of the active materials.[3,8,23-27] However, since the cycling stability of Fe_3O_4-based anode materials is still reduced by pulverization of the active materials, preparation of Fe_3O_4-based anode materials with a specialized structure that prevents the negative effect of pulverization is still challenging and necessary.

In this study, we combined these design criteria into a hierarchical structured composite of the graphene-wrapped Fe_3O_4-graphene nanoribbons (G-Fe_3O_4-GNRs). In this structure, reduced graphene oxide and GNRs are in good electrical contact with Fe_3O_4, which improves composite conductivity and also buffers volume changes to prevent loss

of Fe_3O_4 during Li-ion conversion, thus improving the overall electrochemical stability. More importantly, reduced graphene oxide is a softer coating layer when compared to other carbon coatings that are formed through calcinations or encapsulation of the active materials.[3,8,21] The soft graphene-based layer would alleviate the problems of having a more rigid carbon framework, which could not effectively release strain caused by volume changes and impede the lithium ions in the core of the active material. G-Fe_3O_4-GNRs as anode materials demonstrate high capacity, good rate performance, and improved cycling performance. Thus G-Fe_3O_4-GNRs are a superb candidate composite for use as an anode electrode material for energy storage of LIBs.

7.2. Experiments

7.2.1. Materials synthesis

7.2.1.1. Synthesis of Fe_3O_4-GNRs

GNRs were prepared by treatment of multiwalled carbon nanotubes with NaK in 1,2-dimethoxyethane and quenching of the reaction with MeOH as described previously.[28] Fe_3O_4-GNRs were synthesized according to the multi-step protocol. Two intercalation steps are needed to achieve high content of Fe_3O_4 in the composite. The Fe_3O_4-GNRs were synthesized by adding 100 mg of GNRs and 300 mg of $FeCl_3$ to a glass ampule that was sealed under vacuum using an acetylene torch. The ampule was placed in an oven at 350 °C for 24 h to afford intercalation of the $FeCl_3$ into the GNRs. The $FeCl_3$-GNRs was transferred into a 250 mL round bottom glass flask, sealed and carefully purged with nitrogen. Next, 35 mL of freshly distilled 1,2-dimethoxyethane (DME) and 1 mL of

Na/K alloy were added to the flask and the solution was stirred for 15 h at room temperature. The reaction was quenched with 30 mL of methanol, and then carefully filtered by vacuum filtration and washed with DI water, methanol, acetone and diethyl ether and dried under vacuum (~ 7 mmHg) at 100 °C for 24 h. 426 mg of this product was placed in a glass ampule with 600 mg of $FeCl_3$, sealed under vacuum and placed at 350 °C in the oven for 24 h for final intercalation. 35 mL of freshly distilled DME and 1.2 mL Na/K alloy were carefully added and reacted at room temperature with stirring for 20 h. 30 mL of methanol was added to quench the reaction mixture. 778 mg of Fe_3O_4-GNRs was obtained after vacuum filtration followed by washing sequentially with water, methanol, acetone and diethyl ether, followed by drying in a vacuum oven (~ 7 mmHg) at 100 °C for 24 h. Fe_3O_4-G, Fe_3O_4-GO, and Fe_3O_4 was prepared using the same procedure without the addition of GNRs.

7.2.1.2. Synthesis of G-Fe_3O_4-GNRs

G-Fe_3O_4-GNRs were synthesized in two steps. The first step was to positively charge Fe_3O_4-GNRs. 70 mg of Fe_3O_4-GNRs was dispersed in 70 mL of D.I. water containing 0.7 mL of poly(diallyldimethylammonium chloride) (PDADMAC, Sigma-Aldrich). After stirring for 5 h at room temperature, positively charged PDADMAC-Fe_3O_4-GNRs (62 mg) was obtained *via* vacuum filtration followed by washing with 500 mL of D.I. water, 100 mL of ethanol, and then drying in a vacuum oven (~ 7 mmHg) at 80 °C for 10 h. Next, 60 mg of PDADMAC-Fe_3O_4-GNRs was dispersed in 60 mL of D.I. water by ultrasonication (Cole-Parmer Instrument company, 17 W) and the solution pH was adjusted to ~ 8 using 1 M ammonia in ethanol. Reduced graphene oxide was prepared by reduction of 30 mg of graphene oxide in 60 mL of D.I. water adjusted to pH ~ 8 using 1 M ammonia

with 33.9 µL of hydrazine. The PDADMAC-Fe_3O_4-GNRs suspension was added to the reduced graphene oxide solution and the mixture was stirred for 5 h. 60 mg of G-Fe_3O_4-GNRs was obtained after vacuum filtration followed by washing sequentially with 500 mL of D.I. water and 100 mL of ethanol, followed by drying in a vacuum oven (~ 7 mmHg) at 80 °C for 10 h. G-Fe_3O_4 was prepared using the same method as above.

7.2.2. Materials characterization

Products were characterized by X-ray diffraction (XRD, Rigaku D/Max Ultima II); X-ray photoelectron spectroscopy (XPS, PHI Quantera); scanning electron microscopy (SEM, JEOL 6500); thermogravimetric analysis (TGA, TA Instruments, Q50); and transmission electron microscopy (TEM, JEM2100F TEM).

7.2.3. Device fabrication

The anode was prepared by mixing 80 wt% of the active composite, 10 wt% of carbon black (Super P), and 10 wt% of polyvinylidene difluoride (PVDF, Alfa Aesar) dissolved in *N*-methyl-2-pyrrolidone (NMP, Sigma-Aldrich) to form a slurry that was then coated onto a copper foil substrate. Electrochemical tests were performed using a CR2032 battery with a lithium metal foil as the counter electrode. The electrolyte was 1 M $LiPF_6$ in ethylene carbonate and diethyl carbonate (EC: DEC, 1:1 in volume) and the separator was a Celgard 2300 membrane.

7.2.4. Electrochemical measurement

CV tests were done on a CHI660D electrochemical station at a current density of 0.40 mV/s; EIS measurements were carried out on the CHI660D at an open circuit potential

from 100 kHz to 10 MHz, and the galvanostatic discharge charge tests were carried out on a LAND CT2001A battery system at room temperature. Capacity values were based on the mass of the active composite.

7.3. Results and Discussion

7.3.1. Synthesis and structure analysis

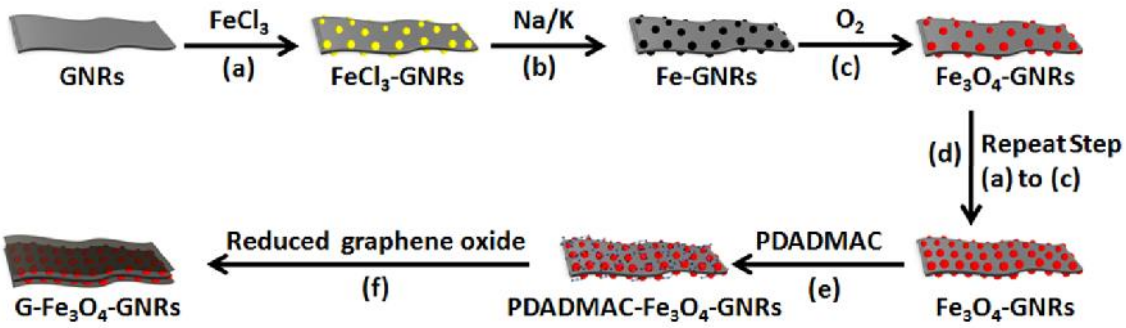

Figure 7.1. Schematic illustration of the synthesis of G-Fe3O4-GNRs.

The synthesis of G-Fe_3O_4-GNRs is depicted in Figure 7.1. GNRs are scalable and have high surface area and electrical conductivity, making them a suitable template for loading Fe_3O_4. The GNRs were prepared using a previously described solution-based chemical splitting of multi-walled carbon nanotubes in 1,2-dimethoxyethane.[28] Fe_3O_4-GNRs were synthesized according to a multi-step protocol, where $FeCl_3$ is loaded onto GNRs forming $FeCl_3$-GNRs, which is then reduced by Na/K alloy to form Fe-GNRs and finally oxidized to Fe_3O_4-GNRs under ambient conditions.[28] Next, Fe_3O_4-GNRs were dispersed in an aqueous solution of poly(diallyldimethylammonium chloride) (PDADMAC) to form positively charged PDADMAC-Fe_3O_4-GNRs. Finally, G-Fe_3O_4-

GNRs were obtained through electrostatic interaction between PDADMAC-Fe_3O_4-GNRs and reduced graphene oxide.[30-32] Reduced graphene oxide-Fe_3O_4 (G-Fe_3O_4), Fe_3O_4-reduced graphene oxide (Fe_3O_4-G), and Fe_3O_4-Graphene oxide (Fe_3O_4-GO) as control samples were also prepared using the same procedures.

The morphologies of G-Fe_3O_4-GNRs, Fe_3O_4-GNRs, G-Fe_3O_4, Fe_3O_4-G, Fe_3O_4-GO, Fe_3O_4, and GNRs were studied by scanning electron microscopy (SEM) and transmission electron microscopy (TEM). Figure 7.2a,b show SEM images of Fe_3O_4-GNRs at different magnifications where Fe_3O_4 had grown around GNRs (Figure 7.3a,b). Figure 7.2c shows a TEM image of one strip of Fe_3O_4-GNRs, where Fe_3O_4 nanoparticles have uniformly coated the GNR surface. High resolution TEM imaging of Fe_3O_4-GNRs (Figure 7.2d) shows that the diameter of Fe_3O_4 nanoparticles is ~ 10 nm. Without GNRs, Fe_3O_4 is consistent with different size particles and flakes as shown in Figure 7.3c,d, demonstrating GNRs induce the formation of uniform Fe_3O_4 nanoparticles. Figure 7.3e,f show SEM images of G-Fe_3O_4 at different magnifications, indicating Fe_3O_4 is in reduced graphene oxide. TEM images of G-Fe_3O_4 further show the Fe_3O_4 in the form of nanoparticles and flakes in reduced graphene oxide (Figure 7.3g-h). Figure 7.3i,j show SEM images of Fe_3O_4-G at different magnifications indicating Fe_3O_4 in graphene, which is further confirmed by TEM images in Figure 7.3k,l. Fe_3O_4-GO demonstrates the similar morphology as shown in Figure 7.3m-p. Figure 7.2e shows an SEM image of G-Fe_3O_4-GNRs, where reduced graphene oxide serves as a binder to connect the separated Fe_3O_4-GNRs together forming the entirety of G-Fe_3O_4-GNRs. The ribbon-like morphology of Fe_3O_4-GNRs was still observed within G-Fe_3O_4-GNRs (Figure 7.2f).

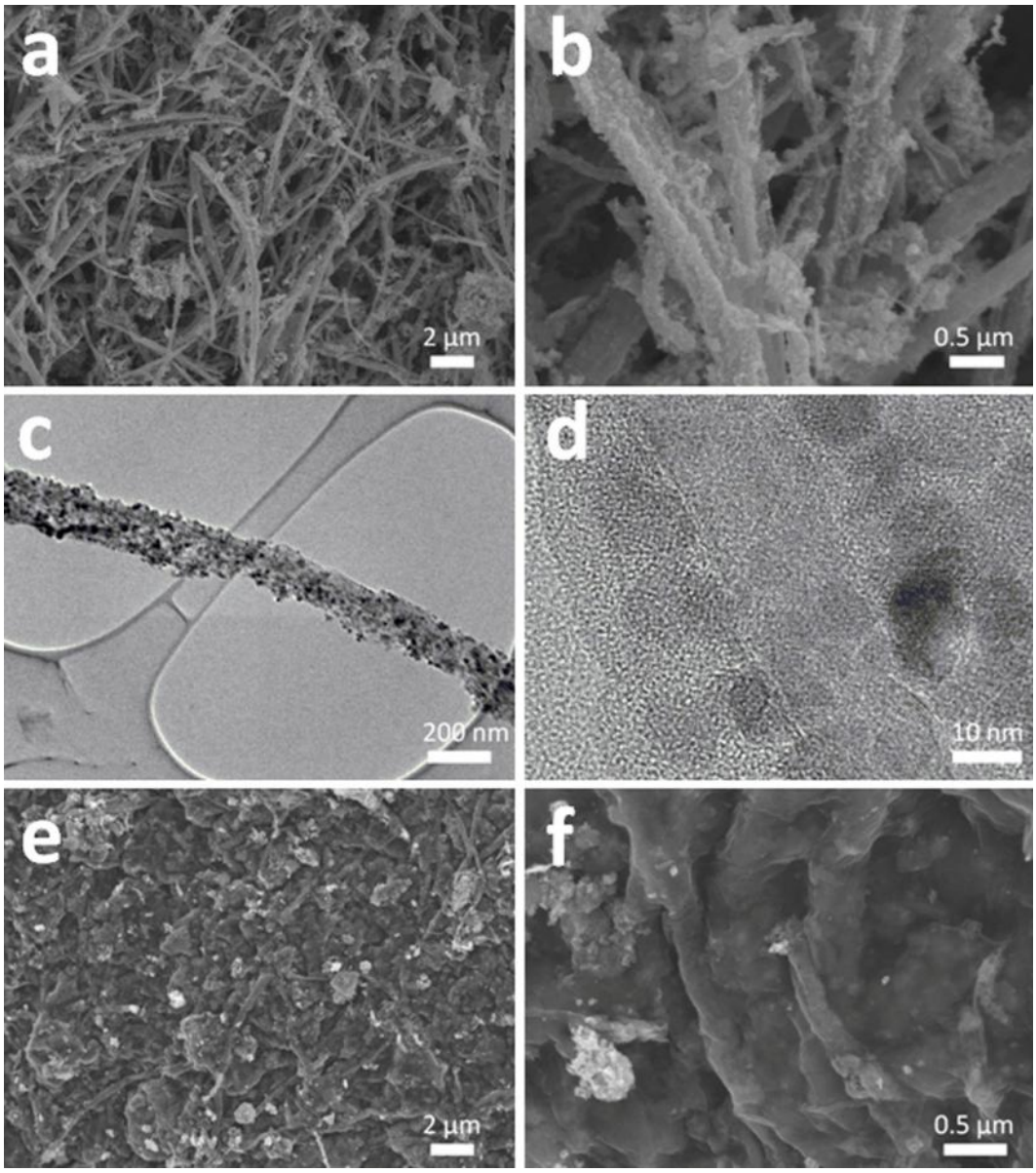

Figure 7.2. (a, b) SEM images of Fe3O4-GNRs at different magnifications. (c, d) TEM images of Fe3O4-GNRs at different magnifications. (e, f) SEM images of G-Fe3O4-GNRs at different magnifications.

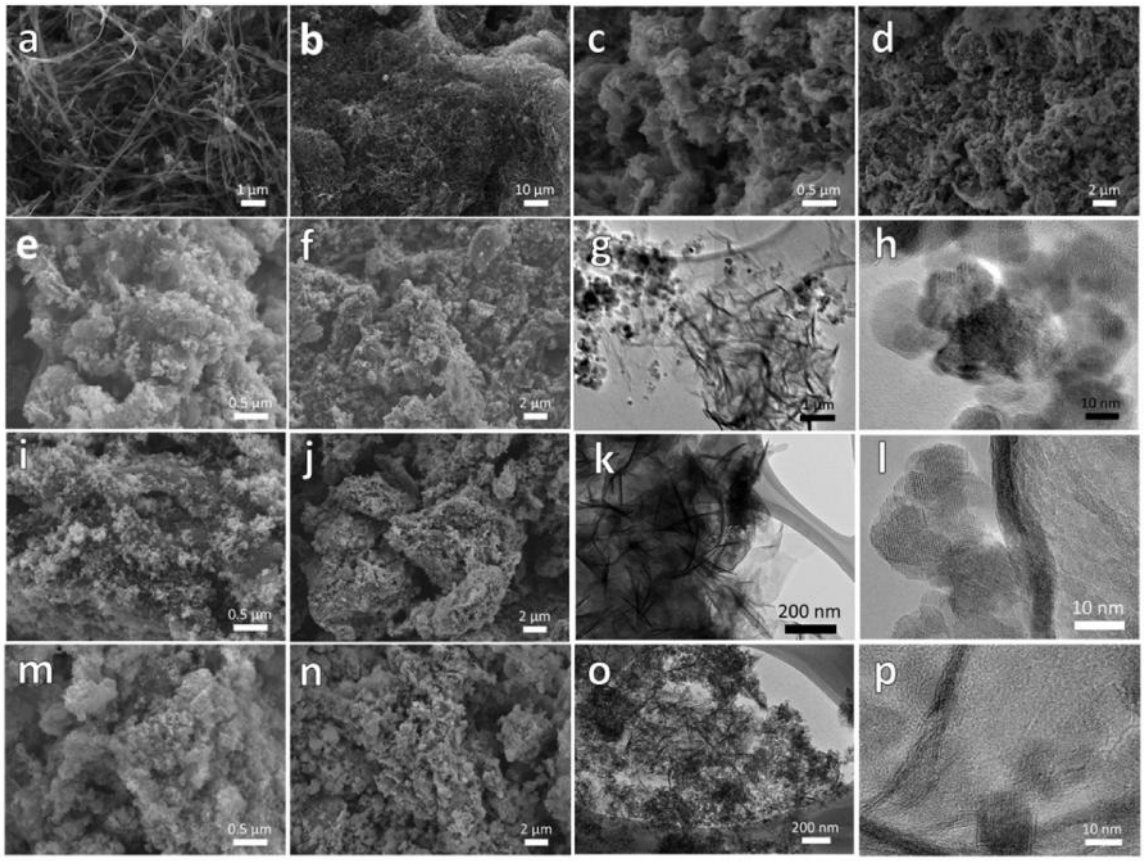

Figure 7.3. (a,b) SEM images of GNRs at different magnifications, showing GNRs with widths of ~ 300 nm and a length of ~ 5 µm that were used in the syntheses of the Fe_3O_4-GNRs and G-Fe_3O_4-GNRs. (c,d) SEM images of Fe_3O_4 at different magnifications, showing Fe_3O_4 with different size particles and flakes, which are not uniform. (e,f) SEM images of G-Fe_3O_4 at different magnifications. (g,h) TEM images of G-Fe_3O_4 at different magnifications, showing the morphology of Fe_3O_4 in graphene. (i,j) SEM images of Fe_3O_4-G at different magnifications. (k,l) TEM images of Fe_3O_4-G at different magnifications, showing the morphology of Fe_3O_4 in graphene. (m,n) SEM images of Fe_3O_4-GO at different magnifications. (o,p) TEM images of Fe_3O_4-GO at different magnifications, showing the morphology of Fe_3O_4 in graphene.

X-ray diffraction (XRD) and X-ray photoelectron spectroscopy (XPS) were also used to characterize the composites. Figure 7.4a showed the XRD patterns of GNRs, Fe_3O_4-GNRs, and G-Fe_3O_4-GNRs. The GNRs demonstrated the strong diffraction peak

(002) of graphite at 26.5°.[24,33] The XRD pattern showed that the iron oxide growing from the GNRs was Fe_3O_4.[34-36] Both the characteristic peaks of GNRs and Fe_3O_4 can be observed from the XRD patterns of Fe_3O_4-GNRs and G-Fe_3O_4-GNRs.

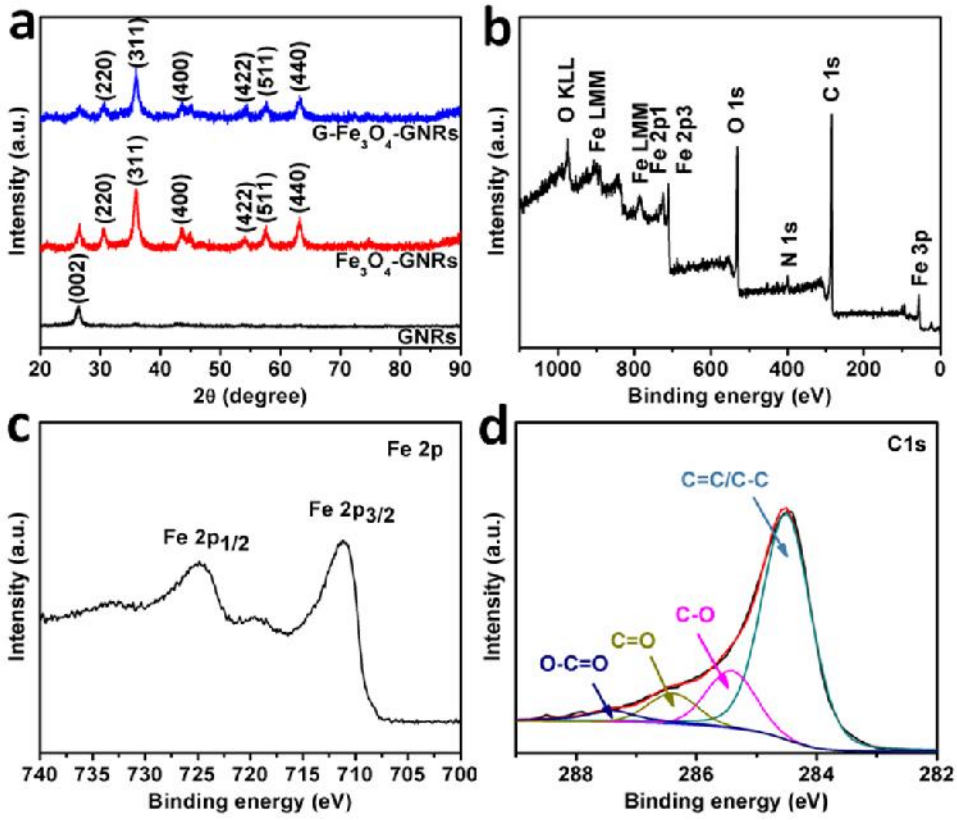

Figure 7.4. (a) XRD patterns of GNRs, Fe3O4-GNRs, and G-Fe3O4-GNRs. (b) XPS spectra of G-Fe3O4-GNRs. (c) Fe 2p XPS spectrum of G-Fe3O4-GNRs. (d) XPS spectrum of C 1s for G-Fe3O4-GNRs.

Figure 7.4b showed XPS spectra of G-Fe_3O_4-GNRs revealing that the composite contains Fe, C, O with trace amounts of N from hydrazine introduced by reduced graphene oxide. The two characteristic peaks of Fe 2p3/2 and Fe 2p1/2 depicted in the fine spectra of Fe 2p were centered at 711 and 725 eV, confirming the formation of Fe_3O_4 in the composite (Figure 7.4c), hence the graphene coating process did not change electronic state

of Fe_3O_4 in the composite.[37,38] Figure 7.4d showed the fine XPS spectra of C1s of G-Fe_3O_4-GNRs with four peaks located at 284.5, 285.4, 286.4, and 287.4 eV assigned to C=C/C-C, C-O, C=O, O-C=O, respectively.[39-41] The analysis of C1s of G-Fe_3O_4-GNRs showed that the graphene oxide was not completely reduced by hydrazine. The data demonstrates that Fe_3O_4 nanoparticles were indeed grown on the G-Fe_3O_4-GNRs.

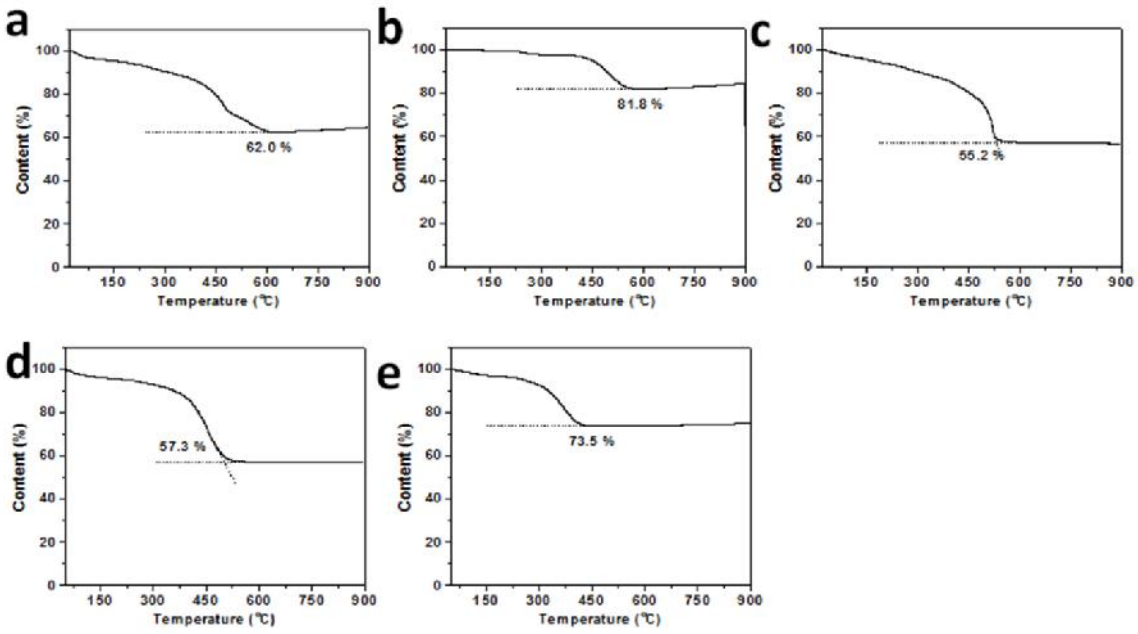

Figure 7.5. TGA curves of (a) G-Fe_3O_4-GNRs showing 60.4% Fe_3O_4 content, (b) Fe_3O_4-GNRs showing 79.1% Fe_3O_4 content, (c) G-Fe_3O_4 showing 53.4% Fe_3O_4 content, (d) Fe_3O_4-G showing 55.4%, and (e) Fe_3O_4-G showing 71.0% Fe_3O_4 content, recorded in air at a heating rate of 10 °C/min. The residential of G-Fe_3O_4-GNRs, Fe_3O_4-GNRs, G-Fe_3O_4, Fe_3O_4-G, and Fe_3O_4-GO, is Fe_2O_3. Fe_3O_4 content in the composites was calculated based on the TGA plots considering the weight gain of Fe_2O_3 transformed from Fe_3O_4.

TGA experiments were carried out to determine the Fe_3O_4 content in the composites (Figure 7.5). After graphene wrapping, the Fe_3O_4 content decreased from 79.1% to 60.4%

(Figure 6.5a,b). G-Fe_3O_4, Fe_3O_4-G, and Fe_3O_4-GO as control samples show 53.4%, 55.4%, and 71.0% Fe_3O_4 content, respectively (Figure 7.5c-e).

7.3.2. Electrochemical evaluation

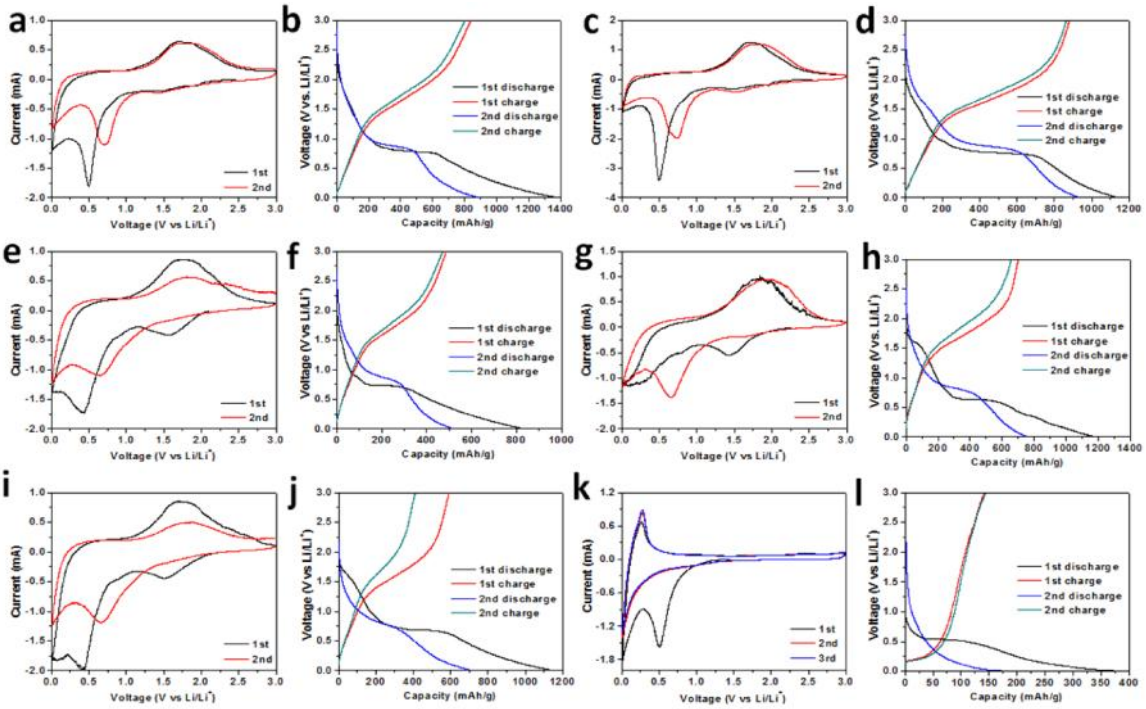

Figure 7.6. Cyclic voltammetry curves of G-Fe_3O_4-GNRs (a), Fe_3O_4-GNRs (c), G-Fe_3O_4 (e), Fe_3O_4-G (g), Fe_3O_4-GO (i), and GNRs (k) in the potential range of 0.01 and 3.0 V (vs. Li/Li+) at a scan rate of 0.4 mV/s. The first two discharge charge curves of G- Fe_3O_4-GNRs (b) in the potential range of 0.01 and 3.0 V (vs. Li/Li^+) at a current density of 0.1 A/g, Fe_3O_4-GNRs (d), G- Fe_3O_4 (f), Fe_3O_4-G (h), Fe_3O_4-GO (j), and GNRs (l) at a current density of 0.4 A/g.

The electrochemical performance of G-Fe_3O_4-GNRs as anodes in LIBs was studied. Figure 7.6 showed the cyclic voltammetry (CV) curves and the first two discharge charge profiles of G-Fe_3O_4-GNRs, Fe_3O_4-GNRs, and GNRs. As shown in Figure 7.6a, there were three cathodic peaks at 1.47 V, 0.73 V, and 0.50 V in the first cycle of CV. The

cathodic peak at 1.47 V corresponded to the structure transition caused by lithium interaction with crystalline Fe_3O_4, as shown in the equation 7.1 ($Fe_3O_4 + xLi^+ + xe^- \rightleftharpoons Li_x(Fe_3O_4)$ $(0 \leq x \leq 2)$). The peak at 0.73 V resulted from further reduction of $Li_x(Fe_3O_4)$ to Fe(0) as shown in the equation 7.2 of $Li_x(Fe_3O_4) + (8 - x)Li^+ + (8 - x)e^- \rightleftharpoons 3Fe + 4Li_2O$ $(0 \leq x \leq 2)$.[12,42-44] The cathodic peak at 0.50 V was a characteristic of the solid electrolyte interface (SEI) formed on the electrode surface which mainly occurred in the first cycle, and disappeared in the second cycle. There were two anodic peaks at 1.69 V and 2.00 V corresponding to the gradual oxidation of Fe(0) to $Li_x(Fe_3O_4)$ and further to Fe^{3+} in two steps during the first cycle of CV. Figure 7.6b showed the discharge-charge profiles of G-Fe_3O_4-GNRs at a current density of 0.1 A/g. There was a plateau at ~ 0.80 V in the discharge process and two plateaus at ~ 1.5 V and 2.0 V in the charge process, which was consistent with peaks in the corresponding CV curves. Fe_3O_4-GNRs, G-Fe_3O_4, Fe_3O_4-G, and Fe_3O_4-GO display similar phenomena (Figure 7.6c-j). Figure 7-6k,l show the CV and charge discharge curves of GNRs. All the discharge capacities of GNRs, Fe_3O_4-GO, Fe_3O_4-G, G-Fe_3O_4, Fe_3O_4-GNRs and G-Fe_3O_4-GNRs had a great loss in the second cycle compared to the first cycle likely due to the irreversible reaction of the electrodes, the SEI formation on the surface of the electrodes, and the decomposition of electrolyte.[12,21]

The rate performance of G-Fe_3O_4-GNRs was studied in the potential window of 0.01 to 3.0 V as shown in Figure 7.7a. The stable capacity at different current densities was observed. When the current density reduced from 1.0 A/g to 0.1 A/g, the value of specific capacity of G-Fe_3O_4-GNRs almost had no decay. For example, the value of discharge capacity was 787 mAh/g at the 30^{th} cycle and 796 mAh/g at the 55^{th} cycle in the same current density of 0.1 A/g. The results demonstrated the good rate performance of G-

Fe_3O_4-GNRs after extended rate cycles. After 55 cycles of rate test, the morphology of G-Fe_3O_4-GNRs has no obvious change as shown in Figure 7.8.

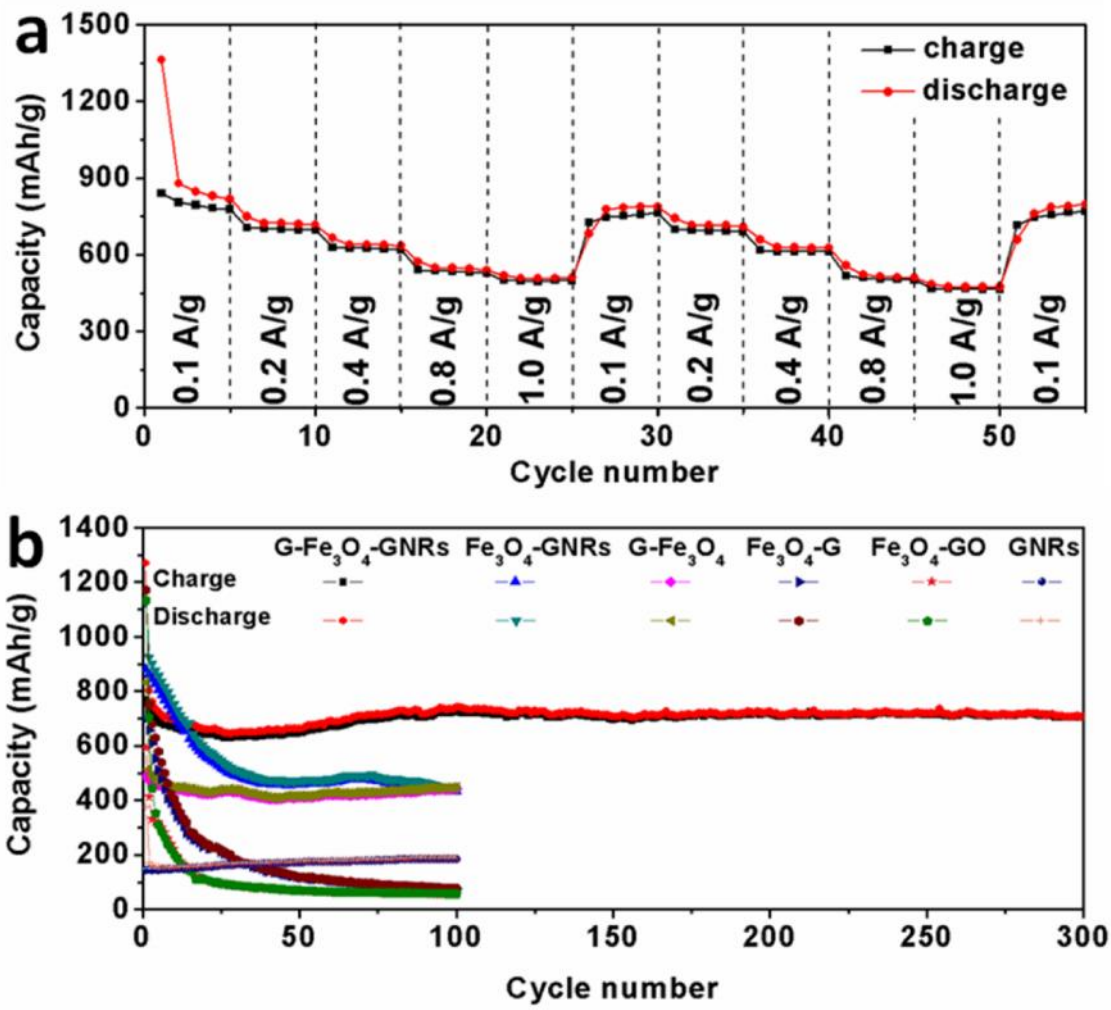

Figure 7.7. (a) Rate performance of G-Fe_3O_4-GNRs at various current densities from 0.1 A/g to 1.0 A/g. (b) Cycling performance of G-Fe_3O_4-GNRs, Fe_3O_4-GNRs, G-Fe_3O_4, Fe_3O_4-G, Fe_3O_4-GO, and GNRs at a current density of 0.4 A/g.

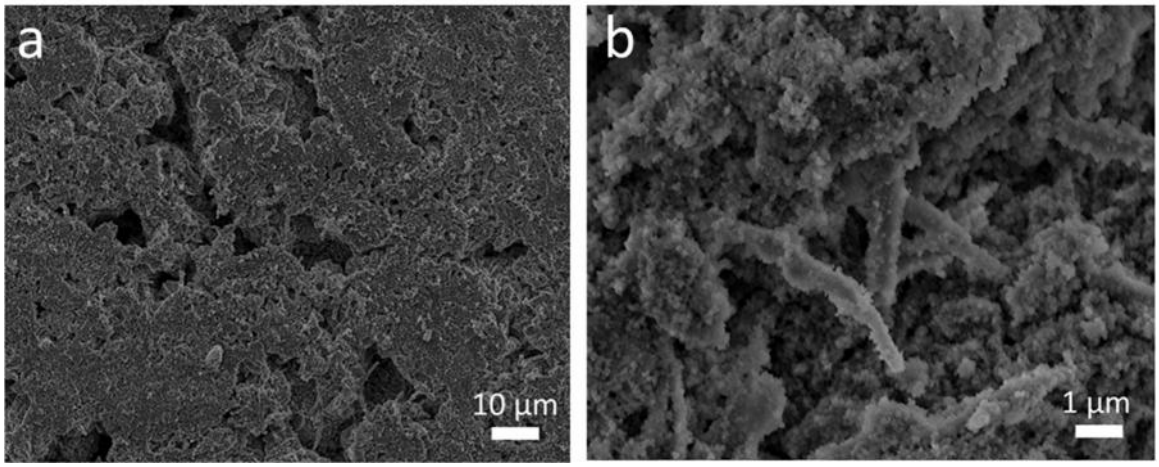

Figure 7.8. (a,b) SEM images of G-Fe_3O_4-GNRs electrodes after 55 cycles discharge-charge processes at different current densities from 0.1 to 1 A/g in the potential range of 0.01 to 3.0 V. The particles on surface are $LiFeF_6$ which are not completely cleansed by the mixture solution of ethylene carbonate and diethyl carbonate (1:1 vol:vol).

The cycling performance for G-Fe_3O_4-GNRs was also evaluated. Figure 7.7b compared the cycling performance of G-Fe_3O_4-GNRs, Fe_3O_4-GNRs, G-Fe_3O_4, Fe_3O_4-G, Fe_3O_4-GO, and GNRs in LIBs at a constant current density of 0.4 A/g within the same potential window. GNRs showed a very low, yet stable discharge capacity that increased from 172 mAh/g at the 2nd cycle to 186 mAh/g by the 100th cycle. Fe_3O_4-GNR, Fe_3O_4-G, and Fe_3O_4-GO electrodes exhibited a sharp decline in discharge capacity from 926, 752, and 703 mAh/g in the 2nd cycle to 544, 211, and 95 mAh/g by the 25th cycle and finally only 442, 77, and 57 mAh/g by the 100th cycle, respectively. G-Fe_3O_4 electrodes show the low discharge capacity, and gradually decreased from 513 mAh/g at the second cycle to 447 mAh/g at the 100th cycle. However, after graphene wrapping of Fe_3O_4-GNR, the discharge capacity of G-Fe_3O_4-GNRs slowly decreased from 800 mAh/g at the second cycle to 652 mAh/g at the 25th cycle and then rose to 740 mAh/g at the 100th cycle. It finally

reached a stable discharge capacity of 708 mAg/g after 300 cycles. More importantly, the Coulombic efficiency of G-Fe_3O_4-GNRs was maintained ~ 99.5%, excluding the first several cycles. Therefore, these results demonstrated that the unique hierarchical sandwich structure effectively reduced the capacity decay and greatly improved the cycling performance of G-Fe_3O_4-GNRs with a higher Coulombic efficiency in LIBs.

Electrochemical impedance spectroscopy (EIS) experiments were carried out to clarify the enhanced electrochemical performance of G-Fe_3O_4-GNRs (Figure 7.9a). An equivalent circuit model for this system was established as shwon in Figure 7.9b. In this model, R_s is the internal resistance of the tested battery, R_{SEI} and R_{ct} represents the SEI surface and charge-transfer resistance, CPE_1 and CPE_2 are associated with constant phase element, Z_w is the Warburg resistance related to the lithium diffusion process, and the C_{int} is the interaction capacitance.[45] In the Figure 7.9a, the plots consist of two semicircles in the high and intermediate frequency range, which result from the Li^+ ion transport through the SEI film (R_{SEI}) and the interfacial charge transfer reaction (R_{ct}) combined with CPE_1 and CPE_2, respectively. They also have a sloping line because of the solid-state Li diffusion into the active materials (Z_w).[45,46] Table 7.1 showed the fitted impedance parameters based on the experimental Nyquist plots using the established model in Figure 6.9b. Both R_{SEI} (32.46 Ω) and R_{ct} (9.60 Ω) of G-Fe_3O_4-GNRs are lower than that of Fe_3O_4-GNRs (R_{SEI} = 47.42 Ω and R_{ct} = 21.66 Ω), G-Fe_3O_4 (R_{SEI} = 73.22 Ω and R_{ct} = 35.73 Ω), Fe_3O_4-G (R_{SEI} = 52.01 Ω and R_{ct} = 53.34 Ω), and Fe_3O_4-GO (R_{SEI} = 46.11 Ω and R_{ct} = 97.53 Ω), which means G-Fe_3O_4-GNRs have a more stable surface film and faster charge transfer process than the other control samples.[46] It indicates that incorporation of graphene and GNRs on

G-Fe_3O_4-GNRs can greatly improve its electrical conductivity and mechanical stability, resulting in significant improvement in the electrochemical performance.

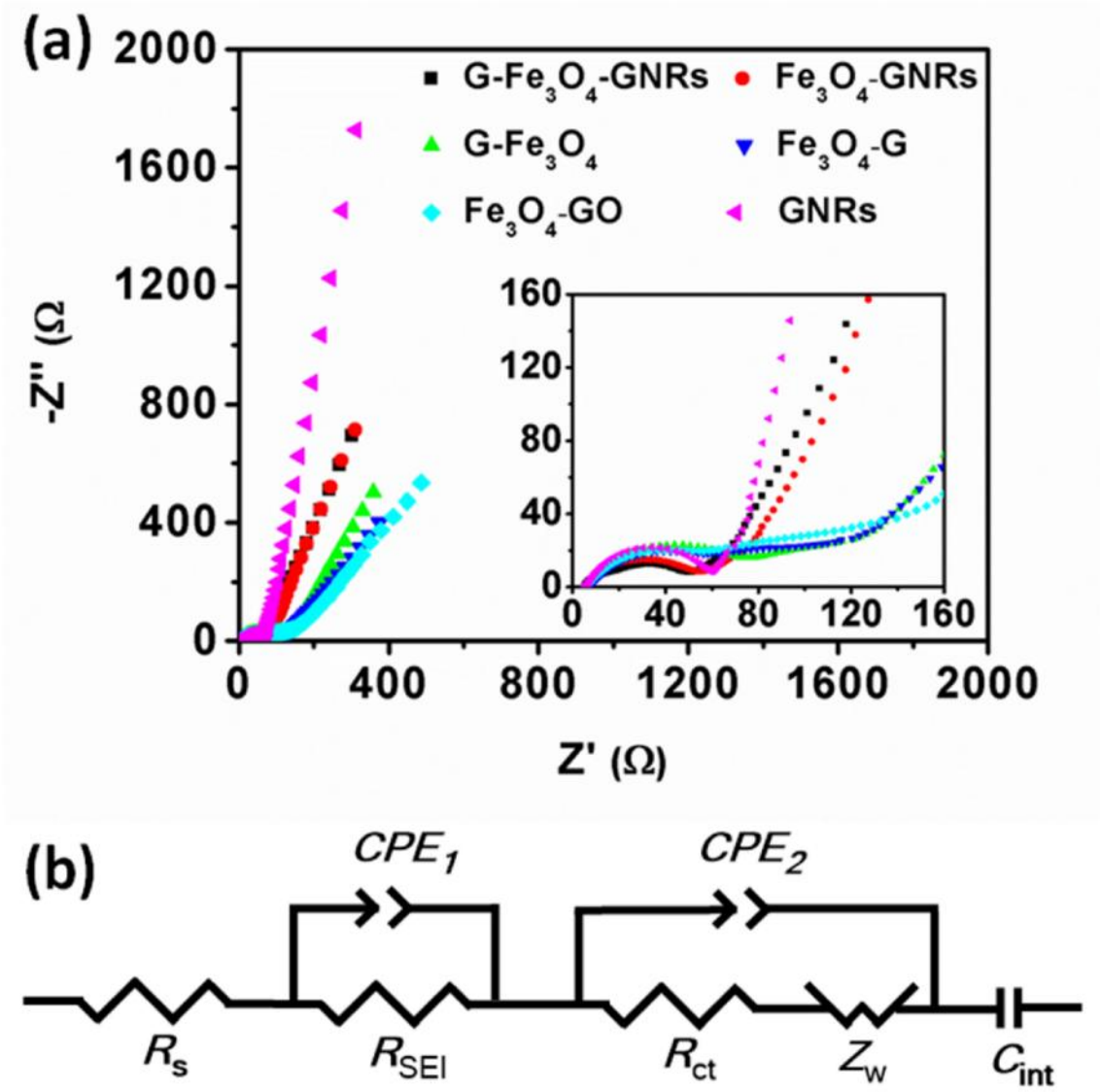

Figure 7.9. (a) Nyquist plots of G-Fe_3O_4-GNRs, Fe_3O_4-GNRs, G-Fe_3O_4, Fe_3O_4-G, Fe_3O_4-GO, and GNRs. The insert is the enlarged high frequency region. (b) Equivalent circuit that is used to fit the experimental data.

Table 7.1. The EIS simulation parameters of G-Fe_3O_4-GNRs, Fe_3O_4-GNRs, G-Fe_3O_4, Fe_3O_4-G, and GNRs.

Active material	R_s (Ω)	CPE_1 (μF)	R_{SEI} (Ω)	R_{ct} (Ω)	CPE_2 (μF)	Z_w (Ω)	C_{int}(mF)
G-Fe_3O_4-GNRs	5.05	96.88	32.46	9.60	5.89	77.70	31.26
Fe_3O_4-GNRs	5.70	63.46	47.42	21.66	456.40	96.62	31.80
G-Fe_3O_4	6.34	40.00	73.22	35.73	709.70	79.43	53.00
Fe_3O_4-G	7.60	38.68	52.01	53.34	587.60	93.37	101.9
Fe_3O_4-GO	6.24	30.08	46.11	97.53	85.48	119.15	63.58
GNRs	5.62	33.88	46.98	2.16	14.92	64.06	9.16

7.4. Conclusion

In summary, we successfully designed and synthesized a nanoscale sandwiched composite of graphene-Fe_3O_4-graphene nanoribbons. In this composite, graphene flakes tightly sandwiched the nanosized Fe_3O_4 which grew directly on the GNRs. Electrochemical experiments demonstrate that the G-Fe_3O_4-GNRs exhibit good rate performance and improved cycling stability as anode materials due to the synergy among Fe_3O_4, reduced graphene oxide, and GNRs. The design concept developed here opens up a new avenue for constructing anodes with an improved electrochemical stability for lithium ion batteries.

7.5. References

1. Li, L.; Kovalchuk, A.; Fei, H. L.; Peng, Z. W.; Li, Y.L.; Kim, N.D.; Xiang, C. S.; Yang, Y.; Tour, J. M. Enhanced Cycling Stability of Lithium Ion Batteries Using Graphene-Fe_3O_4-Graphene Nanoribbons as Anode Materials **In revision**. (L.L. conceived and designed the experiments. L.L., K.A. and P.Z.W. prepared the materials. L.L., F.H.L., L.Y.L., K.N.D., X.C.S., and Y.Y. performed material characterization. L.L. tested the devices and wrote the paper. Finally, T.J.M. oversaw all research phases, provided

regular guidance to the research and revised the manuscript. All authors discussed and commented on the manuscript.)

2. Etacheri, V.; Marom, R.; Elazari, R.; Salitra, G.; Aurbach, D., Challenges in the development of advanced Li-ion batteries: a review. *Energy Environ. Sci.* **2011**, *4*, 3243-3262.

3. Lee, J. E.; Yu, S.-H.; Lee, D. J.; Lee, D.-C.; Han, S. I.; Sung, Y.-E.; Hyeon, T., Facile and economical synthesis of hierarchical carbon-coated magnetite nanocomposite particles and their applications in lithium ion battery anodes. *Energy Environ. Sci.* **2012**, *5*, 9528-9533.

4. Tarascon, J.-M.; Armand, M.,Issues and Challenges FacingRechargeable Lithium Batteries. *Nature* **2001**, *414*, 359-367.

5. Wang, B.; Li, X.; Zhang, X.; Luo, B.; Jin, M.; Liang, M.; Dayeh, S. A.; Picraux, S. T.; Zhi, L., Adaptable Silicon–Carbon Nanocables Sandwiched between Reduced Graphene Oxide Sheets as Lithium Ion Battery Anodes. *ACS Nano* **2013**, *7*, 1437-1445.

6. Aricò, A. S.; Bruce, P.; Scrosati, B.; Tarascon, J. M.; Schalkwijk, W. Nanostructured materials for advanced energy conversion and storage devices *Nat. Mater.* **2005**, *4*, 366.

7. Reddy, M. V.; Subba Rao, G. V.; Chowdari, B. V. R., Metal Oxides and Oxysalts as Anode Materials for Li Ion Batteries. *Chem. Rev.* **2013**, *113*, 5364-5457.

8. Zhou, G.; Wang, D.-W.; Li, F.; Zhang, L.; Li, N.; Wu, Z.-S.; Wen, L.; Lu, G. Q.; Cheng, H.-M., Graphene-Wrapped Fe_3O_4 Anode Material with Improved Reversible Capacity and Cyclic Stability for Lithium Ion Batteries. *Chem. Mater.* **2010**, *22*, 5306-5313.

9. Zhang, W.-M.; Wu, X.-L.; Hu, J.-S.; Guo, Y.-G.; Wan, L.-J., Carbon Coated Fe_3O_4 Nanospindles as a Superior Anode Material for Lithium-Ion Batteries. *Adv. Funct. Mater*. **2008**, *18*, 3941-3946.

10. Wei, W.; Yang, S.; Zhou, H.; Lieberwirth, I.; Feng, X.; Müllen, K., 3D Graphene Foams Cross-linked with Pre-encapsulated Fe_3O_4 Nanospheres for Enhanced Lithium Storage. *Adv. Mater.* **2013**, *25*, 2909-2914.

11. Bruce, P. G.; Scrosati, B.; Tarascon, J.-M., Nanomaterials for Rechargeable Lithium Batteries. *Angew. Chem. Int. Ed.* **2008**, *47*, 2930-2946.

12. Jia, X.; Chen, Z.; Cui, X.; Peng, Y.; Wang, X.; Wang, G.; Wei, F.; Lu, Y., Building Robust Architectures of Carbon and Metal Oxide Nanocrystals toward High-Performance Anodes for Lithium-Ion Batteries. *ACS Nano* **2012**, *6*, 9911-9919.

13. Cheng, J.; Wang, B.; Park, C.-M.; Wu, Y.; Huang, H.; Nie, F., CNT@ Fe_3O_4@C Coaxial Nanocables: One-Pot, Additive-Free Synthesis and Remarkable Lithium Storage Behavior. *Chem. Eur. J.* **2013**, *19*, 9866-9874.

14. Wu, Y.; Wei, Y.; Wang, J.; Jiang, K.; Fan, S., Conformal Fe_3O_4 Sheath on Aligned Carbon Nanotube Scaffolds as High-Performance Anodes for Lithium Ion Batteries. *Nano Lett.* **2013**, *13*, 818-823.

15. Liu, J.; Ni, J.; Zhao, Y.; Wang, H.; Gao, L., Grapecluster-like Fe_3O_4@C/CNT nanostructures with stable Li-storage capability. *J. Mater. Chem. A* **2013**, *1*, 12879-12884.

16. Zhang, F.; Zhang, T.; Yang, X.; Zhang, L.; Leng, K.; Huang, Y.; Chen, Y., A high-performance supercapacitor-battery hybrid energy storage device based on graphene-enhanced electrode materials with ultrahigh energy density. *Energy Environ. Sci.* **2013**, *6*, 1623-1632.

17. Chen, D.; Quan, H.; Liang, J.; Guo, L., One-pot synthesis of hematite@graphene core@shell nanostructures for superior lithium storage. *Nanoscale* **2013**, *5*, 9684-9689.

18. Zhuo, L.; Wu, Y.; Wang, L.; Ming, J.; Yu, Y.; Zhang, X.; Zhao, F., CO_2-expanded ethanol chemical synthesis of a Fe_3O_4@graphene composite and its good electrochemical properties as anode material for Li-ion batteries. *J.Mater. Chem. A* **2013**, *1*, 3954-3960.

19. Dong, Y.; Ma, R.; Hu, M.; Cheng, H.; Yang, Q.; Li, Y. Y.; Zapien, J. A., Thermal evaporation-induced anhydrous synthesis of Fe_3O_4-graphene composite with enhanced rate performance and cyclic stability for lithium ion batteries. *Phys. Chem. Chem. Phys.* **2013**, *15*, 7174-7181.

20. Chen, Y.; Song, B.; Lu, L.; Xue, J., Ultra-small Fe_3O_4 nanoparticle decorated graphene nanosheets with superior cyclic performance and rate capability. *Nanoscale* **2013**, *5*, 6797-6803.

21. He, C.; Wu, S.; Zhao, N.; Shi, C.; Liu, E.; Li, J., Carbon-Encapsulated Fe_3O_4 Nanoparticles as a High-Rate Lithium Ion Battery Anode Material. *ACS Nano* **2013**, *7*, 4459-4469.

22. Wang, L.; Liang, J.; Zhu, Y.; Mei, T.; Zhang, X.; Yang, Q.; Qian, Y., Synthesis of Fe_3O_4@C core-shell nanorings and their enhanced electrochemical performance for lithium-ion batteries. *Nanoscale* **2013**, *5*, 3627-3631.

23. Derrien, G.; Hassoun, J.; Panero, S.; Scrosati, B., Nanostructured Sn-C Composite as an Advanced Anode Material in High-Performance Lithium-Ion Batteries. *Adv. Mater.* **2007**, *19*, 2336-2340.

24. Li, L.; Raji, A.-R. O.; Tour, J. M., Graphene-Wrapped MnO_2-Graphene Nanoribbons as Anode Materials for High-Performance Lithium Ion Batteries. *Adv. Mater.* **2013**, *25*, 6298-6302.

25. Hu, Y.-S.; Demir-Cakan, R.; Titirici, M. M.; Müller, J. O.; Schlögl, R.; Antonietti, M.; Maier, J., Superior Storage Performance of a Si@SiOx/C Nanocomposite as Anode Material for Lithium-Ion Batteries. *Angew. Chem. Int. Ed.* **2008**, *47*, 1645-1649.

26. Lou, X. W.; Chen, J. S.; Chen, P.; Archer, L. A., One-Pot Synthesis of Carbon-Coated SnO_2 Nanocolloids with Improved Reversible Lithium Storage Properties. *Chem. Mater.* **2009**, *21*, 2868-2874.

27. Wang, L.; Yu, Y.; Chen, P. C.; Zhang, D. W.; Chen, C. H., Electrospinning synthesis of C/Fe_3O_4 composite nanofibers and their application for high performance lithium-ion batteries. *J. Power Sources* **2008**, *183*, 717-723.

28. Genorio, B.; Lu, W.; Dimiev, A. M.; Zhu, Y.; Raji, A.-R. O.; Novosel, B.; Alemany, L. B.; Tour, J. M., In Situ Intercalation Replacement and Selective Functionalization of Graphene Nanoribbon Stacks. *ACS Nano* **2012**, *6*, 4231-4240.

29. Genorio, B.; Peng, Z.; Lu, W.; Price Hoelscher, B. K.; Novosel, B.; Tour, J. M., Synthesis of Dispersible Ferromagnetic Graphene Nanoribbon Stacks with Enhanced Electrical Percolation Properties in a Magnetic Field. *ACS Nano* **2012**, *6*, 10396-10404.

30. D. Li, M. B. Muller, S. Gilje, R. B. Kaner, G. G. Wallace, Processable Aqueous Dispersions of Graphene Nanosheets *Nat. Nano.* **2008**, *3*, 101-105.

31. Marcano, D. C.; Kosynkin, D. V.; Berlin, J. M.; Sinitskii, A.; Sun, Z.; Slesarev, A.; Alemany, L. B.; Lu, W.; Tour, J. M., Improved Synthesis of Graphene Oxide. *ACS Nano* **2010**, *4*, 4806-4814.

32. Lei, Z.; Shi, F.; Lu, L., Incorporation of MnO_2-Coated Carbon Nanotubes between Graphene Sheets as Supercapacitor Electrode. *ACS Appl. Mater. Interfaces* **2012**, *4*, 1058-1064.

33. Campos-Delgado, J.; Romo-Herrera, J. M.; Jia, X.; Cullen, D. A.; Muramatsu, H.; Kim, Y. A.; Hayashi, T.; Ren, Z.; Smith, D. J.; Okuno, Y.; Ohba, T.; Kanoh, H.; Kaneko, K.; Endo, M.; Terrones, H.; Dresselhaus, M. S.; Terrones, M., Bulk Production of a New Form of sp2 Carbon: Crystalline Graphene Nanoribbons. *Nano Lett.* **2008**, *8*, 2773-2778.

34. Lee, S. H.; Yu, S.-H.; Lee, J. E.; Jin, A.; Lee, D. J.; Lee, N.; Jo, H.; Shin, K.; Ahn, T.-Y.; Kim, Y.-W.; Choe, H.; Sung, Y.-E.; Hyeon, T., Self-Assembled Fe_3O_4 Nanoparticle Clusters as High-Performance Anodes for Lithium Ion Batteries via Geometric Confinement. *Nano Lett.* **2013**, *13*, 4249-4256.

35. Cong, H.-P.; Ren, X.-C.; Wang, P.; Yu, S.-H., Macroscopic Multifunctional Graphene-Based Hydrogels and Aerogels by a Metal Ion Induced Self-Assembly Process. *ACS Nano* **2012**, *6*, 2693-2703.

36. Zhao, N.; Wu, S.; He, C.; Wang, Z.; Shi, C.; Liu, E.; Li, J., One-pot synthesis of uniform Fe_3O_4 nanocrystals encapsulated in interconnected carbon nanospheres for superior lithium storage capability. *Carbon* **2013**, *57*, 130-138.

37. Wu, Z. S.; Yang, S.; Sun, Y.; Parvez, K.; Feng, X.; Müllen, K., 3D Nitrogen-Doped Graphene Aerogel-Supported Fe_3O_4 Nanoparticles as Efficient Electrocatalysts for the Oxygen Reduction Reaction. *J Am. Chem. Soc.* **2012**, *134*, 9082-9085.

38. Su, J.; Cao, M.; Ren, L.; Hu, C., Fe_3O_4-Graphene Nanocomposites with Improved Lithium Storage and Magnetism Properties. *J. Phys. Chem. C* **2011**, *115*, 14469-14477.

39. Yang, S.; Yue, W.; Zhu, J.; Ren, Y.; Yang, X., Graphene-Based Mesoporous SnO_2 with Enhanced Electrochemical Performance for Lithium-Ion Batteries. *Adv. Funct. Mater.* **2013**, *23*, 3570-3576.

40. Utsumi, S.; Honda, H.; Hattori, Y.; Kanoh, H.; Takahashi, K.; Sakai, H.; Abe, M.; Yudasaka, M.; Iijima, S.; Kaneko, K., Direct Evidence on C-C Single Bonding in Single-Wall Carbon Nanohorn Aggregates. *J. Phys. Chem. C* **2007**, *111*, 5572-5575.

41. Some, S.; Kim, Y.; Yoon, Y.; Yoo, H.; Lee, S.; Park, Y.; Lee, H. High-quality reduced graphene oxide by a dual-function chemical reduction and healing process. *Sci. Rep.* **2013**, *3*, 1929.

42. Xu, F.; Kang, W.; Wang, X.; Liu, R.; Zhao, C.; Shen, Q., A chemical composition evolution for the shape-controlled synthesis and energy storage applicability of Fe_3O_4-C nanostructures. *CrystEngComm* **2013**, *15*, 4431-4437.

43. Zhu, X.; Zhu, Y.; Murali, S.; Stoller, M. D.; Ruoff, R. S., Nanostructured Reduced Graphene Oxide/Fe_2O_3 Composite As a High-Performance Anode Material for Lithium Ion Batteries. *ACS Nano* **2011**, *5*, 3333-3338.

44. Wang, Z.; Luan, D.; Madhavi, S.; Hu, Y.; Lou, X. W., Assembling carbon-coated Fe2O3 hollow nanohorns on the CNT backbone for superior lithium storage capability. *Energy Environ. Sci.* **2012**, *5*, 5252-5256.

45. M. S. Wu, P. C. Chiang, J. C. Lin Electrochemical Investigations on Advanced Lithium-Ion Batteries by Three-Electrode Measurements *J. Electrochem. Soc.* **2005**, *152*, A47.

46. G. M. Zhou, D. W. Wang, L. C. Yin, N. Li, F. Li, H. M. Cheng Oxygen Bridges Between NiO Nanosheets And Graphene for Improvement of Lithiu Storage *ACS Nano*, **2012**, *6*, 3214.

Chapter 8

Sandwich Structured Graphene-FeS-graphene Nanoribbons with Improved Cycling Stability for Lithium Ion Batteries

This chapter was entirely copied from reference 1.

8.1. Introduction

Environmental issues and the decreasing supply of fossil fuels become the serious social problems nowadays. They have triggered great research efforts on sustainable and renewable energy resources.[2,3] As an important part of energy conversion, energy storage devices provide a way to use energy in a clean, efficient, and versatile manner in applications. Lithium ion batteries (LIBs) are considered among the most practical and effective technologies for electrochemical energy storage.[4,5] LIBs can be wildly used in electric vehicles, multifunctional electric devices, communication equipments, and the renewable energy integration.[6,7] Therefore, developing LIBs with high energy density,

super power density, and excellent cycling performance becomes critical. Numerous efforts have been devoted to develop the new electrode materials satisfying these demands of LIBs.[5,7] Electrochemically active metal sulfide (MS_x) are used as promising candidates for anode materials due to their high theoretical capacity and natural abundance.[8-15] Among these metal sulfide, iron sulfide (FeS) has attracted great attention thanks to its outstand electrochemical properties, low cost, and natural abundance.[15-18]

However, there are still two obstacles hindered the applications of FeS-related anode materials in LIBs. The first problem is the large volume variation of FeS in conversion reaction. The 200% volume change of FeS results in the pulverization of the electrode materials, leading to the quick capacity decay.[16] The other one is that the intermediate of lithium polysulfide (Li_sS_x $1<x<8$) produced in the discharge/charge processes is soluble in electrolyte. This causes the loss of the active materials. The soluble polysulfide can also migrate to the cathode side and react with both the cathode and anode.[16,17] This results in poor cycling stability of the electrodes in LIBs. Large amounts of efforts have been devoted to solve these problems based on carbon coating and nanosized FeS.[16] For example, Xu *et al*. reported the carbon coated FeS nanosheet demonstrated high capacities with stable cycling stability at fast charge/discharge rates. The discharge capacity can retain at 260 mAh/g at a current density of 6,000 mA/g (10C) at the 100th cycle.[15] Wang *et al*. prepared TiO_2 modified FeS nanostructures showed the reversible capacity of 510 mAh/g after 100 discharge/charge cycles at 200 mA/g.[18] Recently, our group developed sandwich structured nanocomposites of graphene-MnO_2-graphene nanoribbons demonstrated great improvement in cycling stability of anode

materials based on the conversion reactions.[19] This nanostructure might solve the problems regarding the FeS related anode materials.

In this study, the sandwich structured graphene-FeS-graphene nanoribbons (G@FeS-GNRs) were designed and prepared. In this structure, graphene and graphene nanoribbons (GNRs) improve the electrical conductivity of the composite G@FeS-GNRs due to their high electrical conductivity and the good contact with FeS. They can also buffer the volume change and mitigate the negative effect of pulverization caused by volume change. More importantly, they can prevent the direct contact between the polysulfide and electrolyte, reducing the solubility of intermediate polysulfide during Li ion conversion reaction with Li, thus improving its electrochemical stability. G@FeS-GNRs as anode materials demonstrate high capacity, excellent rate and cycling performance. The reversible discharge capacity of G@FeS-GNRs can reach 693 mAh/g at 0.1 A/g at second cycle and retained 536 mAh/g after 100 cycles at 0.4 A/g. Thus, G@FeS-GNRs are the superb candidates of the anode materials in LIBs.

8.2. Experiments

8.2.1. Materials synthesis

8.2.1.1. Synthesis of Fe_3O_4-GNRs

GNRs were prepared through the solution-based chemical unzipping multi-walled carbon nanotubes in 1,2-dimethoxyethane as described previously.[20] 50 mg of GNRs and 150 mg of $FeCl_3$ were placed in the glass ampule and sealed under vacuum using acetylene torch. The ampule was placed in the oven at 350 ^oC for 24 h to conduct the intercalation

process. After this, the $FeCl_3$-GNR intercalation product was transferred into the glass flask, sealed and carefully purged with nitrogen. Next, 17.5 ml of freshly distilled DME and 0.5 ml of Na/K alloy was added in the flask. The reaction mixture was stirred within 15 h at room temperature. After the end of the reaction, methanol was added, and the obtained product was carefully purified by filtration with water, methanol, acetone and diethyl ether and dried under vacuum. In a next step, the synthesized iron oxide-GNR product was placed in the glass ampule with 300 mg of $FeCl_3$, sealed under vacuum and placed at 350 ^oC in the oven for 24 h for the second intercalation step. The product of double intercalation was transferred into the glass flask, sealed and purged with nitrogen. Freshly distilled DME (17.5 ml) and Na/K alloy (0.6 ml) were added and reacted at room temperature under magnetic stirring within 20 h. Finally, methanol was added to the reaction mixture and the target product was collected, filtered with water, methanol, acetone and diethyl ether and dried under vacuum. 0.38 g of product was obtained in final.

8.2.1.2. Synthesis of G@Fe_3O_4-Gs

G@Fe_3O_4-Gs were prepared in two steps. The first step was to positively charge the Fe_3O_4-GNRs by dispersing it in aqueous polydiallyldimethylammonium chloride (PDADMAC, Sigma-Aldrich). 50 mg of Fe_3O_4-GNRs was dispersed in 50 mL D.I. water containing 0.5 mL of PDADMAC. After 5 h stirring at room temperature, positively charged PDADMAC-Fe_3O_4-GNRs (38 mg) was obtained *via* vacuum filtration and washing the solid with D.I. water (400 mL) and ethanol (100 mL), and drying it in a vacuum oven (~ 6 mmHg) at 80 °C for 10 h. Then, 38 mg of PDADMAC-Fe_3O_4-GNRs was dispersed in 40 mL D.I. water by ultrasonic treatment and the solution was adjusted to pH ~8 using 1 M ammonia in ethanol. The PDADMAC-Fe_3O_4-GNRs suspension was added

to a negatively charged graphene solution that was prepared by reduction of 20 mg of graphene oxide in 40 mL D.I. water adjusted to pH ~8 using 1 M ammonia with 22.6 µL of hydrazine, and the mixture was stirred for 5 h. 40 mg of G-Fe_3O_4-GNRs was obtained after vacuum filtration followed by washing sequentially with D.I. water (400 mL) and ethanol (100 mL) and drying in a vacuum oven (~ 6 mmHg) at 80 °C for 10 h.

8.2.1.3. Synthesis of G@FeS-GNRs

G@FeS-GNRs were prepared by vulcanization of G@Fe_3O_4-Gs in the CVD system. G@Fe_3O_4-GNRs (30 mg) were loaded into the CVD system in the mixture flow of Ar (190 sccm) and H_2 (10 sccm). The sulfur source (1 g) was placed ~ 15 cm away from the G@Fe_3O_4-GNRs at the upstream zone of the horizontal quartz tube at in the furnace. The reaction chamber was evaporated to ~ 16 mT by completely open the vacuum valve and kept this condition for 10 min in order to completely remove the oxygen in the chamber. Then, the vacuum valve was turn off and the chamber pressure was adjusted to ambient pressure. The temperature was increased to 380 °C from room temperature at the heating rate of 20 °C/min and kept at 380 °C for 1 h. After the reaction, the heating power was shut off and G@FeS-GNRs (29 mg) was obtained after the sample was naturally cooled down to room temperature in the flow of Ar.

8.2.2. Materials Characterization

Products were characterized by XRD (Rigaku D/Max Ultima II), XPS (PHI Quantera), SEM (JEOL 6500), TEM (JEM2100F TEM), and thermogravimetric analysis (TGA, TA Instruments, Q50).

8.2.3. Device fabrication

The anode was prepared by mixing 80 wt% of the active composite, 10 wt% of carbon black (Super P), and 10 wt% of polyvinylidene difluoride (PVDF, Alfa Aesar) dissolved in *N*-methyl-2-pyrrolidone (NMP, Sigma-Aldrich) to form a slurry that was coated on a copper foil substrate. The electrode was dried in vacuum oven (~ 6 mmHg) at 100 °C for 10 h. Electrochemical tests were performed using CR2032 coin-type cells with lithium metal foil as the counter electrode. The electrolyte was 1 M $LiPF_6$ in ethylene carbonate and diethyl carbonate (EC: DEC, 1:1 in volume) and the separator was Celgard 2300 membrane.

8.2.4. Electrochemical measurement

CV tests were done on a CHI660D electrochemical station at a current density of 0.40 mV/s. EIS measurements were carried out on the CHI660D at the open circuit potential in the frequency ranges of 100 kHz to 10 mHz. The galvanostatic discharge charge tests were carried out on the LAND CT2001A battery system at ambient environment. The capacity was obtained based on the total mass of the active materials.

8.3. Results and Disussion

8.3.1. Synthesis and Structure Analysis

The synthesis of G@FeS-GNRs is depicted in Figure 8.1. $FeCl_3$ was loaded on GNRs forming the $FeCl_3$-GNRs, which were reduced by Na/K alloy to Fe-GNRs. Fe_3O_4-GNRs were obtained by the oxidation of Fe-GNR under ambient condition. Following this,

Fe_3O_4-GNRs were positively charged by dispersing them in aqueous solution of polydiallyldimethylammonium chloride (PDADMAC) forming PDADMAC-Fe_3O_4-GNRs. G@Fe_3O_4-Gs were obtained through the electrostatic interaction between the positively charged PDADMAC-Fe_3O_4-GNRs and the negatively charged reduced graphene oxide, which was prepared by reduction of graphene oxide in hydrazine. Finally, G@FeS-GNRs was obtained after the vulcanization of G@Fe_3O_4-GNRs. As a control, FeS-graphene nanoribbons (FeS-GNRs) were prepared in the same procedure without the graphene wrapping process.

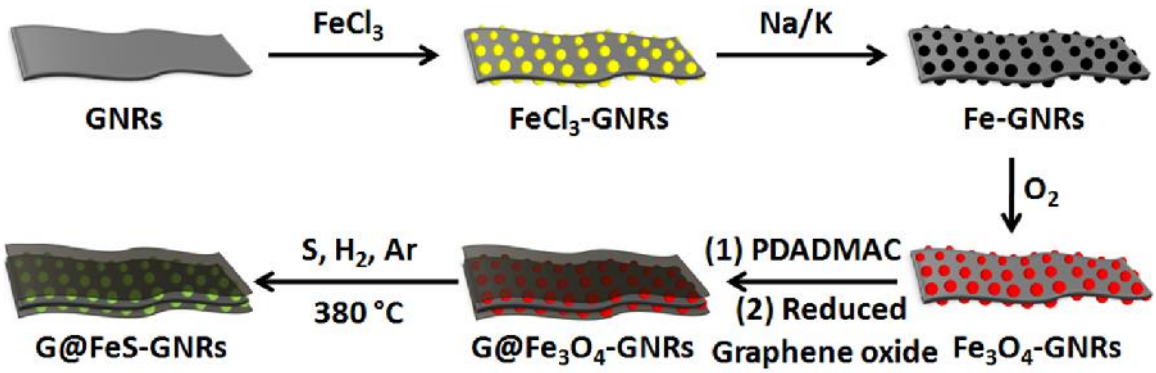

Figure 8.1. Schematic Illustration of the Synthesis of G@FeS-GNRs.

The morphologies of the FeS-GNRs and G@FeS-GNRs were characterized by scanning electron microscopy (SEM) and transmission electron microscopy (TEM). Figure 8.2a,b showed the structure of FeS-GNRs at various magnifications. FeS homogeneously grew on the surface of GNRs. The high resolution TEM image of FeS-GNRs demonstrated that the synthesized FeS were nanosized particles with the size of ~ 30 nm as shown in Figure 8.2e,f. The morphology of FeS-GNRs was further studied by the elemental mapping of C, O, Fe, and S. As shown in Figure 8.2e-h, these elements were uniformly distributed

in the GNRs. After the graphene wrapping, the morphology of G@FeS-GNRs was characterized by SEM as shown in Figure 8.2c,d. Graphene connected FeS-GNRs forming a utility. The separated FeS-GNRs can be observed on its surface in the high resolution (Figure 8.2d).

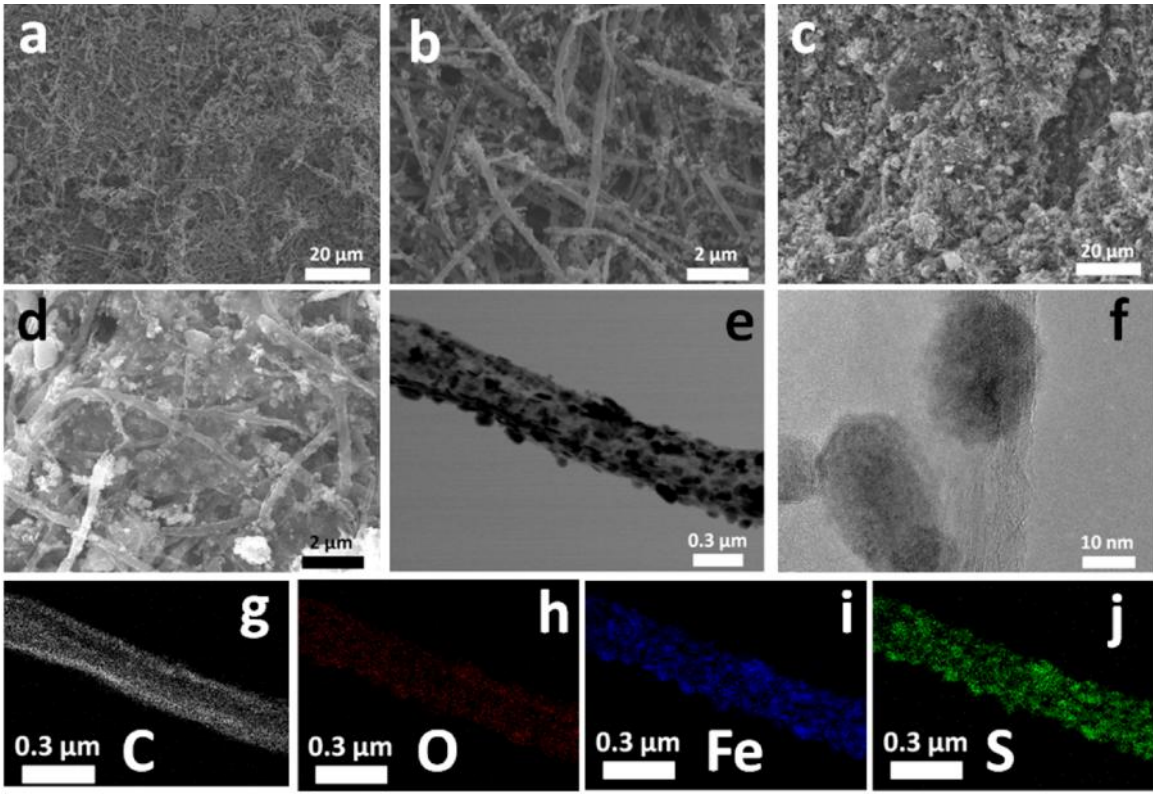

Figure 8.2. SEM images of FeS-GNRs (a,b) and G@FeS-GNRs (c,d). TEM images of FeS-GNRs (e,f) and corresponding elemental mapping of (e) C, (f) O, (g) Fe, and (h) S.

The composites were also characterized by X-ray diffraction (XRD), X-ray photoelectron spectroscopy (XPS), and thermogravimetric analysis (TGA). Figure 8.3a showed the XRD pattern of GNRs, G@Fe_3O_4-Gs, and G@FeS-GNRs. The GNRs demonstrated a strong diffraction peak (002) of graphite centered at 24.6°.[19,21] This peak

was obvious in the composites of G@Fe_3O_4-GNRs and G@FeS-GNRs. All the other diffraction peaks of G@FeS-GNRs can be attributed to FeS (JCPDS 65-9124).[17] It demonstrated that Fe_3O_4 was totally converted to FeS in the composites. Figure 8.3b was the survey XPS spectrum of G@FeS-GNRs. It can be seen that G@FeS-GNRs contained C, N, Fe, and O. O probably arises from the oxidation of FeS forming the iron oxide.[22]

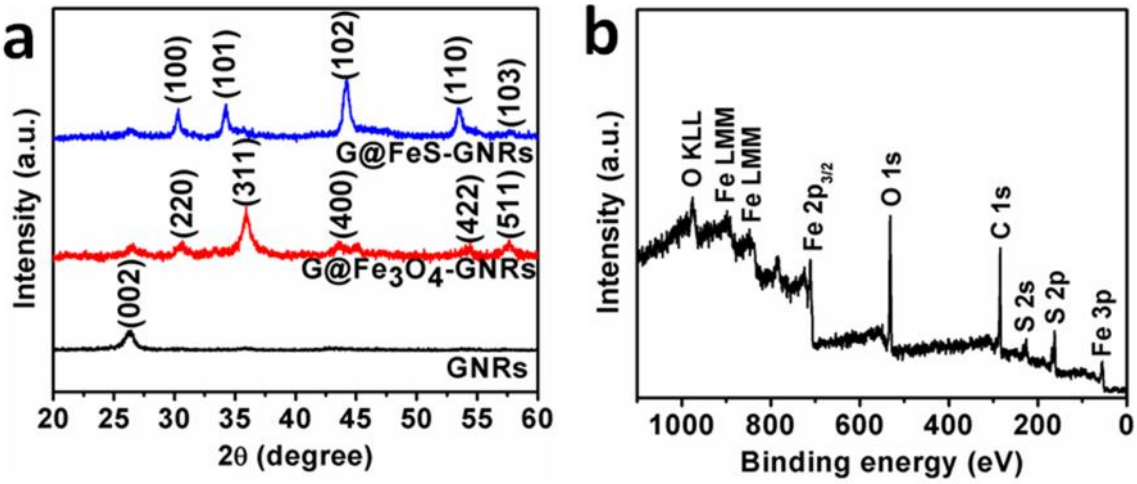

Figure 8.3. (a) XRD patterns of GNRs, G@Fe3O4-Gs, and G@FeS-GNRs. (b) XPS spectrum of G@FeS-GNRs.

TGA experiment was also carried out to determine the FeS content in the composite. As shown in Figure 7-4, the TGA curve showed 37.4 wt% loss of G@FeS-GNRs heated in air up to 900 °C, implying that the FeS content in the composite was 68.9 %.

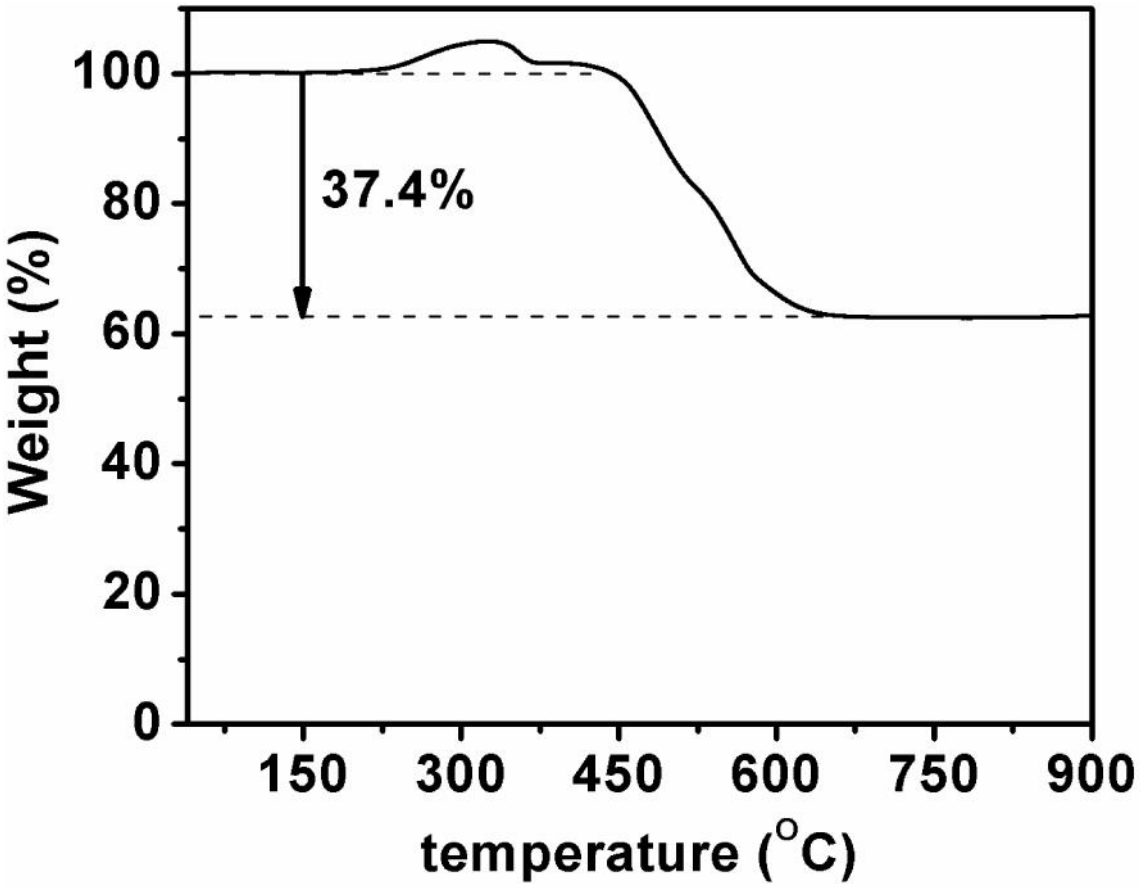

Figure 8.4. TGA curve of G@FeS-GNRs.

8.3.2. Electrochemical Evaluation

The electrochemical performance of G@FeS-GNRs as anodes in LIBs was analyzed. Cyclic voltammetry (CV) was taken place in order to understand the redox reaction of the electrode materials as shown in Figure 8.5a. In the first discharge cycle, the peak at 1.60 V was related to the reduction of Li with FeS forming Li_2FeS.[15,17,23] The sharp cathodic peak at 1.05 V resulted from the conversion reaction between Li and FeS, which formed Li_2S and Fe.[24,25] The peak at 0.66 V was from the formation of solid electrolyte interface (SEI) on the surface of the electrode materials.[17,19,26] In the following

charging process, the anodic peak at 1.97 V was caused by the oxidation of Fe to $Li_{2-x}FeS_2$ ($0 \leq x \leq 2$).[5,27,28] There was a sharp anodic peak at 2.40 V, which was also showed in the discharge charge curves with a small plateaus at 2.33 V in Figure 7-5b. In the second cycle and subsequent cycles, the cathodic peak at 0.66 V disappeared demonstrated that SEI mainly formed at the first cycle. The anodic peak at 2.40 V in CV (2.33 V in discharge charge curves) also disappeared. At the same time, the new cathodic peaks at 0.75 V became weaker and weaker with the augment of cycles number. All these abnormal peaks might result from the oxidation of FeS forming the iron oxide in the composite.[21,22] This phenomena were also observed in other published works using FeS related materials as anodes.[15,16] The peaks at 1.90 V and 1.32 V were related to the formation of Li_2FeS from $Li_{2-x}FeS$. The anodic peaks around 2.00 V was the reversible processes from $Li_{2-x}FeS$ to Li_2FeS.[28] In the first two discharge-charge profiles, the plateaus in the discharging and charging processes were consistent with the CV data. In addition, the first discharge capacity of G@FeS-GNRs were higher in value when compared to the theoretical capacity, which might result from decomposition of electrolyte, irreversible electrode reactions and/or the surface formation of SEI on the electrodes.[19] FeS-GNRs demonstrated the similar phenomena in CV and discharge charge curves as shown in Figure 8.5c,d.

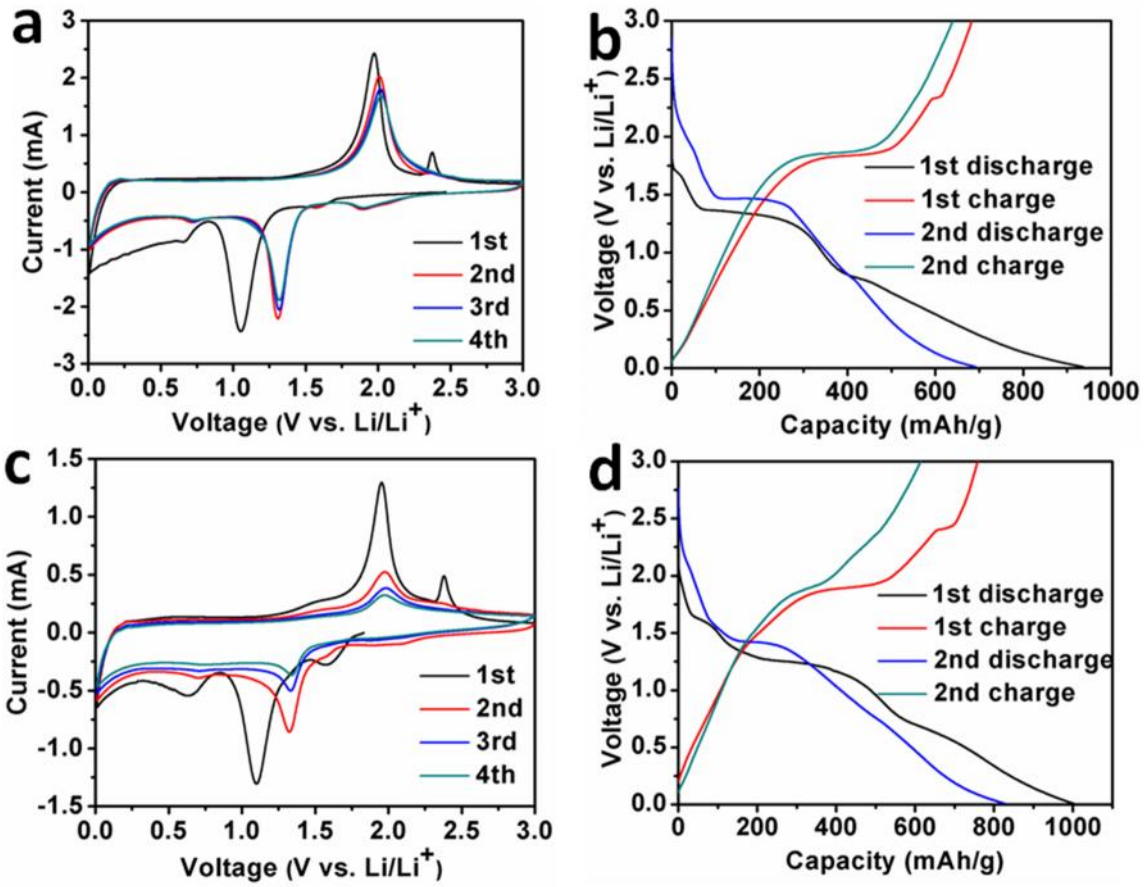

Figure 8.5. Cyclic voltammetry curves of G@FeS-GNRs (a) and FeS-GNRs (c) in the potential range of 0.01 and 3.0 V (vs. Li/Li+) at the scan rate of 0.4 mV/s. The discharge charge curves of G@FeS-GNRs (b) and FeS-GNRs (d) in the potential range of 0.01 and 3.0 V (vs. Li/Li$^+$) at the current density of 0.1 A/g.

The rate characteristics of G@FeS-GNRs were measured in the potential range of 0.01 and 3.0 V (vs. Li/Li$^+$) as indicated in Figure 8.6a. The stable capacity is observed at the same current densities in the range of 0.1 A/g to 1.0 A/g. At a current density of 0.1 A/g, the capacity of G@FeS-GNRs was 693 mAh/g at the second cycle. At the high current density of 1.0 A/g, its discharge capacity was 498 mAh/g at the 25th cycle. When the current density was reduced back from 1.0 A/g to 0.1 A/g, the value of capacity at different current densities not only returned, but also increased with the augment of cycle numbers,

such as the discharge capacity of 731 mAh/g at the 55th cycle in the current density of 0.1 A/g. On the contrary, FeS-GNRs showed low capacity that was only 78 mAh/g at the 25th cycle and bad rate performance. These results demonstrate that G@FeS-GNRs have improved rate performance in high capacity.

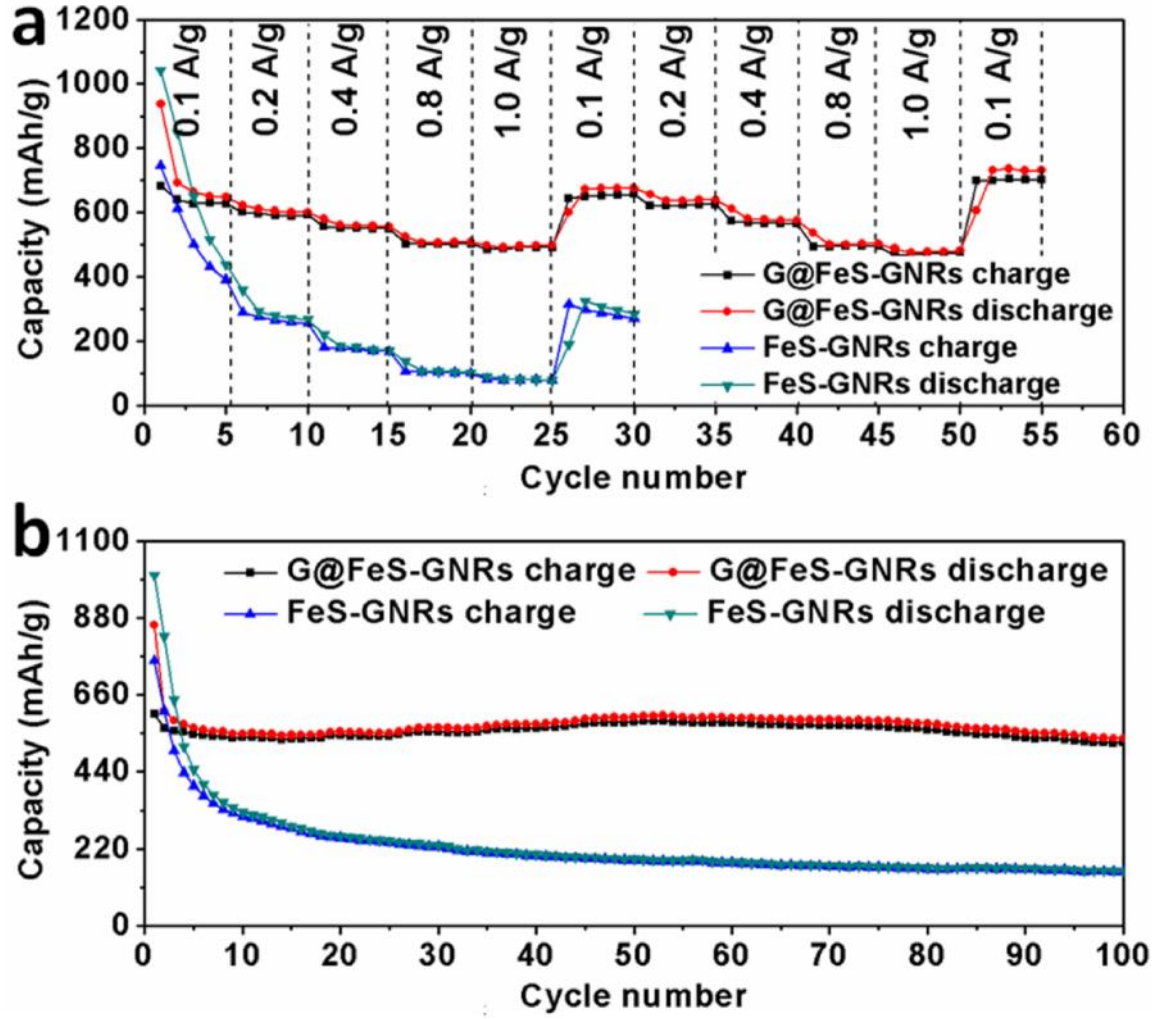

Figure 8.6. (a) Rate performance of G@FeS-GNRNRs at various current densities from 0.1 A/g to 1.0 A/g with respect to the cycle numbers. (b) Cycling performance of FeS-GNRs and G@FeS-GNRs at the current density of 0.4 A/g.

The cycling performance for G@FeS-GNRs was also evaluated using extended discharge-charge experiments at a current density of 0.4 A/g in the same potential range as indicated in Figure 8.6b. The reversible discharge capacity of G@FeS-GNRs was 616 mAh/g at second cycle. It still maintained a high capacity and reached 536 mAh/g after 100 cycles. FeS-GNRs suffered the rapid capacity decay. The discharge capacity decreased from 826 mAh/g on second cycle to 324 mAh/g after 10 cycles, only 157 mAh/g retained after 100 cycles. G@FeS-GNRs demonstrated a greatly improved cycling performance in LIBs compared to FeS-GNRs. Therefore, the design strategy worked efficiently and resulted in good electrochemical performance of G@FeS-GNRs in the LIBs.

EIS was utilized to study the kinetic properties of the G@FeS-GNRs, which have made significant improvements in capacity, rate performance, and cycling stability in the LIBs. Figure 8.7 shows the Nyquist plots of initial G@FeS-GNRs and FeS-GNRs. The insert is the equivalent circuit model.[10,19,29-31] The intercepts between the plot of G@FeS-GNRs and FeS-GNRs and x-axis stand for the internal resistance of the tested battery (R_s). The semicircles in the high and intermediate frequency range result from the Li^+ ion transport through the SEI film and the interfacial charge transfer reaction (R_{SEI+ct}) combined with the constant phase element and the electrochemical double-layer capacitive behaviors *CPE*. The sloping line with an angle ~ 45° to the real axis in the low frequency region is attributed to the solid-state Li diffusion into the active materials (Z_w).[19] The experimental Nyquist plots are modeled based on the equivalent circuit. The fitted impedance parameters are listed in Table 8.1. The R_{SEI+ct} of FeS-GNRs is 188.7 Ω and decreases to 39.6 Ω for G@FeS-GNRs. This demonstrates the graphene wrapping greatly

enhances the electrical conductivity of G@FeS-GNRs. This change is consistent with the variation in rate performance and cycling performance of G@FeS-GNRs and FeS-GNRs.

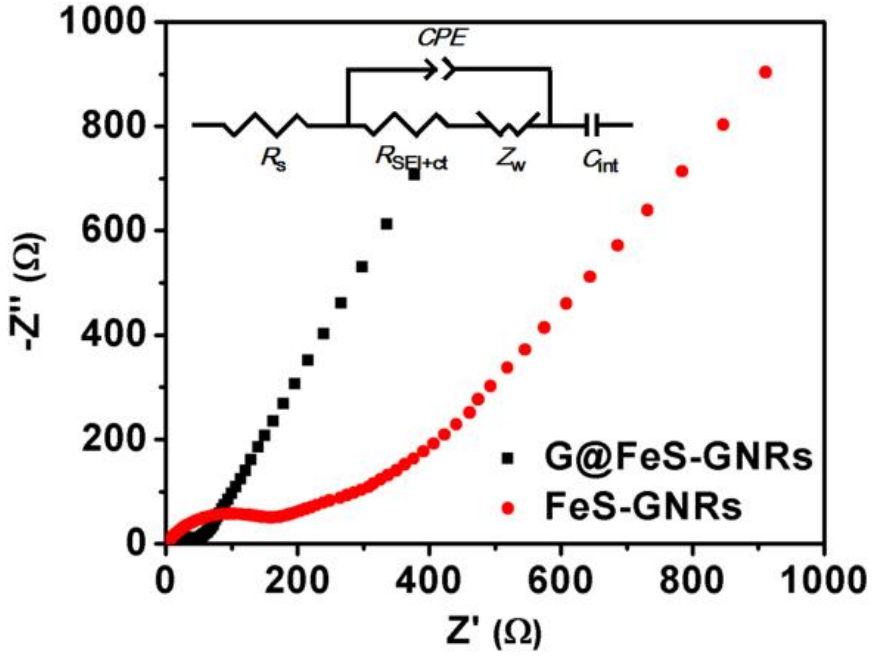

Figure 8.7. Nyquist plots of FeS-GNRs and G@FeS-GNRs. The insert is the equivalent circuit that was used to fit the experimental data.

Table 8.1. The EIS simulation parameters of G@FeS-GNRs and FeS-GNRs.

Active material	R_s (Ω)	*CPE* (μF)	R_{SEI+ct} (Ω)	Z_w (Ω)	C_{int}(mF)
G@FeS-GNRs	5.8	1.9	39.6	94.2	32.0
FeS-GNRs	3.0	0.4	188.7	303.0	135

8.4. Conclusion

In summary, we have successfully designed and synthesized sandwich structured graphene-FeS-graphene nanoribbons (G@FeS-GNRs). In this composite, the nanosized FeS particles were sandwiched between the graphene and graphene nanoribbons.

Electrochemical experiments demonstrate that G@FeS-GNRs exhibit high capacity, good rate performance, and improved cycling stability as anode materials due to the synergic effect among the graphene, graphene nanoribbons, and FeS. The method developed here is practical for the large-scale development of anode materials for lithium ion batteries.

8.5. References

1. Li, L.; Kovalchuk, A**.;** Peng, Z. W.; Gao, C. T.; Fei, H. L.; Yang, Y.; Zhong, Q. F.; Ruan, G. D.; Tour, J. M. Sandwich Structured Graphene-FeS-graphene Nanoribbons with Improved Cycling Stability for Lithium Ion Batteries **In preparation**. (L.L. conceived and designed the experiments. L.L. and K.A. prepared the materials. L.L., P.Z.W., G.C.T., F.H.L., Y.Y., Z.Q.F., and R.G.D. performed material characterization. L.L. tested the devices and wrote the paper. Finally, T.J.M. oversaw all research phases, provided regular guidance to the research and revised the manuscript. All authors discussed and commented on the manuscript.)
2. Wei. W.; Cui, X.; Chen, W.; Ivey, D. G. Manganese oxide-based materials as electrochemical supercapacitor electrodes. *Chem. Soc. Rev.* **2011,** *40*, 1697-1721
3. Zhu, J.; Yang, D.; Yin, Z.; Yan, Q.; Zhang, H. Graphene and Graphene-Based Materials for Energy Storage Applications. *Small* **2014**, n/a-n/a.
4. Su, Y.; Li, S.; Wu, D.; Zhang, F.; Liang, H.; Gao, P.; Cheng, C.; Feng, X. Two-Dimensional Carbon-Coated Graphene/Metal Oxide Hybrids for Enhanced Lithium Storage. *ACS Nano* **2012,** *6*, 8349-8356.

5. Etacheri, V.; Marom, R.; Elazari, R.; Salitra, G.; Aurbach, D. Challenges in the development of advanced Li-ion batteries: a review. *Energy Environ. Sci.* **2011,** *4*, 3243-3262.
6. Tarascon, J. M.; Armand, M. Issues and Challenges FacingRechargeable Lithium Batteries. *Nature* **2001,** *414*, 359-367.
7. Wang, B.; Li, X.; Zhang, X.; Luo, B.; Jin, M.; Liang, M.; Dayeh, S. A.; Picraux, S. T.; Zhi, L. Adaptable Silicon–Carbon Nanocables Sandwiched between Reduced Graphene Oxide Sheets as Lithium Ion Battery Anodes. *ACS Nano* **2013,** *7*, 1437-1445.
8. Whittingham, M. S. Lithium Batteries and Cathode Materials. *Chem. Rev.* **2004,** *104*, 4271-4302.
9. Wang, H.; Dai, H. Strongly coupled inorganic-nano-carbon hybrid materials for energy storage. *Chem. Soc. Rev.* **2013,** *42*, 3088-3113.
10. Chang, K.; Chen, W. l-Cysteine-Assisted Synthesis of Layered MoS_2/Graphene Composites with Excellent Electrochemical Performances for Lithium Ion Batteries. *ACS Nano* **2011,** *5*, 4720-4728.
11. Su, Q.; Xie, J.; Zhang, J.; Zhong, Y.; Du, G.; Xu, B. In Situ Transmission Electron Microscopy Observation of Electrochemical Behavior of CoS_2 in Lithium-Ion Battery. *ACS Appl Mater Interfaces* **2014,** *6*, 3016-3022.
12. Su, C. W.; Li, J.-M.; Yang, W.; Guo, J. M. Electrodeposition of Nis3S2/Ni Composites as High-Performance Cathodes for Lithium Batteries. *J. Phys. Chem. C* **2013,** *118*, 767-773.

13. Stephenson, T.; Li, Z.; Olsen, B.; Mitlin, D. Lithium ion battery applications of molybdenum disulfide (MoS_2) nanocomposites. *Energy Environ. Sci.* **2014,** *7*, 209-231.
14. Zheng, S.; Chen, Y.; Xu, Y.; Yi, F.; Zhu, Y.; Liu, Y.; Yang, J.; Wang, C. In Situ Formed Lithium Sulfide/Microporous Carbon Cathodes for Lithium-Ion Batteries. *ACS Nano* **2013,** *7*, 10995-11003.
15. Xu, C.; Zeng, Y.; Rui, X.; Xiao, N.; Zhu, J.; Zhang, W.; Chen, J.; Liu, W.; Tan, H.; Hng, H. H.; Yan, Q. Controlled Soft-Template Synthesis of Ultrathin C@FeS Nanosheets with High-Li-Storage Performance. *ACS Nano* **2012,** *6*, 4713-4721.
16. Wu, B.; Song, H.; Zhou, J.; Chen, X. Iron sulfide-embedded carbon microsphere anode material with high-rate performance for lithium-ion batteries. *Chem. Commun.* **2011,** *47*, 8653-8655.
17. Fei, L.; Lin, Q.; Yuan, B.; Chen, G.; Xie, P.; Li, Y.; Xu, Y.; Deng, S.; Smirnov, S.; Luo, H. Reduced Graphene Oxide Wrapped FeS Nanocomposite for Lithium-Ion Battery Anode with Improved Performance. *ACS Appl Mater Interfaces* **2013,** *5*, 5330-5335.
18. Wang, X. F.; Xiang, Q. Y.; Liu, B.; Wang, L. J.; Tao Luo, Chen, D.; Shen, G. S. TiO_2 modified FeS Nanostructures with Enhanced Electrochemical Performance for Lithium-Ion Batteries *Sci*. *Reports* 2007, 3.
19. Li, L.; Raji, A. R. O.; Tour, J. M. Graphene-Wrapped MnO_2-Graphene Nanoribbons as Anode Materials for High-Performance Lithium Ion Batteries. *Adv. Mater.* **2013,** *25*, 6298-6302.

20. Genorio, B.; Lu, W.; Dimiev, A. M.; Zhu, Y.; Raji, A. R. O.; Novosel, B.; Alemany, L. B.; Tour, J. M. In Situ Intercalation Replacement and Selective Functionalization of Graphene Nanoribbon Stacks *ACS Nano* **2012**, *6*, 4231-4240.
21. Campos-Delgado, J.; Romo-Herrera, J. M.; Jia, X.; Cullen, D. A.; Muramatsu, H.; Kim, Y. A.; Hayashi, T.; Ren, Z.; Smith, D. J.; Okuno, Y.; Ohba, T.; Kanoh, H.; Kaneko, K.; Endo, M.; Terrones, H.; Dresselhaus, M. S.; Terrones, M. Bulk Production of a New Form of sp^2 Carbon: Crystalline Graphene Nanoribbons. *Nano Lett.* **2008,** *8*, 2773-2778.
22. Dong, C.; Zheng, X.; Huang, B.; Lu, M. Enhanced electrochemical performance of FeS coated by Ag as anode for lithium-ion batteries. *Applied Surface Science* **2013,** *265*, 114-119.
23. Saadat, S.; Tay, Y. Y.; Zhu, J.; Teh, P. F.; Maleksaeedi, S.; Shahjamali, M. M.; Shakerzadeh, M.; Srinivasan, M.; Tay, B. Y.; Hng, H. H.; Ma, J.; Yan, Q. Template-Free Electrochemical Deposition of Interconnected ZnSb Nanoflakes for Li-Ion Battery Anodes. *Chem. Mater.* **2011,** *23*, 1032-1038.
24. Kim, Y.; Goodenough, J. B. Lithium Insertion into Transition-Metal Monosulfides: Tuning the Position of the Metal 4s Band. *J. Phys. Chem. C* **2008,** *112*, 15060-15064.
25. Golodnitsky, D.; Peled, E. Pyrite as cathode insertion material in rechargeable lithium/composite polymer electrolyte batteries. *Electrochimica Acta* **1999,** *45*, 335-350.

26. Lai, H.; Li, J.; Chen, Z.; Huang, Z. Carbon Nanohorns As a High-Performance Carrier for MnO_2 Anode in Lithium-Ion Batteries. *ACS Appl Mater Interfaces* **2012,** *4*, 2325-2328.
27. Seo, J.-w.; Jun, Y.-w.; Park, S.W.; Nah, H.; Moon, T.; Park, B.; Kim, J.-G.; Kim, Y. J.; Cheon, J. Two-Dimensional Nanosheet Crystals. *Angew. Chem. Int. Ed.* **2007,** *46*, 8828-8831.
28. Kim, B. C.; Takada, K.; Ohta, N.; Seino, Y.; Zhang, L.; Wada, H.; Sasaki, T. All solid state Li-ion secondary battery with FeS anode. *Solid State Ionics* **2005,** *176* (31–34), 2383-2387.
29. Qian, D.; Xu, B.; Cho, H.-M.; Hatsukade, T.; Carroll, K. J.; Meng, Y. S. Lithium Lanthanum Titanium Oxides: A Fast Ionic Conductive Coating for Lithium-Ion Battery Cathodes. *Chem. Mater.* **2012,** *24*, 2744-2751.
30. Yang, S.; Feng, X.; Zhi, L.; Cao, Q.; Maier, J.; Müllen, K. Nanographene-Constructed Hollow Carbon Spheres and Their Favorable Electroactivity with Respect to Lithium Storage. *Adv. Mater.* **2010,** *22*, 838-842.
31. Han, H.; Song, T.; Lee, E. K.; Devadoss, A.; Jeon, Y.; Ha, J.; Chung, Y.-C.; Choi, Y.-M.; Jung, Y.-G.; Paik, U. Dominant Factors Governing the Rate Capability of a TiO_2 Nanotube Anode for High Power Lithium Ion Batteries. *ACS Nano* **2012,** *6*, 8308-8315.

Chapter 9

SnO_2-Reduced Graphene Oxide Nanoribbons As Anode for Lithium Ion Batteries with Enhanced Cycling Stability

This chapter was entirely copied from reference 1.

9.1. Introduction

The electrochemical storage of energy using lithium ion batteries (LIBs) is a most effective and practical technology.[2,3] LIBs need high power and energy density with excellent performance during cycling to meet critically important needs of growing applications in electric vehicles, multifunctional electrical devices and communications equipment. LIBs will also be important in storing the energy produced using renewable energy sources since such sources may be far from existing electrical grids.[4,5] The development of better electrode materials has been the subject of intense research.[2,3,6] Tin oxide (SnO_2) has attracted attention because it has a theoretical reversible capacity of ~

790 mAh/g, which is almost two times higher than that of anodes based on graphite.[7,8] However, the reversible charging and discharging process is accompanied by a large volume variation. The volume change can result in the pulverization of SnO_2 and the loss of electric contact. These causes quick capacity decay upon extending cycling.[7,9] Therefore, the development of SnO_2-based anodes with enhanced cycling stability and high capacity is becoming important.

Research based on different strategies for improvement of SnO_2-based anodes has been reported. One approach is to prepare the SnO_2-based composites using different carbon materials, such as amorphous carbon,[9-12] graphene,[13-17] carbon nanotubes,[18-20] and graphene nanoribbons.[21] The carbon materials not only relax the volume variation, but also improve the electrical conductivity of the composites. Another approach is the use of nanostructured SnO_2 such as nanotubes,[22,23] nanowires[24] and nanosheets,[25] to buffer the volume variation. At the same time, the nanostructures can improve the kinetic properties of the electrode materials, stabilize the solid electrolyte interface (SEI), and improve the rate performance.[9,26] To prepare the SnO_2 composites with other matrix elements or metal oxides and control the proper voltage range of the batteries can be also helpful to reduce the negative effect caused by the volume changes.[17,18,27-29] These strategies have made improvements in the electrochemical performance of the SnO_2 based anode materials. However, the cycling stability of the SnO_2 based anode materials has not been similarly improved. Therefore, preparation of high capacity SnO_2-based anode materials with improved cycling stability remains a challenge worth pursuing.

In this study, we developed a facile strategy to fabricate SnO_2-reduced graphene oxide nanoribbons (SnO_2-rGONRs), which have both the merits of SnO_2 nanostructures

and carbon materials aimed at the improvement of LIBs energy storage, especially the cycling performance. The synthesis of graphene oxide nanoribbons (GONRs) is scalable; GONRs have a high surface area, making them suitable templates on which to directly grow SnO_2 nanoparticles without aggregation using a wet chemistry process in water to form the SnO_2-GONRs.[30,31] SnO_2-rGONRs were produced by reduction with hydrazine.[32] rGONRs maintain contact with the SnO_2 nanparticles, producing good electrical conductivity of the SnO_2-rGONRs. More importantly, rGONRs improve the electrochemical stability characteristics of the composite, thereby buffering volume changes, thus. The non-aggregated, nanosized SnO_2 particles effectively relieve volume change stress due to their high surface area. What is more, the nanosized structure can reduce the diffusion path length of the metal particles that are forming through the alloy-dealloy process, increasing the concentration of Li ion in the active materials, leading to the enhancement of the anode kinetic and current rate capabilities.[26] SnO_2-rGONRs as anode materials demonstrate high capacity, good rate performance, and excellent cycling operation. The reversible discharge capacity was 640 mAh/g at 3.0 A/g after 160 cycles and 1027 mAh/g at 0.1 A/g after 165 cycles with current rates varying from 0.1 to 3.0 A/g. The discharge capacity shows no decay and increases about 2.2% after 600 cycles compared to the second cycle at a current density of 1.0 A/g. Based on this data, SnO_2-rGONRs are superb candidates for use as anode materials with great cycling stability in LIBs.

9.2. Experiments

9.2.1. Materials synthesis

9.2.1.1. Synthesis of graphene oxide nanoribbons

Graphene oxide nanoribbons (GONRs) were prepared as previously described.[29] Briefly, 300 mg of MWCNTs were suspended in the mixture of concentrated H_2SO_4 (72 mL) and H_3PO_4 (8 mL), and 1500 mg of $KMnO_4$ were added. The reaction mixture was then heated to 65 °C for 2 h and worked up as previously described.

9.2.1.2. Synthesis of SnO_2-reduced graphene oxide nanoribbons

SnO_2-graphene oxide nanoribbons (SnO_2-rGONRs) were prepared by a modified polyol method followed by the chemical reduction of GONRs. In a typical procedure, GONRs (200 mg) were dispersed in a solution of deionized water (D.I. water, 50 mL) and ethylene glycol (150 mL) by bath sonication (30 min, Cole Parmer ultrasonic cleaner) and tip sonication (5 min, Misonix Sonicator 3000). $SnCl_2$ (1000 mg, 4.4 mmol) was added to the above dispersion and the mixture was bath sonicated for 5 min, followed by adding NaOH (solid, 400 mg, 10 mmol). The reaction was kept at 160 °C for 2 h. SnO_2-GONRs (750 mg) was collected after centrifugation with D.I. water and methanol (4 cycles of 20 min each) and drying in a vacuum oven of 3.1 inch Hg at 60 °C for 20 h. Finally, SnO_2-GONRs were dispersed in D.I. water and were reduced by hydrazine (0.035 mL, 0.72 mmol) and NH_4OH (0.15 mL, 2.1 mmol) at 95 °C for 2 h. SnO_2-rGONRs were obtained after centrifugation with D.I. water (50 mL, 2 times) and methanol (50 mL, 2 times), followed by drying in a vacuum oven of 3.1 inches Hg at 60 °C for 20 h.

For comparison purposes, rGONRs without SnO_2 were obtained after the reduction of GONRs with hydrazine similar to the procedure described above.

9.2.2. Materials characterization

Products were characterized by XRD (Rigaku D/Max Ultima II); XPS (PHI Quantera); SEM (JEOL 6500); TGA (TA Instruments, Q50); and TEM (JEM2100F TEM).

9.2.3. Device abrication

80 wt% of active composite, 10 wt% of carbon black (Super P), and 10 wt% of polyvinylidene difluoride (PVDF, Alfa Aesar) were dissolved in *N*-methyl-2-pyrrolidone (NMP, Sigma-Aldrich) to form the slurry. The slurry was coated on a copper foil substrate and was dried in vacuum oven at 120 °C for 10 hours forming the anode. The mass laoding of the electrodes is ~ 0.7g/cm^2. Electrochemical tests were performed using CR2032 coin-type cells with lithium metal foil as the counter electrode. The electrolyte was 1 M $LiPF_6$ in a solution of ethylene carbonate and diethyl carbonate (1:1 vol:vol). Celgard 2300 membrane was used as separator.

9.2.4. Electrochemical measurement

Cyclic voltammetry (CV) tests were done on a CHI660D electrochemical station at a current density of 0.60 mV/s; Electrochemical impedance spectroscopy (EIS) measurements were carried out on the CHI660D at the open circuit potential in the frequency range of 100 kHz to 10 mHz, and the galvanostatic discharge charge test was carried out on the LAND CT2001A battery system at room temperature. The capacity value was based on the mass of the active materials of SnO_2-rGONRs.

9.3. Results and Discussion

9.3.1. Synthesis and structure analysis

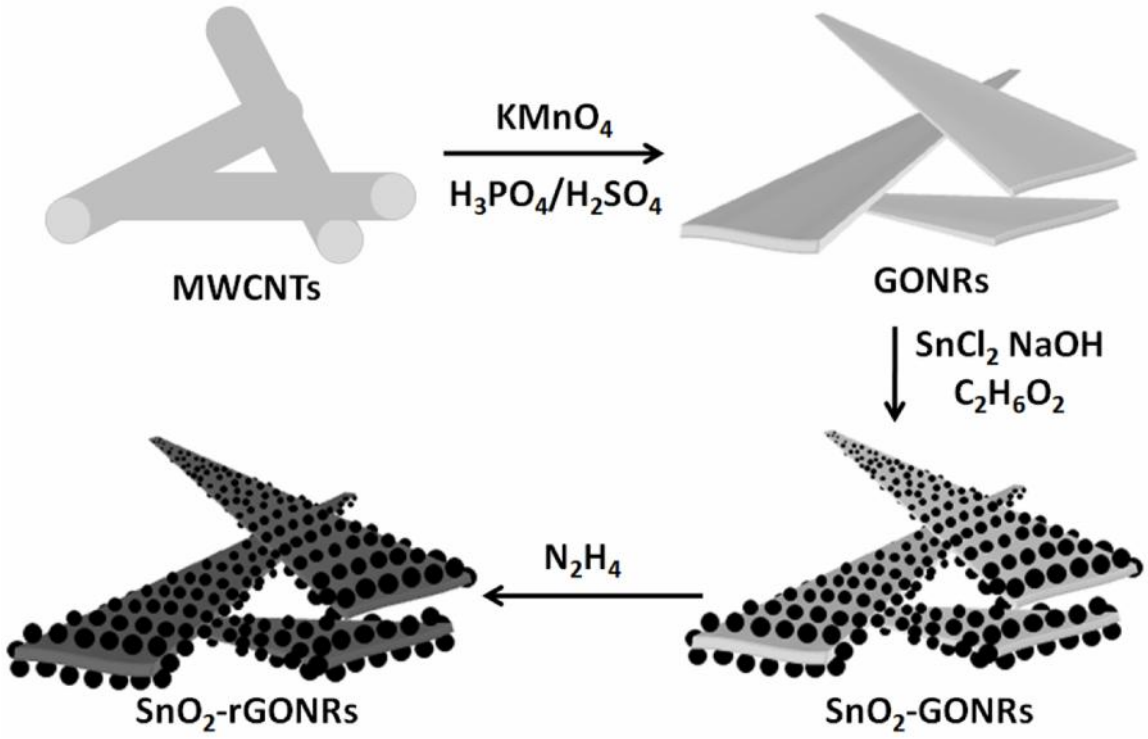

Figure 9.1. Schematic illustration of the synthesis of SnO2-rGONRs.

The preparation of SnO_2-rGONRs is shown in Figure 9.1. Multiwalled carbon nanotubes (MWCNTs) were used to prepare the GONRs by unzipping using solution chemistry. Then, SnO_2-GONRs were obtained through the reaction between $SnCl_2$ and NaOH in the presence of GONRs in ethylene glycol. Finally, SnO_2-rGONRs was obtained by hydrazine reduction. In order to well study the morphology of SnO_2-rGONRs, rGONRs were also prepared in the same way of SnO_2-rGONRs.

The structure of the SnO_2-rGONRs and rGONRs was characterized by scanning electron microscopy (SEM) and transmission electron microscopy (TEM). Figure 9.2a-d show the morphology of rGONRs at a width of ~ 300 nm and ~ 8 µm length. Figure 9.2e,f depict the structure of SnO_2-rGONRs at various magnifications. Nanosized SnO_2 particles homogeneously grew on the surface of rGONRs. The high resolution TEM images of SnO_2-rGONRs in Figure 9.2g,h demonstrate that the synthesized SnO_2 were nanosized particles, which formed a thin surface layer on rGONRs.

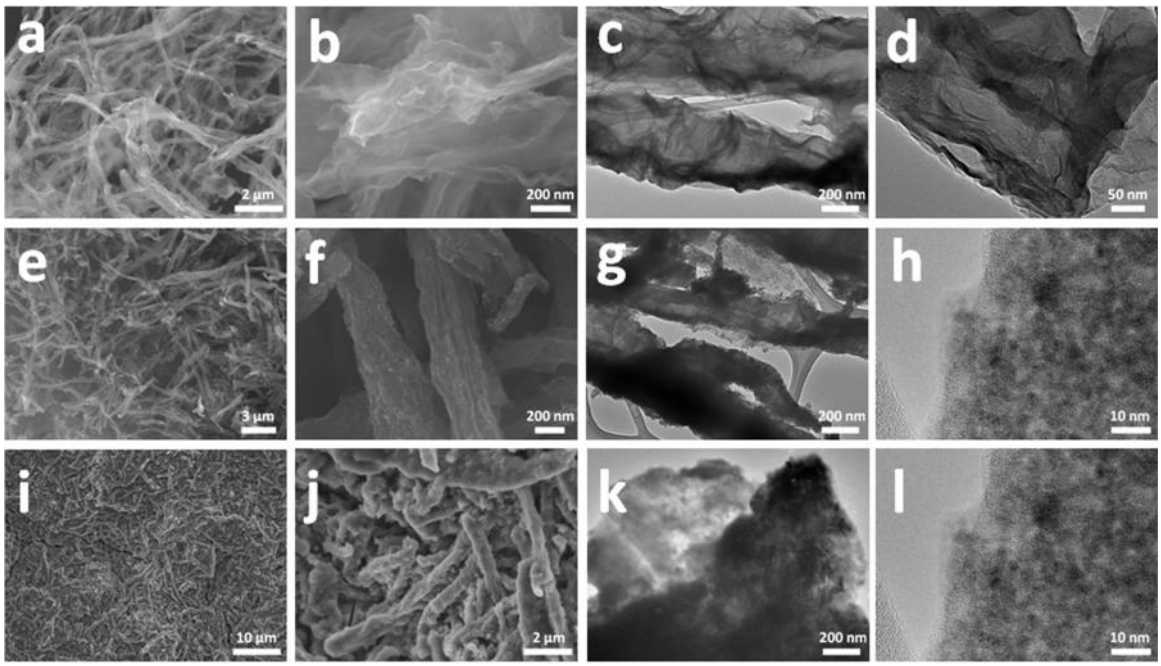

Figure 9.2. SEM images of rGONRs (a, b), SnO2-rGONRs (e, f), and SnO2-rGONRs-200 (i, j) at different resolutions. TEM images of rGONRs (c, d), SnO2-rGONRs (g, h), and SnO2-rGONRs-200 (k, l) at different resolutions.

The composites were also characterized by X-ray diffraction (XRD) and X-ray photoelectron spectroscopy (XPS). The XRD pattern of rGONRs and SnO_2-rGONRs is shown in Figure 9.3a. The rGONRs demonstrated the diffraction peak (002) of graphite

centered at 24.6°.[33] This peak was absent in the SnO_2-rGONRs because SnO_2 nanoparticles covered the surface of the rGONRs and the strong XRD peaks of SnO2 overlapped those of the rGONRs. Figure 9.3b is the survey XPS spectrum of composite SnO_2-rGONRs**.** From this analysis it is seen that SnO_2-rGONRs only contained Sn, C, O, and trace amounts of N, the last probably arises from the hydrazine. Moreover, Sn 3d3/2 and Sn 3d5/2 were detected in the fine spectrum of Sn 3d, confirming the formation of SnO_2-containing SnO_2-rGONRs (Figure 9.3c). Figure 9.3d shows the fine XPS C1s spectrum of of SnO_2-rGONRs, which was deconvoluted into five peaks located at 284.5, 285.5, 286.4, 287.6, and 289.1, which were assigned to C=C (sp^2 C), C-C (sp^3 C), C-O, C=O and O-C=O, respectively.[30,33,34] The low concentration of oxidized carbon in the SnO_2-rGONRs suggests that the GONRs were almost completely reduced by hydrazine.[30,33] The data demonstrates that SnO_2 nanoparticles are indeed grown on the rGONRs.

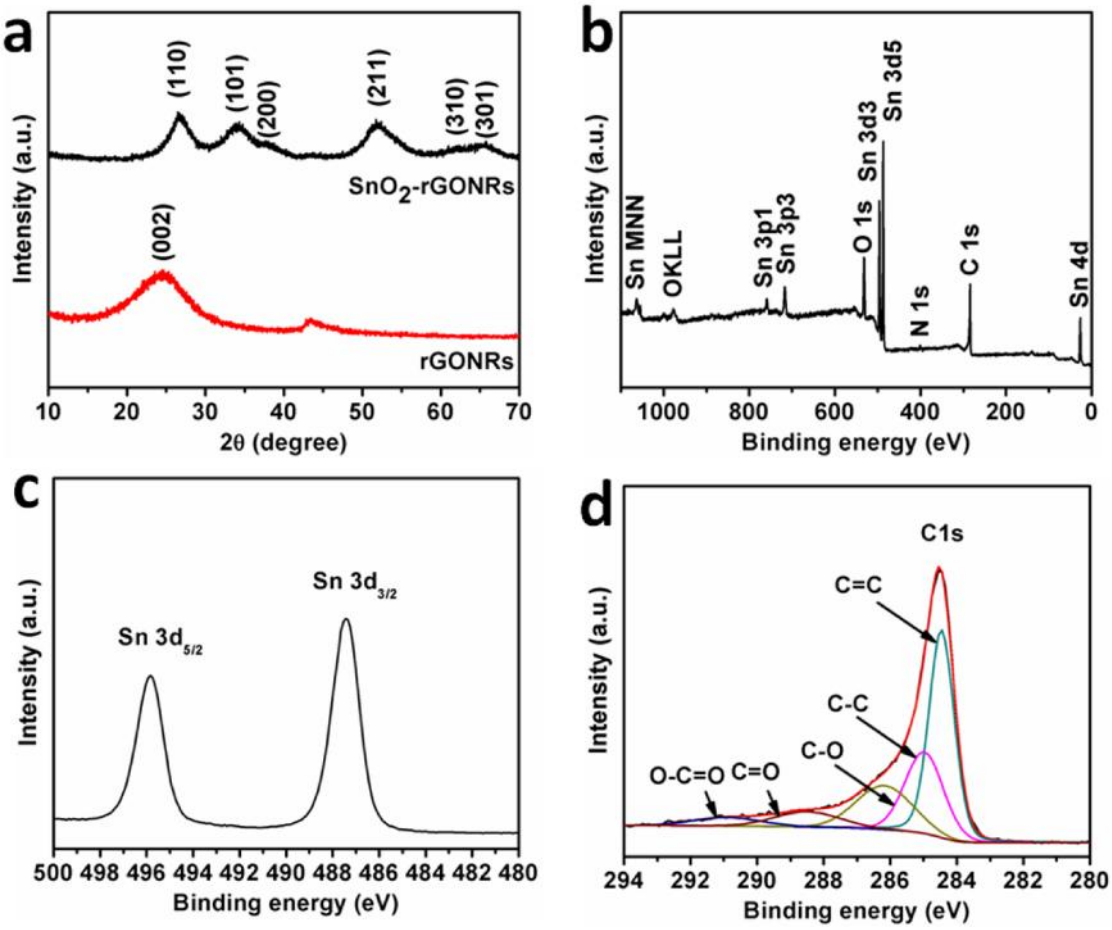

Figure 9.3. (a) XRD pattern of SnO2-rGONRs and rGONRs. (b) XPS spectra of SnO2-rGONRs. (c) Sn 3d XPS spectra of SnO2-rGONRs. (d) C1s XPS spectra of SnO2-rGONRs.

TGA experiment was also carried out to determine the SnO_2 content in the composite. Figure 9.4 showed the TGA curve of SnO_2-rGONRs demonstrating 70% SnO_2 content in the composite measured in air at the heating rate of 5 °C min^{-1}.

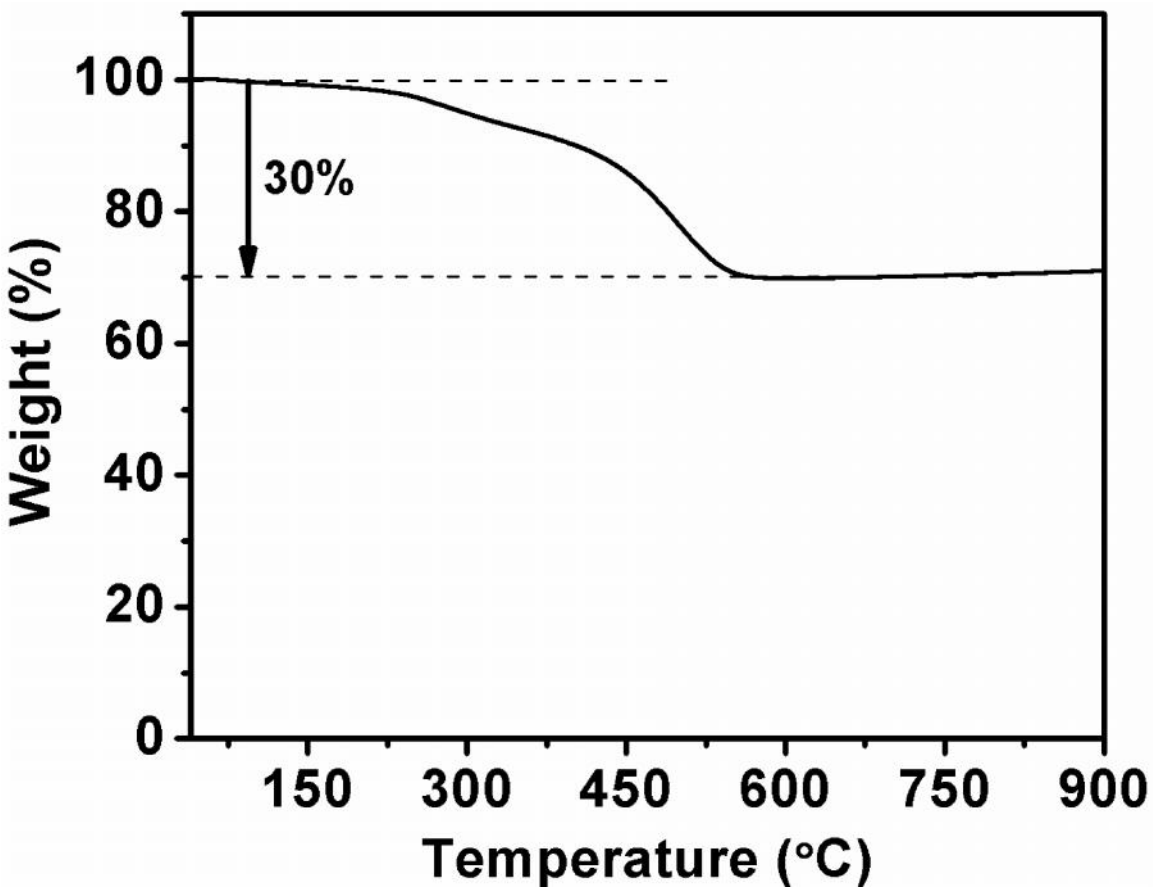

Figure 9.4. TGA curves of SnO2-rGONRs showing 70% SnO2 content recorded in air at a heating rate of 5 °C min^{-1}.

9.3.2. Electrochemical evaluation

The electrochemical performance of SnO_2-rGONRs as anodes in LIBs was analyzed. Figure 9.5a shows the first two cycles of CV. In the first discharge cycle, there are three cathodic peaks centered at 1.3 V, 0.8 V, and 0.06 V. The peak at 1.3 V results from the reduction of SnO_2 to SnO and the formation of Li_2O; the broad cathodic peaks ~ 0.8 V result from the reduction of SnO_2 to Sn and Li_2O, SnO to Sn, and the formation of solid electrolyte interface; the peak at 0.06 V is from the alloying of Sn and Li and the

intercalation of lithium ion into the rGONRs. At the same time, there are two anodic peaks at 0.57 V and 1.26 V. The former peak is the dealloying of Sn and Li, the other peak results from the partial conversion of Sn to SnO_2 and SnO.[9,35] In the second cycle, the broad peak at 0.8 V disappears and a new appears at 0.96 V. This demonstrates that the formation of SEI mainly occurs in the first cycle and the new peak results from the peak shift of the reduction reaction of SnO_2.[9] The CV curves mostly overlap, indicating the good reversibility of the electrochemical reaction. In the first two discharge-charge profiles, two plateaus in the discharging and charging processes are consistent with the CV data (9.5b). In addition, the first discharge capacity of SnO_2-rGONRs is higher in value when compared to the theoretical capacity, which might result from decomposition of electrolyte, irreversible electrode reactions and/or the surface formation of SEI on the electrodes.[9,35]

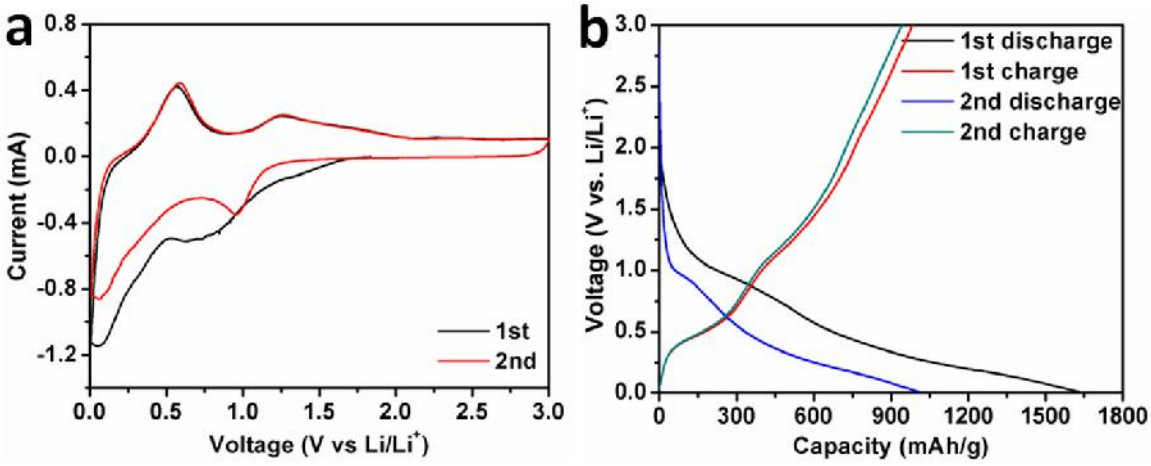

Figure 9.5. (a) CV voltammograms of SnO2-rGONRs at the scan rate of 0.4 mV/s in the potential range of 0.01 and 3.0 V (vs. Li/Li+). (b) The first two discharge-charge curves of SnO2-rGONRs at a current density of 0.1 A/g in the potential range of 0.01 and 3.0 V (vs. Li/Li+).

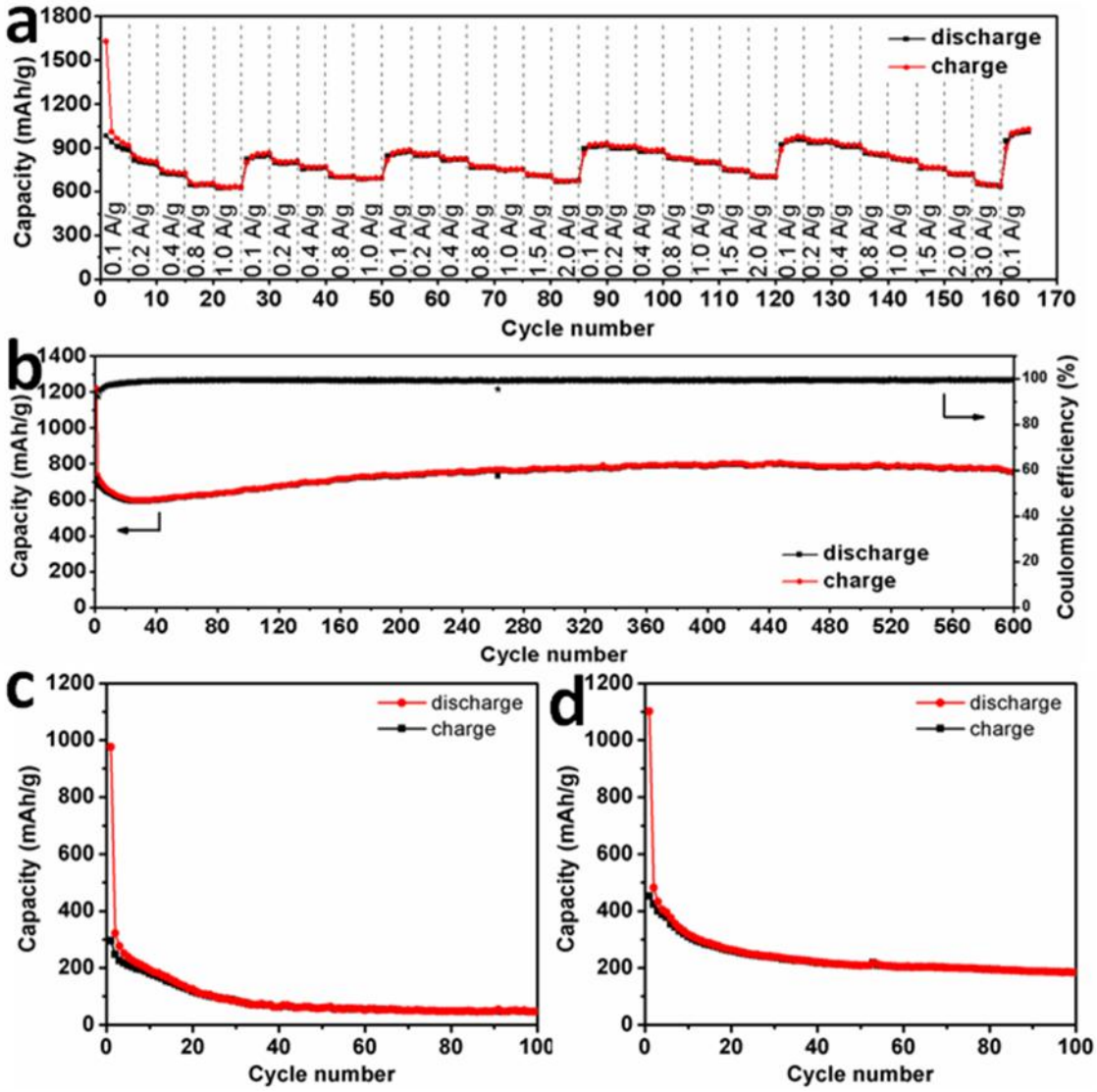

Figure 9.6. Rate performance of SnO2-rGONRs (a) at various current rates from 0.1 A/g to 3.0 A/g with respect to the cycle number. (b) Cycling performance of SnO2-rGONRs, SnO2 (c), and rGONRs (d) at 1.0 A/g.

The rate characteristics of the SnO_2-rGONRs were evaluated in the same potential window as indicated in Figure 9.6a. The stable capacity is observed at different current densities from 0.1 A/g to 3 A/g. At a current density of 0.1 A/g, the capacity of SnO_2-rGONRs was 942.8 mAh/g at the 2nd cycle. At the high current density of 3 A/g, the

discharge capacity of SnO_2-rGONRs was ~ 640 mAh/g. When the current density was reduced back from 3.0 A/g to 0.1 A/g, the value of specific capacity at different current densities returned to its original value and then, at the same current density, increased as the cycle numbers increased. An increase in the capacity to 1027 mAh/g at the 165^{th} cycle was obtained at a current density of 0.1 A/g. These results demonstrate that SnO_2-rGONRs electrode materials have high capacity and good rate performance.

The cycling performance for SnO_2-rGONRs was also measured using discharge-charge repetition at a current density of 1.0 A/g as indicated in Figure 9.6b. The reversible discharge capacity of SnO_2-rGONRs was 737 mAh/g on its second cycle. The value dropped slowly to 598 mAh/g at the 30^{th} cycle, but then increased in the following cycles and reached 806 mAh/g at the 448^{th} cycle. The increase of the capacity in the following cycles indicated that the materials of SnO_2-rGONRs might have an activation step. The electrolyte did not well contact with inner part of SnO_2-rGONRs. It took some time for the electrolyte to flood the inner part of the active materials. When they contacted with each other with the augment of the cycle numbers, the inner part of SnO_2-rGONRs became electrochemically active, leading to the capacity increase. It still maintained a high capacity and reached 753 mAh/g after 600 cycles. In addition, the Coulombic efficiency of SnO_2-rGONRs remained at > 99.5% excluding the first several cycles. On the contrary, the discharge capacity of pure SnO_2 was only 322 mAh/g at the 2^{nd} cycle as shown in Figure 8-6c. It also suffered serious capacity decay with less than 20% capacity retained after 40 cycles from the 2^{nd} cycle. Figure 9.6d showed the cycling performance of rGONRs. Therefore, the materials of SnO_2-rGONRs demonstrate a greatly improved cycling performance in LIBs. The morphology of SnO_2-rGONRs after 200 cycles discharge-charge

processes (SnO_2-rGONRs-200) (Figure 9.2i,j) almost has no change compared to the initial morphology of SnO_2-rGONRs in Figure 9.2e,f. The morphology of SnO_2-rGONRs-200 was also analyzed by TEM shown in Figure 9.2k,l. The particle still had good crystal structure. Therefore, the design strategy worked well and resulted in good electrochemical performance in the LIBs.

EIS was utilized to study the kinetic properties of the SnO_2-rGONRs, which have made significant improvements in rate performance, capacity, and especially the excellent cycling stability in the LIBs. Figure 9.7a shows the Nyquist plots of initial SnO_2-rGONRs and SnO_2-rGONRs-200. The insert is the enlarged part in the high frequency region. For this system, Figure 9.7b illustrates the equivalent circuit model. In Figure 9.7b, Rs is the internal resistance of the tested battery, RSEI and Rct represents the SEI surface and charge-transfer resistance, CPE1 and CPE2 are associated with constant phase element and double layer capacitance across the surface, Zw is the Warburg resistance related to the lithium diffusion process, and the Cint is the interaction capacitance.[36,37] In Figure 8-7a, the inset plot of SnO_2-rGONRs-200 shows two semicircles in the high and intermediate frequency range and a sloping line with an angle ~ 45° to the real axis in the low frequency region. The two semicircles result from the Li^+ ion transport through the SEI film (R_{SEI}) and the interfacial charge transfer reaction (R_{ct}) combined with the constant phase element and the electrochemical double-layer capacitive behaviors $CPE1$ and CPE_2, respectively. The sloping line is attributed to the solid-state Li diffusion into the active materials (Z_w).[36] The experimental Nyquist plots are modeled based on the equivalent circuit. The fitted impedance parameters are listed in Table 9.1. The R_{SEI} of fresh SnO_2-rGONRs is 0.8 Ω and increases to 13.16 Ω for SnO_2-rGONRs-200. The stable SEI film is beneficial for the

cycling stability of the electrodes.[38] Therefore, SnO_2-rGONRs have demonstrated greatly improved LIBs cycling life. The R_{ct} of SnO_2-rGONRs decreases to 5.47 Ω after 200 cycles from 33.37 Ω of the fresh SnO_2-rGONRs. This change is consistent with the variation in rate performance and cycling performance of SnO_2-rGONRs.

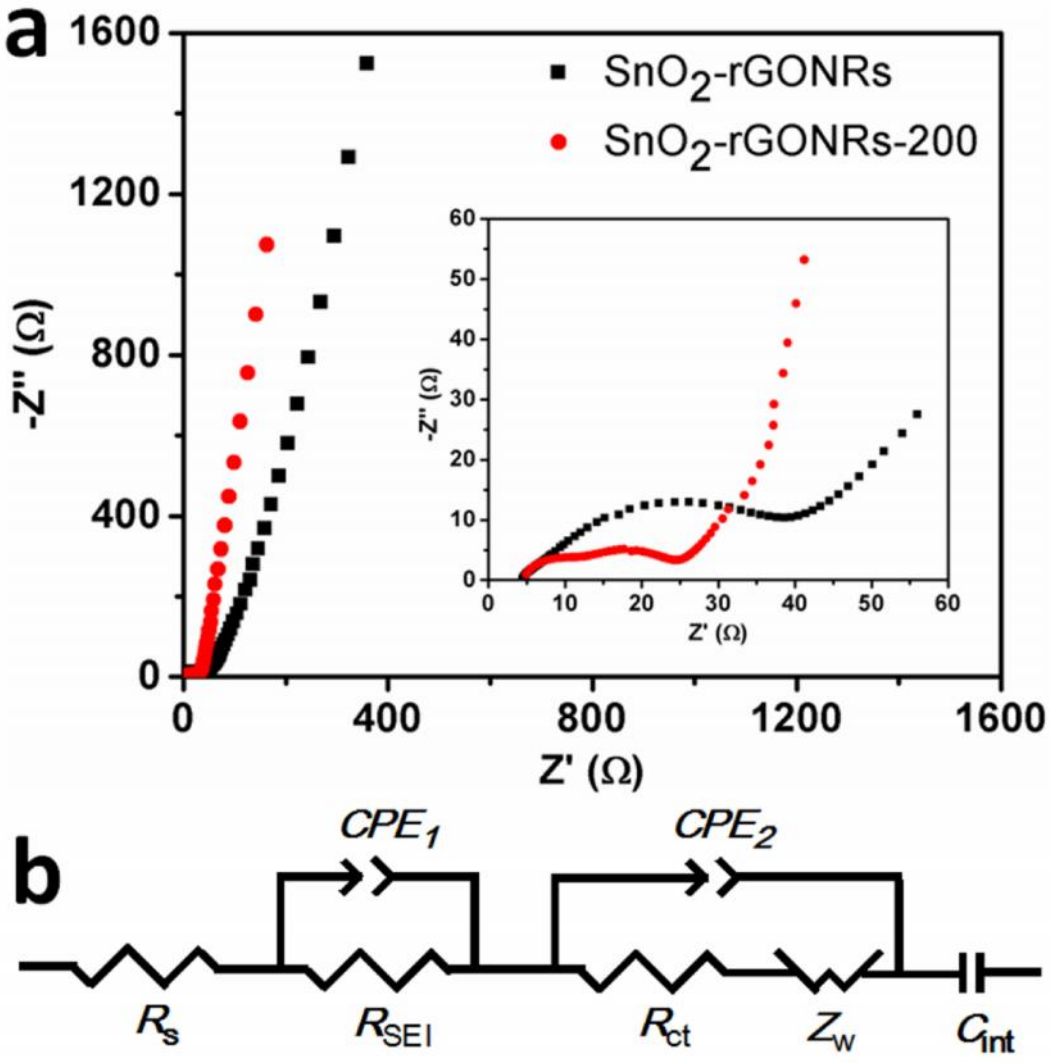

Figure 9.7. (a) Nyquist plots of SnO2-rGONRs. The insert is the enlarged high frequency region. (b) Equivalent circuit that was used to fit the experimental data.

Table 9.1. The EIS simulation parameters of SnO2-rGONRs and SnO2-rGONRs-200.

Active material	R_s (Ω)	CPE_1 (μF)	R_{SEI} (Ω)	R_{ct} (Ω)	CPE_2 (μF)	Z_w (Ω)	C_{int}(mF)
SnO_2-rGONRs	4.60	142.10	0.82	33.37	149.40	110.41	12.00
SnO_2-rGONRs-200	4.93	178.80	13.16	5.47	2.11	39.00	15.76

9.4. Conclusion

In summary, we successfully designed and synthesized nano-structured composite of SnO_2-rGONRs. In this composite, the nanosized SnO_2 particles formed directly on the rGONRs. Electrochemical experiments demonstrate that SnO_2-rGONRs exhibit high capacity, good rate performance, and excellent cycling stability as anode materials due to the synergic effect between the rGONRs and SnO_2. The synthesis of the composite SnO_2-rGONRs produces a component that is effective in improving the electrochemical stability of the electrode materials for the lithium ion batteries.

9.5. References

1. Li, L.‡; Kovalchuk, A.‡; Tour, J. M. SnO_2-Reduced Graphene Oxide Nanoribbons as Anodes for Lithium Ion Batteries with Enhanced Cycling Stability. *Nano research* **2014**, *7*, 1319. (L.L. conceived and designed the experiments. L.L. and K.A. prepared the materials and performed material characterization. L.L. tested the devices and wrote the paper. L.L. and K.A. have the same contribution. Finally, T.J.M. oversaw all research phases, provided regular guidance to the research and revised the manuscript. All authors discussed and commented on the manuscript.)

2. Su, Y.; Li, S.; Wu, D.; Zhang, F.; Liang, H.; Gao, P.; Cheng, C.; Feng, X. Two-Dimensional Carbon-Coated Graphene/Metal Oxide Hybrids for Enhanced Lithium Storage. *ACS Nano* **2012,** *6*, 8349-8356.

3. Etacheri, V.; Marom, R.; Elazari, R.; Salitra, G.; Aurbach, D. Challenges in the development of advanced Li-ion batteries: a review. *Energy Environ. Sci.* **2011,** *4*, 3243-3262.

4. Tarascon, J.-M.; Armand, M. Issues and Challenges FacingRechargeable Lithium Batteries. *Nature* **2001,** *414*, 359-367.

5. Wang, B.; Li, X.; Zhang, X.; Luo, B.; Jin, M.; Liang, M.; Dayeh, S. A.; Picraux, S. T.; Zhi, L. Adaptable Silicon–Carbon Nanocables Sandwiched between Reduced Graphene Oxide Sheets as Lithium Ion Battery Anodes. *ACS Nano* **2013,** *7*, 1437-1445.

6. Arico, A. S.; Bruce, P.; Scosati, B.; Tarascon, J. M. Nanostructured materials for advanced energy conversion and storage devices *Nat. Mater.* **2005,** *4*, 366-377.

7. Chen, J. S.; Lou, X. W., SnO_2-Based Nanomaterials: Synthesis and Application in Lithium-Ion Batteries. *Small* **2013,** *9*, 1877-1893.

8. Haag, J. M.; Pattanaik, G.; Durstock, M. F. Nanostructured 3D Electrode Architectures for High-Rate Li-Ion Batteries. *Adv. Mater.* **2013,** *25*, 3238-3243.

9. Zhang, L.; Zhang, G.; Wu, H. B.; Yu, L.; Lou, X. W. Hierarchical Tubular Structures Constructed by Carbon-Coated SnO_2 Nanoplates for Highly Reversible Lithium Storage. *Adv. Mater.* **2013,** *25*, 2589-2593.

10. Lou, X. W.; Li, C. M.; Archer, L. A. Designed Synthesis of Coaxial SnO_2@carbon Hollow Nanospheres for Highly Reversible Lithium Storage. *Adv. Mater.* **2009,** *21*, 2536-2539.

11. Li, Y.; Zhu, S.; Liu, Q.; Gu, J.; Guo, Z.; Chen, Z.; Feng, C.; Zhang, D.; Moon, W. J. Carbon-coated SnO_2@C with hierarchically porous structures and graphite layers inside for a high-performance lithium-ion battery. *J. Mater. Chem.* **2012,** *22*, 2766-2773.
12. He, M.; Yuan, L.; Hu, X.; Zhang, W.; Shu, J.; Huang, Y. A SnO_2@carbon nanocluster anode material with superior cyclability and rate capability for lithium-ion batteries. *Nanoscale* **2013,** *5*, 3298-3305.
13. Wang, X.; Cao, X.; Bourgeois, L.; Guan, H.; Chen, S.; Zhong, Y.; Tang, D.-M.; Li, H.; Zhai, T.; Li, L.; Bando, Y.; Golberg, D. N-Doped Graphene-SnO_2 Sandwich Paper for High-Performance Lithium-Ion Batteries. *Adv. Funct. Mater.* **2012,** *22*, 2682-2690.
14. Yang, S.; Yue, W.; Zhu, J.; Ren, Y.; Yang, X. Graphene-Based Mesoporous SnO_2 with Enhanced Electrochemical Performance for Lithium-Ion Batteries. *Adv. Funct. Mater.* **2013,** *23* , 3570-3576.
15. Zhou, X.; Yin, Y.-X.; Wan, L.-J.; Guo, Y.-G. A robust composite of SnO_2 hollow nanospheres enwrapped by graphene as a high-capacity anode material for lithium-ion batteries. *J. Mater. Chem.* **2012,** *22*, 17456-17459.
16. Ji, G.; Ding, B.; Sha, Z.; Wu, J.; Ma, Y.; Lee, J. Y. Conformal graphene encapsulation of tin oxide nanoparticle aggregates for improved performance in reversible Li+ storage. *Nanoscale* **2013,** *5*, 5965-5972.
17. Wang, L.; Wang, D.; Dong, Z.; Zhang, F.; Jin, J., Interface Chemistry Engineering for Stable Cycling of Reduced GO/SnO_2 Nanocomposites for Lithium Ion Battery. *Nano Lett.* **2013,** *13*, 1711-1716.

18. Wen, Z.; Wang, Q.; Zhang, Q.; Li, J. In Situ Growth of Mesoporous SnO_2 on Multiwalled Carbon Nanotubes: A Novel Composite with Porous-Tube Structure as Anode for Lithium Batteries. *Adv. Funct. Mater.* **2007,** *17*, 2772-2778.

19. Ding, S.; Chen, J. S.; Lou, X. W. One-Dimensional Hierarchical Structures Composed of Novel Metal Oxide Nanosheets on a Carbon Nanotube Backbone and Their Lithium-Storage Properties. *Adv. Funct. Mater.* **2011,** *21*, 4120-4125.

20. Hu, R.; Sun, W.; Liu, H.; Zeng, M.; Zhu, M., The fast filling of nano-SnO_2 in CNTs by vacuum absorption: a new approach to realize cyclic durable anodes for lithium ion batteries. *Nanoscale* **2013**, *5*, 11971-11979.

21. Lin, J.; Peng, Z. W.; Xiang, C. S.; Ruan, G. D.; Yan, Z.; Natelson, D.; Tour,J. M. Graphene Nanoribbon and Nanostructured SnO_2 Composite Anodes for Lithium Ion Batterie *ACS Nano*, **2013**, *7*, 6001-6006.

22. Ye, J.; Zhang, H.; Yang, R.; Li, X.; Qi, L. Morphology-Controlled Synthesis of SnO_2 Nanotubes by Using 1D Silica Mesostructures as Sacrificial Templates and Their Applications in Lithium-Ion Batteries. *Small* **2010,** *6*, 296-306.

23. Wang, Y.; Lee, J. Y.; Zeng, H. C. Polycrystalline SnO_2 Nanotubes Prepared via Infiltration Casting of Nanocrystallites and Their Electrochemical Application. *Chem. Mater.* **2005,** *17*, 3899-3903.

24. Park, M.-S.; Wang, G.-X.; Kang, Y.-M.; Wexler, D.; Dou, S.-X.; Liu, H.-K. Preparation and Electrochemical Properties of SnO_2 Nanowires for Application in Lithium-Ion Batteries. *Angew. Chem. Int. Ed.* **2007,** *119*, 764-767.

25. Wang, C.; Zhou, Y.; Ge, M.; Xu, X.; Zhang, Z.; Jiang, J. Z. Large-Scale Synthesis of SnO_2 Nanosheets with High Lithium Storage Capacity. *J. Am. Chem. Soc.* **2009,** *132*, 46-47.

26. Reddy, M. V.; Subba Rao, G. V.; Chowdari, B. V. R. Metal Oxides and Oxysalts as Anode Materials for Li Ion Batteries. *Chem. Rev.* **2013,** *113*, 5364-5457.

27. Deng, J.; Yan, C.; Yang, L.; Baunack, S.; Oswald, S.; Wendrock, H.; Mei, Y.; Schmidt, O. G., Sandwich-Stacked SnO2/Cu Hybrid Nanosheets as Multichannel Anodes for Lithium Ion Batteries. *ACS Nano* **2013,** *7*, 6948-6954.

28. Zhou, W.; Cheng, C.; Liu, J.; Tay, Y. Y.; Jiang, J.; Jia, X.; Zhang, J.; Gong, H.; Hng, H. H.; Yu, T.; Fan, H. J. Lithium-Ion Batteries: Epitaxial Growth of Branched α-Fe_2O_3/SnO_2 Nano-Heterostructures with Improved Lithium-Ion Battery Performance *Adv. Funct. Mater.* **2011,** *21*, 2385-2385.

29. Wang, Y.; Xu, J.; Wu, H.; Xu, M.; Peng, Z.; Zheng, G. Hierarchical SnO_2-Fe_2O_3 heterostructures as lithium-ion battery anodes. *J. Mater. Chem.* **2012,** *22*, 21923-21927.

30. Higginbotham, A. L.; Kosynkin, D. V.; Sinitskii, A.; Sun, Z.; Tour, J. M. Lower-Defect Graphene Oxide Nanoribbons from Multiwalled Carbon Nanotubes. *ACS Nano* **2010,** *4*, 2059-2069.

31. Liu, B.; Chia, Z.-W.; Lee, Z.-Y.; Cheng, C.-H.; Lee, J.-Y.; Liu, Z.-L. The importance of water in the polyol synthesis of carbon supported platinum–tin oxide catalysts for ethanol electrooxidation. *J. Power Sources* **2012,** *206*, 97-102.

32. Li, D.; Muller, M. B.; Gilje, S.; Kaner, R. B.; Wallace, G. G. Processable aqueous dispersions of graphene nanosheets. *Nat. Nano.* **2008**, *3*, 101.

33. Campos-Delgado, J.; Romo-Herrera, J. M.; Jia, X.; Cullen, D. A.; Muramatsu, H.; Kim, Y. A.; Hayashi, T.; Ren, Z.; Smith, D. J.; Okuno, Y.; Ohba, T.; Kanoh, H.; Kaneko, K.; Endo, M.; Terrones, H.; Dresselhaus, M. S.; Terrones, M. Bulk Production of a New Form of sp2 Carbon: Crystalline Graphene Nanoribbons. *Nano Lett.* **2008,** *8*, 2773-2778.

34. Utsumi, S.; Honda, H.; Hattori, Y.; Kanoh, H.; Takahashi, K.; Sakai, H.; Abe, M.; Yudasaka, M.; Iijima, S.; Kaneko, K., Direct Evidence on C−C Single Bonding in Single-Wall Carbon Nanohorn Aggregates. *J. Phys. Chem. C* **2007,** *111*, 5572-5575.

35. Jiang, Y.; Yuan, T.; Sun, W.; Yan, M. Electrostatic Spray Deposition of Porous SnO_2/Graphene Anode Films and Their Enhanced Lithium-Storage Properties. *ACS Appl. Mater. Interfaces* **2012,** *4*, 6216-6220.

36. Qian, D.; Xu, B.; Cho, H.-M.; Hatsukade, T.; Carroll, K. J.; Meng, Y. S. Lithium Lanthanum Titanium Oxides: A Fast Ionic Conductive Coating for Lithium-Ion Battery Cathodes. *Chem. Mater.* **2012,** *24*, 2744-2751.

37. Chang, K.; Chen, W. l-Cysteine-Assisted Synthesis of Layered MoS_2/Graphene Composites with Excellent Electrochemical Performances for Lithium Ion Batteries. *ACS Nano* **2011,** *5*, 4720-4728.

38. Verma, P.; Maire, P.; Novák, P. A review of the features and analyses of the solid electrolyte interphase in Li-ion batteries. *Electrochim. Acta* **2010,** *55*, 6332-6341.

Chapter 10

Enhanced Cycling Stability of Lithium Sulfur Batteries Using Sulfur-Polyaniline-Graphene Nanoribbons Composite Cathodes

This chapter was entirely copied from reference 1.

10.1. Introduction

The development of high capacity energy storage systems is important for portable electronic devices, power tools, and electric vehicles.[2-5] Lithium sulfur batteries (LSBs) have attracted attention as potential energy storage devices because the sulfur cathode in LSBs has a high theoretical capacity of 1672 mAh/g and energy density of 2567 Wh/kg, almost 5 × higher than conventional cathodes, presuming complete reaction of lithium with sulfur to form Li_2S.[6-9] Elemental sulfur is inexpensive, nontoxic, and abundant in nature.[9,10] However, the practical applications of LSBs are limited by two challenges. The

first challenge is that the sulfur is electrically insulating.[11,12] The second is the severe degradation of the lithium sulfur battery cycle life; a result of the volume change and high solubility of the polysulfide products.[6,13,14] When sulfur is fully converted to Li_2S, the volume increases as much as 80%, which leads to the fading capacity because of the pulverization of battery materials. The high solubility of polysulfide products makes it more likely that they will take part in the sulfur shuttle mechanism, resulting in capacity decay due to the loss of sulfur active materials through redox reactions of lithium polysulfide at both the cathode and anode surfaces.

Extensive effort has been devoted to address these challenges of sulfur's insulating nature and the capacity decay. The poor electrical conductivity of sulfur can be improved by the introduction of conducting materials that form composites, such as graphene,[15,16] carbon nanotubes,[17] conducting polymers,[14,18,19] and other carbon matrixes.[20-23] Many strategies have been developed to enhance the cycling life of LSBs. For example, the electrolyte additive $LiNO_3$ has been shown to be effective in reducing the capacity decay because it enhances the stability of polysulfide in the electrolyte, protects the lithium anode from electrochemical and chemical reactions, and reduces the viscosity of the liquid electrolyte.[24-26] Another method is to protect the anode in LSBs, which can reduce the sulfur shuttle effect, improving the cycling performance.[24,27,28] Various matrixes have been developed to trap the soluble intermediate lithium polysulfide, such as mesoporous carbon,[23] amorphous carbon,[29] carbon nanotubes,[17,30] graphene,[15.16] hollow carbon spheres,[31,32] metal oxides,[33,34] and conducting polymers.[14,18,35] Among all these matrixes, conducting polymers open new possibilities for the cycling life improvement in the LSBs due to their easy preparation and scale-up, mechanical structure, self-healing, and

good electrical conductivity.[13,36] For example, Wu *et al.* prepared the composite sulfur/polythiophene with a core-shell structure, which showed good cycling stability of 67.5% capacity retention after 80 cycles.[18] And Xiao *et al.* synthesized a composite sulfur-polyaniline that improved the cycling life of LSBs with only 24% capacity decay after 500 cycles.[14] Polyaniline is an interesting conducting polymer because it works as a substrate to load sulfur and can be used as a cathode in lithium sulfur batteries. However, polyaniline suffers from two major problems, which hinders its application in lithium sulfur batteries. The first problem is the limited electrical conductivity, and the other is the mechanical degradation caused by its large volumetric change, leading to its poor cycling stability in energy storage devices. Therefore, to mitigate these negative effects, it is important to improve polyaniline related materials for lithium sulfur batteries.

In this study, a unique structure where sulfur was loaded on polyaniline-graphene nanoribbons (PANI-GNRs) was designed to reduce the capacity decay in lithium sulfur batteries. The PANI-GNR composite was prepared by the *in situ* polymerization of aniline in the presence of GNRs.[37,38] GNRs serve as the substrate for polyaniline growth, and increase the electronic conductivity and effective utilization of PANI in the composite. The GNRs also improved the mechanical properties of the composite, resulting in an enhancement of its ability to recover from the volume expansion.[37] Therefore, PANI-GNRs effectively overcome the negative deficience of PANI alone.

Sulfur-PANI-GNRs (SPGs) were prepared by heat treatment of a mixture of elemental sulfur and PANI-GNRs.[14] In the SPGs, PANI-GNRs work as an electronic conductivity framework for sulfur and they enhance the mechanical properties of SPGs. A

fraction of sulfur reacts with polyaniline to form a cross-linked network with the inter-chain or intra-chain disulfide bond interconnectivity during the vulcanization process.[14] The rest sulfur diffuses into the hierarchical network of PANI-GNRs and new formed polymer networks. PANI traps the soluble intermediate lithium polysulfide through strong physical and chemical absorption effects.[14] The GNRs reinforcement reduces the damage that normally occurs from volume change during the electrochemical reaction. Therefore, SPGs as cathode materials demonstrate excellent cycling performance due to the synergetic effect of GNRs, PANI, and sulfur. The stable reversible specific discharge capacity is 567 mAh/g at the 26th cycle and it only decays 9% in the following 374 cycles, at the rate of 0.4 C. Therefore, SPGs are outstanding candidates for use as cathode materials for energy storage in LSBs.

10.2. Experiments

10.2.1. Materials synthesis

10.2.1.1. Synthesis of PANI-GNRs and polyaniline (PANI)

GNRs[37], PANI and PANI-GNRs were prepared as described previously.[36] GNRs were prepared by treatment of multiwalled carbon nanotubes with NaK in 1,2-dimethoxyethane and quenching of the reaction with MeOH. In order to increase their wettability, GNRs (100 mg) were refluxed in 3 M HNO_3 (400 mL) for 12 h. HNO_3-treated GNRs (22.5 mg) were added to 1 M H_2SO_4 solution (40 mL) and the fully dispersed GNR solution was formed by intense sonication (2510 Branson) for 2 h. Aniline (900 mg, 9.65 mmol) was added to the above dispersion solution and kept stirring to form a uniform

mixture in a NaCl-ice bath (-3 °C to -5 °C). The oxidant ammonium persulfate (APS) (554 mg, 2.4 mmol) was dissolved in 40 mL of 1 M H_2SO_4 and cooled in the NaCl-ice bath for 10 min. Then, the two solutions were mixed with continuous stirring in the NaCl-ice bath for 10 h. The black solid sample was collected by vacuum filtration with sequential washing with water and acetone. The final PANI-GNRs (130 mg) were obtained after drying in a vacuum oven at 85 °C for 10 h. PANI was prepared using the same method above without the addition of GNRs.

10.2.1.2. Synthesis of SPGs and SP

Sulfur (200 mg) was dissolved in carbon disulfide (1 mL). PANI-GNRs (50 mg) were added to the solution with continued magnetic stirring for 30 min at room temperature in order to achieve a good dispersion. Then, the mixture was stirred in an open reaction flask in the hood until the carbon disulfide evaporated. The resulting solid mixture was sealed in a vessel under N_2. The heat treatment of the mixture proceeded in two steps. The mixture was first heated at 155 °C for 12 h and then the temperature was raised to 280 °C for another 12 h to complete the vulcanization reaction. SPGs (100 mg) were obtained after the mixture was permitted to cool to room temperature. Unreacted sulfur remained on the walls of the flask. For comparison purpose, SP was obtained using a similar procedure between polyaniline and sulfur.

10.2.2. Materials characterization

Products were characterized by X-ray diffraction (XRD, Rigaku D/Max Ultima II); X-ray photoelectron spectroscopy (XPS, PHI Quantera); scanning electron microscopy

(SEM, JEOL 6500); thermogravimetric analysis (TGA, TA Instruments, Q50); and transmission electron microscopy (TEM, JEM2100F TEM).

10.2.3. Device fabrication

80 wt% active materials (SPGs, SPs, and S), 10 wt% carbon black (Super P, TIMCAL), and 10 wt% polyvinylidene difluoride (PVDF, Alfa Aesar) were dissolved in *N*-methyl-2-pyrrolidone (NMP, Sigma-Aldrich) to form a slurry. Then, the slurry was coated on an aluminum foil substrate to form the cathodes. The typical mass loading of the active materials is around 1.2 mg/cm^2. Electrochemical tests were performed using CR2032 coin-type cells with lithium metal foil as the counter electrode. The electrolyte was 1 M lithium bis(trifluoromethane) sulfonamide (LiTFSI) dissolved in a mixture of 1,3-dioxolane (DOL) and dimethyoxyethane (DME) (1:1 vol:vol) with 1 wt % $LiNO_3$ and the separator was a Celgard 2300 membrane.

10.2.4. Electrochemical measurement

CV tests were done on a CHI660D electrochemical station at a current density of 0.60 mV/s. The galvanostatic discharge charge test was carried out on a LAND CT2001A battery system at room temperature. The capacity was evaluated based on the mass of the sulfur in the composite.

10.3. Results and Discussion

10.3.1. Synthesis and structure analysis

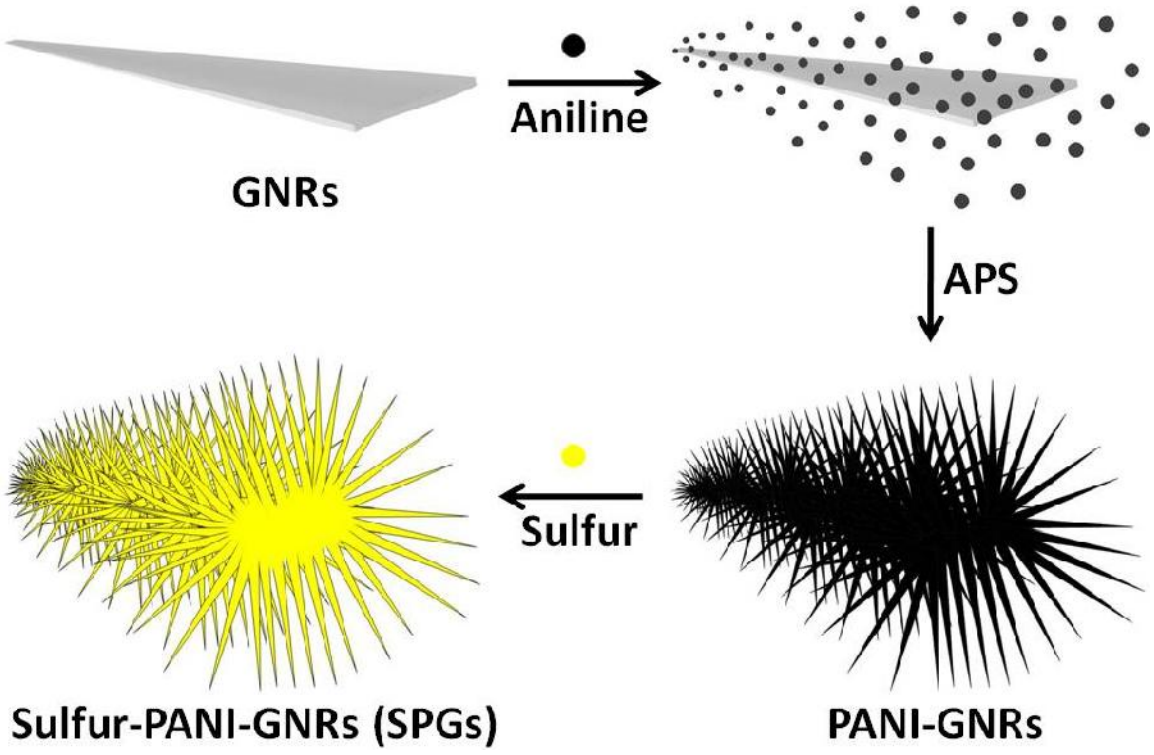

Figure 10.1. Schematic illustration of the synthesis of SPGs.

The synthesis of the SPGs, as described in the experimental section, is schematically depicted in Figure 10.1.[14]

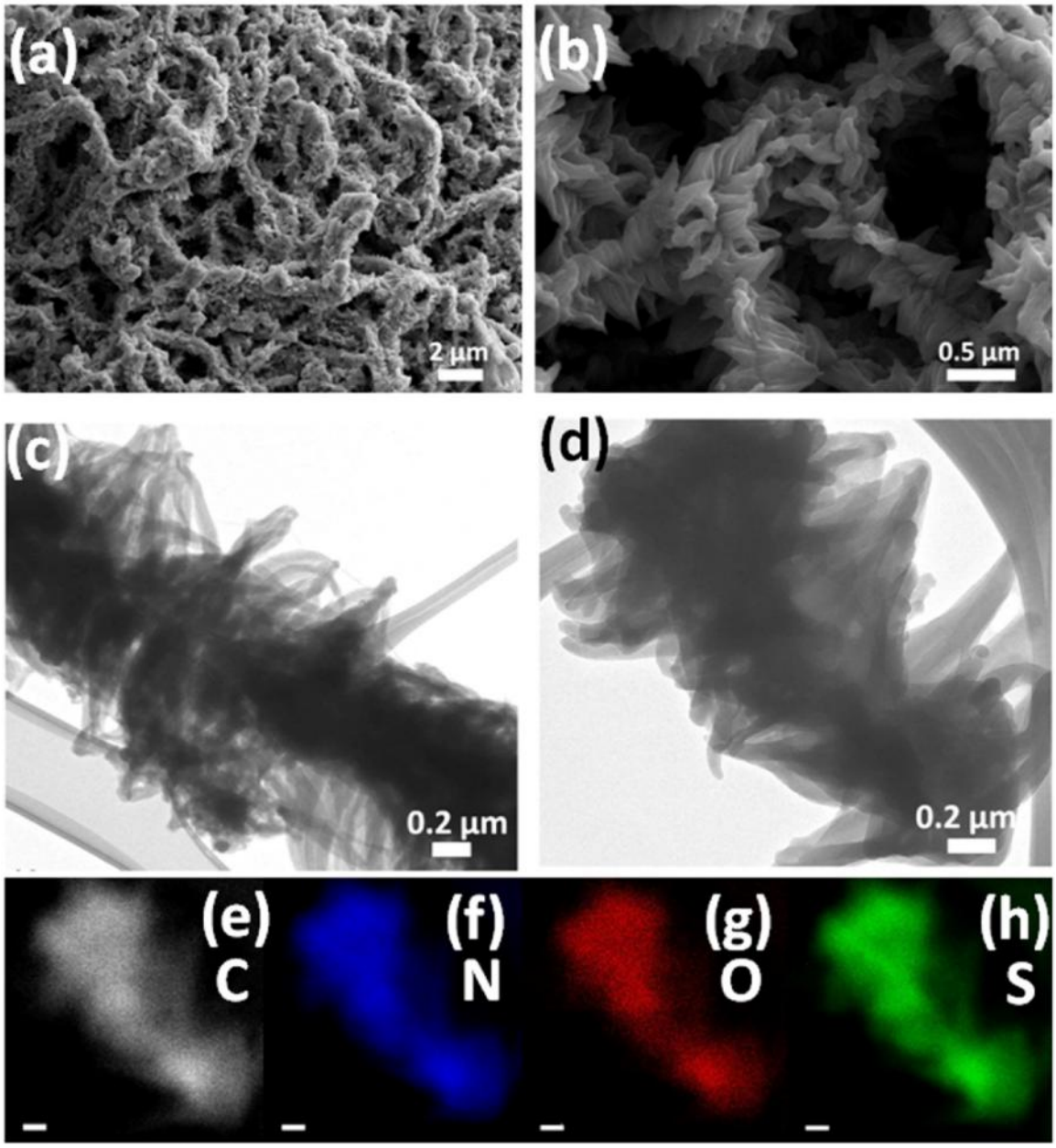

Figure 10.2. (a, b) SEM images of SPGs at different resolution. (c, d) TEM images of SPGs and corresponding elemental mapping of (e) carbon, (f) nitrogen, (g) oxygen, and (h) sulfur. The scale bars in e-h are 0.2 µm.

The morphology of SPGs, SP, PANI-GNRs and PANI were characterized by SEM and TEM as shown in Figure 10.2 and Figure 10.3. Figure 10.2a,b are the low and high

resolution SEM images of SPGs, respectively. The ordered, vertically aligned PANI was directly growing on and around the GNRs with brush-like structure. The morphology was well maintained after the sulfur loading compared to PANI-GNRs as shown in Figure 10.3a. The structure was also established by the TEM images as shown in Figure 10.2c,d. The structure of SPGs was further studied by the elemental mapping of carbon, nitrogen, oxygen, and sulfur. As shown in Figure 10.3e-h, these elements were uniformly distributed in the SPGs. TEM images of SPGs revealed that sulfur was homogenously loaded on PANI nanorods and the morphology of PANI-GNRs was still well-maintained. As shown in Figure 10.3b, irregular PANI was intertwined together. PANI could not form the brush-like structure without the graphene nanoribbons. After the sulfur loading, the morphologies of SPs had no obvious change as shown in Figure 10.3c-f.

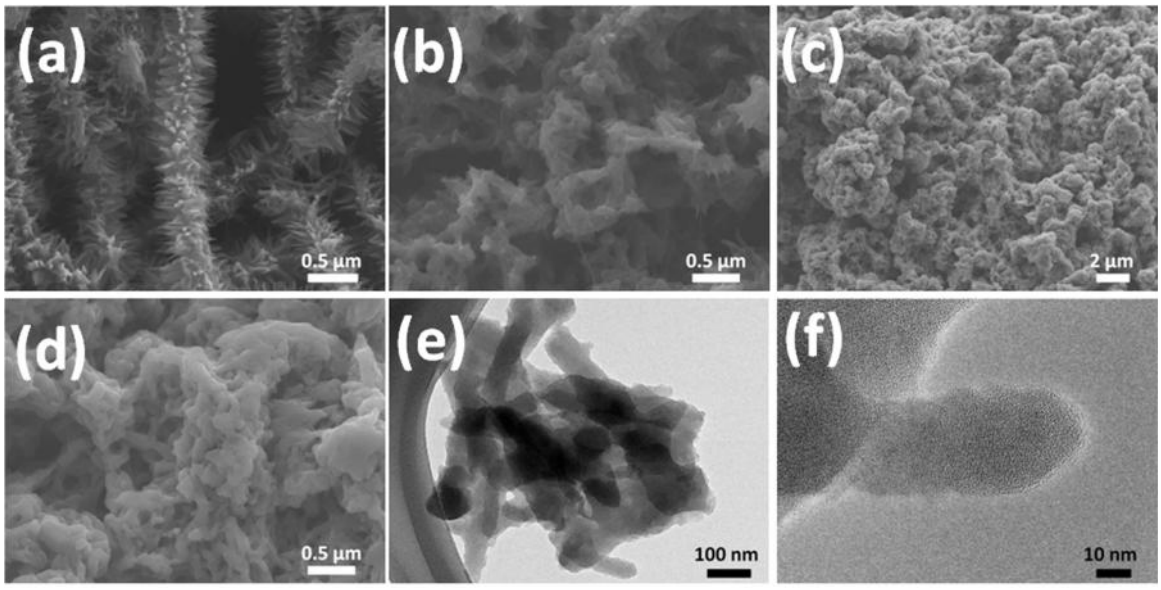

Figure 10.3. SEM images of (a) PANI-GNRs (b) PANI and (c, d) SPs. (e, f) TEM images of SPs at different resolutions.

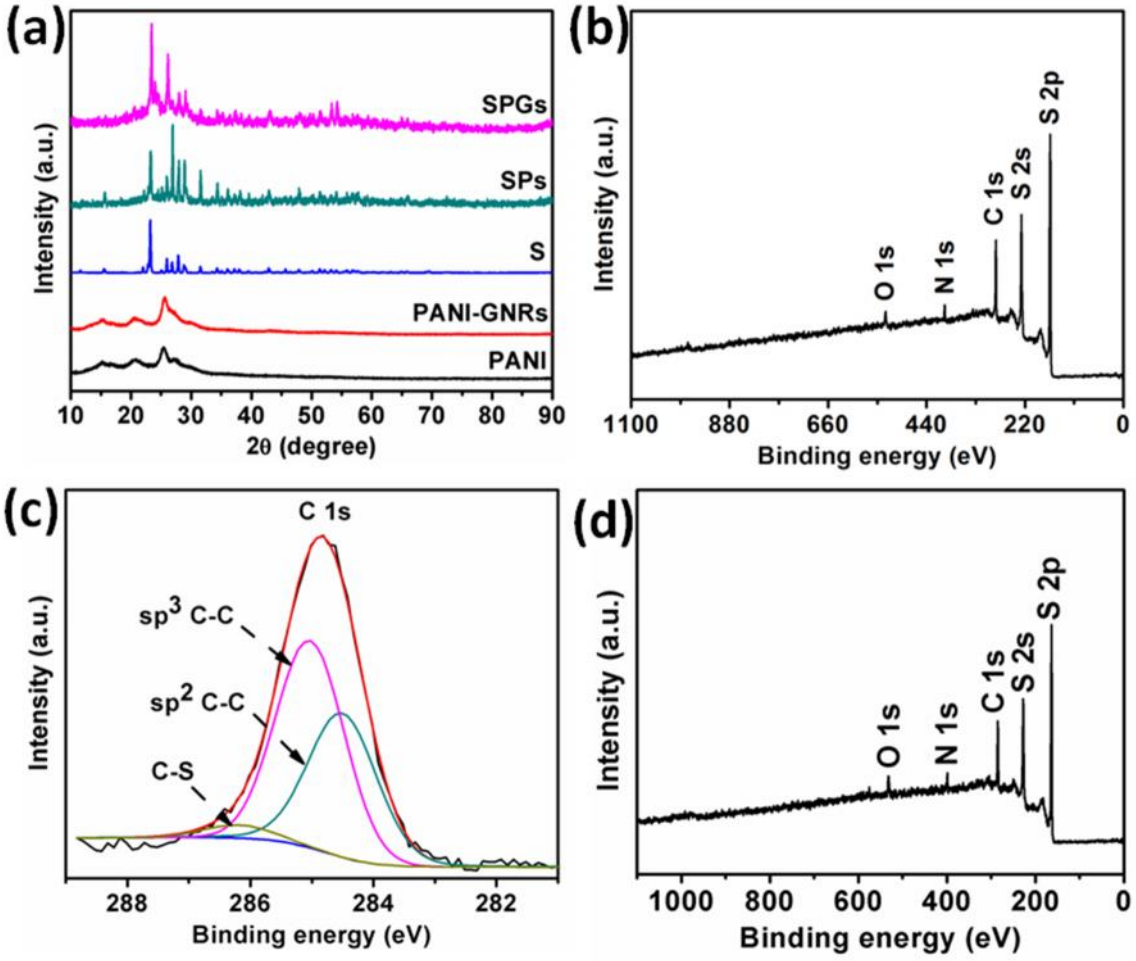

Figure 10.4. (a) XRD patterns of PANI, PANI-GNRs, S, SPs, and SPGs. (b) XPS scan spectrum of SPGs. (c) C 1s core level XPS of SPGs. (d) XPS scan spectrum of SPs.

XRD and XPS were used to characterize the SPGs and SPs. Figure 10.4a shows the XRD pattern of PANI, PANI-GNRs, S, SPs, and SPGs. The XRD pattern of PANI-GNRs showed the four characteristic peaks at 2θ of 15.3°, 21.0°, 25.6°, and 26.5°.[38-40] The XRD pattern of composite SPGs had similar peaks as sulfur, including the obvious increase in peak intensity of 2θ at 26.1° due to the incorporation of sulfur into PANI-GNRs and a new

peak at 21.0° because of the PANI-GNRs in the composite. XPS indicates that the composite SPGs only contained four elements, S, C, N, and trace O from the APS and/or sulfuric acid (Figure 10.4b). As shown in Figure 10.4c, the deconvolution of the C 1s core-level XPS of SPGs leads to three peaks, resulting from three different electronic states. The peaks with binding energy of 284.5 eV can be attributed to sp^2 hybridized carbon atoms, 285.0 eV to sp^3 hybridized carbon atoms, and 286.2 eV to carbon-sulfur chains.[41]

TGA experiments were also carried out to analysis the sulfur content in SPGs and SPs. The samples were measured in argon at a heating rate of 5 °C min^{-1}. As shown in Figure 10.5a, SPGs had 62% sulfur, while 59% sulfur content in SPs (Figure 10.5b).

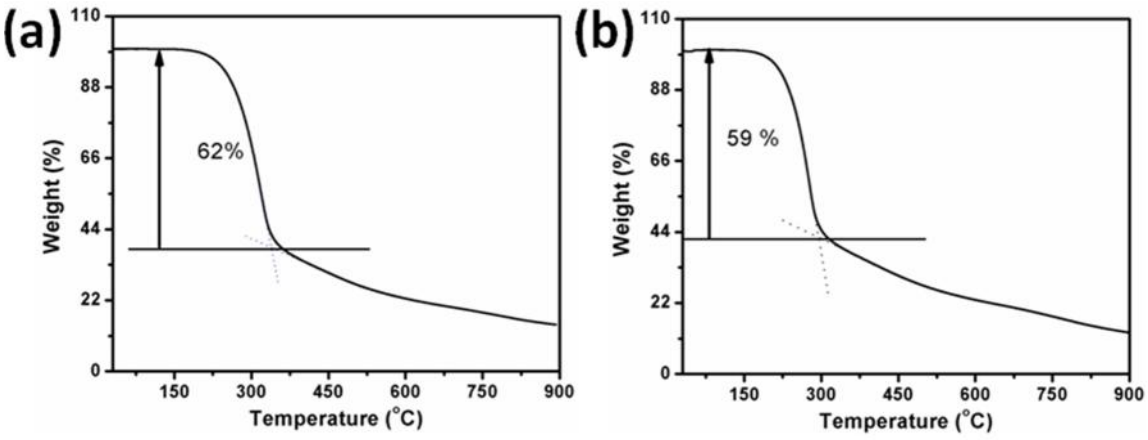

Figure 10.5. TGA curves of (a) SPGs and (b) SPs.

10.3.2. Electrochemical evaluation

In order to evaluate the electrochemical performance of SPGs as cathodes in LSBs, cyclic voltammetry (CV) and galvanostatic discharge charge experiments were carried out in CR2032 coin cells. Figure 10.6a showed the CV that was used to study the electrochemical reaction mechanism of the SPG cathodes in the LSBs in the potential range of 1.7 to 3.0 V.[24] During the cathodic reduction process, there are two peaks at 2.25 and 1.88 V (vs. Li/Li^+). According to the reaction mechanism of sulfur reduction and oxidation during the discharge and charge processes,[2,24,42] the peak at 2.25 V results from the reduction of sulfur to higher-order polysulfides. The peaks at 1.88 V correspond to the reduction of sulfur from higher-order polysulfides to Li_2S_2/Li_2S. In the subsequent anodic scan, a broad oxidation peak was observed at 2.56 V with a shoulder at 2.67 V in the first cycle; the peak shifted to 2.60 V with a shoulder peak at 2.67 in the following cycles. The two overlapping oxidation peaks related to the conversion among Li_2S, polysulfides and elemental sulfur. After the first cycle, both the peak positions and area of the CV peaks remain almost without obvious change, demonstrating relatively good capacity retention. For comparison, Figure 10.6b,c show the CV profile of SPs and sulfur with little difference between the two. Figure 9-6d shows the voltage profile of SPGs at the rate of 0.1 C. There were two obvious plateaus in the discharge curve, relating to the formation of higher-order polysulfides and Li_2S_2/Li_2S. This result was consistent with the CV. The stable, reversible discharge capacity of the 2nd cycle can reach 714 mAh/g.

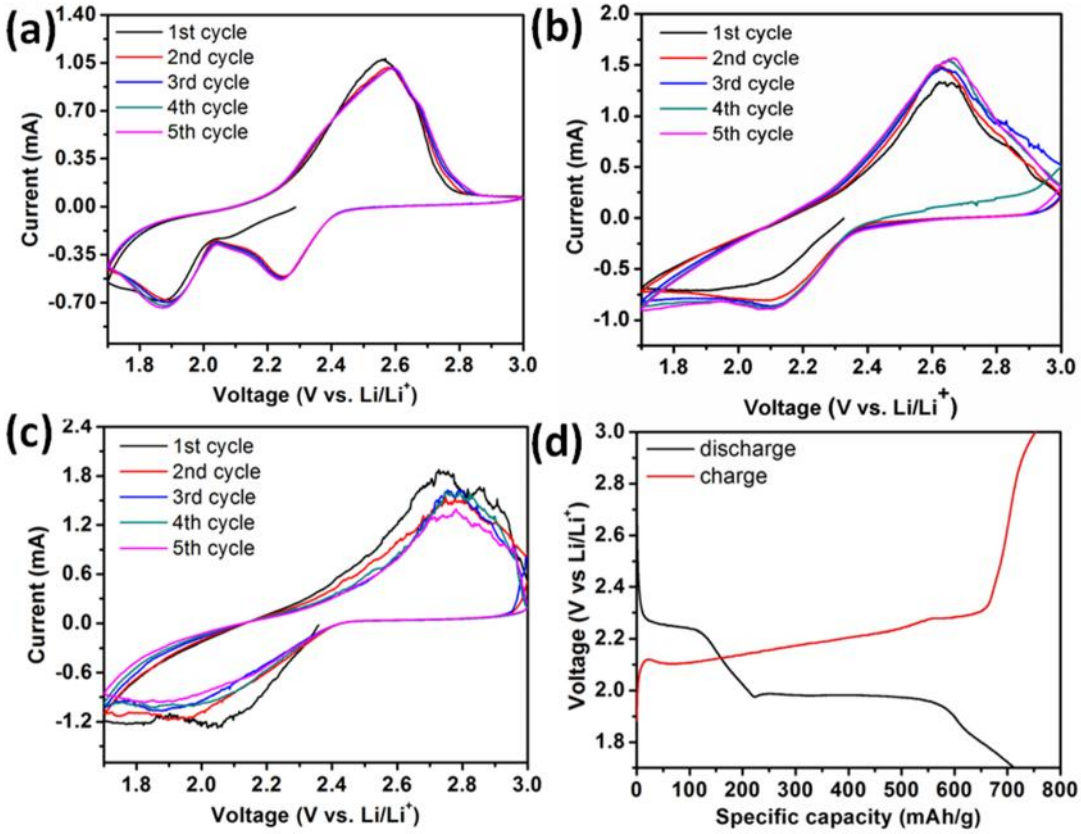

Figure 10.6. The first five cyclic voltammograms of the composite SPGs (a), SPs (b), and S (c) at a sweep rate of 0.4 mVs-1. The discharge and charge voltage vs. specific capacity profiles of SPGs (d) at 3.0 to 1.7 V at 0.1 C.

The rate performance of the SPGs was studied in the same potential range as shown in Figure 10.7a. For the first five cycles, the capacity decreased with the increase in cycle numbers at the rate of 0.1 C. A stable capacity at different current densities was observed. When the rate was reduced from 1.0 C to 0.1 C, the value of specific capacity of SPGs was still 688 mAh/g at the 80th cycle. The rate performance demonstrates that the SPGs remained stable after extended rate cycles. The cycling performance for SPGs was also evaluated by discharge-charge experiments. For comparison, SPs and sulfur were first

tested as cathodes in the LSBs at the rate of 0.4 C. The specific capacity of SPs can reach 614 mAh/g at the 9^{th} cycle as shown in Figure 10.7b. However, it deceased quickly in the following cycles with only 417 mAh/g at the 90^{th} cycle. For the pure sulfur cathode, the specific discharge capacity quickly decreased to 120 mAh/g at the 100^{th} cycle from 291 mAh/g at the 2^{nd} cycle; only 41% capacity remained as shown in Figure 10.7c. This demonstrated that PANI increased the specific capacity and cycling stability of sulfur cathodes. Figure 10.7d shows the cycling performance of SPGs tested under the same conditions. The specific discharge capacity was 673 mAh/g in the first cycle and decreased to 567 mAh/g in the 26^{th} cycle due to the loss of sulfur at the surface of SPGs. Then, the specific discharge capacity increased slightly with the increase in cycle numbers, and reached 588 mAh/g at the 113^{th} cycle. In the following cycles, the value of the specific discharge capacity decreased slowly as the cycle numbers increased and reached 514 mAh/g at the 400^{th} cycle. A capacity decay of 9% occurred after 374 cycles from the 26^{th} cycle. The coulombic efficiency of SPGs quickly increased to almost 100% in several cycles and stayed optimal for more than 30 cycles. Then, it decreased with the increase in cycles but was maintained over 90% when the cycles increased to 400. It is presumed that the PANI-GNRs could not completely trap the polysulfide, and the additive $LiNO_3$ was consumed during the discharge and charge process.[25] The shuttle effect was still present, leading to a lower Coulombic efficiency when the batteries operated for extended periods. The graphene nanoribbons indeed enhanced mechanical properties of PANI-GNRs, which improved the cycling stability of SPGs during the extended cycles. Therefore, PANI-GNRs effectively trapped the polysulfide during the discharge and charge processes, resulting in great improvements in the cycling performance of the LSBs.

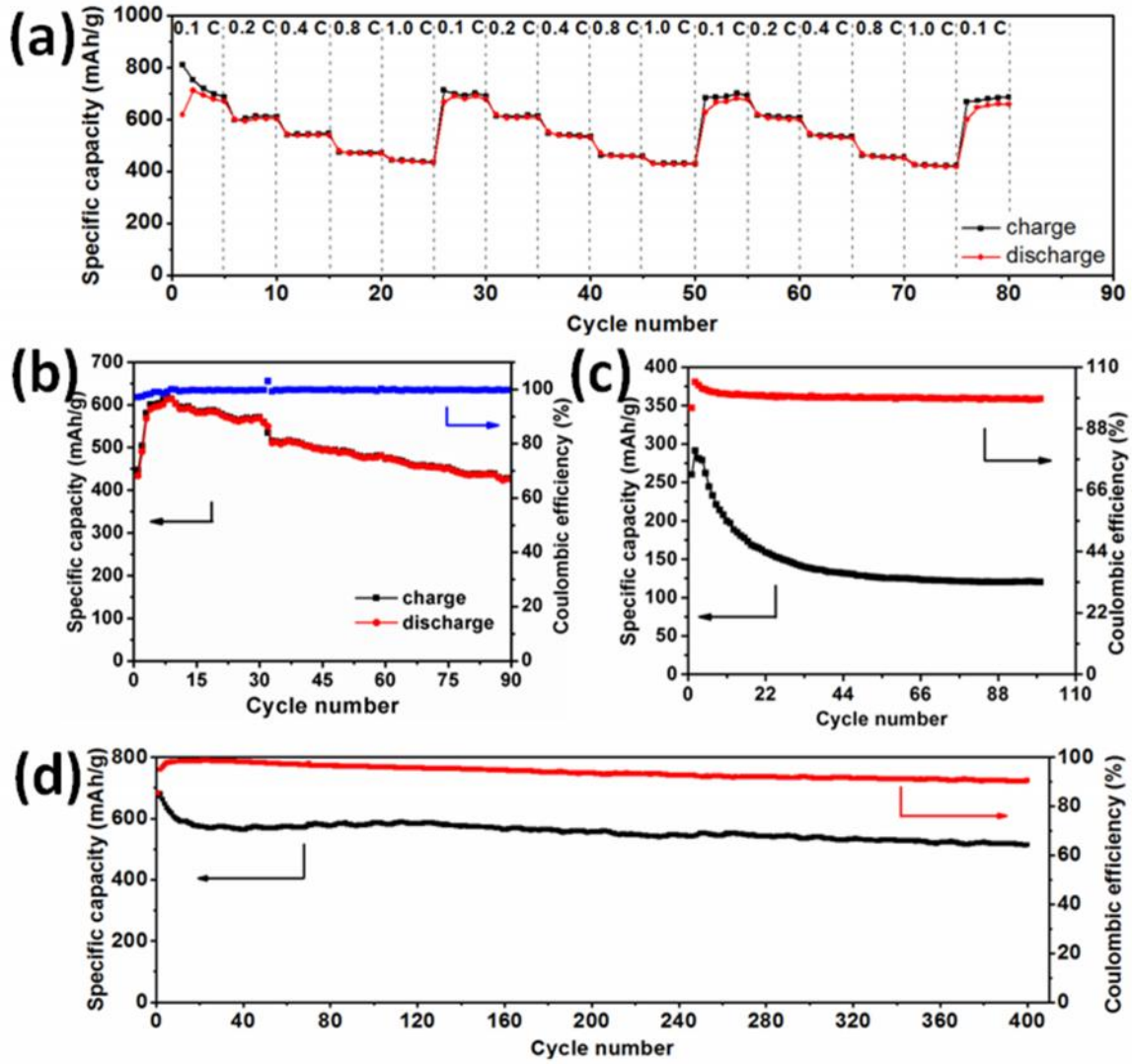

Figure 10.7. Rate performance of SPGs (a) at various rates from 0.1 C to 1.0 C with respect to the cycle numbers. Cycling performance of SPs (b), S (c), and SPGs (d) at a rate of 0.4 C.

In order to study the SPGs electrochemical performance in LSBs, electrochemical impedance spectroscopy (EIS) experiments were carried out after 5 cycles for sulfur, SPs, and SPGs as shown in Figure 10.8a. Figure 10.8b shows the equivalent circuit model of this system.[18,43] In this model, R_s is the internal resistance of the tested battery, R_p and R_{ct}

represent the passivation film and charge-transfer resistance, respectively, CPE_1 and CPE_2 are associated with constant phase element of space charge capacitance and double layer capacitance, respectively, and Z_w is the Warburg resistance related to the lithium diffusion process. In Figure 10.8a, the plots consist of two semicircles in the high and intermediate frequency range and a sloping line with an angle ~ 45° to the real axis in the low frequency region. The two semicircles result from the Li^+ ion transport through the passivation film and the interfacial charge transfer reaction (R_p and R_{ct}) combined with the electrochemical capacitive behaviors CPE_1 and CPE_2, respectively. The sloping line is attributed to the solid-state Li diffusion into the active materials (Z_w). The experimental Nyquist plots are modeled based on the equivalent circuit. The fitted impedance parameters are listed in Table 10.1. The sum value of R_p (159.10 Ω) and R_{ct} (100.70 Ω) of SPs was 259.80 Ω, which was significantly lower than that of sulfur (494.25 Ω) with R_p (66.15 Ω) and R_{ct} (428.10 Ω). This demonstrated that the incorporation of polyaniline can improve the electrical conductivity of the composite of SPs. After the introduction of GNRs in polyaniline, the sum value of R_p (95.29 Ω) and R_{ct} (82.58 Ω) in SPGs became to 177.87 Ω compared to 259.80 Ω in SPs. This proved that the GNRs enhanced the electrical conductivity of the SPGs, resulting in the improvement in the electrochemical performance.

Table 10.1. The EIS simulation parameters of sulfur, SPs, and SPGs.

Cathodes	R_s (Ω)	CPE_1 (μF)	R_p (Ω)	R_{ct} (Ω)	CPE_2 (μF)	Z_w (Ω)
Sulfur	3.50	199.10	66.15	428.10	12.90	32.32
SPs	4.06	23.06	159.10	100.70	17.91	29.46
SPGs	7.58	376.20	95.29	82.58	12.40	9.91

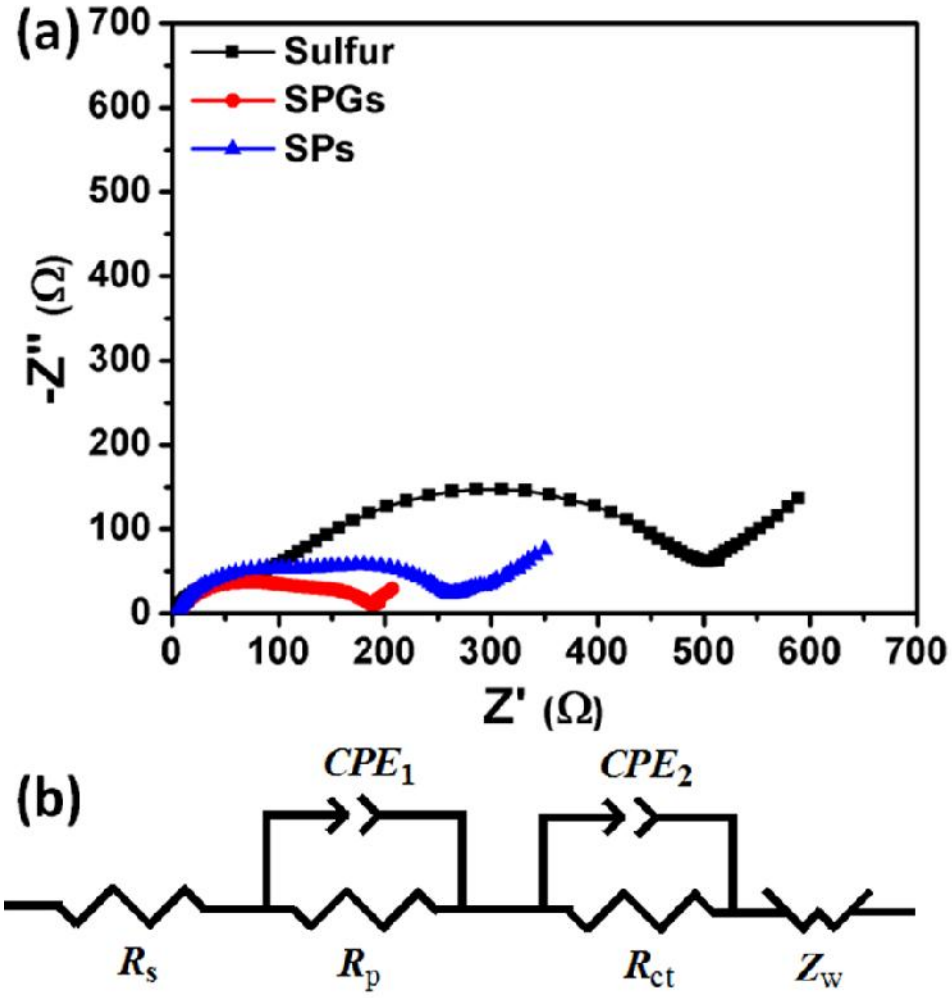

Figure 10.8. (a) Nyquist plots of sulfur, SPs, and SPGs. (b) The equivalent circuit that is used to fit the experimental data.

10.4. Conclusion

In summary, we successfully designed and synthesized a hierarchical structure composite of sulfur-polyaniline-graphene nanoribbons. In this composite, GNRs greatly improved the mechanical properties of the whole system. PANI-GNRs provided a good platform for loading sulfur with improved electronic conductivity. Electrochemical experiments demonstrate that the SPGs exhibit good rate performance and high cycling stability as cathode materials, compared to pure elemental sulfur and sulfur-polyaniline, due to the synergic effect between the PANI, GNRs and sulfur. The synthesis of the SPGs composite has been shown to produce an effective component to improve the electrochemical stability of the electrode materials for LSBs.

10.5. References

1. Li, L.; Ruan, G. D.; Peng, Z. W.; Yang, Y.; Fei H. L.; A.-R. O.; Samuel, E. L. G.; Tour, J. M. Enhanced Cycling Stability of Lithium Sulfur Batteries Using Sulfur-Polyaniline-Graphene Nanoribbons Composite Cathodes. *ACS Appl. Mater. Interfaces* **2014**, *6*, 15033-15039. (L.L. conceived and designed the experiments. L.L. and R.G.D. prepared the materials. L.L., P.Z.W., Y.Y., F.H.L., A.R.O., and S.E.L.G. performed material characterization. L.L. tested the devices and wrote the paper. Finally, T.J.M. oversaw all research phases, provided regular guidance to the research and revised the manuscript. All authors discussed and commented on the manuscript.)

2. Yang, Y.; Yu, G.; Cha, J. J.; Wu, H.; Vosgueritchian, M.; Yao, Y.; Bao Z.; Cui, Y. Improving the Performance of Lithium-Sulfur Batteries by Conductive Polymer Coating. *ACS Nano* **2011**, *5*, 9187-9193.

3. Tarascon, J. M.; Armand, M. Issues and Challenges Facing Rechargeable Lithium Batteries. *Nature* **2001**, *414*, 359-367.

4. Arico, A. S.; Bruce, P.; Scrosati, B.; Tarascon, J. M.; Schalkwijk, W. V. Nanostructured Materials for Advanced Energy Conversion and Storage Devices. *Nat. Mater.* **2004**, *4*, 366-377.

5. Whittingham, M. S. Lithium Batteries and Cathode Materials. *Chem. Rev*. **2004**, *104*, 427-4302.

6. Zhou, G.; Yin, L. C.; Wang, D. W.; Li, L.; Pei, S.; Gentle, I. R.; Li F.; Cheng, H. M. Fibrous Hybrid of Graphene and Sulfur Nanocrystals for High-Performance Lithium-Sulfur Batteries. *ACS Nano* **2013**, *7*, 5367-5375.

7. Ji, X. L.; Lee K. T.; Nazar L. F. A Highly Ordered Nanostructured Carbon-Sulphur Cathode for Lithium-Sulphur Batteries. *Nat. Mater.* **2009**, *8*, 500-506.

8. Ellis, B. L.; Lee, K. T.; Nazar L. F. Positive Electrode Materials for Li-Ion and Li-Batteries. *Chem. Mater.* **2010**, *22*, 691-714.

9. Rauh, R. D.; Abraham, K. M.; Pearson, G. F.; Surprenant J. K.; Brummer, S. B. A Lithium/Dissolved Sulfur Battery with an Organic Electrolyte. *J. Electrochem. Soc.* **1979**, *126*, 523-527.

10. Barchasz, C.; Molton, F.; Duboc, C.; Leprêtre, J. C.; Patoux S.; Alloin, F. Lithium/Sulfur Cell Discharge Mechanism: An Original Approach for Intermediate Species Identification. *Anal. Chem.* **2012**, *84*, 3973-3980.

11. Evers, S.; Nazar, L. F. New Approaches for High Energy Density Lithium-Sulfur Battery Cathodes. *Acc. Chem. Res.* **2012**, *46*, 1135-1143.

12. Dean, J. A.; Lange's Handbook of Chemistry, 3rd ed.; McGraw-Hill: New York, 1985; pp 3-5.

13. Yang, Y.; Zheng G.; Cui, Y. Nanostructured Sulfur Cathodes. *Chem. Soc. Rev.* **2013**, *42*, 3018-3032.

14. Xiao, L.; Cao, Y.; Xiao, J.; Schwenzer, B.; Engelhard, M. H.; Saraf, L. V.; Nie, Z.; Exarhos, G. J.; Liu, J. A Soft Approach to Encapsulate Sulfur: Polyaniline Nanotubes for Lithium-Sulfur Batteries with Long Cycle Life. *Adv. Mater.* **2012**, *24*, 1176-1181.

15. Wang, H.; Yang, Y.; Liang, Y.; Robinson, J. T.; Li, Y.; Jackson, A.; Cui Y.; Dai, H. Graphene-Wrapped Sulfur Particles as a Rechargeable Lithium-Sulfur Battery Cathode Material with High Capacity and Cycling Stability. *Nano Lett.* **2011**, *11*, 2644-2647.

16. Evers S.; Nazar, L. F. Graphene-Enveloped Sulfur in a One Pot Reaction: A Cathode with Good Coulombic Efficiency and High Practical Sulfur Content. *Chem. Commun.* **2012**, *48*, 1233-1235.

17. Guo, J.; Xu Y.; Wang, C. Sulfur-Impregnated Disordered Carbon Nanotubes Cathode for Lithium-Sulfur Batteries. *Nano Lett.* **2011**, *11*, 4288-4294.

18. Wu, F.; Chen, J.; Chen, R.; Wu, S.; Li, L.; Chen S.; Zhao, T. Sulfur/Polythiophene with a Core/Shell Structure: Synthesis and Electrochemical Properties of the Cathode for Rechargeable Lithium Batteries. *J. Phys. Chem. C* **2011**, *115*, 6057-6063.

19. Yu, X.; Xie, J.; Li, Y.; Huang, H.; Lai C.; Wang, K. Stable-cycle and High-capacity Conductive Sulfur-Containing Cathode Materials for Rechargeable Lithium Batteries. *J. Power Sources* **2005**, *146*, 335-339.

20. Li, X.; Cao, Y.; Qi, W.; Saraf, L. V.; Xiao, J.; Nie, Z.; Mietek, J.; Zhang, J. G.; Schwenzer, B.; Liu, J. Optimization of Mesoporous Carbon Structures for Lithium-sulfur Battery applications. *J. Mater. Chem.* **2011**, *21*, 16603-16610.

21. Zheng, G.; Yang, Y.; Cha, J. J.; Hong, S. S.; Cui, Y. Hollow Carbon Nanofiber-Encapsulated Sulfur Cathodes for High Specific Capacity Rechargeable Lithium Batteries. *Nano Lett.* **2011**, *11*, 4462-4467.

22. Zheng, G.; Zhang, Q.; Cha, J. J.; Yang, Y.; Li, W.; Seh Z. W.; Cui, Y. Amphiphilic Surface Modification of Hollow Carbon Nanofibers for Improved Cycle Life of Lithium Sulfur Batteries. *Nano Lett.* **2013**, *13*, 1265-1270.

23. Li, D.; Han, F.; Wang, S.; Cheng, F.; Sun Q.; Li, W. C. High Sulfur Loading Cathodes Fabricated Using Peapodlike, Large Pore Volume Mesoporous Carbon for Lithium-Sulfur Battery. *ACS Appl. Mater. Interfaces* **2013**, *5*, 2208-2213.

24. Zhang, S. S. Liquid Electrolyte Lithium/sulfur Battery: Fundamental Chemistry, Problems, and Solutions. *J. Power Sources* **2013**, *231*, 153-162.

25. Zhang, S. S. Role of $LiNO_3$ in Rechargeable Lithium/sulfur Battery. *Electrochim. Acta* **2012**, *70*, 344-348.

26. Barchasz, C.; Leprêtre, J. C.; Alloin, F.; Patoux, S. New Insights into the Limiting Parameters of the Li/S Rechargeable Cell. *J. Power Sources* **2012**, *199*, 322-330.

27. Nimon, Y. S.; Chu M. Y.; Visco, S. J. US Patent 6632573, **2003**.

28. Lee, Y. M.; Choi, N. S.; Park, J. H.; Park, J. K. Electrochemical Performance of Lithium/sulfur Batteries with Protected Li Anodes. *J. Power Sources* **2003**, *119*, 964-972.

29. Li, K.; Wang, B.; Su, D.; Park, J.; Ahn, H.; Wang, G. Enhanced Electrochemical Performance of Lithium Sulfur Battery Through a Solution-Based Processing Technique. *J. Power Sources* **2012**, *202*, 389-393.

30. Wu, F.; Chen, J. Z.; Li, L.; Zhao, T.; Chen, R. J. Improvement of Rate and Cycle Performence by Rapid Polyaniline Coating of a MWCNT/Sulfur Cathode. *J. Phys. Chem. C* **2011**, *115*, 24411-24417.

31. Jayaprakash, N.; Shen, J.; Moganty, S. S.; Corona, A.; Archer, L. A. Confining Sulfur in Double-Shelled Hollow Carbon Spheres for Lithium-Sulfur Batteries. *Angew. Chem. Int. Ed.* **2011**, *50*, 5904-5908.

32. Zhang, C.; Wu, H. B.; Yuan, C.; Guo, Z.; Lou, X. W. Confining Sulfur in Double-Shelled Hollow Carbon Spheres for Lithium-Sulfur Batteries. *Angew. Chem. Int. Ed.* **2012**, *51*, 9592-9595.

33. Seh, Z. W.; Li, W. Y.; Cha, J. J.; Zheng, G. Y.; Yang, Y.; Mcdowell, M. T.; Hsu, P. C.; Cui, Y. Sulphur–TiO_2 Yolk–shell Nanoarchitecture with Internal Void Space for Long-cycle Lithium-sulphur Batteries. *Nat. Commun.* **2012**, *4*, 1331-1336.

34. Evers, S.; Yim, T.; Nazar, L. F. Understanding the Nature of Absorption/Adsorption in Nanoporous Polysulfide Sorbents for the Li-S Battery. *J. Phys. Chem. C* **2012**, *116*, 19653-19658.

35. Li, G. C.; Li, G. R.; Ye, S. H.; Gao, X. P. A Polyaniline-Coated Sulfur/Carbon Composite with an Enhanced High-Rate Capability as a Cathode Material for Lithium/Sulfur Batteries. *Adv. Energy. Mater.* **2012**, *2*, 1238-1245.

36. Hager, M. D.; Greil, P.; Leyens, C.; Van der Zwaag, S.; Schubert, U. S. Self-Healing Materials. *Adv. Mater.* **2010,** *22*, 5424-5430.

37. Li, L.; Raji, A. R. O.; Fei, H.; Yang, Y.; Samuel, E. L. G.; Tour, J. M. Nanocomposite of Polyaniline Nanorods Grown on Graphene Nanoribbons for Highly Capacitive Pseudocapacitors. *ACS Appl. Mater. Interfaces* **2013**, *5*, 6622–6627.

38. Genorio, B.; Lu, W.; Dimiev, A. M.; Zhu, Y.; Raji, A.R. O.; Novosel, B.; Alemany, L. B.; Tour, J. M. *In Situ* Intercalation Replacement and Selective Functionalization of Graphene Nanoribbon Stacks. *ACS Nano* **2012,** *6*, 4231-4240.

39. Cao, Y.; Li, X.; Aksay, I. A.; Lemmon, J.; Nie, Z.; Yang, Z.; Liu, J. Sandwich-type Functionalized Graphene Sheet-sulfur Nanocomposite for Rechargeable Lithium Batteries. *Phys. Chem. Chem. Phys.* **2011,** *13*, 7660-7665.

40. Li, N.; Zheng, M.; Lu, H.; Hu, Z.; Shen, C.; Chang, X.; Ji, G.; Cao, J.; Shi, Y. High-rate Lithium-sulfur Batteries Promoted by Reduced Graphene Oxide Coating. *Chem. Commun.* **2012,** *48*, 4106-4108.

41. Semmelhack, H. C.; Höhne, R.; Esquinazi, P.; Wagner, G.; Rahm, A.; Hallmeier, K. H.; Spemann, D.; Schindler, K. Growth of Highly Oriented Graphite Films at Room Temperature by Pulsed Laser Deposition Using Carbon-sulfur Targets. *Carbon* **2006,** *44*, 3064-3072.

42. Ji, L.; Rao, M.; Zheng, H.; Zhang, L.; Li, Y.; Duan, W.; Guo, J.; Cairns, E. J.; Zhang, Y. Graphene Oxide as a Sulfur Immobilizer in High Performance Lithium/Sulfur Cells. *J. Am. Chem. Soc.* **2011,** *133*, 18522-18525.

43. Zu, C.; Su, Y. S.; Fu, Y.; Manthiram, A. Improved lithium–sulfur cells with a treated carbon paper interlayer *Physi. Chem. Chem. Phys.*, 2013**, 15**, 2291-2297.